Metal-organic porous materials for carbon dioxide valorization, water adsorption and photocatalytic hydrogen production

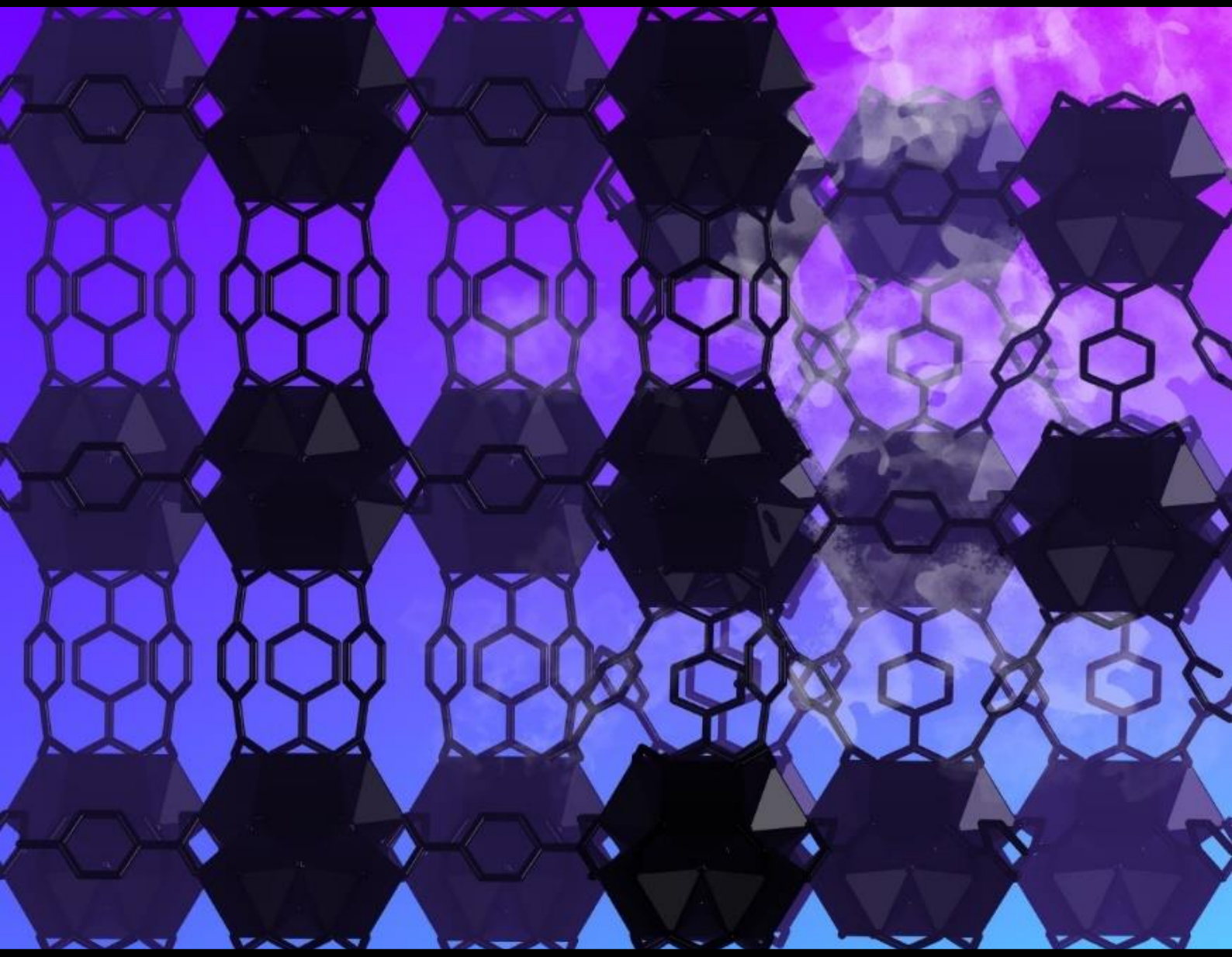

PhD Thesis

Maite Perfecto Irigaray

eman ta zabal zazu
Universidad del País Vasco
Euskal Herriko Unibertsitatea

Leioa, January 2023

Universidad del País Vasco Euskal Herriko Unibertsitatea
ZIENTZIA ETA TEKNOLOGIA FAKULTATEA
FACULTAD DE CIENCIA Y TECNOLOGÍA

ORGANIC AND INORGANIC CHEMISTRY DEPARTMENT
DEPARTAMENTO DE QUÍMICA ORGÁNICA E INORGÁNICA

FCT/ZTF, UPV/EHU

Metal-organic porous materials for carbon dioxide valorization, water adsorption and photocatalytic hydrogen production

Materiales porosos metal-orgánicos para la revalorización de dióxido de carbono, adsorción de agua y producción fotocatalítica de hidrógeno

PhD Thesis

Tesis Doctoral

MATERIALS SCIENCE AND TECHNOLOGY PhD PROGRAMME

PROGRAMA DE DOCTORADO EN CIENCIA Y TECNOLOGÍA DE MATERIALES

Manuscript submitted by
Memoria presentada por

MAITE PERFECTO IRIGARAY

under the supervision of
bajo la dirección de

GARIKOITZ BEOBIDE PACHECO
SONIA PÉREZ YÁÑEZ

Leioa, enero de 2023

A mi padre

A mi madre

A mi tato

Contents

Resumen

Esta tesis doctoral se basa en el desarrollo de materiales meta-orgánicos porosos como son las denominadas redes metal-orgánicas (*metal-organic frameworks*, MOFs), los geles metal-orgánicos (*metal-organic gels*, MOGs) y los aerogeles metal-orgánicos (*meta-organic aerogels*, MOAs), utilizados a lo largo del trabajo enla valorización de CO_2, la adsorción de agua y la producción fotocatalítica de hidrógeno. Cada tipo de material ha sido diseñado específicamente para obtener el mejor rendimiento en cada específica: (i) MOFs heterometálicos de Cu(II) para la conversión electroquímica de CO_2 a alcoholes, (ii) MOFs robustos de Zr(IV)- y Hf(IV) para mejorar la estabilidad tanto durante la conversión electroquímica de CO_2 como en la adosrción de vapor de agua, y (iii) MOGs y MOAs de Ti(IV) para la reducción CO_2 y la producción de hidrógeno fotoquímicas.

De esta forma, la primera parte de la tesis (Capítulo 3) describe la síntesis y el desempeño electroquímico de MOFs basados en cobre (HKUST-1(Cu,MD) y mezclas de HKUST-1(Cu) y CAU-17(Bi) , que a pesar de conducir a velocidades de reacción y eficiencias Faradaicas mucho mayores que otras redes metal-orgánicas analizadas previamente, carecen de estabilidad a largo plazo. Por esta razón, en el Capítulo 4, se sintetiza una nueva familia de MOFs robustos de Zr(IV) y Hf(IV) y ligandos dicarboxilato (benceno-1,4-dicarboxilato, BDC y 2-aminobenceno-1,4-dicarboxylato, NH_2BDC), denominada familia EHU-30 (de Euskal Herriko Unibertsitatea) Su rendimiento como catalizadores electroquímicos en la reducción CO_2 no supera los resultados obtenido con la familia HKUST-1, pero las tasas de producción y eficiencias farádicas no decaen a lo largo del tiempo de reacción explorado (400 min), lo que se puede atribuir a una mayor estabilidad de la red de coordinación. Así mismo, se evalúa su capacidad como adsorbentes de vapor de agua, presentando un carácter más hidrofílico que su familia de polimorfos, la familia UiO-66.

En la última parte de la tesis (Capítulo 5) se desarrollan de MOGs y MOAs de Ti(IV) y BDC/NH_2BDC constituidos por partículas nanoscópicas entrelazadas en una estructura meso-/macroporosa con la capacidad de comportarse como fotocatalizadores bajo luz visible. La funcionalización de estos MOGs de Ti(IV) con Cu/porfirina mejora considerablemente los rendimientos en la reducción de CO_2 aportados por MOFs de naturaleza similar y catalizadores inorgánicos. La presencia de Cu(II) mejora considerablemente la selectividad hacia productos más reducidos de interés, como el etanol. Finalmente, los MOGs de Ti(IV) testados en la producción de hidrógeno presentan rendimientos bajos, pero su actividad muestra una tendencia de interesantes cunado se someten exclusivamente a radiación visible, requiriéndose de más estudios para entender el comportamiento y poder aplicarlo en el desarrollo de mejores fotocatalizadores.

Abstract

Herein presented PhD thesis is based on the development of metal-organic porous materials, such as metal-organic frameworks (MOFs), metal-organic gels (MOGs) and metal-organic aerogels (MOAs), which are further employed for CO_2 valorization, water adsorption and photocatalytic hydrogen production. Each type of material has been specifically designed with the aim of obtaining the best performance in a specific application: (i) Cu(II)-based heterometallic MOFs for electrochemical conversion of CO_2 into alcohols, (ii) robust Zr(IV)- and Hf(IV)-based MOFs for improving the stability in electrochemical conversion of CO_2 and water-vapour adsorption, and (iii) Ti(IV) based MOGs and MOAs for photochemical CO_2 reduction and hydrogen production.

In this way, the first part of this thesis (chapter 3) describes the synthesis and electrochemical performance of copper-based MOFs (HKUST-1(Cu,M_D) and blends of HKUST-1(Cu) and CAU-17(Bi), which despite of leading to reaction rates and Faradaic efficiencies far greater than any previously analyzed metal-organic framework, they lack of stability. For this reason, in chapter 4, we develope a new family of robust MOFs named as EHU-30 and based on group 4 metals (Zr(IV) and Hf(IV)) and benzene-1,4-dicarboxylato ligand with or without amino-type functional groups. Their use as electrocatalysts in the electrochemical CO_2 reduction, demonstrates that the achieved performance does not surpass that achieved with HKUST-1 family, but conversely, the production rates and Faradic efficiencies do not decay along the explored reaction time (400 min) which can be ascribed to the greater stability of the coordination framework. Besides, profiting the chemical stability of the EHU-30 series we have assessed their potential as water harvesting materials.

The last part of the thesis (chapter 5) is related to the development of Ti(IV) MOGs and MOAs consisting of nanoscopic metal-organic framework particles entangled into a meso-/macroporous structure with the capability of behaving as photocatalysts under visible light. The functionalization of these Ti(IV) MOGs with Cu/porphyrine demonstrated to photocatalyze the CO_2 photoreduction into alcohols with performances that overpassed that reported for MOFs and inorganic catalysts. Interestingly, the presence of Cu(II) played a crucial role counterbalancing the selectivity towards more demanding ethanol production. Moreover, pristine Ti(IV) MOGs showed relatively low yields in the hydrogen evolution reaction, but their activity was markedly boosted upon the *in situ* addition of platinum in the reaction media or by doping with platinum the gel framework. Despite of this improvement, the overall performance is still below that provided by conventional materials, but they show interesting trends and thus, further work is still required for understanding and to improve their photocatalytic activity.

Chapter 1

PhD Thesis contextualization and objectives

1.1. INTRODUCTION

Porosity in the solid state has always been a striking point in materials science, but in the last decades the study of this type of compounds has experienced an outstanding development due to the appearance of new porous materials such as MOFs that are extending from the nanoscale to the macroscale with endless underlying applications.[1]

1.1.1. Metal-organic frameworks: features and generalities

Metal-organic frameworks (MOFs, also known as porous coordination polymers or PCPs) have led to an overwhelming number of research articles which get the attention of the scientific community devoted to chemistry, physics, materials science or to any other bordering research area during the last edcades.[2] The structures of MOFs can be rationalised as the assembly of inorganic nodes, isolated metal atoms or metal clusters and organic ligands into coordination networks containing potential voids. Despite there are endless possibilities of combining inorganic nodes and organic linkers, they can be judiciously selected in order to accomplish a rational design of the structure. The archetypical organic units are ditopic or polytopic organic carboxylates (and other similar negatively charged molecules, like polyazines), which, when linked to metal-containing units, yield architecturally robust MOF structures with a typical porosity greater than 50% of the crystal volume. The surface area values of such MOFs typically range from 1000 to 7000 m^2/g, thus exceeding those of traditional porous materials such as zeolites and carbons. To date, MOFs with permanent porosity are more extensive in their variety and multiplicity than any other class of porous materials.

Accordingly, these structures can be tuned almost at will with the aim of developing materials with desired applications, since, the physical and chemical properties of these compounds can be directed as a consequence of an accurate selection of the building blocks.[3] In fact, MOFs have demonstrated to meet successfully porosity with a series of appealing properties such as luminescence, magnetism or electrical conductivity, since they benefit from their hybrid metal-organic nature.[4] Moreover, the design of the building blocks (SBUs, 'secondary building units' comprises by the metal/metal cluster and part of the organic ligand; and the so as called bridging organic linker) allows also to integrate specific interaction sites inside the framework with the aim of invigorating gas storage capacity, adsorption selectivity, stimuli-response behaviour, or catalytic activity which response for the most remarkable applications of MOFs.[5]

In this way, MOFs are considered potentially suitable materials to face some of the concerns of our planet since they are being investigated for addressing matters such as storage systems for cleaner energy vectors (hydrogen and methane fuels) and for the capture and sequestration of carbon dioxide as the urgent response to ongoing climate change.[6] It is also promising their application in sensoric, where a change of

physical properties of the framework caused by the guest molecule is used to detect the latter.[7] Another application worth of mentioning relies on their use as drug delivery systems as it has been demonstrated that the ability to tune their structures and porosities can provide better drug interactions and high loadings.[8] Chemical transformations can also be regarded as an outstanding application of MOFs having specific active catalytic sites in the framework or the pores.

Nonetheless, conventional MOFs based on divalent transition metal (*i.e.* Zn(II), Cu(II), Co(II), Ni(II), Cd(II), etc.) usually suffer from weak stability, such as poor acid/base stability, water stability, thermal stability, and/or mechanical stability. Thus, much effort has been devoted recently to synthesise MOFs with increased stability in order to overcome aforementioned drawbacks. In this sense, group 4 metal based ones, that is Ti-, Zr-, and Hf-based MOFs, are one of the most attractive families of MOFs owing to their superior chemical stability and structural tenability.[9] This stability of group 4 metal-based MOFs is due to the high oxidation state they have (*i.e.* IV). Actually, when the oxidation state increases, the cation becomes harder and the polarization of the bond with the oxygen of the carboxylate group rises, leading to a more robust bond. Moreover, a higher charge of the cation leads to a greater connectivity between nodes or clusters to compensate for the charge, which as a result strengthens further the stability of the coordination network.[10]

Among these MOFs, Zr-based were the first one developed and have been widely explored since its discovery. The synthesis of UiO-66, -67 and -68[11] was a major step in the area of MOFs, which boosted the development of Zr-MOFs.[12] The secondary building unit of these structures, $[Zr_6(\mu_3\text{-}O)_4(\mu_3\text{-}OH)_4(\mu\text{-}COO)_{12}]$ is 12-fold connected by means of ditopic linkers (phenyl, biphenyl and terphenyl, respectively) to yield a face centred cubic net. Figure 1.1 shows the structure of the aforementioned UiO-66 with formula $[Zr_6(\mu_3\text{-}O)_4(\mu_3\text{-}OH)_4(\mu_4\text{-}C_8H_4O_4)_6]_n$, in which the hexanuclear Zr clusters are connected by twelve benzene-1,4-dicarboxylato ligands forming a face centred cubic (fcc) structure.

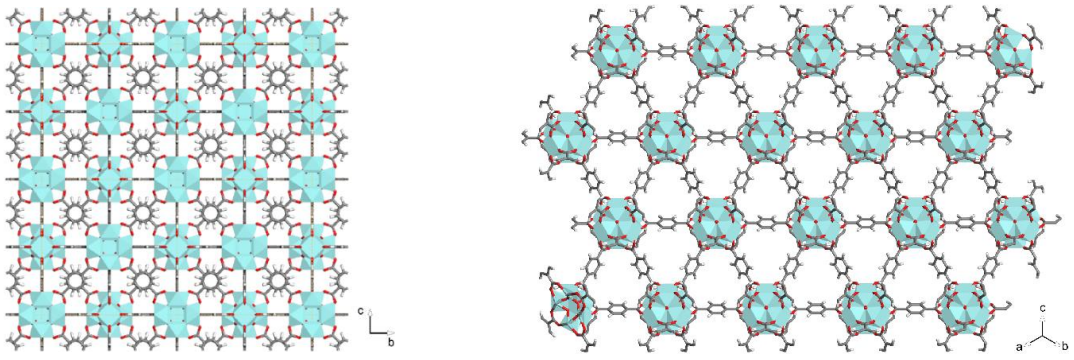

(a) (b)

Figure 1.1. (a) Crystal packing view of UiO-66 along [100] crystallographic direction. (b) Bidimensional hexagonal subnets (**hxl**) of UiO-66 in which six of the BDC ligands are linking six coplanar Zr-SBUs.

1.1.2. Metal-organic gels and aerogels

In the last few years, metal-organic gels (MOGs)[13] and aerogels (MOAs)[14] have emerged as an alternative material to MOFs. To get a better understanding of what MOG and MOAs are, attention must be paid to their formation process. In this regard, during the gel formation, the coordination polymer grows as nanoscopic primary particles that crosslink stochastically into the reaction media creating a three-dimensional solid network that entraps all synthesis solvent within. Once the MOG is formed, it can be subjected to a supercritical drying process, which allows removing the solvent without collapsing their microstructure, and it leads to materials so-called metal-organic aerogels (MOAs). Consequently, porosity in MOGs and MOAs has a microstructural origin and not strictly crystallographic one like in MOFs. Thus, the gelation approach enables to prepare porous materials from almost any metal-organic system as it is possible to dispense of the prerequisites imposed by the reticular design when MOFs are aimed to be synthesised. Keeping in mind that the examples of MOGs and MOAs are relatively scarce, there is still an exciting chance to prepare metal-organic porous materials from coordination polymers that lack of crystalline origin porosity but gather striking electrical, magnetic and/or optical properties.[15]

Regarding their porosity, MOAs are featured by a markedly high specific pore volume which makes them hundred times lighter than MOFs. Furthermore, the stochastic nature of the gelling process generates open voids of random shape and size with distribution modes usually located in the meso- and macroporous range (2–50 nm and > 50 nm, respectively). A larger pore facilitates migration and diffusion of chemical species and allows the passage of macromolecules, what suppose an advantage with respect to MOFs for some applications. The augmentation of MOF channel sizes to mesoporous range still poses a great challenge. Ligand extension is an apparent option, but MOFs built from large ligands tend to collapse upon guest removal and often are accompanied by framework interpenetration.[16] They are usually non-crystalline materials, but their features make them excellent candidates to compete or surpass MOFs in some applications, especially in the adsorption and catalysis-related topics due to their exceptional porosity nature.[17]

1.1.3. CO_2 capture and conversion and green hydrogen production

The large-scale consumption of fossil fuels for the production of energy has raised CO_2 levels from a preindustrial level of about 280 ppm to surpass the 400 ppm.[18] According to International Energy Agency (IEA) statistics, oil, coal, and natural gas still represent 80.9% of the total energy supply in the world in 2019, while renewable energies only accounted for 14.1%. Total CO_2 emissions from energy combustions and industrial processes have substantially grow accordingly, going from less than 5 Gt in 1900 to more than 35 Gt in 2021.[19,20] The natural carbon cycle has been exceeded, causing

severe environmental problems. Therefore, the development of methodologies to reduce CO_2 emissions has been a priority in the research agenda worldwide the last decades. These methodologies may be used to produce alternative energy sources and value-added chemicals, and thus, they may mitigate the negative effects of global warming by reducing the rising levels of CO_2 emissions into the atmosphere.[21]

In order to face the problem research efforts are made to develop capture, storage and revalorization solutions, apart from the use of cleaner energies. There are two major viable promising options to reduce the CO_2 emissions to the atmosphere: (i) to Capture and Storage CO_2 (CCS) for long periods, or rather (ii) convert CO_2 into useful low-carbon fuels in a Carbon Capture and Utilization (CCU) approach. CCU is nowadays recognized as a feasible and promising cutting-edge area of exploration in energy and environmental research that can perfectly complement the storage of huge quantities of CO_2 via CCS. In this regard, CO_2 can be considered an appealing carbon source for the synthesis of valuable chemicals. The success of such kind of transformation process would imply to make of CO_2 an indispensable by-product instead an undesired emission. To this end, several methods are being intensively studied for the conversion of CO_2 such as chemical, thermochemical, photochemical, biochemical, electrochemical photoelectrochemical and hydrothermal methods.[22] Among them, electrocatalytic and photocalytic valorization stands out due to its simple procedure and ambient operation conditions. If the synthesis of chemicals using solar energy, the so-called "artificial photosynthesis" (*i.e.* the photo- and photoelectro-catalytic reduction of CO_2 with H_2O) can be practically applied, a carbon circulation system would then be feasible to produce stable energy carriers, which implies both saving the environment and supplying future energy.[23]

Among the heterogeneous photocatalysts, the use of semiconductors such as TiO_2 has been widely explored. Few years ago, MOFs demonstrated to be suitable catalyst for the none-illuminated electrochemical transformation of CO_2 into alcohols such as methanol and ethanol.[24] It has been also proven that the use of heterometallic MOFs can assist more efficiently certain steps of the cascade reaction that implies the CO_2 conversion and as a result, the overall performance and selectivity can be markedly enhanced. More recently, metal-organic frameworks (MOFs) have emerged as promising photocatalytic materials for the light-driven CO_2 reduction. In these works, products such CO, HCOOH and CH_3OH were claimed. Furthermore, some of the reported MOFs exhibited photoactivity under visible radiation which can be pointed as an advantage with regard to benchmark TiO_2 with a bandgap corresponding to UV energy. However, the performance of MOF in the CO_2 photoreduction is still limited, thus taking into the inexhaustible chemical and structural versatility of these kind of materials there is an appealing chance to reach meaningful advances in the photochemical transformation of CO_2. In this sense, reported works make use of a

sacrificial reagent (oxidation substrate) which worsens the atomic efficiency of the overall process.[25] Thus, getting metal-organic photocatalyst that provide high performance and avoiding the use of sacrificial reagent is still a current challenge that this PhD aims to deal with.

The term green hydrogen is related to the hydrogen (H_2) produced by means of renewable energy sources that imply zero or neglible emissions of greenhouse gases. Green hydrogen must be distinguished from other hydrogen production methods, such as that consisting of natural gas steam reforming technique, which nowadays represents 95% of the commercial market.[26] There are several ways to produce green hydrogen,[27] among which stand out the electrolysis of water with the electricity produced by low-carbon energy sources. Alternatively, photochemical and photo-electrochemical methods have demonstrated to prompt the green hydrogen production from water. It deserves to note, that despite photochemical and photoelectrochemical methods show a lower technology readiness level than electrocatalytic methods, ideally they do not require an external energy input to conduct the hydrogen production reaction and thus, they have the potential to overcome more easily the emission of greenhouse gases.

The commonly employed electrocatalyst and photocatalyst for hydrogen evolution reaction have involved conventional inorganic catalyst (metallic nanoparticles, semiconductors, etc…), hover, rather recently, metal-organic frameworks have bounced into this field providing a promising alternative, which is currently yielding many high-impact publications.[28,29]

Further details about MOFs, MOGs and their applications in these fields will be described and discussed in the following chapters of this PhD thesis manuscript.

1.2. OBJECTIVES

As commented, despite several technologies have been posited as sustainable solutions for CO_2 conversion and hydrogen production, those based on the electrochemical and photochemical methods can be considered as two of the most promising ones. Note that despite the electrochemical methods require an energy input to operate, this can be provided by a renewable energy source, such as photovoltaic energy. In both methods the design of the reactor and of the catalyst (*i.e.* the so-called, electrocatalyst and photocatalyst) play a crucial role in the overall performance. Regarding the catalysts, as it will be further analyzed in the following chapters, metal-organic materials have been posited as considerable alternative to the more conventional inorganic materials, specially due to the high-surface area and the tunabiltiy of pore-size, surface-chemistry and electronic properties of the former ones.

Hovewer, considering that metal-organic materials are incipient electro- and photocatalysts compared to conventional inorganic materials, this PhD thesis has aimed to explore this valuable chance in order to get deeper insights into the possibilities that metal-organic materials can provide in the electrochemical and photochemical conversion of CO_2 and hydrogen production.

The first specific objective has pursued to analyze the synthesis and application of copper-based heterometallic MOFs in the electrochemical conversion of CO_2 into alcohols. The results of this objective are gathered in Chapter 3 and they led to the publication of two research articles: (1) *RSC Advances*, **2018**, 8, 21092–21099 (https://doi.org/10.1039/C8RA02676A) and (2) *Journal of CO_2 Utilization*, **2019**, 33, 157–165 (https://doi.org/10.1016/j.jcou.2019.05.025).

The second specific objective has aimed to develop a new family of robust MOFs based on groups 4 metals (zirconium(IV) and hafnium(IV)) that can constitute a more competitive alternative for the electrochemical conversion of CO_2 to alcohols, in term of performance and stability, than the up-to-date reported works. Besides, profiting the pursued chemical stability improvement we will aim to assess the water vapour harvesting behavior of the EHU-30 series. The obtained results are described in Chapter 4 and they have led to the publication of the following three research papers: (1) *Chemical Communications*, **2019**, 55, 5954–5957 (https://doi.org/10.1039/C9CC00802K), (2) *Inorganic Chemistry Frontiers*, **2021**, 8, 4767–4779 (https://doi.org/10.1039/D1QI00997D) and (3) *Scientific Reports*, **2022**, 12, 8505 (https://doi.org/10.1038/s41598-022-11846-w).

Finally, the third specific objective have aspired to develop new metal-organic gels comprised by the group 4 metal titanium(IV) and to explore their performance into the photochemical CO2 reduction and hydrogen evolution reactions. Note that the pore-size of MOGs (meso-/macroporous) is far greater than the one corresponding to the intrinsic porosity of MOFs, and thus MOGs have a potential advantage in terms of the mass transport of reagents and products which can produce a performance improvement of the reactions. The results related to this last objective are gathered in Chapter 5, and are still unpublished.

1.3. References

1 D. W. Bruce, D. O'Hare, R. I. Walton, *Porous Materials*; Wiley, 2011.

2 L. Jiao, J. Yen, R. Seow, W. S. Skinner, Z. U. Wang, Metal-organic frameworks: structures and functional applications, *Materials Today,* **2019**, 27, 43–68.

3 J. -C. Tan, B. Civalleri, Metal-organic frameworks and hybrid materials: from

fundamentals to applications, *CrystEngComm* **2015**, 17, 197–198

4 H.-C. Zhou, S. Kitagawa, Metal-organic frameworks (MOFs), *Chem. Soc. Rev.* **2014**, 43, 5415–5418.

5 B. Li, M. Chrzanowski, Y. Zhang, S. Ma, Applications of metal-organic frameworks featuring multi-functional sites, *Coord. Chem. Rev.*, **2016**, 307, 106–129.

6 A. Schoedel, Z. Ji, O. M. Yaghi, The role of metal-organic frameworks in a carbon neutral energy cycle, *Nature Energy* **2016**, 1, 16034.

7 Z. Hu, B. J. Deiberta , J. Li, Luminescent metal-organic frameworks for chemical sensing and explosive detection, *Chem. Soc. Rev.* **2014**, 43, 5815–5840.

8 M. Giménez-Marqués, T. Hidalgo, C. Serre, P. Horcajada, Nanostructured metal-organic frameworks and their bio-related applications, *Coord. Chem. Rev.* **2016**, 307, 342–360.

9 S. Yuan, J. –S. Qin, C. T. Lollar, H.-C. Zhou, Stable Metal–Organic Frameworks with Group 4 Metals: Current Status and Trends. *ACS Cent. Sci.* **2018**, 4, 440–450.

10 R. G. Pearson, Hard and Soft Acids and Bases. *J. Am. Chem. Soc.* **1963**, 85, 3533–3539.

11 J. H. Cavka, S. Jakobsen, U. Olsbye, N. Guillou, C. Lamberti, S. Bordiga, K. P. Lillerud, A New Zirconium Inorganic Building Brick Forming Metal Organic Frameworks with Exceptional Stability. *J. Am. Chem. Soc.* **2008**, 130, 13850–13851.

12 Y. Bai, Y. Dou, L.-H. Xie, W. Rutledge, J.-R. Li, H.-C. Zhou, Zr-Based Metal–Organic Frameworks: Design, Synthesis, Structure, and Applications. *Chem. Soc. Rev.* **2016**, 45, 2327–2367.

13 A. Y. -Y. Tam, V. W. -W. Yam, Recent advances in metallogels, *Chem. Soc. Rev.* **2013**, 42, 1540–1567.

14 D. Vallejo-Sánchez, P. Amo-Ochoa, G. Beobide, O. Castillo, M. Fröba, F. Hoffmann, A. Luque, P. Ocón, S. Pérez-Yáñez, Chemically resistant, shapeable, and conducting metal-organic gels and aerogels built from dithiooxamidato ligand, *Adv. Funct. Mater.* **2017**, 27, 1605448

15 J. H. Jung, J. H. Lee, J. R. Silverman, G. John, Coordination polymer gels with important environmental and biological applications, *Chem. Soc. Rev.* **2013**, 42, 924–936.

16 I. Senkovska and S. Kaskel, Ultrahigh porosity in mesoporous MOFs: promises and limitations, *Chem. Commun.*, **2014**, 50, 7089.

17 J. K. Wychowaniec, H. Saini, B. Scheibe, D. P. Dubal, A. Schneemann and K. Jayaramulu, Hierarchical porous metal–organic gels and derived materials: from fundamentals to potential applications, *Chem. Soc. Rev.*, **2022**, 51, 9068–9126.

18 National Ocean and Atmospheric Admisnistration (NOAA), National Centers for Environmental Information, Global Climate Change Indicators, *https://www.climate.gov/news-features/understanding-climate/climate-change-atmospheric-carbon-dioxide,* (accesed: January 2023).

19 International Energy Agent, Key world energy statistics 2021 – Statistics Report, *IEA Publ.*, 2021, 1–82.

20 Internaional Energy Agent, Global energy review: CO_2 emissions in 2021, *IEA Publ.*, 2021, 1–14.

21 J. Albo, M. Alvarez-Guerra and A. Irabien, Electro-, photo-, and photoelectro-chemical reduction of CO_2, in Heterogeneous Catalysts: Advanced Design, Characterization and Applications, eds. W. Y. Teoh, A. Urakawa, Y. H. Ng and P. Sit, WILEY-VCH GmbH, First Edit., 2021, pp. 649–669.

22 G. Centi, S. Perathoner, Opportunities and prospects in the chemical recycling of carbon dioxide to fuels, *Catal. Today.* **2009**, 148, 191–205.

23 J. Xu, L. Lu, C. Zhu, Q. Fang, R. Liu, D. Wang, Z. He, S. Song and Y. Shen, Insights into conduction band flexibility induced by spin polarization in titanium-based metal–organic frameworks for photocatalytic water splitting and pollutants degradation, *J. Colloid Interface Sci.*, **2023**, 630, 430–442.

24 J. Albo, D. Vallejo, G. Beobide, O. Castillo, P. Castaño, A. Irabien, Copper-based metal-organic porous materials for CO_2 electrocatalytic reductions to alcohols, *ChemSusChem.* **2016**, 10, 1100.

25 R. Li, W. Zhang and K. Zhou, Metal–organic-framework-based catalysts for photoreduction of CO_2, *Adv. Mater.*, **2018**, 30, 1705512.

26 Global Hydrogen Review 2022, IEA: International Energy Agency; https://www.iea.org; Access: 10/01/2022.

27 R. Raman, V. K. Nair, V. Prakash, A. Patwardhan, P. Nedungadi, Green-hydrogen research: what have we achieved, and where are we going? Bibliometrics analysis, *Energy Reports*, **2022**, 8, 9242–9260.

28 J. Wang, A. S. Cherevan, C. Hannecart, S. Naghdi, S. P. Nandan, T. Gupta and D. Eder, Ti-based MOFs : New insights on the impact of ligand composition and hole scavengers on stability, charge separation and photocatalytic hydrogen evolution, *Appl. Catal. B Environ.*, **2021**, 283, 119626.

32 F. Anaya-Rodríguez, J. C. Durán-Álvarez, K. T. Drisya, R. Zanella, The Challenges of Integrating the Principles of Green Chemistry and Green Engineering to Heterogeneous Photocatalysis to Treat Water and Produce Green H_2. *Catalysts* **2023**, 13, 154.

Chapter 2

Characterization techniques, experimental set-ups and computational details

2.1. REAGENTS

Table 2.1 and Table 2.2 show the reagents and solvents employed, respectively and sorted alphabetically, along with some data of interest and the role played in the experimental process they were involved. All of them were used as commercially available.

Table 2.1. Reagents employed in the thesis experimental methods.[a]

Reagent	Formula	Commercial House	Assay (%)	ρ (20 °C) (g/cm³)	MW (g/mol)	Process
2-aminobenzene-1,4-dicarboxylic acid / 2-aminoterephthalic acid	$C_8H_7NO_4$ (*H_2NH_2BDC*)	Sigma Aldrich	99	–	181.15	Organic ligand
Benzene-1,4-dicarboxylic acid / terephthalic acid	$C_8H_6O_4$ (*H_2BDC*)	Sigma Aldrich	98	–	166.13	Organic ligand
Bismuth(III) nitrate pentahydrate	$Bi(NO_3)_3 \cdot 5H_2O$	Sigma Aldrich	100	–	485.07	Bismuth(III) source
Cobalt(II) nitrate hexahydrate	$Co(NO_3)_2 \cdot 6H_2O$	Sigma Aldrich	98	–	291.03	Cobalt(II) source
Copper(II) acetate monohydrate	$Cu(CH_3COO)_2 \cdot H_2O$	Sigma Aldrich	99	–	199.65	Copper(II) source
Copper(II) nitrate hemi(pentahydrate)	$Cu(NO_3)_2 \cdot 2.5H_2O$	Sigma Aldrich	98	–	232.59	Copper(II) source
Hafnium(IV) isopropoxide isopropanol adduct	$Hf(OCH(CH_3)_2)_4$	Sigma Aldrich			414.84	Hafnium(IV) source
Hexachloroplatinic(IV) acid hydrate	H_2PtCl_6 xH2O	Sigma Aldrich	99.9	–	409.81 (anhydrous)	Platinum(IV) source
Hydrochloric acid	HCl	Labkem	35-38 (w/w) AGR	1.12	36.46	Acidification and digestion
Iron(II) chloride	$FeCl_2$	Sigma Aldrich	98	–	126.75	Iron(II) source
Isobutyric acid	$(CH_3)_2CHCO_2H$	Sigma Aldrich	99	0.950	88.11	Synthesis modulator
Manganese(II) nitrate tetrahydrate	$Mn(NO_3)_2 \cdot 4H_2O$	Panreac	97	–	251.01	Manganese(II) source
meso-Tetra(4-carboxy-phenyl)porphine	$C_{48}H_{30}N_4O_8$ (*H_4TCPP*)	Apollo Scientific	97	–	790.77	Organic ligand
Methacrylic acid	$H_2C=C(CH_3)COOH$	Sigma Aldrich	99	1.015 (25 °C)	86.09	Synthesis modulator
Nafion dispersion 5% w/w in water and 1-propanol	$C_7HF_{13}O_5S \cdot C_2F_4$	Alfa Aeser	–	–	–	GDEs preparation
Nickel(II) nitrate hexahydrate	$Ni(NO_3)_2 \cdot 6H_2O$	Sigma Aldrich	98.5	–	290.79	Nickel(II) source
Nitric acid	HNO_3	Sigma Aldrich	69	1.416	63.01	Sample digestion
Palladium(II) acetate	$Pd(CH_3COO)_2$	Sigma Aldrich	98	–	224.51	Palladium(II) source
Potassium hydrogencarbonate	$KHCO_3$	Panreac	99.5	–	100.12	CO_2 electro-reduction process
Potassium hydrogencarbonate	$KHCO_3$	Panreac	97	–	100.12	Electrolyte

Pottasium bromide	KBr	Sigma Aldrich	99	–	119.00	FTIR pellets preparation
Ruthenium(III) chloride hydrate	$RuCl_3 \cdot xH_2O$	Sigma Aldrich	100	–	207.43 (anhydrous)	Ruthenium(III) source
Sodium hydroxyde	NaOH	Sigma Aldrich	98	–	40.00	Basification
Titanium(IV) n-butoxide	$Ti(CH_3CH_2CH_2CH_2O)_4$	Sigma Aldrich	98	1.00	340.32	Titanium(IV) source
trans-Butenedioic acid / fumaric acid	$HO_2CCH=CHCO_2H$	Sigma Aldrich	99	–	116.07	^{1}H-NMR internal standard
Triethanolamine	$(HOCH_2CH_2)_3N$	Sigma Aldrich	98	–	149.19	Electron donor
Trimesic acid (Benzene-1,3,5-tricarboxylic acid)	$C_9H_6O_6$ (*H3BTC*)	Sigma Aldrich	95	–	210.14	Organic ligand
Zinc nitrate hexaydrate	$Zn(NO_3)_2 \cdot 6H_2O$	Fluka	99	–	297.49	Zinc(II) sorce
Zinc(II) acetate dihydrate	$Zn(CH_3COO)_2 \cdot 2H_2O$	Sigma Aldrich	99	–	219.51	Zinc(II) source
Zirconium(IV) propoxide	$Zr(OCH_2CH_2CH_3)_4$	Sigma Aldrich	70 (wt in 1-propanol)	1.044 (25 °C)	327.57	Zirconium(IV) source

[a] ρ: density, MW: molecular weight, GDE: gas diffusion electrode, FTIR: Fourier-transform infrared, ^{1}H-NMR: Proton nuclear magnetic resonance.

Table 2.2. Solvents employed in the thesis experimental methods.[a]

Solvent	Formula	Commercial House	Assay (%)	ρ (20 °C) (g/cm³)	MW (g/mol)	Process
Butan-2-ol	$CH_3CH_2CH(OH)CH_3$	Sigma Aldrich	99	0.81	74.12	Synthesis and cleaning solvent
Absolute ethanol	CH_3CH_2OH / C_2H_5OH (*EtOH*)	Scharlab	ACS	0.789	46.07	Synthesis and cleaning solvent
Deionized water	DI H_2O	–	–	0.998	18.01	Cleaning solvent
Deuterium oxide / deuterated water	D_2O	Sigma Aldrich	99.9	1.11	20.03	^{1}H-NMR digestions
Isopropanol (propan-2-ol)	$(CH_3)_2CHOH$	Sigma Aldrich	99.7	0.784	60.10	GDEs preparation
Methanol	CH_3OH (*MeOH*)	Labkem	99.8	0.792	32.04	Synthesis and cleaning solvent
N,N-dimethylformamide	$(CH_3)_2NCHO$ (*DMF*)	Labkem	99.9	0.95	73.09	Synthesis and cleaning solvent

[a] ρ: density, MW: molecular weight, ^{1}H-NMR: Proton nuclear magnetic resonance, GDE: gas diffusion electrode.

2.2. CHARACTERIZATION TECHNIQUES

2.2.1. Chemical characterization

Electrospray ionization mass spectrometry (ESI-MS) measurements were performed in a high resolution mass spectrometer (Synapt G2 from Waters Cromatografia S.A., time of flight analyser (TOF)) of the General Research Services of the UPV/EHU (*SGIker*), equipped with an electrospray ionization source in positive and negative mode. The high resolution spectra were recorded in scan mode, with a mass range of 30–1200 Da in resolution mode (FWHM ≈ 20 000) and a scan time of 0.1 s. The source and desolvation temperatures were 120 and 350 °C, respectively. The capillary voltage was set to 2.5 kV (negative), while the cone voltage maintained at 15 V. N_2 was used as the desolvation and cone gas, with flow rates of 600 and 10 L/h. Prior to analysis, the mass spectrometer was calibrated using a sodium formate solution and a leucine-enkephalin solution for the lock mass correction, monitoring the ions at mass-to-charge ratio (m/z) 556.2771. All of the acquired spectra were automatically corrected during acquisition based on the lock mass.

Fourier-transform infrared (FTIR) spectra of the samples were recorded at a resolution of 4 cm^{-1} in the 4000–400 cm^{-1} region using a FTIR 8400S Shimadzu or JASCO 4100 spectrometers of the Department of Organic and Inorganic Chemistry of the UPV/EHU. FTIR spectra were recorded in transmission mode by preparing KBr pellets, or in reflectance mode, directly on powder samples, by coupling attenuated total reflectance (ATR) module equipped with a zinc selenide (ZnSe) crystal.

Ultraviolet-visible (UV-Vis) absorption spectroscopy on aqueous solutions was performed in a JENWAY 6705 Uv/Vis spectrophotometer within the spectral range of 300 to 800 nm and using quartz cuvettes to analyse the samples.

X-ray fluorescence (XRF) data was acquired in three different equipments of the General Research Services of the UPV/EHU (*SGIker*):

- In Chapter 3, using the Fischerscope X-ray system XDRL equipment with 50 KeV power, using a nickel filter and a 0.1 dm collimator.
- In Chapter 4, using the MIDEX SD micro fluorescence X-ray spectrometer (Spectro) with ED-XRF energy dispersion for elemental analysis. The equipment is provided with an automatic XYZ tray, an automatic collimator changer, an X-ray tube with Mo anode and a silicon drift detector (SDD) with an area of 30 mm^2.
- In Chapter 5, using an AXIOS sequential X-ray fluorescence spectrometer (PANalytica) by wavelength dispersion (WDXRF) equipped with an Rh tube, and

three detectors (gas flow, scintillation and Xe sealing) working under vacuum conditions.

X-ray photoelectron spectroscopy (XPS) measurements were performed on a Phoibos 150 1D-DLD (SPECS) energy analyser of the General Research Services of the UPV/EHU (*SGIker*), equipped with a Focus 500 monochromatic radiation source, an Al/Ag dual anode, and a SED-200 secondary electron detection system.

Proton nuclear magnetic resonance (^{1}H-NMR) spectra were acquired in a Bruker AVANCE 5OO (one-bay; 500 MHz) of the General Research Services of the UPV/EHU (*SGIker*), at 293 K. Previously to measure samples were digested in 2 mL of a 1 M NaOH solution (in deuterated water, D_2O). The digestion was prolonged for 24 h, after which the solid residue corresponding to ZrO_2, HfO_2 or TiO_2 was filtered off and the NMR spectrum was taken on the liquid fraction.

Carbon solid state nuclear magnetic resonance (^{13}C CPMAS NMR) spectra were recorded on a Bruker AVANCE III 9.4 T system of the General Research Services of the UPV/EHU (*SGIker*), equipped with a 4 mm MAS DVT Double Resonance HX MAS probe. Larmor frequencies were 400.17 MHz and 100.63 MHz for ^{1}H and ^{13}C nuclei, respectively. Chemical shifts were calibrated indirectly with glycin, carbonil peak at 176 ppm. Sample rotation frequency was 10 kHz and relaxation delay was 5 s. The number of scans was 12240. Polarization transfer was achieved with RAMP cross-polarization (ramp on the proton channel) with a contact time of 5 ms. High-power SPINAL 64 heteronuclear proton decoupling was applied during acquisition.

Elemental analysis of carbon, hydrogen and nitrogen (CHN analysis) data was achieved by Eurovector EA 3000. Calibration samples were prepared in tin capsules packed with acetanilide. The prepared calibration and analysis samples were placed in the auto-sampler from where they were periodically tipped into a vertical quartz reactor heated at a temperature of 980 °C with a constant flow of helium stream. The resulting components N_2, CO_2, H_2O are separated in a chromatographic column and detected by a thermo-conductivity detector. The obtained signals were analyzed by Callidus® software.

Inductively coupled plasma optical emission spectrometry (ICP-OES) data was obtained in an Agilent 5100 of the General Research Services of the UPV/EHU (*SGIker*), equipped with dual vision, axial and radial. Argon plasma flow was 12 $L \cdot min^{-1}$, nebulization of 0.7 $mL \cdot min^{-1}$ and auxiliary gas input 1.0 $mL \cdot min^{-1}$ with 1300 W of power. The samples of Chapter 4 (70 mg) were dissolved with 35 mL of HNO_3 and 15 mL of HCl in a microwave equipment at 200 °C

Gas chromatography–mass spectrometry (GC-MS) measurements were performed on an Agilent HP 6890 gas chromatograph of the General Research Services of the UPV/EHU (*SGIker*) coupled to an Agilent HP5973 mass spectrometer to analyse the formation of sub-products during the synthesis of EHU-30 in Chapter 4. Accordingly, a liquid-solid extraction was carried out on the doughy reaction product using methanol as solvent (0.05:1) mass ratio, afterwhich, aliquots of 1 μL were taken and injected on the spectrometer. A HP 5 MS chromatography column was employed, with helium as gas carrier and a flux of 1.3 $mL \cdot min^{-1}$. The injection was done in split mode at 300 °C, and the temperature of the oven was heated up from 60 ˚C to 300 °C with a heating rate of 15 $°C \cdot min^{-1}$.

Gas chromatograph-mass spectrometry measurements (GC-MS/FID) for determining alcohols concentration from electroreduction experiments in Chapter 3 were performed in a headspace gas chromatograph (GCMS-QP2010 Ultra Shimadzu) of the Department of Chemical and Biomolecular Engineering equipped with a Flame Ionization Detector (FID) and a 30 m x 0.25 μm DB-Wax column using He as gas carrier (50 $mL \cdot min^{-1}$).

A four-channel gas michromatogaph microGC 3000 (Inficon) of the Department of Chemical and Biomolecular Engineering of the University of Cantabria, equipped with a thermal conductivity detector (TCD) and using He and Ar of high purity (99.9999%) as gas carriers was used for determining gas-products from electroreduction experiments (i.e. H_2, CO, C_2H_4) in Chapter 3.

Ion chromatography for determining formate ($HCOO^-$) concentration from electroreduction experiments in Chapter 3 was performed in a Dionex ICS 1100 of the Department of Chemical and Biomolecular Engineering of the University of Cantabria, equipped with an AS9-HC column, using a 4.5 mM Na_2CO_3 aqueous solution as the eluent at a flow rate of 1 $mL \cdot min^{-1}$ and operating pressure of approximately 14 MPa.

Gas chromatography-Dielectric-Barrier Discharge Ionization Detector (GC-BID) measurments for determining H_2 production in Chapter 5 was performed on a Shimadzu Nexis GC-2030 gas chromatograph of Chemistry Department from Swansea University, equipped with a barrier-discharge ionisation detector (BID) and a molecular sieve column. The total run time of the method was 5 minutes. The GC was calibrated using calibration gas (2000 ppm H_2, BOC), diluted with N_2 at different ratios using a set of mass flow controllers (Bronkhorst) to provide known concentrations of H_2. Gas samples were programmed to auto-inject into the GC via a multiport stream selector valve directing the selected sample purge gas stream through a 2 mL sample loop before injection.

2.2.2. Thermal characterization

Thermal analysis (TGA) was performed on a METTLER TOLEDO TGA/SDTA851 thermal analyser of the Department of Organic and Inorganic Chemistry of the UPV/EHU, from room temperature to 800 °C, using a heating rate of 5 °C·min^{-1}, synthetic air (80% N_2, 20% O_2) flux of 50 cm^3·min^{-1} and a sample size of about 10–20 mg per run.

Variable temperature powder X-ray diffraction (TDX) data were collected on a Bruker D8 Advance diffractometer of the General Research Services of the UPV/EHU (*SGIker*), operating at 30 kV and 20 mA, equipped with a Cu tube (equipped with Cu-K_α radiation, λ = 1.5418 Å), a Vantec-1 PSD detector, and an Anton Parr HTK2000 high-temperature furnace. The powder patterns were recorded in the 5–38° 2θ range using steps of 0.033° and 1 s per step. Data sets were recorded in air atmosphere each 10 °C from 30 to 500 °C, using a heating rate of 0.166 °C·s^{-1}.

2.2.3. Optical characterization

Fluorescence spectroscopy measurements were performed mode on a Varian Cary Eclipse (Agilent Technologies) optical spectrometer of the Department of Organic and Inorganic Chemistry of the UPV/EHU, equipped with a Xenon flash lamp of 450 W, a monochromator and a 90°–located photomultiplier (PMT). The measurments performed in emission scan mode were recorded in the 600 – 900 nm range using an excitation wavelength of 420 nm, 800 V PMT, and a 600 nm·min^{-1} scan rate.

UV-Vis diffuse reflectance spectroscopy (UV-Vis DRS) analysis were carried out in a Cary 7000 (Agilent Technologies) of the Department of Physical Chemistry of the UPV/EHU, equipped with a wolfram halogen (visible) and deuterium arc (UV) light sources. The spectra were recorded in reflectance mode in the 300 – 800 nm range and with a 600 nm·min^{-1} scan rate.

2.2.4. Structural characterization

Routine powder X-ray diffraction (PXRD) measurements were performed on a Phillips X'PERT diffractometer of the General Research Services of the UPV/EHU (*SGIker*), (equipped with Cu-K_α radiation, λ = 1.5418 Å) over the 5–70° 2θ range with a step size of 0.02°, a variable automatic divergence slit and an acquisition time of 2.5 s per step, at 20 °C.

High resolution PXRD data were collected on a Bruker D8 Advance diffractometer of the General Research Services of the UPV/EHU (*SGIker*), equipped with a Cu tube, Ge(111) incident beam monochromator (equipped with Cu-$K_{\alpha1}$ radiation, λ = 1.5406 Å) and 1-D LynxEye detector (active length in 2θ 2.7°). Samples were mounted on zero

background silicon wafers embedded in generic sample holders. Data were collected from 5 to 80° 2θ (step size 0.02° and time per step = 20 s) at 20 °C. Fixed divergence and anti-scatter slits of 1°, giving a constant volume of sample illumination, were used.

2.2.5. Microstructural characterization

Scanning electron microscopy (SEM) images were obtained in the FEG-SEM JEOL 7000F system of the General Research Services of the UPV/EHU (*SGIker*), in second (SE) and backscattered (BSE) modes, at magnifications between x200 and x200k, using an accelerating voltage of 10 kV, a current intensity of 0.1 nA, and an approximate working distance of 10 mm. The samples for SEM were adhered to the sample holder using double-sided adhesive carbon tape and coated with a Cr layer (20 nm) by sputtering using the Q150T sample preparation kit (Quorum Technologies Ltd.). In addition, conductive Cu tape was used at the ends of the sample holder to minimize the potential effect of electrical charge on imaging, and was subsequently removed for analysis. The microscope was also equipped with an EDX INCA X-sight Serie Si(Li) pentaFET detector for punctual elemental analysis.

Transmission electron microscopy (TEM) studies were done in a TECNAI G2 20 TWIN system of the General Research Services of the UPV/EHU (*SGIker*), operated at 200 kV and equipped with LaB_6 filament, STEM unit with brightfield/darkfield detector and X-ray microanalysis unit (EDX). TEM micrographs were taken on aerogels, as well as on hydrogels, thanks to the single tilt sample holder (±70°) cooling (Gatan model 626 DH) with temperature control up to liquid nitrogen (Gatan model 900). The samples for room temperature TEM were prepared by a dry dispersion of the aerogels onto a TEM copper grid (300 Mesh) covered by a holey carbon film. The samples for cryogenic TEM (cryoTEM) were prepared by applying 3 μL aliquot of hydrogel suspension into a glow-discharged 300 mesh lacey carbon TEM grid and freezing in liquid ethane by immersion on a FEI Vitrobot Mark IV.

2.2.6. Gas physisorption characterization

Dinitrogen and carbon dioxide adsorption measurements: N_2 (77 K) and CO_2 (273 and 298 K) physisorption data were recorded with a Quantachrome Autosorb-iQ MP analyser of the Department of Organic and Inorganic Chemistry of the UPV/EHU. Prior to measurements, all samples were outgassed under vacuum at 140 °C for 6 hours. The surface area values were obtained by the fittings of the N_2 adsorption data to Brunauer-Emmett-Teller (BET) equation.[1] In order to choose the appropriate pressure range and to avoid ambiguity when reporting the BET surface area of MOFs, we used the three consistency criteria proposed by Rouquerol et al.: (1) The pressure range selected should have values of V(1-p/p°) increasing with p/p°. (2) The points used to calculate

the BET surface area must be linear with an upward slope in such a way that the linear regression must yield a positive y-intercept (i.e., positive C value). (3) The p/p° value corresponding to V_m should be within the BET fitting range.[2] To estimate CO_2 adsorption enthalpies (Q_{st}), the isotherms were fitted to the modified Clausius−Clapeyron equation.[3,4] The micropore volume of the samples was estimated according to the t-plot method.[5,6]

Water sorption isotherms were carried out using a gravimetric water sorption analyser (Aquadyne DVS, Quantachrome Instruments) of the Department of Chemistry of the Royal Military Academy of Brussels in collaboration with Dr. Leticia F. Velasco. Before the experiments, the samples were outgassed under vacuum at 140 °C for 6 hours. The measurements were performed at different temperatures (15, 25, 35 and 45 °C) using nitrogen 6.0 as carrier gas and an equilibrium criterion corresponding to 0.0004% of mass change per minute at a given relative humidity. The water sorption cyclability of the materials was also evaluated, with an isothermal purging step between the cycles.

2.2.7. Synchrotron and neutron characterization

Synchrotron XRD: High resolution synchrotron X-ray diffraction pattern of polycrystalline EHU-30 was measured at I11 Beamline of Diamond Light Source (Oxfordshire, England) equipped with a multi-analyser crystal detector (MAC) and using a wavelength of λ = 0.82448(10) Å.[7] The sample was mounted in a borosilicate capillary and outgassed at 353 K under vacuum. After cooling down to room temperature, the capillary was thermally sealed. PXRD data was collected at 293 K. Data treatment was performed in collaboration with Dr. Ivan da Silva González.

Synchrotron pair distribution function (PDF) analysis: Total X-ray scattering data suitable for PDF analyses were collected at the P02.1 beamline at PETRA III, DESY (Hamburg, Germany), using monochromatic synchrotron X-rays with a fixed energy of 60.0 keV (0.2068 Å). Powder samples were packed in glass capillaries with a diameter of 0.8 mm. The patterns were collected with a Varex XRD 4343CT flat panel detector (150 × 150 μm^2 pixel size, 2880 x 2880 pixel area) with a sample-to-detector distance (SDD) of 292 mm and exposure times of 1800 seconds, capturing quarters of the Debye-Scherrer rings. Calibration of the detector and the SDD was performed measuring LaB_6 (NIST 660b) as standard material. An empty capillary was measured in order to compensate for the contribution of glass to the diffraction patterns. PDFs were obtained from the total scattering data within xPDFsuite[8] to a Qmax = 22 $Å^{-1}$. Differential PDFs were calculated by subtracting the PDF of the pristine EHU-30 from that of the copper metalated material. Simulated PDF data of the EHU-30 framework

was obtained using the PDFgui software.[9] Data acquisition and treatment were performed in collaboration with Dr. Ana E. Platero-Prats.

Time-of-flight (TOF) neutron powder diffraction. TOF neutron diffraction measurements for understanding the mechanism and the nature of the host-guest interactions that determine the water adsorption were performed on GEM instrument (General Materials Diffractometer) of ISIS Neutron and Muon Source (Oxfordshire, England).[10] Prior to measurements the samples were conditioned by an outgassing procedure at 120 °C for 12 h and, after cooling down, they were immersed in deuterated water, which was lengthen for 3 days with fresh D_2O exchanges every 24 h. Samples were then loaded into 6 mm-diameter cylindrical vanadium cans and measured at room temperature, using a beam with size of 10 x 40 mm^2 (H x V). Powder diffraction patterns from detector banks 1 to 4 were simultaneously fitted for each refinement, using Topas-Academic v5 program.[11] Data acquisition and treatment were performed in collaboration with Dr. Ivan da Silva González.

2.2.8. Electrochemical characterization

Cyclic voltammetry measurements: A MSTAT4 (Arbin Instruments) potentiostat of the Department of Chemical and Biomolecular Engineering of the University of Cantabria was used to evaluate the voltage-current curves by employing a conventional three electrode electrochemical cell. The cyclic voltammetries are obtained with a scan rate of 50 $mV \cdot s^{-1}$ at potentials ranging from 0 to -2 V vs. Ag/AgCl (0.63 to -1.37 V vs. RHE) in a 0.5 M $KHCO_3$ aqueous solution as electrolyte. The electrolyte was pre-saturated with CO_2 or deaerated with N_2 by bubbling the gas for 30 min. Portions of the bimetallic-GDEs were used as working electrodes, while a glassy carbon and Ag/AgCl (sat. KCl) were used as counter and reference electrode, respectively.

2.3. EXPERIMENTAL SET-UPS FOR CATALYSIS

2.3.1. CO_2 electroreduction experimental set-up

The experimental laboratory system for the continuous electro-reduction of CO_2 included two tanks, two pumps, a potentiostat/galvanostat, and an electrochemical cell as shown in Figure 2.1. The cell is a filter-press or parallel-plate type cell and was divided into two compartments by a Nafion 117 membrane as shown in Figure 2.2a. The filter-press electrochemical system possesses three inputs (catholyte, anolyte and CO_2 separately) and two outputs (catholyte-CO_2 and anolyte), what makes it possible the formation of a gas-solid-liquid interface for the electrocatalytic reduction of CO_2 in gas phase (Figure 2.2b). The cathode side of the reactor is fed with CO_2 gas (99.99%) with a flow/area ratio of $Q_{g/A}$= 10 $mL \cdot min^{-1} \cdot cm^{-2}$, adjusted by a rotameter. A 0.5 M

$KHCO_3$ aqueous solution is used as both, catholyte and anolyte solutions. Prior to the experiments, the aqueous electrolyte is saturated with CO_2 by bubbling for 30 min. The electrolytes are pumped to the cell by two peristaltic pumps (Watson Marlow 320, Waton MarlowPumps Group) at a flow rate of $Q_{e/A}$= 2 mL·min^{-1}·cm^{-2}. In the electrochemical cell (Micro Flow Cell, ElectroCell A/S), electroreduction of CO_2 takes place due to the current supplied by the potentiostat/galvanostat (AutoLabPGSTAT 302N, Metrohm). A platinised titanium electrode is used as the counter-electrode. The working electrode is a GDE loaded with the prepared materials. A leak-free Ag/AgCl (sat. KCl) reference electrode is assembled close to the surface of the working electrode.[12–14]

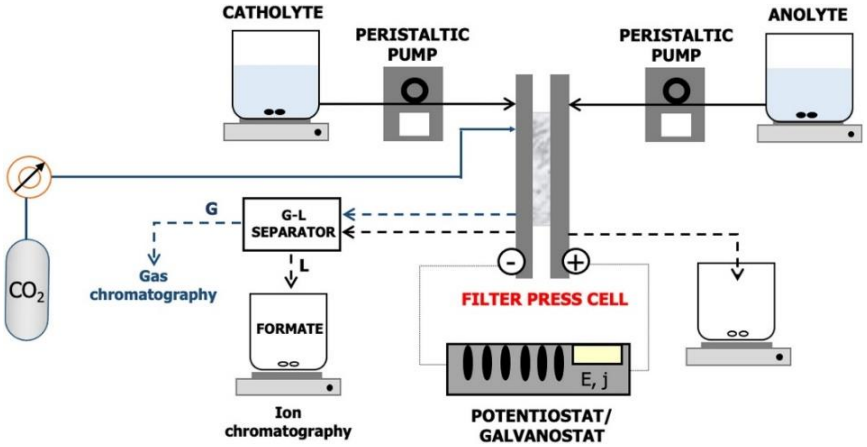

Figure 2.1. CO_2 continuous electroreduction reactor setup scheme. Reproduced from reference 14.

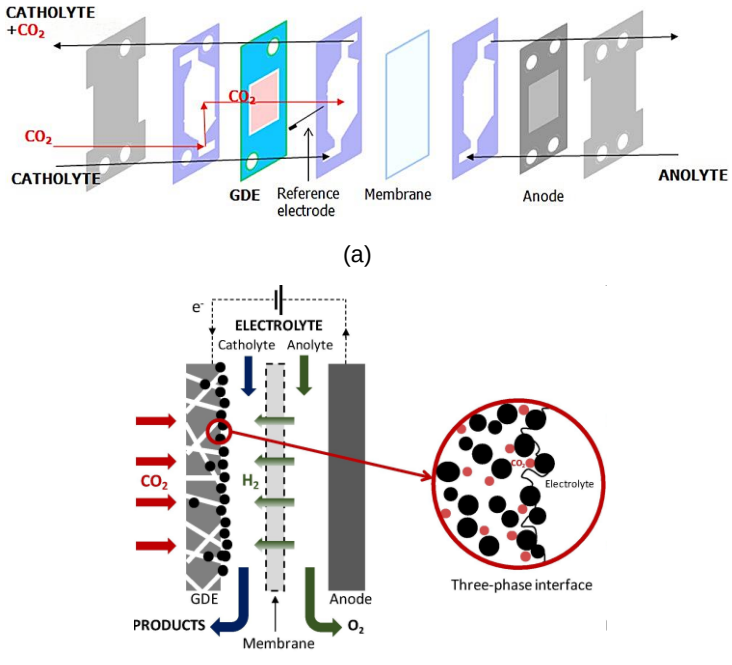

Figure 2.2. (a) Filter-press electrochemical cell configuration and (b) schematic representation of the gas-solid-liquid interface formation in the cell. Reproduced from references 12 and 13, respectively.

Experiments were carried out at ambient temperature and pressure, and the cell was operated in continuous mode. All experiments were performed at galvanostatic conditions (*i.e.* at a constant current density), meaning that the total amount of charge passed at the end of each test was simply the product of the current density (j), the electrode area (10 cm^2), and the time of operation, that is established to 90 min, when pseudo-stable conditions are achieved. Long term experiments in selected samples were prolonged for 300 min. An average concentration was obtained for each experiment. Due to the variability of the process, three experiments were performed for each point. The performance of the process was assessed using the rate of formate production and the Faradaic efficiency.

Figure 2.3. shows the real experimental system and filter-press cell employed for the CO_2 electroreduction performed in collaboration with Dr. Jonathan Albo from the Department of Chemical and Biomolecular Engineering at the University of Cantabria.

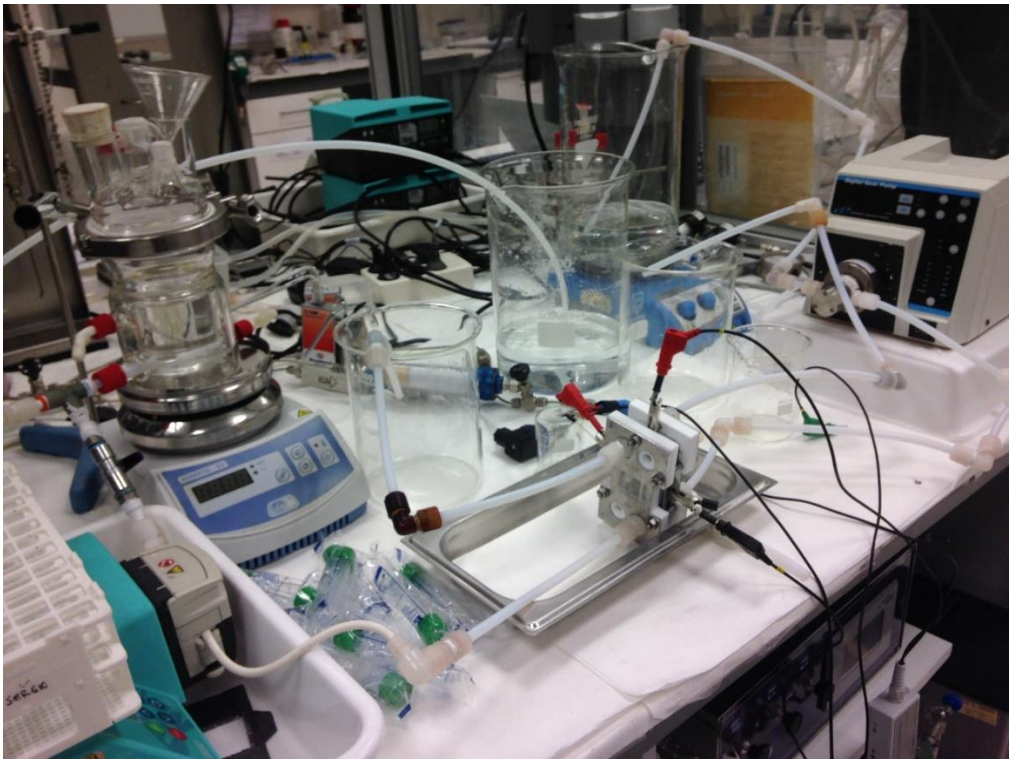

Figure2.3. Experimental set-up for continuous CO_2 electroreduction process.

2.3.2. CO_2 photoreduction experimental set-up

Figure 2.4 schematically represents the lab scale plant for continuous photoreduction of CO_2, which consists of a microreactor, one inlet (solution + CO_2) and one outlet (solution + CO_2 + products). The former consist of a home-made planar optofluidic microreactor (APRIA Systems S.L.) equipped with a reaction microchamber of 1 cm^2 and 75 µL that provides high-surface-area-to-volume ratio, uniform light distribution

and mass transfer for the continuous light-driven transformation of carbon dioxide. The porous carbon paper containing the light responsive material is sandwiched with PTFE gaskets between two highly transparent (light transmission of 90% at λ > 365 nm) polymethylmethacrylate, PMMA (Altuglas-Arkema) plates and a stainless-steel plate on the top (see Figure 2.5a). The optofluidic microreactor is placed in a ventilated dark box and the temperature controlled with an infrared thermometer (*ca.* 20 °C). During the light-driven process the microchamber is irradiated with LED lights (peak at 450 nm) with a light intensity of E = 5 $mW \cdot cm^{-2}$ measured by a radiometer (Photoradiometer Delta OHM) and controlled by adjusting the LED intensity and the distance between the microreactor and the LED. Blank test experiments in dark conditions were also performed for comparison. Photographs of the micro-optofluidic reactor applied in dark and under visible light irradiation are gathered in Figure 2.5b.[15,16]

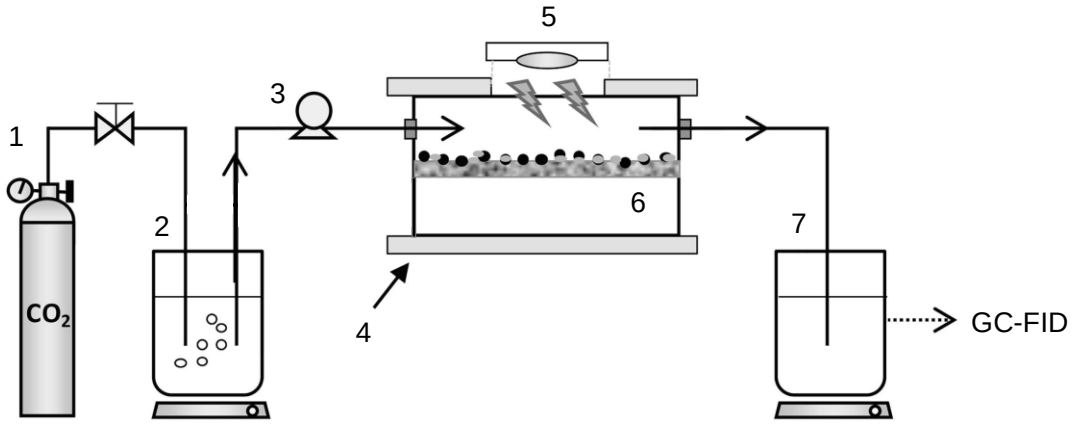

1. CO_2 cylinder
2. Solution vessel
3. Micropump
4. Microreactor
5. Vis LED
6. Photoactive surface
7. Collection vessel

Figure 2.4. Scheme of the experimental set-up for CO_2 photoreduction in a micro-optofluidic reactor. Adapted from reference 15.

A CO_2 saturated 0.5 M $KHCO_3$ aqueous solution (pH = 7.38 ± 0.03) prepared with ultra-pure water (18.2 MΩ·cm at 273 K, MilliQ Millipore system) was supplied to the microchamber with a peristaltic pump (Minipuls 3 Gilson) at a flow rate of Q_L = 100 $\mu L \cdot min^{-1}$. Blank tests using a 0.5 M $KHCO_3$ aqueous solution no saturated with CO_2 (pH = 8.29 ± 0.04) were also performed. The photochemical CO_2 reduction tests for each photoactive prepared material were carried out by duplicate in continuous mode for 180 min, when a pseudo-stable performance is reached. The concentration of alcohols in each sample was analysed by duplicate in a headspace gas chromatograph (GCMS-QP2010 Ultra Shimadzu) equipped with a flame ionization detector (FID). An average concentration was obtained for each point.

These experiments were performed in collaboration with Dr. Jonathan Albo and Dr. Ivan Merino from the Department of Chemical and Biomolecular Engineering at the University of Cantabria.

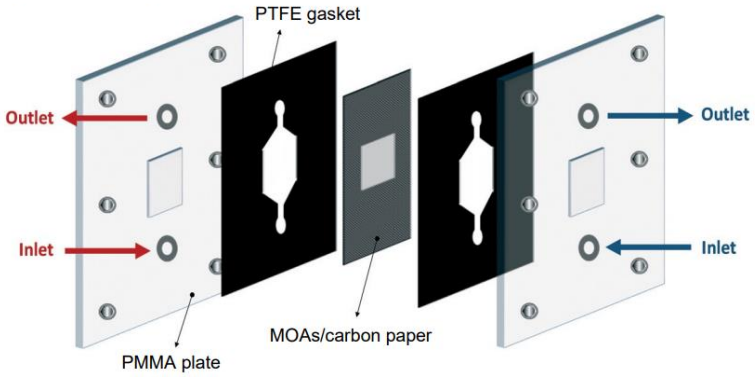

(a)

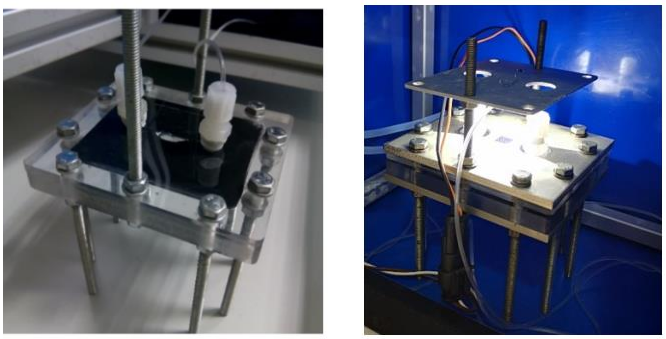

(b)

Figure 2.5. (a) Internal cell components and (b) images of the micro-optofluidic reactor: dark-left; visible light irradiation-right. MOAs denote for metal-organic aerogels, that will be described in Chapter 5.

2.3.3. HER experiments set-up

Solar-light-driven H_2 production experiments were performed in the set up shown in Figure 2.6. Photocatalytic materials sealed in a glass vial (Chromacol 10-SV, Fisher) along with the reagent solution (2 mL) are located in a thermostated water bath (25 °C) with continuous stirring and irradiated using a solar light simulator (Thermo Oriel 92194-1000) equipped with an AM 1.5G filter (Newport) with an intensity of 1 sun. The sample headspace is subjected to a constant purge of N_2 of 5 mL·min^{-1} controlled by a flow controller (Bronkhorst). H_2 evolution is monitored by a gas chromatograph (Shimadzu Nexis 2030) using an auto-sampler programmed to inject 2 mL of the selected headspace stream. Nine samples can be measured simultaneously by starting the exposure to light of one sample each 2 min. GC measurement conditions are explained in previous section. H_2 evolution rates are calculated from the measured H_2 concentration in the purge gas and the purge gas flow rate. Cumulative H_2 production

is calculated from the H_2 evolution rate and time passed since the previous measurement, assuming a constant H_2 evolution rate between time points.

These experiments were performed during my placement at Chemistry Department of Swansea University (Swansea, Wales) under the supervision of Dr. Moritz Kuehnel.

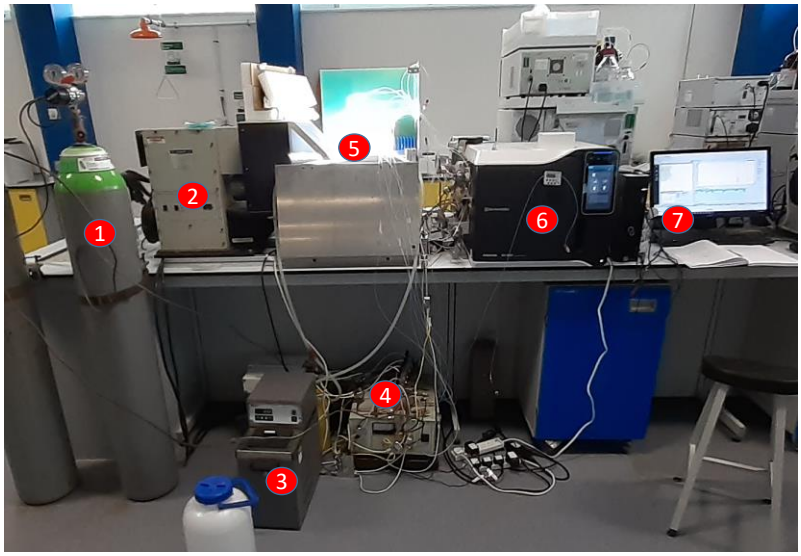

1 N_2 cylinder
2 Solar simulator
3 Water bath thermostat
4 Mass flow controlers
5 Sample holder
6 Gas chromatograph
7 Computer-controler

(a)

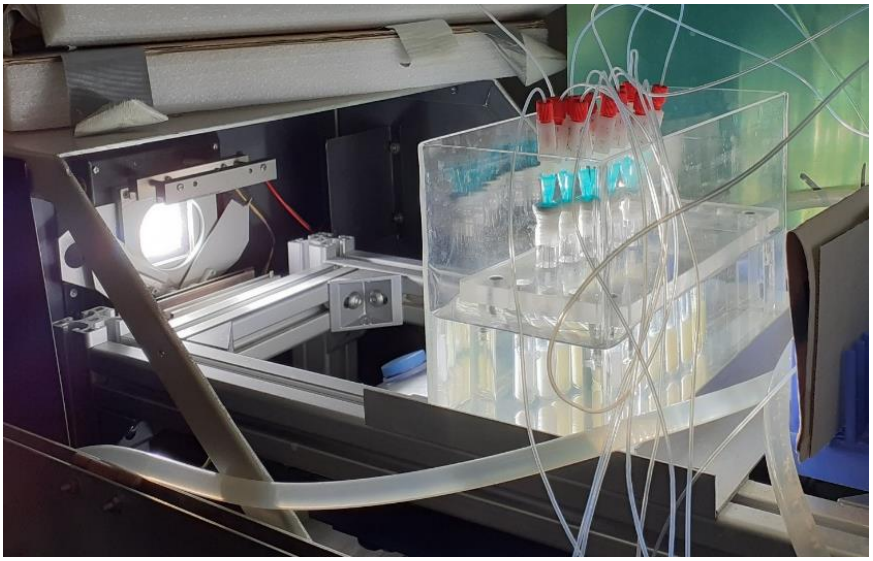

(b)

Figure 2.6. HER experiments (a) set-up and (b) samples disposition in water bath.

2.4. COMPUTATIONAL DETAILS

2.4.1. Geometric pore size distribution

Geometric pore size distribution (PSD) was computed by means of a Monte Carlo procedure implemented within a code developed by L. Sarkisov, in which the Lennard-

Jones (LJ) universal force field parameters are used to describe the MOF atoms while the accessible pore volume is assessed by both a gradually increasing probe and a He probe.[17]

2.4.2. Periodic DFT calculations

Periodic density-functional theory calculations were conducted by means of the code CASTEP, which uses a plane-wave basis set and pseudopotentials.[18] To accomplish the calculations a plane-wave cut-off of 380 eV and ultrasoft pseudopotentials were selected. The PBE exchange-correlation functional was used in the calculations. The structural models were built using the crystallographic data of EHU-30 and UiO-66 (CSD code: *RUBTAK*). Non-located hydrogen atoms corresponding to the hydroxide bridges were added geometrically. To save computational time, the calculations were carried out for the converted primitive cells, using one k-point located at the Γ-point.

2.4.3. Simulation of adsorption isotherms

Adsorption isotherms of pure components (CO_2 and N_2) and binary mixtures (water and N_2) were calculated using the software package RASPA[19] in collaboration with Prof. Dr. Sofía Calero from the Department of Applied Physics & Eindhoven School of Education at Eindhoven University of Technology (TU/e) and Dr. Juan José Gutierrez Sevillano from the Department of Physical, Chemical and Natural Systems at Pablo de Olavide University. We used Grand Canonical Monte Carlo simulations, where chemical potential, volume, and temperature were kept fixed. We used the Peng-Robinson equation and the fugacity coefficient to relate the chemical potential to pressure. Absolute loading (n_{abs}) obtained in the simulations was converted to excess loading (n_{exc}) by using the following equation 2.1:

$$n_{exc} = n_{abs} - V^g \rho^g \qquad \text{equation 2.1}$$

where V^g is the pore volume of the adsorbent and ρ^g is the molar density of the bulk gas phase.[20]

During the simulation, system configurations are generated by randomly selecting a molecule and applying random moves. These moves can be rotation, translation, regrow, insertion/deletion, and identity change in the case of mixtures. At least 4×10^5 equilibration steps and 6×10^6 production steps were used to ensure equilibrium in case of single gas isotherm. For the binary mixtures at least 10^6 and 10^7 steps for equilibration and production were used. We used Lennard-Jones (L-J) and Coulombic potentials to define the interactions between the atoms of the system and generic Lorentz-Berthelot mixing rules were applied to compute guest-guest and host-guest L-J interactions. The Ewald summation method is employed to calculate the Coulombic interactions with a relative precision of 10^{-6}. L-J and Coulombic potentials were cut and

shifted at a cut off distance of 12 Å. We used periodic boundary conditions and the simulation box contained as many unit cells of each structure as needed to ensure that the dimensions of the simulation box are at least twice the cut off.

For CO_2, we used the model developed by García-Sanchez et al.[21] which is a rigid full atom model with C-O distance = 1.149 Å. For N_2 we used the model reported by Martin-Calvo et al.[22] consisting of two Lennard-Jones interaction centres at a distance of 1.10 Å and an additional dummy bead placed at the centre of mass of the molecule. In the case of water, we used the Tip4pEw model. It is a rigid planar four-site interaction model consisting of a single Lennard-Jones interaction centre located at the atom of oxygen while the atoms of hydrogen and the dummy bead have charges.[23]

To model the structures, we used the crystallographic position of the atoms obtained from the crystal structure of the materials. The hydrogen atoms of the hydroxide groups were geometrically sited with a d_{O-H} = 0.94 Å and M–O–H = 111-112°. The structures are considered as rigid frameworks with Lennard-Jones and point charges assigned. Most L-J parameters are taken from DREIDING force field[24] except those for the metal atoms that are taken from UFF force field.[25] The point charges to model the electrostatic potential of the adsorbents were previously calculated by means of Density Functional Theory (DFT) calculations using the ESP method as described by Singh and Kollman,[26] which is implemented in the DMol3 code.[27] To accomplish the DFT calculations DNP basis set and the PBE exchange-correlation functional were employed.[28] To conduct the ESP charge calculations neutral finite cluster models of formula $[M_6O_4(OH)_4(L)_{12}]$ (M: Zr, Hf; L: BDC, NH_2-BDC) were built for each MOF (Figures 2.7 to 2.9) All Lennard-Jones parameters are listed in Table 2.3 while the charges of the atoms are included in the Tables 2.4 to 2.7.

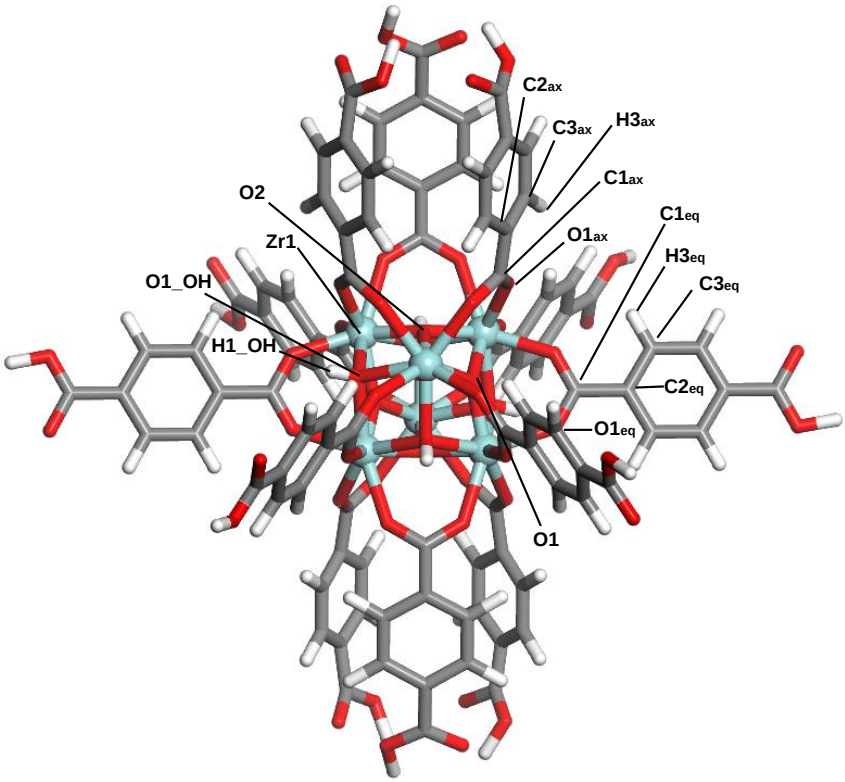

Figure 2.7. Finite cluster model of EHU-30(Zr) employed to calculate the ESP charges and labelling of the atoms.

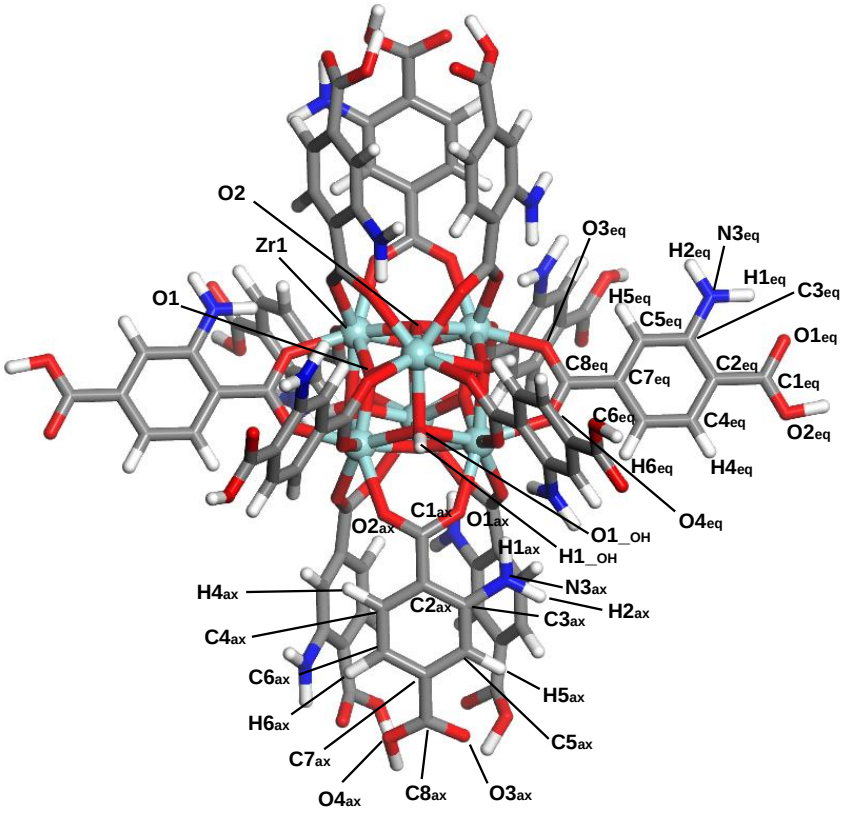

Figure 2.8. Finite cluster model of EHU-30-NH_2(Zr) employed to calculate the ESP charges and labelling of the atoms. Same finite cluster and labels were stablished for EHU-30-NH_2(Hf), but changing Zr1 by Hf1.

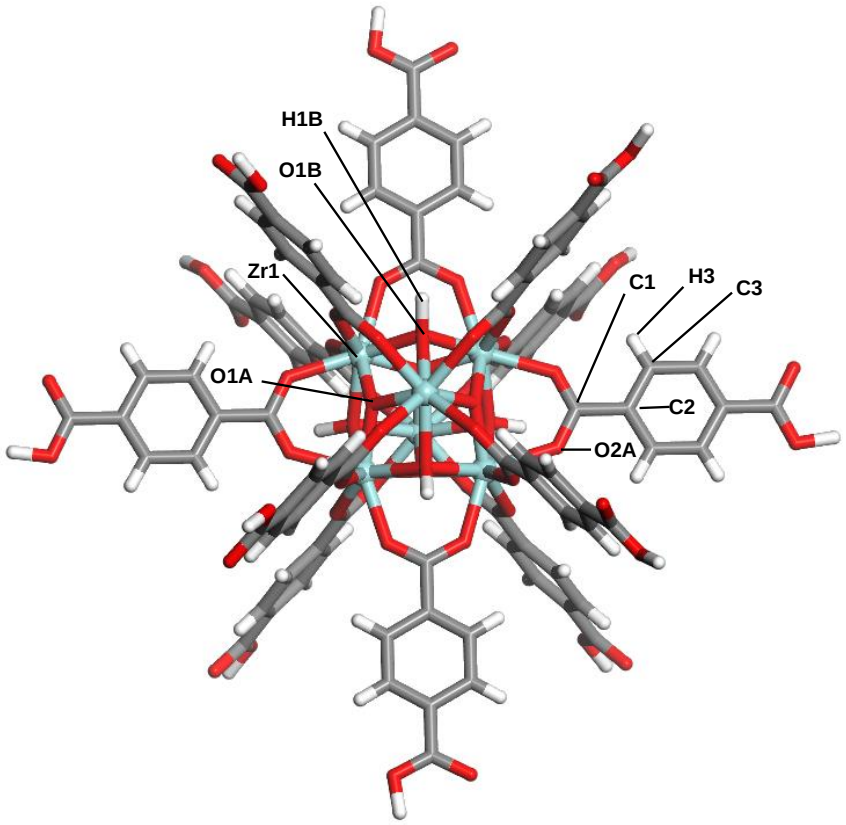

Figure 2.9. Finite cluster model of UiO-66(Zr) employed to conduct the ESP charges and labelling of the atoms.

Table 2.3. Lennard Jones parameters employed in the simulations.

Interaction centre	ε/kB [K]	σ [Å]	q [e]
C_CO2	29.933	2.742	0.6512
O_CO2	85.671	3.017	-0.3256
N_N2	38.298	3.306	-0.40484
Dummy_N2	-	-	0.8096
O_water	81.899	3.164	0
H_water	-	-	0.524
Dummy_water	-	-	-1.048
Hf_framework	36.269	2.798	Tables 2.4 to 2.7
Zr_framework	34.722	2.783	
C_framework	47.86	4.473	
O_framework	48.19	3.033	
H_framework	7.65	2.846	
N_framework	38.949	3.262	

Table 2.4. ESP charges (q / e) for the atoms of the structural model of EHU-30.

EHU-30			
Cluster		**Equatorial BDC**	
atom	charge	atom	charge
Zr1	2.4325087070470	C1eq	0.9545087218285
O1	-1.0834912061690	C2eq	-0.1124912351370
O2	-0.8094912767410	C3eq	-0.1214912310243
O1_OH	-1.1994911432270	H3eq	0.1605087667704
H1_OH	0.5355087518692	O1eq	-0.8224912285805
Axial BDC (triad)			
atom	charge	atom	charge
C1ax	0.6455087661743	H3ax	0.1145087629557
C2ax	-0.1484912335873	O1ax	-0.6194912195206
C3ax	-0.0604912340641		

Table 2.5. ESP charges (q / e) for the atoms of the structural model of EHU-30-NH_2(Zr).

EHU-30-NH_2(Zr)			
Cluster			
atom	charge	atom	charge
Zr1	2.3109524250030	O1_OH	-1.0730476379390
O1	-1.1180477142330	H1_OH	0.4759523570538
O2	-0.9130476117134		
Equatorial NH_2-BDC			
atom	charge	atom	charge
O1eq	-0.8030475974083	H4eq	0.1709523797035
O2eq	-0.8590475916862	C5eq	-0.3550476431847
C1eq	1.1119523048400	H5eq	0.2199523746967
C2eq	-0.4420476257801	C6eq	-0.2060476243496
C3eq	0.6229524016380	H6eq	0.1719523817301
N3eq	-1.0610476732250	C7eq	-0.1320476233959
H1eq	0.4699523746967	C8eq	1.0859522819520
H2eq	0.4289523661137	O3eq	-0.8940476179123

C4eq	-0.0530476197600	O4eq	-0.8200476169586
Axial NH_2-BDC (triad)			
atom	charge	atom	charge
O1ax	-0.3630476295948	H4ax	0.1379523873329
O2ax	-0.5110476016998	C5ax	-0.3840476274490
C1ax	0.4629523754120	H5ax	0.1639523804188
C2ax	-0.2280476242304	C6ax	-0.2550476193428
C3ax	0.6339523792267	H6ax	0.1499523818493
N3ax	-1.1580476760860	C7ax	-0.0150476172566
H1ax	0.4299523532391	C8ax	0.6019523739815
H2ax	0.4589523673058	O3ax	-0.5700476169586
C4ax	-0.1100476160645	O4ax	-0.5740476250648

Table 2.6. ESP charges (q / e) for the atoms of the structural model of EHU-30-NH_2(Hf).

EHU-30-NH_2(Hf)			
Cluster			
atom	charge	atom	charge
Hf1	2.0369682312010	O1_OH	-0.9790318012238
O1	-0.9750317931175	H1_OH	0.4659682512283
O2	-0.7750317454338		
Equatorial NH_2-BDC			
atom	charge	atom	charge
O1eq	-0.7490317821503	H4eq	0.1699682623148
O2eq	-0.7940317988396	C5eq	-0.3560317456722
C1eq	1.0719683170320	H5eq	0.2179682552814
C2eq	-0.4480317533016	C6eq	-0.2500317394733
C3eq	0.6439682245255	H6eq	0.1749682575464
N3eq	-1.0880317687990	C7eq	-0.1180317550898
H1eq	0.4899682700634	C8eq	1.0379682779310
H2eq	0.4359682500362	O3eq	-0.8500317931175
C4eq	-0.0520317479968	O4eq	-0.7420317530632
Axial NH_2-BDC (triad)			
atom	charge	atom	charge
O1ax	-0.2960317432880	H4ax	0.1399682611227

O2ax	-0.4330317378044	C5ax	-0.4350317418575
C1ax	0.3649682700634	H5ax	0.1749682575464
C2ax	-0.1800317466259	C6ax	-0.2830317318439
C3ax	0.6299682259560	H6ax	0.1539682596922
N3ax	-1.1840317249300	C7ax	0.0609682537615
H1ax	0.4459682703018	C8ax	0.4979682564735
H2ax	0.4699682593346	O3ax	-0.4890317320824
C4ax	-0.1320317387581	O4ax	-0.5250317454338

Table 2.7. ESP charges (q / e) for the atoms of the structural model of UiO-66(Zr).

UiO-66			
Cluster		**Equatorial BDC**	
atom	charge	atom	charge
Zr1	2.5890879631040	C1	0.8610876798630
O1A	-1.0379120111470	C2	-0.1529123038054
O1B	-1.5949120521550	C3	-0.0864122733474
H1B	0.5800877213478	H3	0.1530877053738
		O2A	-0.7259122729301

2.5. REFERENCES

1 S. Brunauer, P. H. Emmet and E. Teller, Adsorption of Gases in Multimolecular Layers, *J. Am. Chem. Soc.*, 1938, **60**, 309–319.

2 J. Rouquerol, P. Llewellyn and F. Rouquerol, Is the BET equation applicable to microporous adsorbents?, in *Studies in Surface Science and Catalysis*, Elsevier B.V., 2007, vol. 160, pp. 49–56.

3 K. Sumida, D. L. Rogow, J. A. Mason, T. M. McDonald, E. D. Bloch, Z. R. Herm, T. H. Bae and J. R. Long, Carbon dioxide capture in metal-organic frameworks, *Chem. Rev.*, 2012, **112**, 724–781.

4 H. Pan, J. R. Ritter and P. B. Balbuena, Isosteric Heats of Adsorption on Carbon Predicted by Density Functional Theory, *Ind. Eng. Chem. Res.*, 1998, **37**, 1159–1166.

5 B. C. Lippens and J. H. Boer, Studies on Pore Systems in Catalysts V. The t Method, *J. Catal.*, 1965, **4**, 319–323.

6 J. Rouquerol, F. Rouquerol and K. Sing, Adsorption by Powders and Porous Solids, Academic Press, 1998, p. 467.

7 S. P. Thompson, J. E. Parker, J. Potter, T. P. Hill, A. Birt, T. M. Cobb, F. Yuan and C. C. Tang, Beamline I11 at Diamond: A new instrument for high resolution powder diffraction, *Rev.*

Sci. Instrum., 2009, **80**, 075107.

8 X. Yang, P. Juhas, C. L. Farrow and S. J. L. Billinge, XPDFsuite: An end-to-end software solution for high throughput pair distribution function transformation, visualization and analysis. arXiv 2014, 1402.3163. arXiv.org e-Print archive. https://arxiv.org/abs/1402.3163v3 (accessed: September, 2021), .

9 C. L. Farrow, P. Juhas, J. W. Liu, D. Bryndin, E. S. Božin, J. Bloch, T. Proffen and S. J. L. Billinge, PDFfit2 and PDFgui: computer programs for studying nanostructure in crystals, *J. Phys. Condens. Matter*, 2007, **19**, 335219.

10 S. Pérez-Yáñez, G. Beobide, O. Castillo, A. Luque, M. Perfecto-Irigaray and I. da Silva, Determining the water adsorption in zirconium MOFs related to the well-known UiO-66 and UiO-67, *STFC ISIS Neutron Muon Source 2020*.

11 A. A. Coelho, TOPAS and TOPAS-Academic: An optimization program integrating computer algebra and crystallographic objects written in C++, *J. Appl. Crystallogr.*, 2018, **51**, 210–218.

12 A. Del Castillo, M. Alvarez-Guerra and A. Irabien, Continuous electroreduction of CO_2 to formate using Sn gas diffusion electrodes, *AIChE J.*, 2014, **60**, 3557–3564.

13 J. Albo and A. Irabien, Cu_2O-loaded gas diffusion electrodes for the continuous electrochemical reduction of CO_2 to methanol, *J. Catal.*, 2016, **343**, 232–239.

14 I. Merino-Garcia, L. Tinat, J. Albo, M. Alvarez-Guerra, A. Irabien, O. Durupthy, V. Vivier and C. M. Sánchez-Sánchez, Continuous electroconversion of CO_2 into formate using 2 nm tin oxide nanoparticles, *Appl. Catal. B Environ.*, 2021, **297**, 120447.

15 J. Albo, M. I. Qadir, M. Samperi, J. A. Fernandes, I. de Pedro and J. Dupont, Use of an optofluidic microreactor and Cu nanoparticles synthesized in ionic liquid and embedded in TiO_2 for an efficient photoreduction of CO_2 to methanol, *Chem. Eng. J.*, 2021, **404**, 126643.

16 A. Angulo-Ibáñez, M. Perfecto-Irigaray, I. Merino-Garcia, N. Luengo, A. M. Goitandia, J. Albo, E. Aranzabe, G. Beobide, O. Castillo and S. Pérez-Yáñez, Metal-organic aerogels based on titanium(IV) for visible-light conducted CO_2 photoreduction to alcohols, *Mater. Today Energy*, 2022, **30**, 101178.

17 L. Sarkisov and A. Harrison, Computational structure characterisation tools in application to ordered and disordered porous materials, *Mol. Simul.*, 2011, **37**, 1248–1257.

18 S. J. Clark, M. D. Segall, C. J. Pickard, P. J. Hasnip, M. I. J. Probert, K. Refson and M. C. Payne, First principles methods using CASTEP, *Zeitschrift für Krist. - Cryst. Mater.*, 2005, **220**, 567–570.

19 D. Dubbeldam, S. Calero, D. E. Ellis and R. Q. Snurr, RASPA: molecular simulation software for adsorption and diffusion in flexible nanoporous materials, *Mol. Simul.*, 2016, **42**, 81–101.

20 O. Talu and A. L. Myers, Molecular simulation of adsorption: Gibbs dividing surface and comparison with experiment, *AIChE J.*, 2001, **47**, 1160–1168.

21 A. García-Sánchez, C. O. Ania, J. B. Parra, D. Dubbeldam, T. J. H. Vlugt, R. Krishna and S.

Calero, Transferable force field for carbon dioxide adsorption in zeolites, *J. Phys. Chem. C*, 2009, **113**, 8814–8820.

22 A. Martín-Calvo, E. García-Pérez, A. García-Sánchez, R. Bueno-Pérez, S. Hamad and S. Calero, Effect of air humidity on the removal of carbon tetrachloride from air using Cu–BTC metal–organic framework, *Phys. Chem. Chem. Phys.*, 2011, **13**, 11165.

23 H. W. Horn, W. C. Swope, J. W. Pitera, J. D. Madura, T. J. Dick, G. L. Hura and T. Head-Gordon, Development of an improved four-site water model for biomolecular simulations: TIP4P-Ew, *J. Chem. Phys.*, 2004, **120**, 9665–9678.

24 S. L. Mayo, B. D. Olafson and W. A. Goddard, DREIDING: A generic force field for molecular simulations, *J. Phys. Chem.*, 1990, **94**, 8897–8909.

25 A. K. Rappé, C. J. Casewit, K. S. Colwell, W. A. Goddard III and W. M. Skiff, UFF, a Full Periodic Table Force Field for Molecular Mechanics and Molecular Dynamics Simulations, *J. Am. Chem. Soc.*, 1992, **114**, 100021–10035.

26 U. C. Singh and P. A. Kollman, An approach to computing electrostatic charges for molecules, *J. Comput. Chem.*, 1984, **5**, 129–145.

27 B. Delley, From molecules to solids with the DMol3 approach, *J. Chem. Phys.*, 2000, **113**, 7756–7764.

28 J. P. Perdew, K. Burke and M. Ernzerhof, Generalized gradient approximation made simple, *Phys. Rev. Lett.*, 1996, **77**, 3865–3868.

Chapter 3

Copper(II)-based metal-organic frameworks for the electrocatalytic reduction of carbon dioxide into alcohols

3.1. INTRODUCTION

As commented before, the idea that CO_2 can be captured[1] and reconverted[2–4] to useful chemicals sounds like a perfect solution that could potentially be a step forward in the transition to a low-carbon economy.[5] However, and due to the thermodynamic stability and relative kinetic inertness of CO_2, a preliminary activation is required. This can be performed by different methodologies. In particular, the CO_2 electroreduction reaction, that was firstly studied in 1870 by Royer,[6] has attracted increasing research interests in the last decades, owing to its simple procedure and moderate reaction conditions. Besides, the energy required in the activation of CO_2 might be supplied from renewable energy sources, such as solar or wind power, providing viable solutions to the development of carbon-neutral fuels.[7]

3.1.1. General characteristics of electrochemical reduction of CO_2

In this approach, the process takes place in an electrochemical reactor when electrical energy is supplied to establish a potential difference between a cathode and an anode to allow CO_2 to be electrochemically transformed into reduced forms as shown schematically in Figure 3.1. As the main goal is the reduction of CO_2, research efforts have obviously been focused on the cathodic compartment where CO_2 can be converted to different products, simply leaving in the anodic compartment a reaction like oxygen evolution (*i.e.* oxidation of water to give molecular oxygen) that can take place without adversely affecting the reduction of CO_2.[8,9] Different type of electrochemical reactors can be used depending on what we are interested on. Individual cells can be useful for studies that aim at gaining fundamental understanding of the CO_2 electroreduction process, while the separated two-compartment configuration prevents the oxidation in the anode of the desired products obtained from carbon dioxide reduction in the cathode. Among the different types of galvanic reactors, outstand filter-press-type reactors since they allow continuous operation and appear as more suitable for an industrial real application.[8]

The final oxidation state of the carbon atom in the value-added chemicals synthesized with these technological solutions is determined by the specific reaction pathway and the number and rates of electrons exchanged. Table 3.1 shows the sequence of possible reduction reactions with the corresponding redox potentials for CO_2 to reported products.[10] The formation of one or another product depends on both the catalyst and the experimental conditions (*i.e.* configuration of the electrode and the electrochemical cell, electrolyte and operating conditions). Nevertheless, as mentioned, the reactivity of CO_2 is low because it is the most stable carbon-based molecule in nature because of its C=O double bond with bonding

energy of 750 kJ·mol^{-1} (considerably larger than that of C–C (336 kJ·mol^{-1}), C–O (327 kJ·mol^{-1}), or C–H bond (411 kJ·mol^{-1}). Consequently, an input of energy must be supplied to reduce CO_2 and convert it into reduced, useful products. Much larger voltages than the equilibrium cell potentials have to be applied in practice across the two electrodes to drive the conversion. Furthermore, the kinetics for CO_2 reduction are, in general, more sluggish than the two-electron H_2 evolution reaction (HER: $2H^+ + 2e^- \rightarrow H_2$, E = –0.42 V vs NHE at pH = 7), which competes with carbon dioxide reduction in aqueous media.[8,10]

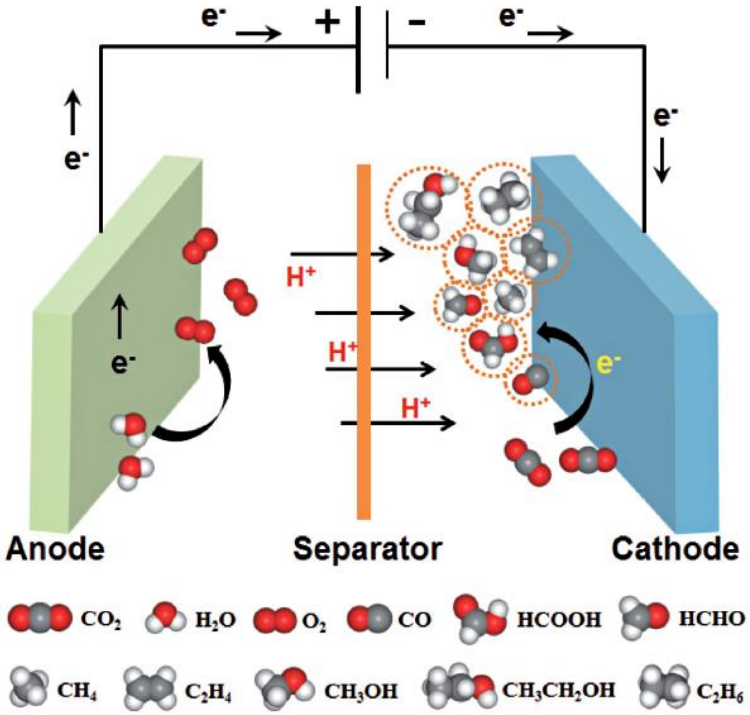

Figure 3.1. Schematic illustration of the electrochemical CO_2 reduction process and the possible products generated in an electrochemical reaction cell. Reproduced from reference 9.

Table 3.1. Electrochemical potentials of possible CO_2 reduction half-reactions in aqueous solutions.

Possible half reaction of CO_2 reduction	E^0 (V vs. NHE) at pH = 7
$CO_2 + e^- \rightarrow CO_2^{\cdot-}$	–1.90
$CO_2 + 2H^+ + 2e^- \rightarrow HCOOH$	– 0.61
$CO_2 + 2H^+ + 2e^- \rightarrow CO + H_2O$	– 0.52
$CO_2 + 4H^+ + 4e^- \rightarrow HCHO + H_2O$	– 0.51
$CO_2 + 6H^+ + 6e^- \rightarrow CH_3OH + H_2O$	– 0.38
$CO_2 + 8H^+ + 8e^- \rightarrow CH_4 + 2H_2O$	– 0.24
$CO_2 + 12H^+ + 12e^- \rightarrow CH_3CH_2OH + 3H_2O$	– 0.42

The electrochemical reaction occurs at the interface between the electrode (an electronic conductor) and the electrolyte (an ionic conductor). It is composed of a series of steps, including (i) the approach of the reactant species to the electrode surface, (ii) the reaction via heterogeneous electron transfer across the interface (actual electrochemical step), and (iii) the transfer of the reduced CO_2 product species away from the reaction area into bulk solution.[11] Most of the proposed mechanisms for direct CO_2 reduction on an electrode involve the initial formation of an intermediate species. That species is usually called $CO_2^{\cdot-}$ although its exact structure is unknown.[12] Hence, $CO_2^{\cdot-}$ does not necessarily represent the bare anion, but it denotes whatever intermediate species is formed when an electron is transferred to the CO_2 molecule, which requires highly energy potential and is considered the responsible for the extra energy that has to be provided for the overall reduction reaction achievement. That extra of voltage to carry out the reaction at a required rate is known as the overpotential (η) and the use of a catalyst trends to reduce its value. Figure 3.2 represents the qualitative reaction scheme for CO_2 conversion with and without the presence of a catalyst.[13]

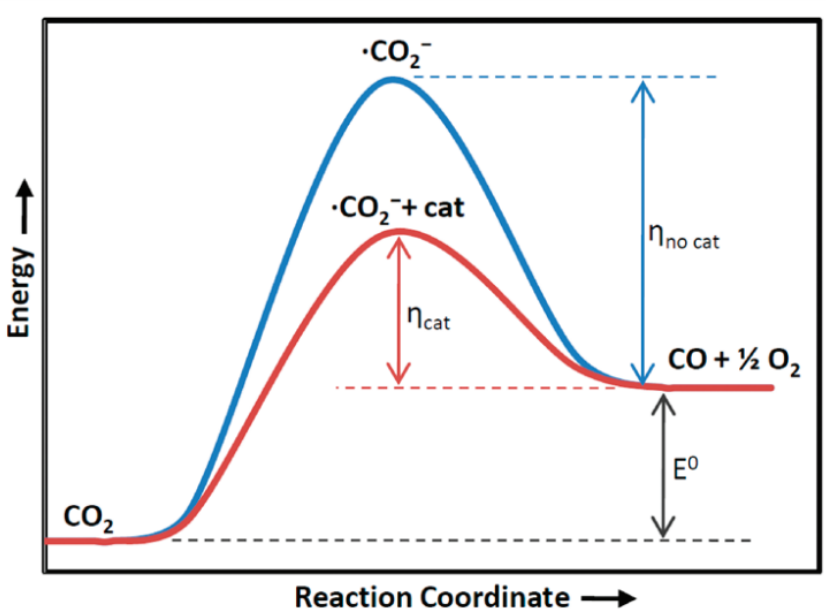

Figure 3.2. Qualitative reaction scheme for CO_2 conversion with and without the presence of a catalyst. Reproduced from reference 13.

To further understand the results of this technique it should be commented the different figures of merit that are commonly used to assess the performance of electrocatalytic CO_2 reduction processes, which are the following:

- **Rate of product formation (r):** The amount of the desired product from CO_2 reduction obtained per unit of cathode area and unit of time (*e.g.* expressed in units of $mol \cdot m^{-2} \cdot s^{-1}$) is sometimes used as a useful figure for

quantifying the rate at which the product can be obtained in the reduction process.

- **Current density (j, usually expressed in mA·cm^{-2}):** The current density is defined as the electric current flow divided by the area of the electrode (usually the geometric area). It measures the rate of the conversion, and a high j as possible is desirable to minimize the area of electrode (and hence the size of the reactor) needed for a desired production rate.

- **Faraday/faradaic efficiency (FE, %):** It is the yield based on the electrical charge passed, *i.e.* the % of the total charge supplied that is used in forming the desired CO_2 reduction product, so ideally it should be as close as possible to 100%. Also known as current efficiency, FE measures the selectivity of the process of reducing CO_2 to a certain product, and it can be calculated using the equation 3.1:

$$FE(\%) = \frac{z \cdot n \cdot F}{q} \cdot 100 \qquad \text{equation 3.1}$$

where z is the number of electrons exchanged, n is the number of moles produced, F is the Faraday constant (F = 96 485 C·mol^{-1}) and q is the total charge applied in the process.

- **Energetic efficiency (EE, %):** It is a measure of the overall energy utilization toward the desired CO_2 reduction products, which can be defined by equation 3.2:

$$EE(\%) = \frac{E^\circ}{E} \cdot 100 \qquad \text{equation 3.2}$$

where E° is the theoretical equilibrium cell potential and E represents the real potential applied in the process (which includes all the cell overpotentials). The EE describes the ratio between energy stored in the desired CO_2 reduction product and the input energy needed to produce it, so a high EE is desirable since this means a small energy penalty of the process.[8]

3.1.2. Materials and electrodes for CO_2 electroreduction performance

During the intense research performed in this field, transition metals and their compounds, such as metal complexes, have been widely evaluated for the electroreduction of CO_2. This is probably because these metals have vacant orbitals and active d electrons, which are believed to be able to energetically facilitate the bonding between the metal and the CO_2 (i.e. adduct formation) and the desorption

of the reduction products.[14] It has been observed that in aqueous media at ambient conditions, CO is the main product with metal electrodes like gold, silver or zinc,[15] whereas indium, tin, mercury or lead are selective for the production of formic acid/formate.[16] Between all of the metal tested, copper seems to be the only capable of breaking the C–O bond in CO_2 and further convert CO to more reduced species such as hydrocarbons (*i.e.* methane and ethylene) and alcohols (*i.e.* methanol and ethanol) at moderate reaction rates over sustainable periods of time. Note that among the different products that CO_2 reduction can yield alcohols such as methanol and ethanol are of especial interest due to their lucrative market as chemical feedstock or high-energy density fuels in the process of replacing fossil fuels.[2] However, elemental copper generates a range of reaction products, and the selectivity of each product tends to be low.[17] For this reason, other Cu-based materials have also been tested to electrocatalytically reduce CO_2, among which copper(I) oxide-based electrodes have exhibited the most prominent performance yielding methanol with high selectivity and current efficiency.[18,19]

Previous literature also proved that metal-organic frameworks (MOFs) are suitable for electrochemical applications because of their versatile chemical composition, tunable electronic properties and highly porous structure where mass transport limitations can be relieved.[20] CO_2 can also be effectively trapped and separated at MOFs structures,[21] which may increase CO_2 concentration at the electrode surface and be beneficial to enhance CO_2 conversion rates and inhibit the competitive HER.[22]

The electroreduction of CO_2 at MOF-based materials has been the subject of research in recent literature,[20,23,24] which denotes the interest on the topic. In this context, the first research work reporting the electrochemical reduction of CO_2 to alcohols using porous coordination polymers was published in 2017 by our research group and demonstrated the suitability of a series of Cu-based metal-organic porous materials (*i.e.* HKUST-1, CuAdeAce, CuDTA and CuZnDTA; Ade: adeninato, Ace: acetate, DTA: dithiooxamidato) to selectively produce methanol and ethanol at modest rates and efficiencies.[25] The electrocatalytic activity of the materials was correlated with the structural features of the electrodes (*i.e.* high surface area, accessibilities and exposure of Cu catalytic centres). One striking feature of the systems was the pseudo-stable behaviour after 6 h of experimental time, which was an unprecedented stability for MOFs-based electrocatalysts in aqueous media. In any case, the rates, Faraday efficiencies and selectivity towards alcohols production are still limited and so the investigation of CO_2 electroreduction at MOF-based electrodes remains a challenge.

On the other hand, bimetallic inorganic electrocatalysts have demonstrated to tune the selectivity towards one specific product with FEs higher than 90% in some

cases.[26] The appealing aspect of these mixed-metal systems is that the electronic and geometric structure around the active sites can be tuned to modulate the relative binding energy of different reaction intermediates in the electrocatalytic surface and alter the local atomic arrangement at the active sites. Compared with single metal catalysts, bimetallic surfaces may also reduce the energy differences between CO_2 and intermediates, eventually offering low overpotentials for corresponding reactions and a controlled selectivity.[22,27–29] Moreover, these mixed-metal systems could become a good approach to replace the edge atoms of single metal preferentially absorbing H_2 with other metal atoms which absorb CO_2 and thus suppress or reduce the competitive HER.[30,31] Overall, the use of Cu-based bimetallic systems may be a potential way to enhance the performance of current CO_2 electroreduction systems for the production of alcohols. The literature, however, shows that even a tiny fraction of a second metal can totally poison the CO_2 conversion ability of Cu.[32,33] This makes the exploration of mixed-metal systems for alcohol evolution a challenging task, although some successful cases have been published for Cu-Zn, Cu-Pd, Cu-Ag or Cu-Au-based electrocatalysts in the production of ethanol.[34–37]

Moreover, apart from the nature of the material used as catalyst, the configuration of the electrode has also a great influence on the performance of the CO_2 electroreduction. Particularly, the configuration of gas diffusion electrodes (GDEs) has resulted to be especially successful. GDEs usually consist of a carbonaceous support, a microporous layer, and a catalytic layer formed by the material to be tested deposited on it.[8] Besides, because of their high porosity and partial hydrophobicity, GDEs form a characteristic gas-solid-liquid three-phase interface, which allows a homogeneous distribution over the catalyst surface. These properties make GDEs especially suitable for CO_2 electroreduction in gas phase.[38]

3.1.3. Objectives

Considering the pioneering results yielded by Cu-based metal-organic material and the potential reported for bimetallic inorganic catalysts, the present study sought to prepare, characterize and evaluate a series of bimetallic metal-organic frameworks consisting of Cu(II) and a second transition metal (zinc (Zn), ruthenium (Ru), palladium (Pd) and bismuth (Bi)) as electrocatalysts for the continuous conversion of carbon dioxide with the aim of achieving a synergistic relationship that surpasses the reported performance of CO_2 electroreduction to alcohols of homometallic MOFs. Furthermore, to enhance the mass transport across the gas-solid-liquid interface, we envisage supporting the bimetallic materials onto porous carbon paper to form gas diffusion electrodes (GDEs).

Precisely, benchmark Cu-based HKUST-1 MOF has been selected as starting platform material due to its demonstrated catalytic activity for the CO_2-to-alcohols reaction.[25,39] This MOF, also called MOF-199 or $[Cu_3(BTC)_2(H_2O)_3]_n$, was first synthesized by Chui et al. in 1999, and since then it has been extensively studied and is among the few commercially available MOFs (Basolite C300).[40] Copper(II) is the metal centre and benzene-1,3,5-tricarboxylate (or trimesic acid, BTC), the organic linker that interconnects dimeric copper entities forming face-centred cubic crystals ($Fm\bar{3}m$) that contain an intersecting three-dimensional system of large squared-shaped pores (9 Å by 9 Å) (Figure 3.3a).[41] The coordination water molecule that completes the coordination sphere of Cu(II) can be reversely released to yield a coordinatively unsaturated site. This fact, along with its highly crystalline nature characterized by a high surface area and a large pore size makes HKUST-1 a promising catalyst (Figure 3.3b).[42,43]

On the other hand, the selected transition metal ions could be prone to establish a synergistic interaction with the Cu(II)-based catalyst, since previous work has shown that Zn(II) can lengthen the stability of Cu(II) catalysts,[44] while Pd(II), Ru(III) and Bi(III) inherently exhibit electrocatalytic properties, and in some cases be able to enhance the formation of key intermediates.[45–50]. Concretely, bismuth has received recent attention as electrocatalysts for CO_2 reduction due to its low cost and toxicity, as well as selectivity for the CO_2-to-HCOOH reaction.[51–60] Bismuth may also potentially enhance the binding of intermediate species (i.e. $COOH^*$ and $OCHO^*$) in the further conversion of CO_2 and reduce the competitive HER due to its positive free energy of hydrogen adsorption.[61]

Two different strategies have been developed for preparing bimetallic HKUST-1-based catalysts: (i) a solventless doping process to get HKUST-1(Cu,M_D) materials (M_D, doping metal = Zn(II), Ru(III), Pd(II) and Bi(III)) and (ii) physical blends of HKUST-1(Cu) with a Bi-based CAU-17 MOF. This MOF with formula $[Bi(BTC)(H_2O)]_n$ was selected for its chemical analogy to HKUST-1 and because it also presents coordinatively unsaturated sites.[62] Its crystal structure, first reported in 2016, is built of left- and right-handed helices of edge-sharing BiO_9-polyhedra that are linked by BTC ligands to form a framework with hexagonal, rectangular and triangular channels with pore diameters of 9.6, 3.6 and 3.4 Å, respectively and $P\bar{3}$ space group (Figure 3.3c). Every Bi(III) ion is coordinated to one terminal H_2O molecule, which can be also removed reversibly (Figure 3.3d).[63]

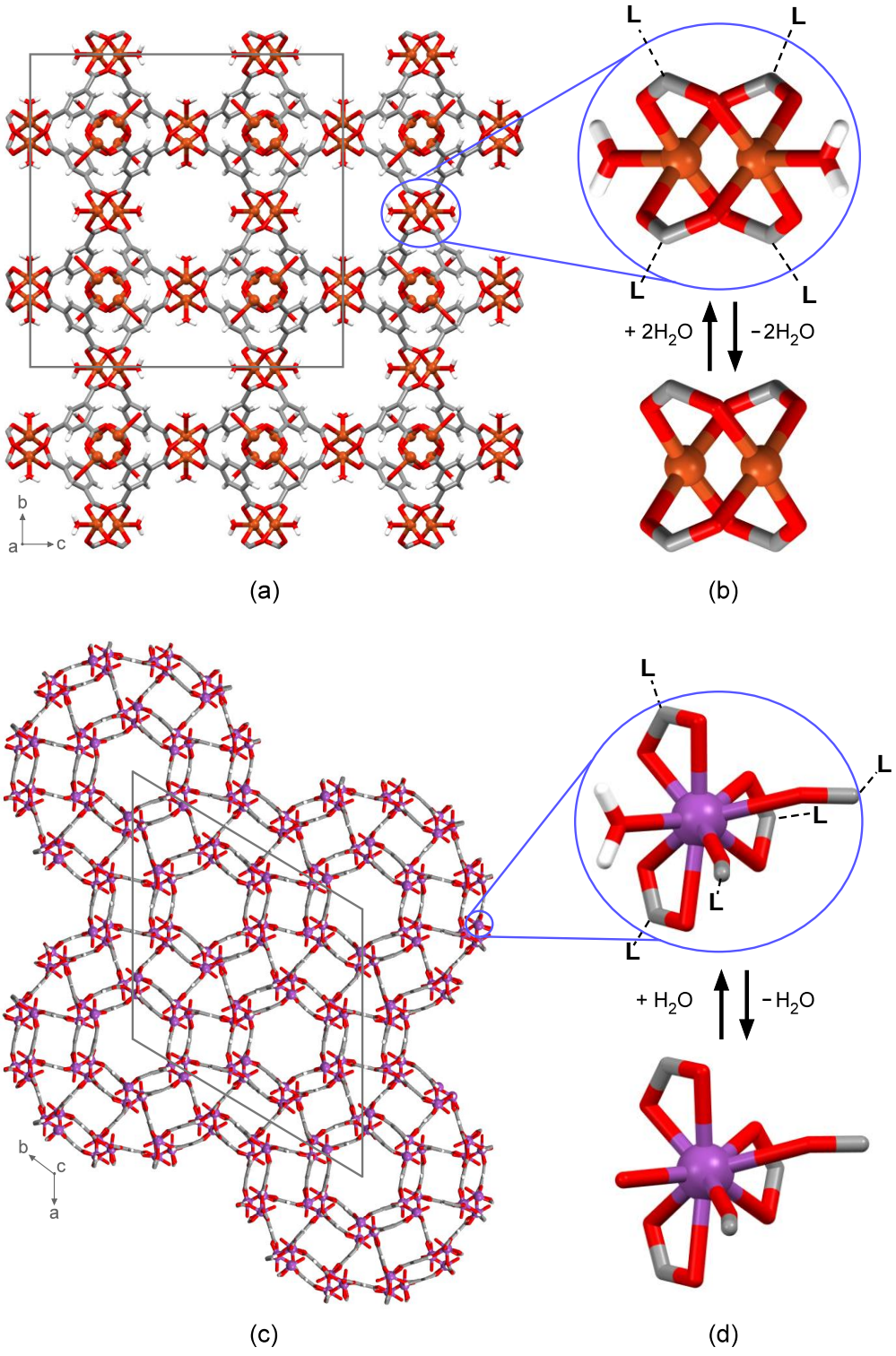

Figure 3.3. (a) Crystal structure of HKUST-1 (view along [100]) with the unit cell marked in grey and (b) reversible release of coordination water molecules from the paddlewheel shaped secondary building unit (SBU). (c) Crystal structure of CAU-17 (view along [001]) with the unit cell marked in grey and (d) reversible release of coordination water molecule from the nonacoordinated Bi(III). Crystallographic data for the structural representation was retrieved from the Cambridge Structural Database[64] (YOZNAE and MAGXOK entries for HKUST-1 and CAU-17, respectively). White stands for hydrogen, grey for carbon, red for oxygen, orange for copper, purple for bismuth and "L" for organic linker.

3.2. HETEROMETALLIC HKUST-1(Cu,M_D) MOFS

3.2.1. EXPERIMENTAL SECTION

In this section the solvent-free synthetic procedure for obtaining doped Cu-based MOFs (dopant metals, M_D: Zn(II), Ru(II), Pd(II) and Bi(III)) with an HKUST-1 structure and their gas diffusion electrodes preparation (MOFs-GDEs) is presented. The electrochemical characterization and CO_2 electroreduction process conditions are also explained.

3.2.1.1. Synthesis of Cu/M/BTC MOFs

All the chemicals were of reagent grade and were used as commercially obtained (Table 2.1 of Chapter 2).

Doped HKUST-1(Cu,M_D) samples were prepared by modifying a synthetic procedure described for the solventless synthesis of pristine homometallic HKUST-1(Cu).[65] The corresponding amounts of $Cu(OAc)_2{\cdot}H_2O$ (OAc: acetate), dopant metal (M_D) source ($Zn(OAc)_2{\cdot}2H_2O$, $RuCl_3{\cdot}xH_2O$, $Pd(OAc)_2$ and $Bi(NO_3)_3{\cdot}5H_2O$) and trimesic acid (H_3BTC: benzene-1,3,5-tricarboxilic acid, 0.40 mmol) to satisfy the stoichiometry of $[(Cu_{1-x}M_{Dx})_3(BTC)_2]_n$ (x = 0, 0.05, 0.10 and 0.20; three doping ratios for each M_D) were hand-grinded thoroughly to obtain a homogeneous mixture.

Table 3.2. gathers the reagent amounts, doping target ratio, achieved doping ratio that determines sample coding (obtained by X-ray fluorescence (XRF) and explained in results section), and reaction yield for each doped sample and for non-doped homometallic HKUST-1(Cu) sample prepared following the same procedure but without the addition of a M_D source with comparative purposes. The final mixture was sealed in a 2-mL glass ampule and heated to 120 °C using a heating rate of 2 °C·h^{-1} in a conventional oven during 48 h (Figure 3.4). The products were washed with water and ethanol twice to remove unreacted reagents. H_Cu, H_Zn and H_Bi samples presented the characteristic light blue colour of HKUST-1 when is hydrated, whereas H_Pd and H_Ru samples acquired light and dark green tonality, respectively, being more prominent the higher the doping content. Once the samples were dried at 120°C to remove the adsorbed solvent and water molecules, all of them changed to an intense/darker blue colour as a consequence of losing the coordinated water molecules from the HKUST-1 dinuclear paddle-wheel. (Figure 3.5a). Even though when exposed to moisture they quickly return to their original colour (Figure 3.5b).

Table 3.2. Synthetic conditions, sample coding and synthesis yield (%) of HKUST-1(Cu) and HKUST(Cu,M_D) samples along with the relative atomic content (%) of dopant metal (M_D) in the synthesis mixture and in the products.[a]

M_D	$Cu(OAc)_2$	H_3BTC	M_D source	Synthesis M_D : Cu ratio	Product M_D : Cu ratio	Yield (%)	Sample code
–	0.60 mmol (0.1210 g)	0.40 mmol (0.0885 g)	–	0 : 100	0 : 100	90	**H_Cu**
Zn	0.57 mmol (0.1150 g)		0.03 mmol (0.0067 g)	5 : 95	5 : 95	70	**H_Zn5**
	0.54 mmol (0.1089 g)		0.06 mmol (0.0133 g)	10 : 90	8 : 92	88	**H_Zn8**
	0.48 mmol (0.0968 g)		0.12 mmol (0.0266 g)	20 : 80	19 : 81	75	**H_Zn19**
Ru	0.57 mmol (0.1150 g)		0.03 mmol (0.0062 g)	5 : 95	3 : 97	86	**H_Ru3**
	0.54 mmol (0.1089 g)		0.06 mmol (0.0125 g)	10 : 90	7 : 93	89	**H_Ru7**
	0.48 mmol (0.0968 g)		0.12 mmol (0.0249 g)	20 : 80	10 : 90	83	**H_Ru10**
Pd	0.57 mmol (0.1150 g)		0.03 mmol (0.0069 g)	5 : 95	3: 97	85	**H_Pd3**
	0.54 mmol (0.1089 g)		0.06 mmol (0.0138 g)	10 : 90	5 : 95	79	**H_Pd5**
	0.48 mmol (0.0968 g)		0.12 mmol (0.0275 g)	20 : 80	11 : 89	77	**H_Pd11**
Bi	0.57 mmol (0.1150 g)		0.03 mmol (0.0146 g)	5 : 95	4 : 96	85	**H_Bi4**
	0.54 mmol (0.1089 g)		0.06 mmol (0.0291 g)	10 : 90	7 : 93	77	**H_Bi7**
	0.48 mmol (0.0968 g)		0.12 mmol (0.0582 g)	20 : 80	11 : 89	43	**H_Bi11**

[a] Samples coding refers to the achieved M_D atomic ratio (%) relative to the total metal content (Cu + M_D) determined by XRF.

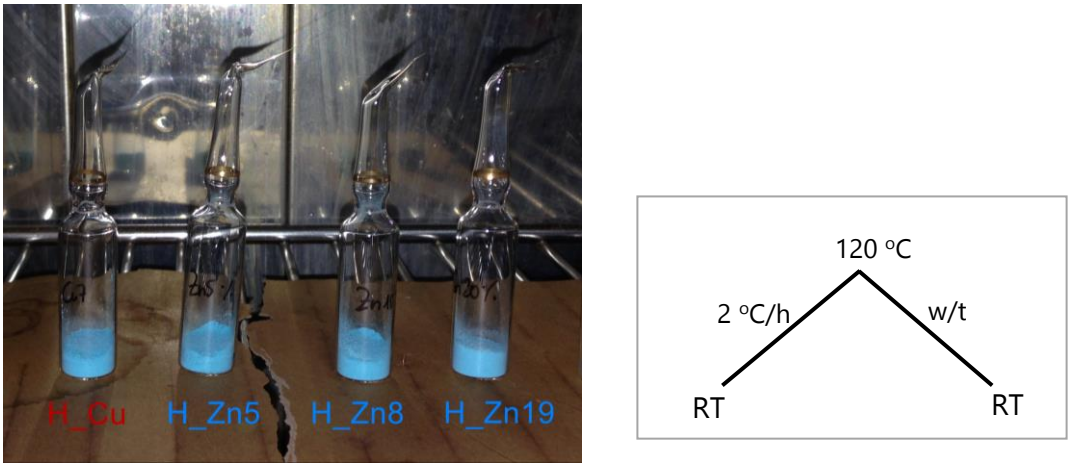

(a) (b)

Figure 3.4. (a) Sealed 2-mL glass ampules containing reaction mixtures for HKUST-1(Cu) and HKUST-1(Cu,Zn). (b) Heat ramp employed for the solventless synthesis of HKUST-1(Cu,M_D) samples in a conventional oven.

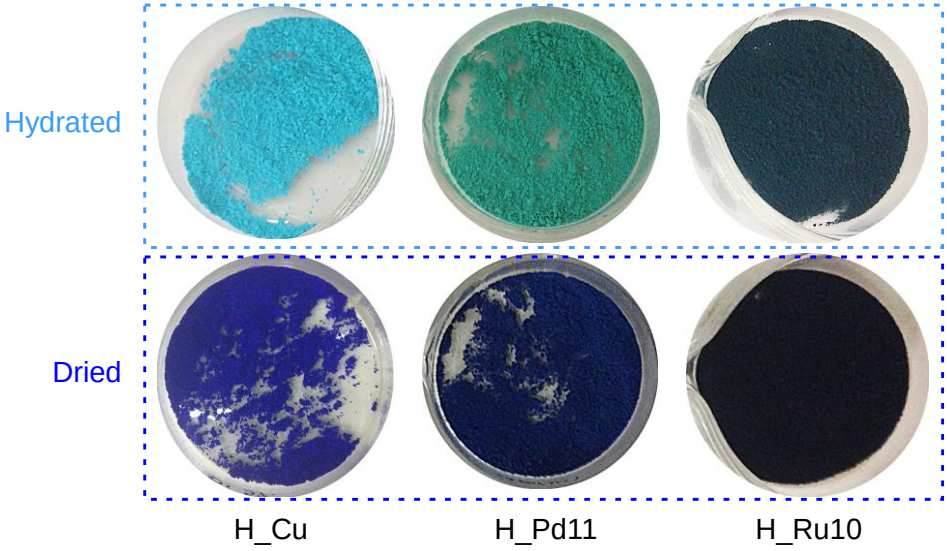

(a)

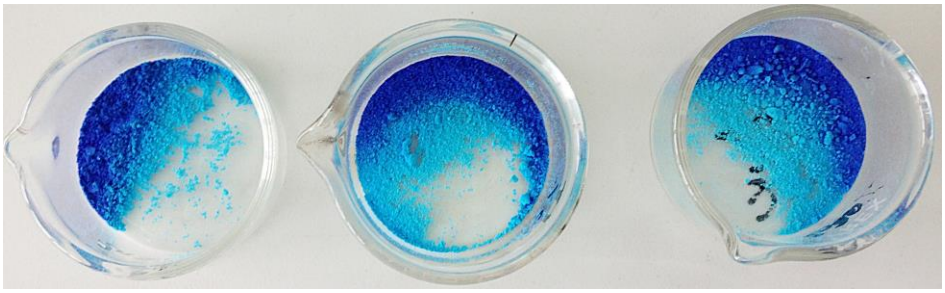

(b)

Figure 3.5. Appearance of (a) H_Cu, H_Pd11 and H_Ru10 samples prior and after a drying process and (b) H_Zn5, H_Zn8 and H_Zn19 dried samples when exposed to atmospheric moisture.

3.2.1.2. Preparation of MOF-GDEs

The MOF-based gas diffusion electrodes GDEs (A = 10 cm^2) were prepared by airbrushing a catalytic ink onto a porous carbon paper type TGP-H-60 (Toray Inc.). This catalytic ink was formed by a mixture of the synthesized HKUST-1(Cu,M_D) as electrocatalysts, Nafion® dispersion 5 wt.% as binder and isopropanol as vehicle, with a 70:30 catalyst/Nafion mass ratio and a 3% solids (catalyst + Nafion) percentage. The mixture was sonicated for 15 min before airbrushing onto the carbon papers and the resulting MOF-GDEs (Figure 3.6) were dried and rinsed with deionised water before use. The catalyst loading in the GDEs was kept at 1 $mg \cdot cm^{-2}$.

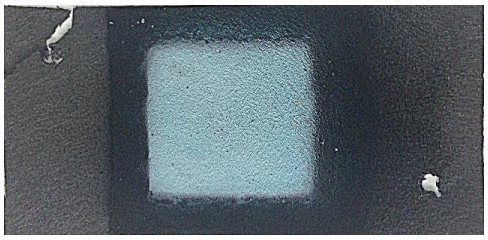

Figure 3.6. Appearance of MOF-GDE of 10 cm^2 obtained after airbrushing catalytic ink keeping 1 $mg \cdot cm^{-2}$ of loading.

3.2.1.3. Cyclyc voltammetry characterization

The electrochemical behaviour of the materials was evaluated by cyclic voltammetries employing a conventional three electrode electrochemical cell. The current-voltage curves were obtained with a scan rate of 50 $mV \cdot s^{-1}$ at potentials ranging from 0 to –2 V vs. Ag/AgCl in a CO_2 saturated 0.5 M $KHCO_3$ aqueous solution as electrolyte. Portions of the MOF-based GDEs were used as working electrodes, while a glassy carbon and Ag/AgCl (sat. KCl) were used as counter and reference electrode, respectively. Current density is expressed as the total current divided by the geometric surface area of the electrodes.

3.2.1.4. Experimental conditions for CO_2 electroreduction

The prepared MOF-GDEs were evaluated for the continuous electrocatalytic reduction of CO_2 using a filter-press electrochemical cell system as explained in detail in Section 2.3.1 of chapter 2. The MOF-GDEs were employed together with a platinised titanium electrode as the anode and a Ag/AgCl (sat. KCl) reference electrode assembled close to the cathode. The cathode side of the reactor was fed with CO_2 gas (99.99%) with a flow/area of $Q_{g/A}$ = 10 $mL \cdot min^{-1} \cdot cm^{-2}$. A 0.5 M $KHCO_3$ aqueous solution is used as both, catholyte and anolyte, with a flow rate of $Q_{e/A}$ = 2 $mL \cdot min^{-1} \cdot cm^{-2}$. All the experiments were performed at galvanostatic conditions (j = 20 $mA \cdot cm^{-2}$). These $Q_{g/A}$, $Q_{e/A}$ and j conditions were previously found to be optimal for the CO_2 reduction using copper(I) and copper(II) type electrocatalysts.[38]

The experimental time was 90 min, where pseudo-stable conditions are ensured, according to previous analyses.[18,38] Liquid samples were taken every 15 min from the catholyte tank for analysing. To quantify the concentration of each product in the liquid phase, the samples were analyzed by duplicate in a headspace gas chromatograph (standard deviations below 12.8%).

The performance of the electrochemical process was evaluated by productivity, r (*i.e.* product obtained per unit of cathode area and time), and the Faraday efficiency, FE (*i.e.* selectivity of the reaction for the formation of the different products).

3.2.2. RESULTS AND DICUSSION

This section addresses, firstly, the chemical and microstructural characterization of HKUST-1(Cu,M_D) doped with Zn(II), Ru(III), Pd(II) and Bi(III) describing the dopant loadings, their distribution and their effect in the crystallinity and microporosity. Thereafter, the performance as cathode material is assessed by means of cyclic voltammetry analyses and continuous reaction in a filter-press electrochemical cell.

3.2.2.1. Characterization of bimetallic Cu/M/BTC samples

Synthesized MOF samples were initially characterized by X-ray fluorescence (XRF) and powder X-ray diffraction (PXRD) to analyse the dopant content and its influence in the HKUST-1 crystalline phase. Table 3.2 presented above collates amount of dopant (M_D) added as reagent in the synthesis mixture and that one incorporated into the synthesis product. In this respect, the relative agreement between dopant content targets and amounts found in the HKUST-1 samples varies with dopant element. In the case of zinc, whose size and atomic number are the closest ones to copper, the amount of dopant incorporated is almost the same as that added in the reagent mixture. Ruthenium, palladium and bismuth are less efficiently assimilated during the synthesis process, giving rise to dopant contents somewhat below the target values. X-ray photoelectron spectroscopy (XPS) measurements taken on H_Ru10 (Figure 3.7) revealed the presence of chloride ions (Cl 2p 199.5 eV) which in turn confirms the presence of ruthenium(III), as they are required to counteract the additional positive charge that implies the use of a trivalent metal. Previous works have reported the solvothermal synthesis of mixed valence HKUST-1(Ru^{II},Ru^{III}) in which chloride acts as counterion to balance the network charge.[50] Ruthenium signal cannot be properly analyse as its more characteristic and intense $3p_{5/2}$ peak would appear at *c.a.* 280 eV, but C 1s signal is observed in this region masking ruthenium peak. Just a residual signal of Ru $3p_{3/2}$ appears at 463.3 eV, what would also match with the presence of Ru(III).[66] Finally, with respect to the reaction yields, they are

comparable or slightly lower (70–89%) than those obtained for undoped HKUST-1 (H_Cu: 90%), except in the case of H_Bi11 whose yield decreases up to a 43%.

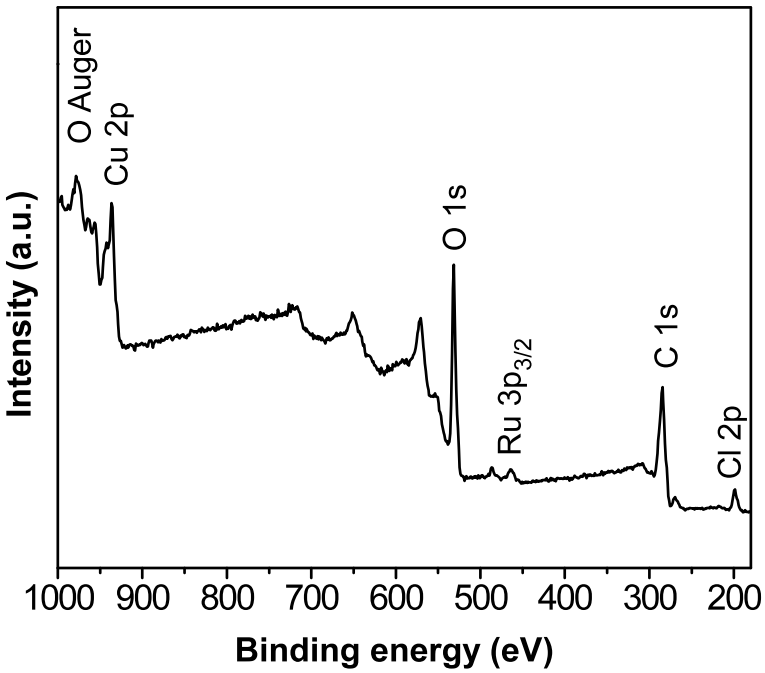

Figure 3.7. XPS spectrum of H_Ru10.

After analyzing by PXRD all the samples, in both the homometallic and the doped samples, the formation of the HKUST-1 type structure is confirmed. Figure 3.8 shows the normalized diffractograms of the samples doped with Zn, Ru, Pd and Bi.

Although all the samples present the characteristic reflections of HKUST-1, in some of them (H_Zn19 and H_Ru7) small peaks are observed that do not correspond to this structure (marked in the figure with an asterisk), which indicates a lower content of other phases formed from copper, and/or dopant metal with trimesate (BTC). In the case of the samples doped with bismuth, the impurity peaks, especially in H_Bi7, are more and more intense, which makes us suspect that Bi(III) has not been incorporated into the HKUST-1 structure, at least significantly. This fact is confirmed later in the analysis by electron microscopy of the samples and may be due to the significantly higher ionic radius of Bi(III) (117 pm) in comparison to Cu(II) (87 pm), whereas Zn(II) and Ru(III) present rather similar ionic radii (88 pm and 82 ppm, respectively). In the case of Pd(II), which ionic radius is established to be 100 pm, a bit higher than Cu(II) but not as big as Bi(III), the incorporation of the dopant metal is allowed with some changes in the crystallinity (higher full width at half maximum, FWHM in Figure 3.8) and in structural parameters as commented below.[67]

It deserves to note that the crystalline impurity peaks could not be ascribed univocally to any known phase comprised by the selected metal ions and/or trimesate anion.

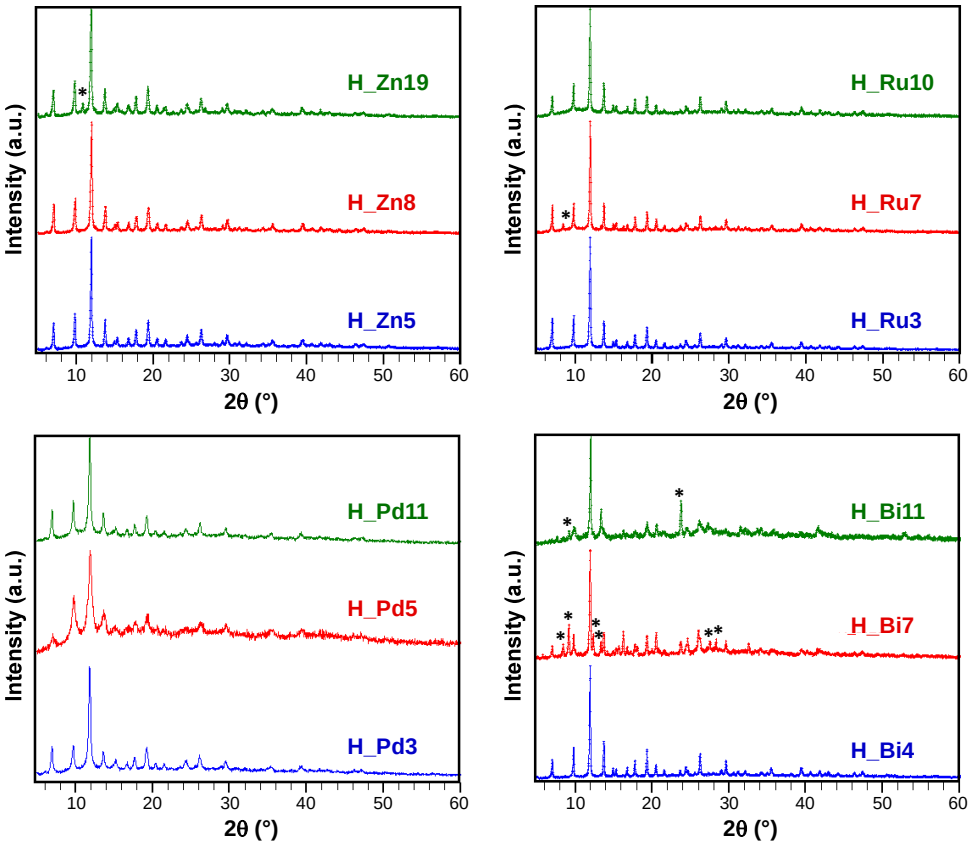

Figure 3.8. Normalized PXRD patterns of HKUST(Cu,M_D) samples. Asterisks denotes for impurities.

For comparative purpose, indexation of the diffraction profiles was made by means of the FULLPROF program (pattern-matching analysis)[68,69] on the bases of the space group and the cell parameters found in the Cambridge Structural Database (CSD)[64] for the single crystal X-ray structure of HKUST-1 (CSD entry: UVIPIZ). Figure 3.9 and Table 3.3 gather the results of the profile fittings carried out on PXRD patterns of H_Cu and of samples with dopant content close to 10% (H_Zn8, H_Ru10 and H_Pd11).

Table 3.3. Cell parameters and agreement factors obtained in the pattern matching performed on H_Cu, H_Zn8, H_Ru10 and H_Pd11.[a]

	H_Cu	H_Zn8	H_Ru10	H_Pd11
a (Å)	26.283(3)	26.322(4)	26.345(2)	26.413(3)
V (Å^3)	18 156(4)	18 238(5)	18 285(2)	18 428(4)
R_b	1.11	1.92	13.9	82.6
R_p	31.2	31.3	49.3	32.0
χ^2	2.27	2.33	1.45	1.77

[a] $R_b = 100\cdot(\sum_h|'I_{obs,h}' - I_{calc,h}|)/(\sum_h|'I_{obs,h}|)$; $R_p = 100\cdot(\sum_{i=l,n}|y_i - y_{c,i}|)/(\sum_{i=l,n} y_i)$; $X^2 = [R_{wp}/R_{exp}]^2$.

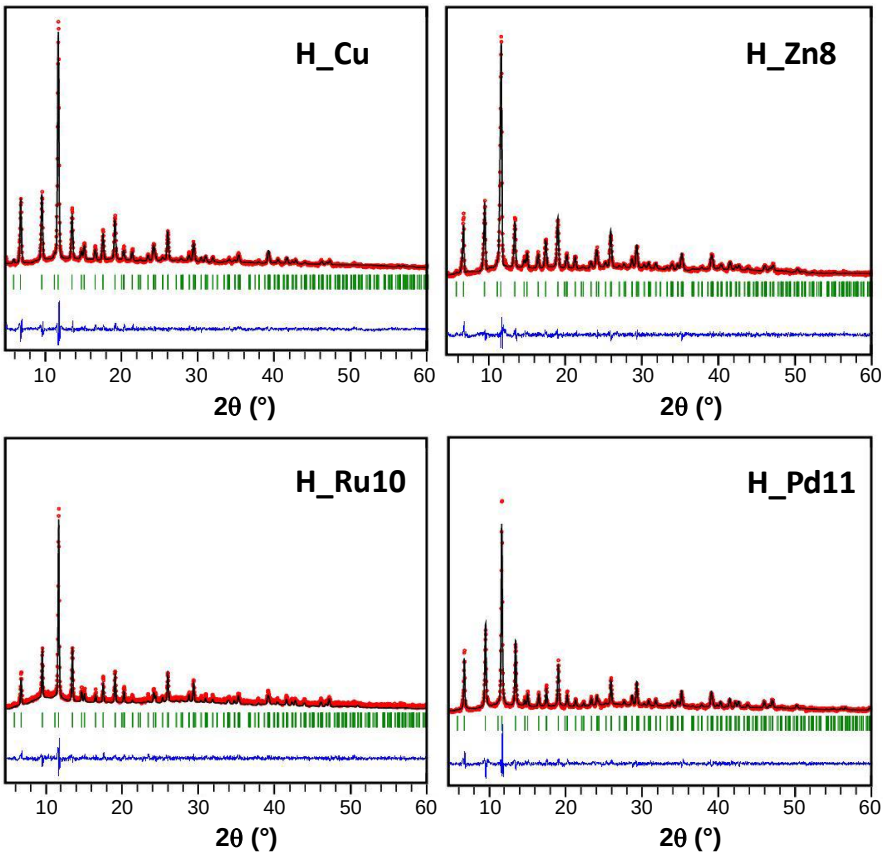

Figure 3.9. PXRD pattern-matching refinement plots for H_Cu, H_Zn8, H_Ru10, and H_Pd11 (green ticks: calculated reflections; red circles: experimental pattern; black line: simulated pattern; blue line: difference between patterns).

The introduction of a doping element implies a slight increase in the cell parameter with respect to the homometallic H_Cu in every case. This fact is attributable to the occurrence of longer M–$O_{carboxylate}$ coordination bond distances that imply the presence of the dopant in the paddle-wheel-shaped dinuclear $[M_2(OOC)_4]$ secondary building unit (SBU). Effectively, in the case of Pd(II), its greater ionic radii values are consistent with the biggest increase in coordination bond distances and cell parameters. In the case of Zn(II) and Ru(III), which exhibit rather similar ionic radii to that of Cu(II), the change in cell parameters can be attributable to the Jahn-Teller effect of Cu(II) (d^9), that implies shorter equatorial coordination distances than those found in analogous paddle-wheel shaped complexes based on metals of similar size.[64] Anyway, despite the above description indicating that the dopant is incorporated in the SBU of the MOF, it cannot discard that part of the dopant might be also appended as a defect in the surface of the framework.[70] Accordingly, a reduction in the surface area and micropore volume might be expected, but a similar effect can also be attributed to slight modifications of the synthetic conditions (such as a change in the starting reagents). To end up with PXRD analysis, it must be pointed out that, despite solventless synthesis has demonstrated to be a suitable procedure to incorporate dopants in MOFs,[71] the method is quite sensitive to hand-

milling and heating procedures and as a result, it can render batches with some minor crystalline impurities in the products.

The homogeneous nature of the samples and their crystallite size was analysed by means of scanning electron microscopy (SEM). Firstly, micrographs of the doped samples with the higher content of M_D taken using backscattered electron (BSE) mode helped us to analyse the homogeneous distribution of dopants along the sample (Figure 3.10). The BSE mode shows phase contrast as a function of the electron density of the material, giving a clearer contrast in most electron-dense areas. It should be noted that the H_Zn19 sample is initially excluded from this analysis, since the absence of contrast is not significant in this case, since Cu and Zn are consecutive elements in the periodic table. Considering this, it seems that in H_Pd11 palladium is quite homogeneous distributed as no differences in contrast are observed. On the other hand, the H_Ru10 sample presents some small lighter areas in a dark matrix, which indicates that there are areas that are richer in ruthenium. For the H_Bi11 sample, this is even more marked, revealing a very notable phase segregation.

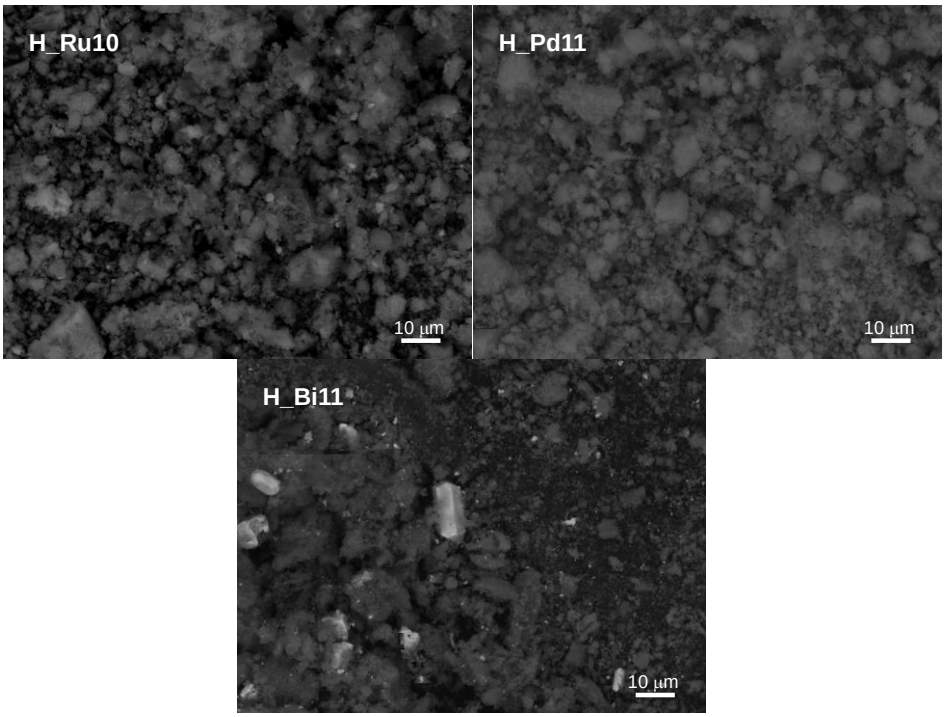

Figure 3.10. SEM micrographs (BSE mode) at 1kX magnifications of H_Ru10, H_Pd11 and H_Bi11.

To further analyse this issue and to determine the homogeneity in H_Zn doped samples, energy-dispersive X-ray spectra (EDX) were also collected in the scanning electron microscope. As it can be seen in Figure 3.11, EDX data confirmed that Zn(II)- and Pd(II)-doped samples show a homogeneous distribution of the dopant metal through all the material, whereas in H_Ru10 sample some Ru(III) enriched areas were

evidenced, but observing the presence of ruthenium over all the samples in greater or lesser concentration. In the case of H_Bi samples, it can be effectively concluded with this study that segregation of phases occurs and consequently, Bi(III) did not reach to be incorporated in HKUST-1 structure as only bismuth was observed when spotting in lighter areas.

To end up with electron microscopy analysis, secondary electron mode (SEI) micrographs of homometallic (H_Cu) and doped samples presented in Figure 3.12 show polycrystalline samples with heaped sub-micrometric crystals in all the cases. Such small sized particles can benefit the performance of the MOF-GDEs as a greater external surface area of the dispersed catalytic material might favour the reaction kinetics. H_Bi samples were excluded from the final analysis, as the doping process resulted unsuccessful. Further details on bismuth-based material are presented in Section 3.3.

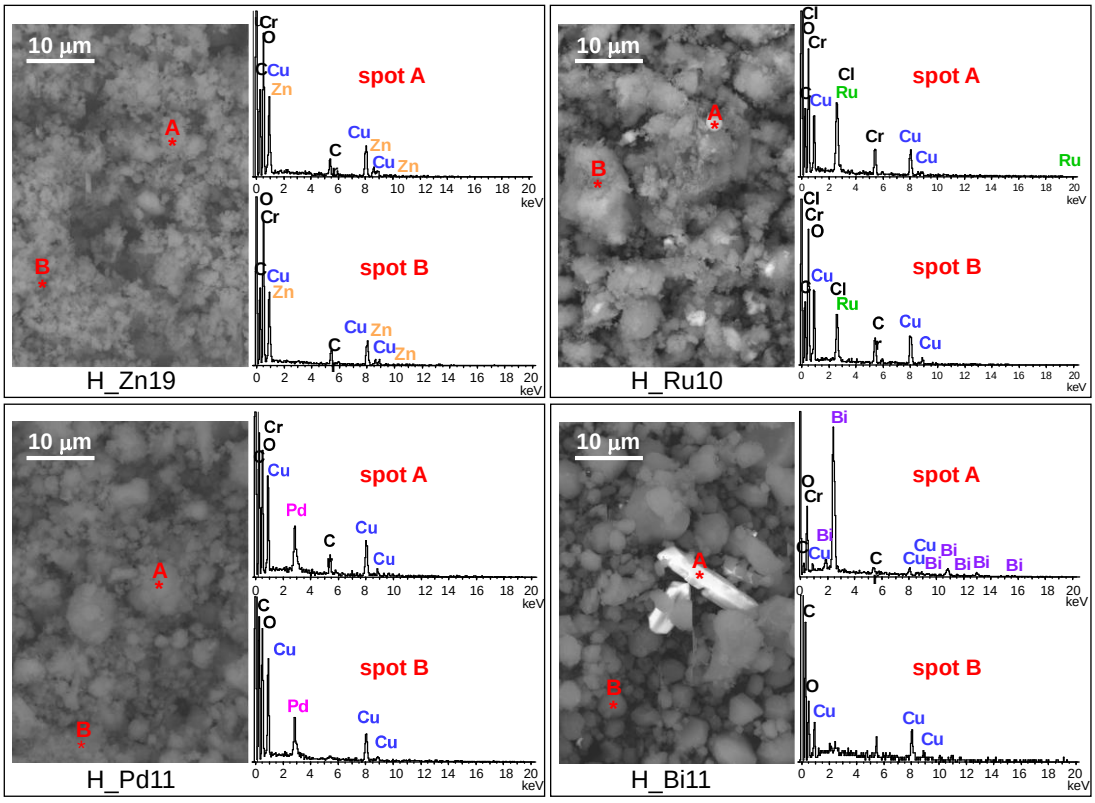

Figure 3.11. SEM and corresponding EDX analysis for H_M_D samples with the higher dopant content. Note that chromium (Cr) comes from the metalation of samples to make them conductive for SEM measurements.

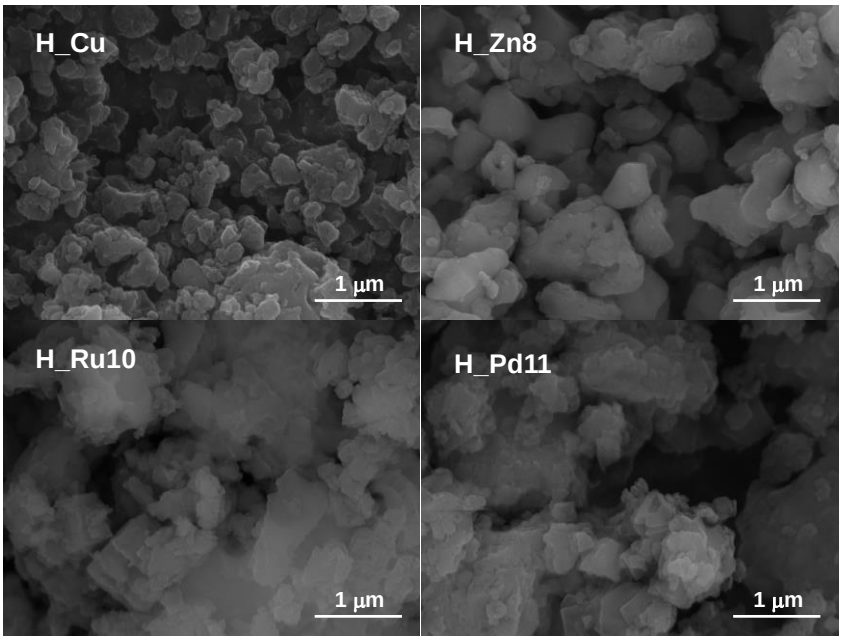

Figure 3.12. SEM micrographs (SEI mode) at 25kX magnifications of H_Cu, H_Zn8, H_Ru10 and H_Pd11.

Finally, the microstructural analysis, N_2 adsorption isotherms were measured at 77 K (Figure 3.13) in the samples with the molar content close to 10%. All of them can be defined, mainly, as type I isotherms according to the IUPAC classification[72] with a marked knee (B-point) at p/p° values smaller than 0.12, which is characteristic of the adsorptive behaviour of microporous compounds. At intermediate pressures, the adsorption presents certain monotonic rise followed by a sudden increase at high relative pressures (p/p° > 0.9). Both phenomena are attributable, respectively, to multilayer adsorption and capillary condensation occurring in the intergranular space of the aforementioned submicrometric MOF particles.

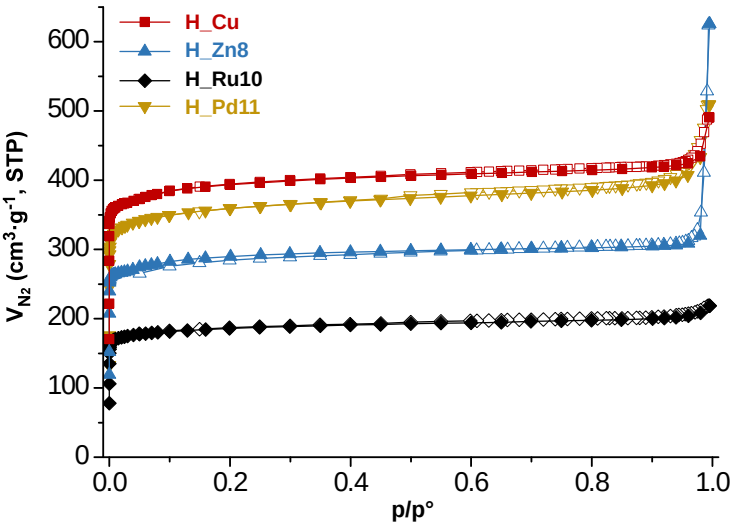

Figure 3.13. N_2 adsorption isotherms at 77 K for H_Cu, H_Zn8, H_Ru10 and H_Pd11. Filled and empty symbols correspond to adsorption and desorption branches, respectively.

The data obtained from the numerical analysis of the isotherms are gathered in Table 3.4. In concordance to the height of the plateau of the isotherms at intermediate pressures, homometallic H_Cu shows the greatest surface area (S_{BET}), while the inclusion of a second transition metal produces in all cases materials with smaller surface areas. This reduction is not only related to the higher atomic weight of the doping metal, since the heaviest of them (Pd) gives greater area values than the lighter ones (Zn and Ru). A possible explanation relies on the influence of the dopant reagent on the crystallinity of the material (consider that a greater number of defects produces a detriment of the porosity). The subtraction of the microporous area to the total surface area leads to external surface area values (area attributable to the outer surface of the MOF particles) ranging from 45 to 284 $m^2 \cdot g^{-1}$. In a rough calculation, using the spherical particle approach and corrected crystallographic densities the surface area (S) can be defined in terms of the material density (ρ) and particle diameter (D) as depicted by equation 3.3. Accordingly, these external area values imply mean particle sizes of 79, 24, 149, and 67 nm for H_Cu, H_Zn8, H_Ru10 and H_Pd11, respectively. Both, the external surface (particle size) and the microporous one (crystal structure of the MOF), are of special relevance in the functionality of the herein studied materials, being beneficial, in general, to achieve high values of both for their use as GDEs.

$$S = \frac{6}{\rho \cdot D} \cdot 100 \qquad \text{equation 3.3}$$

Table 3.4. Surface area values and pore volumes determined for H_Cu, H_Zn8, H_Ru10 and H_Pd11.[a]

Sample	S_{BET} ($m^2 \cdot g^{-1}$)	S_{micro} ($m^2 \cdot g^{-1}$)	S_{ext} ($m^2 \cdot g^{-1}$)	V_{micro} ($cm^3 \cdot g^{-1}$)	V_T ($cm^3 \cdot g^{-1}$)
H_Cu	1560	1474	86	0.574	0.759
H_Zn8	1143	859	284	0.333	0.968
H_Ru10	741	696	45	0.269	0.338
H_Pd11	1425	1325	100	0.515	0.788

[a] S_{BET}: BET surface area; S_{micro}: microporous surface area; S_{ext}: external surface area; V_{micro}: micropore volume; V_T: total pore volume determined at p/p°: 0.993.

3.2.2.2. Cyclic voltammetry characterization

Prior to analyse all the H_M_D samples in the electrochemical reactor, a preliminary test by cyclic voltammetry was performed in a CO_2-saturated (0.5 M $KHCO_3$) aqueous solution in order to qualitatively assess if the doping exerts any influence in the electrochemical behaviour. Figure 3.14 gathers the voltammograms yielded by representative MOF-GDEs after 5 scans (remaining samples exhibit a similar trend). The current densities (j) are normalized to the geometric area of the MOF-GDEs.

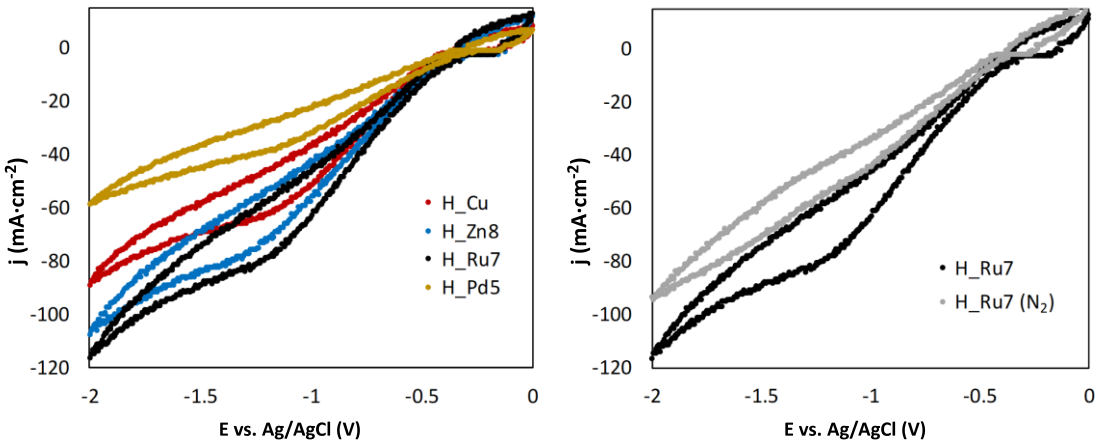

Figure 3.14. Cyclic-voltammetry responses for (a) H_Zn8, H_Ru7 and H_Pd5 in comparison to H_Cu-based GDEs in a medium saturated with CO_2 and, (b) responses for H_Ru10 in the presence and absence of CO_2.

All voltammetric curves show a reduction process starting at *ca.* –1 V vs. Ag/AgCl. This reduction peak may be initially assigned to the reduction of CO_2. The reduction wave is more pronounced for Zn(II)- and Ru(III)-doped samples than for H_Cu which indicates their notable activity as cathode material. It is noteworthy that within the applied voltage, H_Ru10 sample appears to be the most promising candidate, while the incorporation of Pd(II) hinders the electroreduction process of CO_2. These results can be taken as indicative of the activity, and a deeper insight is presented when describing below the results obtained in the reactor cell.

3.2.2.3. Continuous electroreduction of CO_2

The analysis of the liquid fraction shows that the electrocatalytic reduction of CO_2 using the GDEs modified by HKUST-1(Cu,M_D) type materials produces methanol (CH_3OH) and ethanol (C_2H_5OH) as major products. It deserves to note that neat GDEs (*i.e.* carbon paper without MOFs) did not generate any measurable liquid product.

As representative cases of continuous CO_2 reduction capability, Figure 3.15 depicts the time-dependence of the total Faraday efficiency (FE_T) provided by H_Zn8, H_Ru10 and H_Pd11 materials in comparison with H_Cu at fixed current density (j = 20 mA·cm^{-2}), gas flow ($Q_{g/A}$ = 10 mL·min^{-1}·cm^{-2}) and electrolyte flow ($Q_{e/A}$ = 2 mL·min^{-1}·cm^{-2}). The FE values are calculated considering 6-electron-pathway for CO_2 reduction to CH_3OH and 12-electron-pathway to C_2H_5OH. It is noteworthy the outstanding efficiency of Ru(III) doped sample (FE = 47.2 %) which is comparable to those relatively stable values provided by Cu_2O nanoparticles-based electrodes (FE = 54.8%).[38]

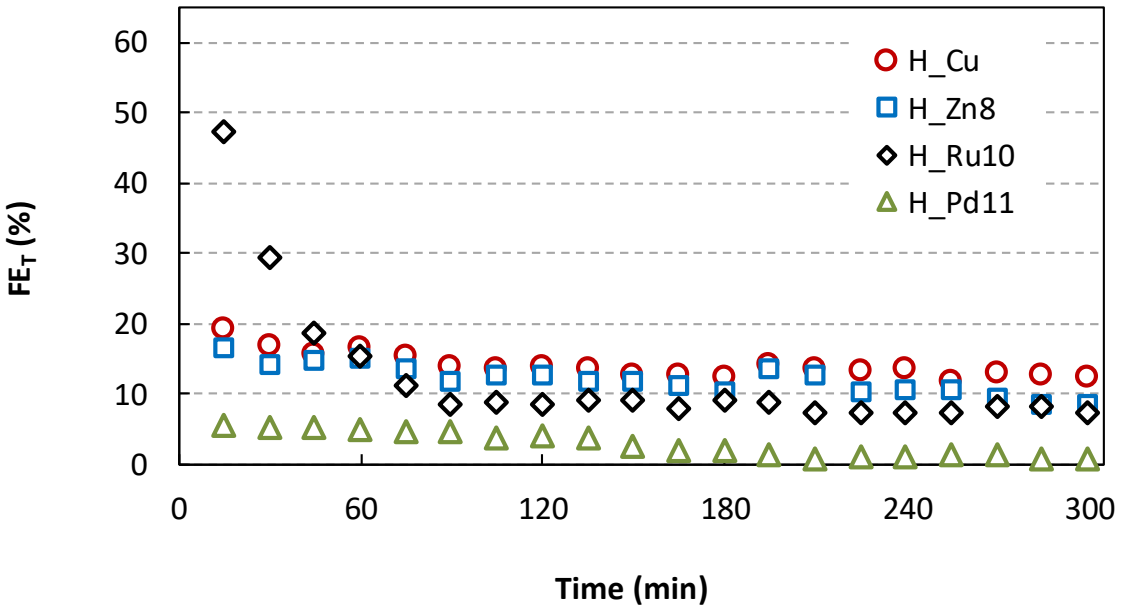

Figure 3.15. Time-dependence of FE for H_Zn8, H_Ru10 and H_Pd11 materials, in comparison to H_Cu.

However, the activity of Ru(III)-doped sample falls abruptly after 60 min of operation to reach a stable plateau close to the 10%. FE values of H_Cu and H_Zn8 show a similar trend but they start from more moderate values (17–19%) and fall monotonically until stabilizing at values within 12–13%. On the contrary, H_Pd11 sample shows markedly lower FE values (close to the 5%) within the first 2 hours of operation, however it falls to a negligible value of 1-2% at longer operation times. Previous works have reported the formation of the less reduced CO as major product when Pd-based materials are employed as cathode materials, so that the worsening in the methanol and ethanol yield observed for HKUST-1(Cu,Pd) materials is probably due to a change in the product selectivity caused by the dopant.[14]

To get deeper insight, the quantitative reduction performances (r and FE) at 90 minutes of operation time for all samples are summarized in Figure 3.16 and Table 3.5. Regarding production rates and Faraday efficiencies, the maximum values are achieved for the smallest and intermediate Ru and Zn loadings (r = 1.78 – 2.22 10^{-5} mol·m^{-2}·s^{-1} and FE of ~22%), in comparison to those values provided by pristine HKUST-1 (2.66 10^{-5} mol·m^{-2}·s^{-1} and 12.9%). In all the cases, further increase of the dopant content produces a lowering of the catalyst performance.

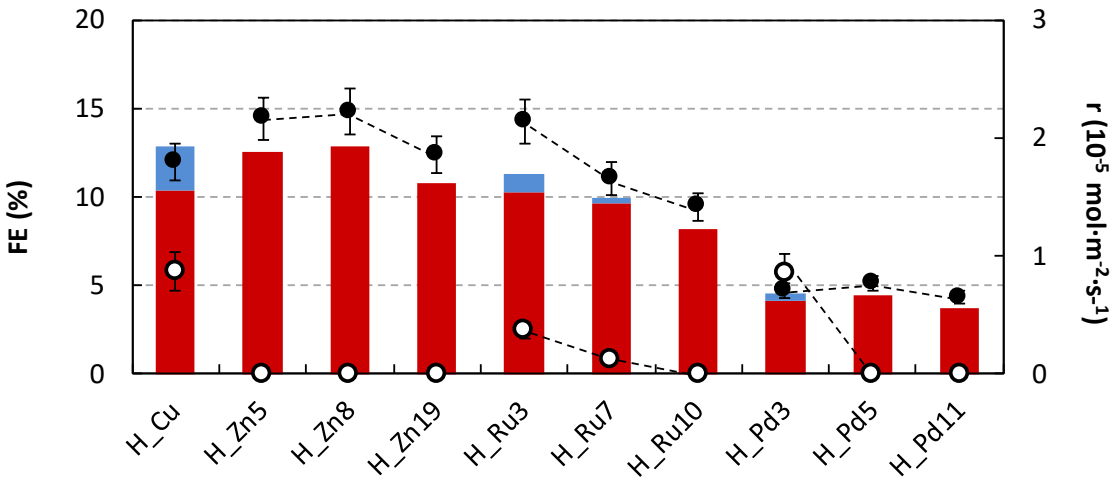

Figure 3.16. FEs for C_2H_5OH (in red) and CH_3OH (in blue) formation and r for C_2H_5OH (•) and CH_3OH (○) in the electrocatalytic reduction of CO_2 at H_Zn, H_Ru and H_Pd in comparison to H_Cu.

Table 3.5. Reaction rates (r) and Faraday efficiencies (FE) in the electrocatalytic conversion of CO_2 at MOF-GDEs after 90 min of operation time. Operating conditions: j = 20·mA·cm^{-2}, $Q_{g/A}$ = 10 mL·min^{-1}·cm^{-2} and $Q_{e/A}$ = 2 mL·min^{-1}·cm^{-2}.

MOF-GDEs	E (V)	r (10^{-5} mol·m^{-2}·s^{-1})			FE (%)		
		CH_3OH	C_2H_5OH	TOTAL	CH_3OH	C_2H_5OH	TOTAL
H_Cu	1.77	0.87	1.79	2.66	2.51	10.37	12.87
H_Zn5	1.87	-	2.16	2.16	-	12.51	12.51
H_Zn8	1.79	-	2.22	2.22	-	12.85	12.85
H_Zn19	1.73	-	1.86	1.86	-	10.75	10.75
H_Ru3	1.84	0.37	2.14	2.51	1.07	10.22	11.29
H_Ru7	1.72	0.13	1.65	1.78	0.36	9.58	9.94
H_Ru10	1.73	-	1.41	1.41	-	8.18	8.18
H_Pd3	1.88	0.86	0.71	1.57	0.44	4.10	4.54
H_Pd5	1.89	-	0.77	0.77	-	4.46	4.46
H_Pd11	1.93	-	0.65	0.65	-	3.73	3.73

Despite ethanol is the major product in the liquid fraction, it seems that the dopant content exerts certain degree of control on the product selectivity, in such a way that the undoped sample and samples containing the smallest dopant loading exhibit the lower selectivity values towards the formation of C_2H_5OH respect to CH_3OH (C_2H_5OH molar selectivity values estimated from production rates: 67, 55, 85 and 45% for H_Cu, H_Zn5, H_Ru3 and H_Pd3). In all cases, further increase of the dopant loading promotes an increase of ethanol selectivity reaching values ranging from 93 to 100%. This fact might be attributable to the increase of the permanence time caused by the establishment of stronger interactions with the dopant metal, and as consequence, it would favor C–C coupling reaction to ethanol. It has been previously hypothesized that C2–C3 products occur through an enol-like surface intermediate,

which desorbs to convert to its alcohol, diol and/or ketone form.[17] The C–C bond formation is one of the most critical factors to be taken into account when designing efficient electrocatalyst, and further experimental work is needed to fully elucidate CO_2 reduction steps to form alcohols using Cu-based GDEs.

Furthermore, to analyse the in-use stability of the MOF-GDEs and its relation with activity decay observed until the mid-term plateau is achieved, PXRD were measured on H_Ru10 fresh electrode and on those subjected to 45 and 300 minutes of continuous reaction (Figure 3.17a). Whereas fresh electrodes exhibit all the distinctive peaks of the HKUST-1 crystalline phase, their intensity falls progressively as the reaction time increases. In fact, in the most aged electrode (300 minutes of reaction) only the most intense reflection of the MOF, *i.e.* (2 2 2) is marginally appreciated. This fact might be related to the material leaching caused by the gas flow at the initial reaction stage. In fact, the comparative SEM images taken on fresh and used electrodes (Figure 3.17b) show flat areas from which MOF particles have been detached. Despite this electrode fatigue is compatible with the aforementioned activity decay, a slow but progressive crystallinity loss of the MOF occurring during operation might also influence. Note that the full width at half maximum (FWHM) of (2 2 2) reflection varies from 0.12° in fresh electrode to 0.14° in that one used during 45 minutes. In any case, it must be pointed out that after 300 min of running, a weak reflection sited at 14.1° emerged, for which a perusal in the powder diffraction files of the Inorganic Crystal Structure Database[73] matches the most intense reflection of copper(II) formate (ICSD: 109965).[74] It deserves to note that the low sample loading, its dispersion in the GDE and the Nafion matrix, inhibit the observation of further peaks and as a consequence, it precludes the univocal identification of the formed crystalline compound. Nonetheless, the formation of copper(II) formate during the reaction would imply a frozen state of a reaction intermediate, which in turn it would be the key that favours the formation of more reduced products, such as alcohols. In any case, further research is required to elucidate this plausible mechanism.

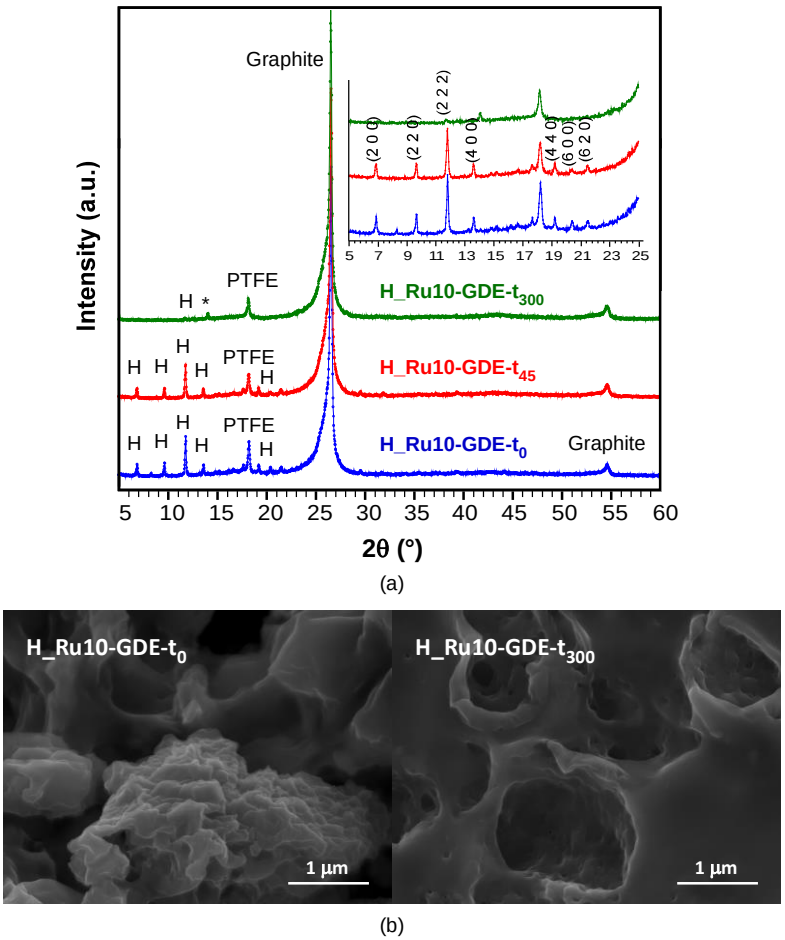

Figure 3.17. Comparative (a) PXRD patterns and (b) SEM images at 10kX magnifications taken on fresh and used H_Ru10-GDEs (t_0, t_{45}, t_{300} stand for GDE subjected to 0, 45 and 300 min, respectively. PTFE stands for polytetrafluoroethylene from Nafion present in the catalytic ink).

3.3. Cu/Bi blends of HKUST-1(Cu) and CAU-17(Bi) MOFs

As all the synthetic efforts to dope HKUST-1(Cu) with Bi(III) were unsuccessful resulting in a segregation of crystalline phases comprsided by HKUST-1(Cu) and unknown phase of Bi(III), in this section an alternative approach to bimetallic Cu/Bi systems is presented. Precisely, physical blends of two homometallic MOFs, HKUST-1(Cu) and CAU-17(Bi), were prepared and characterized to analyse their performance as bimetallic catalysts in the electrochemical conversion of CO_2 and their stability in long-term runs.

3.3.1. EXPERIMENTAL SECTION

3.3.1.1. Preparation of HKUST-1/CAU-17 blends and MOF-based GDEs

HKUST-1 samples were prepared following the same procedure explained in Section 3.2.1.1 for homometallic HKUST-1(Cu). In the case of Bi-based MOF, named CAU-17, it was prepared following the synthetic procedure described elsewhere.[60] This is,

$Bi(NO_3)_3{\cdot}5H_2O$ (1.03 mmol, 0.4996 g) and H_3BTC (1.17 mmol, 0.2588 g) were added to a 70 mL-teflon reactor along with 20 mL of methanol, and heated to 120 °C in a microwave oven during 20 min. The white precipitate was filtered off, washed with methanol and dried at room temperature. Finally, Cu/Bi-based blends were prepared by physical mixing and grinding of both MOFs in different ratios. Table 3.6 shows the nomenclature for HKUST-1/CAU-17 blends prepared, together with the corresponding MOF mass and Cu:Bi atomic ratios determined by X-ray fluorescence (XRF).

Table 3.6. Bimetallic MOF-based systems prepared within mass ratio (%) employed of each MOF and atomic ratio (%) obtained measured by XRF.

Code	Mass ratio (%)		Atomic ratio (%)	
	HKUST-1	CAU-17	Cu	Bi
Cu100	100	-	100	-
CuBi6	89	11	94	6
CuBi9	84	16	91	9
CuBi12	79	21	88	12
CuBi15	74	26	85	15
CuBi18	70	30	82	18
CuBi21	66	34	79	21
CuBi24	62	38	76	24
CuBi60	25	75	40	60
CuBi84	9	91	16	84
Bi100	-	100	-	100

Afterwards, gas diffusion electrodes of physical blends, MOF-GDEs, were prepared as depicted in Section 3.2.1.2.

3.3.1.2. Electrochemical experiments

The cyclic voltammetries and the CO_2 reduction experiments were performed following the same procedure explained in Sections 3.2.1.3 and 3.2.1.4, respectively. Specifically, in this case, all potentials measured with the Ag/AgCl (sat. KCl) reference electrode were converted to reversible hydrogen electrode (RHE) scale, and the electrocatalytic reduction experiments were performed initially at galvanostatic conditions as before ($j = 20\ mA{\cdot}cm^{-2}$) and then, at a current density ranging from $j = 10\ mA{\cdot}cm^{-2}$ to $j = 30\ mA{\cdot}cm^{-2}$.

The performance of the mixed-metal systems for the CO_2-to-alcohols reaction is evaluated in terms of reaction rate (r), Faraday efficiency (FE) and selectivity, S, defined as the ratio between the reaction rate for a specific product and the cumulative reaction rates for all liquid phase products.

3.3.2. RESULTS AND DISCUSSION

3.3.2.1. Physicochemical characterization of MOFs, blends and MOF-GDEs

Prior to preparing the GDEs, as-prepared MOF samples were analysed by PXRD and N_2 adsorption isotherms to assess their crystallinity and microporous features. PXRD patterns fit those expected for HKUST-1 and CAU-17 (Figure 3.18), while fitting of adsorption data (Figure 3.19) to BET equation yielded surface area values of 1559 $m^2 \cdot g^{-1}$ and 1197 $m^2 \cdot g^{-1}$, respectively, as expected from their crystalline and microporous nature. Bimetallic blends prepared from the combination of both MOF systems were also characterised by means of PXRD (Figure 3.20). It can be observed the combination of reflections from both crystalline phases in the diffraction patters, and how some intensities decay and other increase depending on the relative content of each MOF.

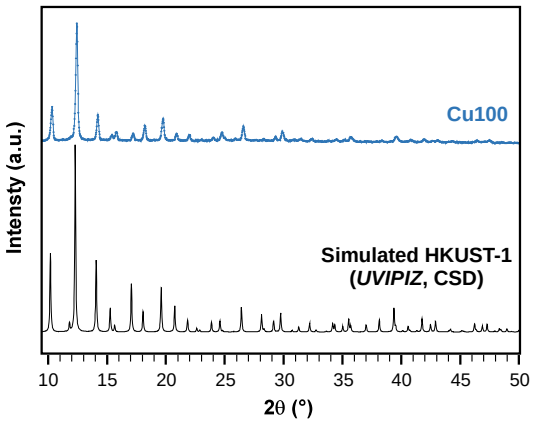

UVIPIZ	
Crystal system	Cubic
Space group	$Fm\bar{3}m$
a (Å)	26.3605
V (Å^3)	18 317.3

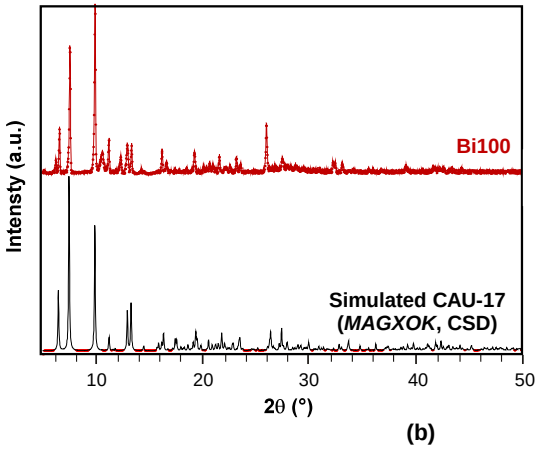

MAGXOK	
Crystal system	Trigonal
Space group	$P\bar{3}$
a (Å)	47.210
b (Å)	47.210
c (Å)	9.968
V (Å^3)	19 240.5

Figure 3.18. Comparison of the experimental and simulated (a) HKUST-1 and (b) CAU-17 diffraction patterns, together with the crystallographic data obtained from the CSD for the structure with UVIPIZ and MAGXOK code, respectively.[64]

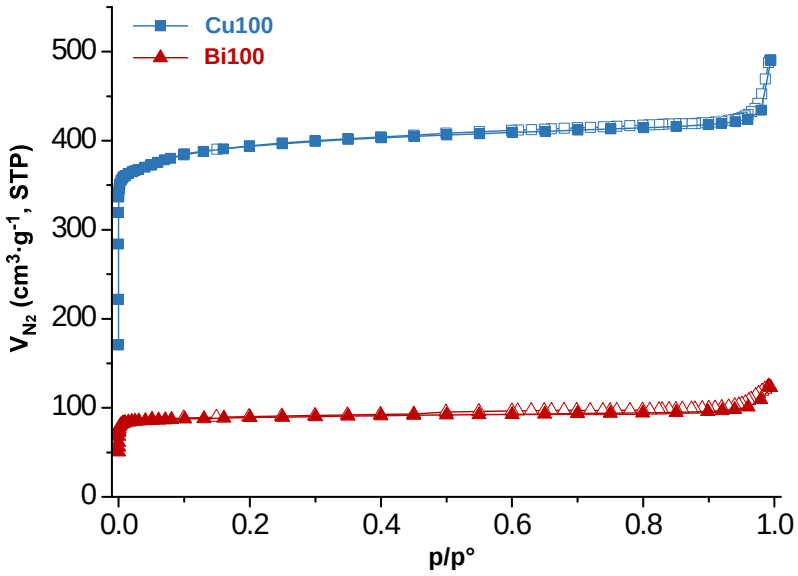

Figure 3.19. N_2 adsorption isotherms at 77 K for Cu100 and Bi100 samples.

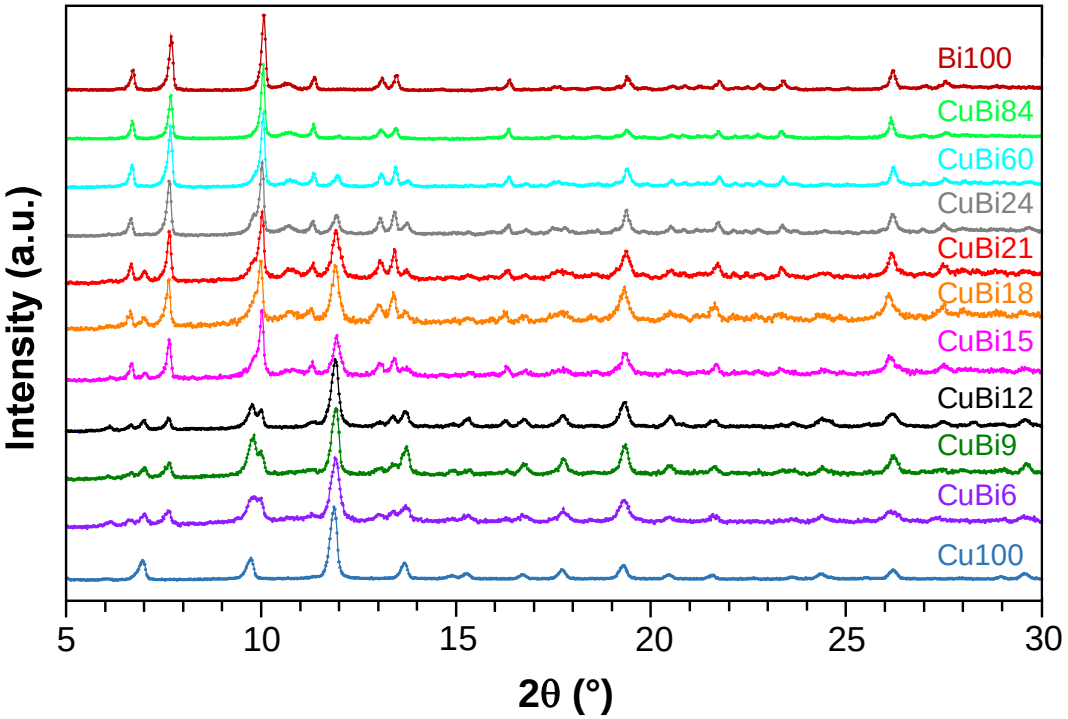

Figure 3.20. Comparison of the PXRD patterns for the different HKUST-1/CAU-17 blends.

Homometallic MOFs and blends were also analysed by scanning electron microscopy (SEM) to determine their microstructural features. In this regard, as representative case, Figure 3.21 shows comparative micrographs for the CuBi12 and CUBi24 using secondary electron (SEI) and backscattered electron (BSE) scanning modes. As observed, MOF blends consist of well dispersed crystallites phases in which CAU-17 micro-metric crystals with hexagonal prism geometry appear embedded in a matrix of sub-micrometric crystals of HKUST-1. Note that in the backscattered electron image the brighter crystals corresponds to more

electrodense Bi containing CAU-17, while the remaining darker crystallites are attributable to HKUST-1.

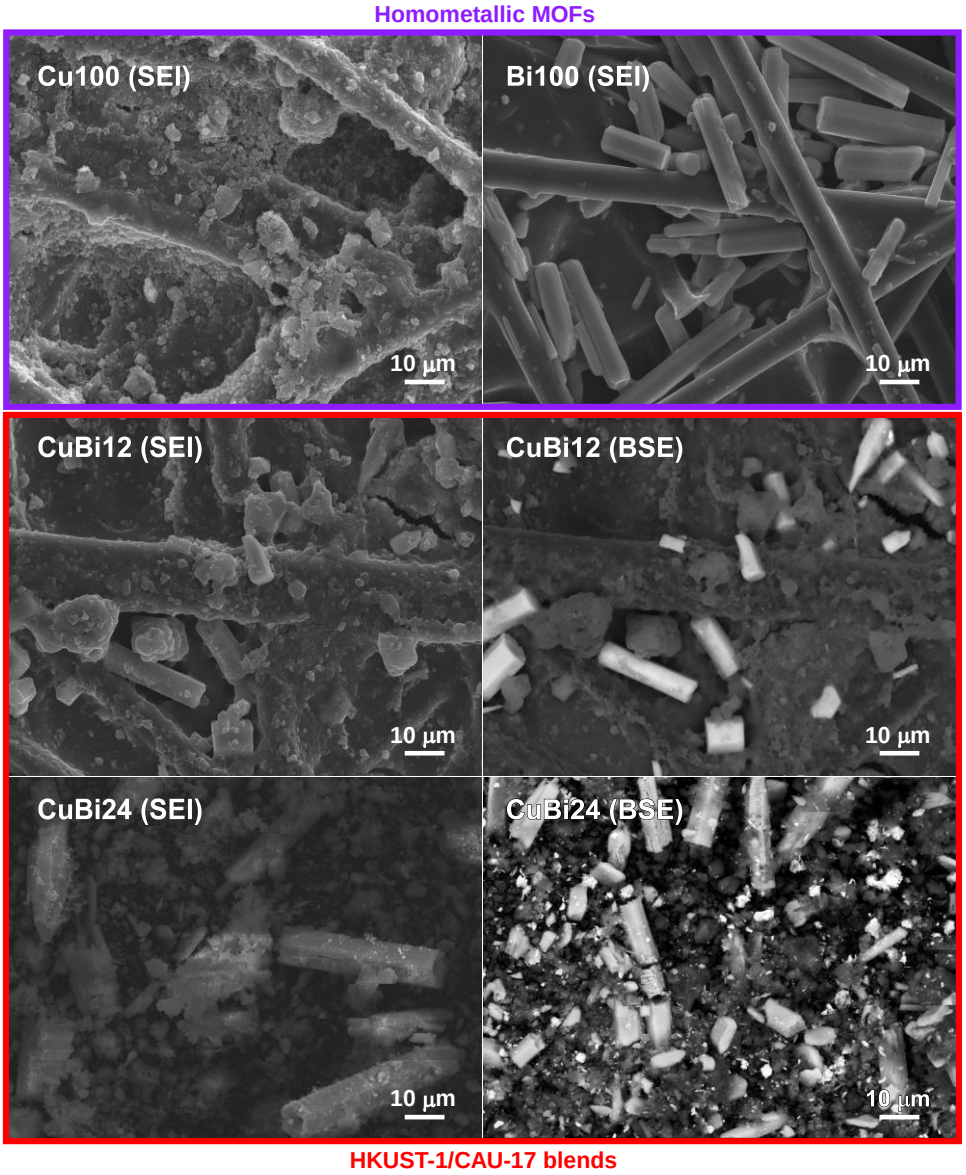

Figure 3.21. SEM micrographs taken at 1000 magnifications for Cu100, Bi100 and selected HKUST-1/CAU-17 blends (CuBi12 and CuBi24). SEI correspond to secondary electron image mode, and BSE to back-scattered electrons mode.

Additionally, Figure 3.22. shows comparative micrographs in SEI and BSE mode taken at 250 and 1000 magnifications for the CuBi12 GDE to corroborate the microstructure and the distribution of both MOFs after MOF-GDEs preparation. Effectively, both phases can be distinguished with their specific crystal morphology in between the bigger fibres of porous carbon support.

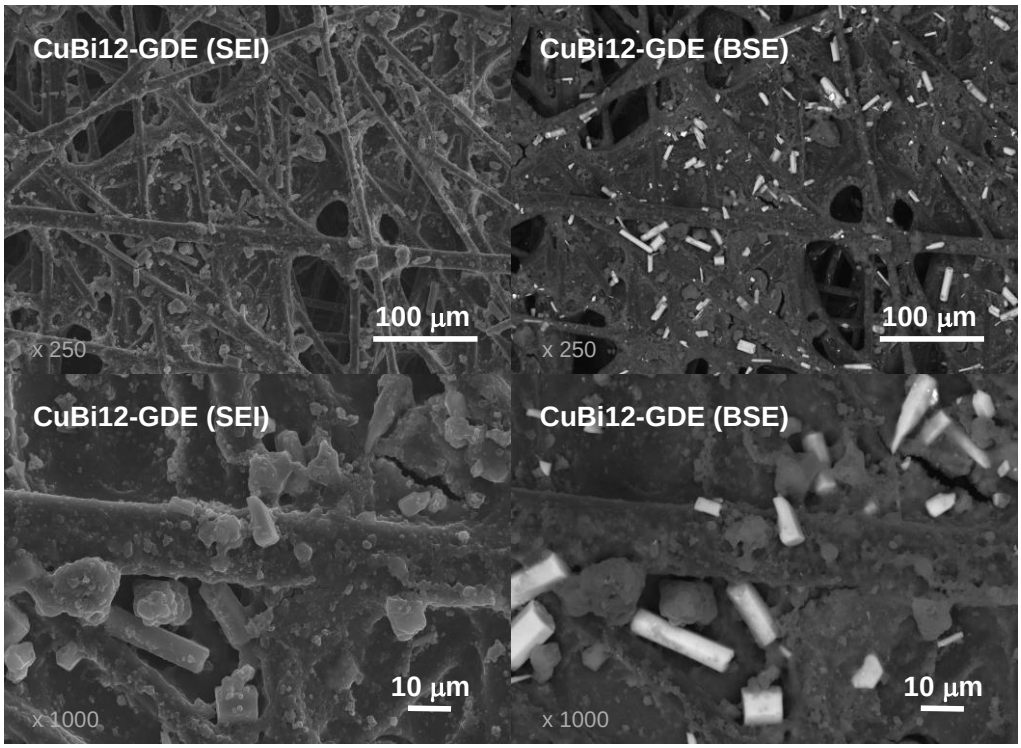

Figure 3.22. SEM micrographs at SEI and BSE for CuBi12@GDE taken at 250 and 1000 magnifications. SEI correspond to secondary electron image mode and BSE to back-scattered electrons mode.

3.3.2.2. Electrochemical characterization of MOF-GDEs

Figure 3.23a gathers the voltage-current responses for the Cu100, CuBi12 and Bi100-based GDEs after 5 scans in a CO_2-saturated (0.5 M $KHCO_3$) aqueous solution, while Figure 3.23b reports the current-voltage curve for CuBi12 in the presence/absence of CO_2.

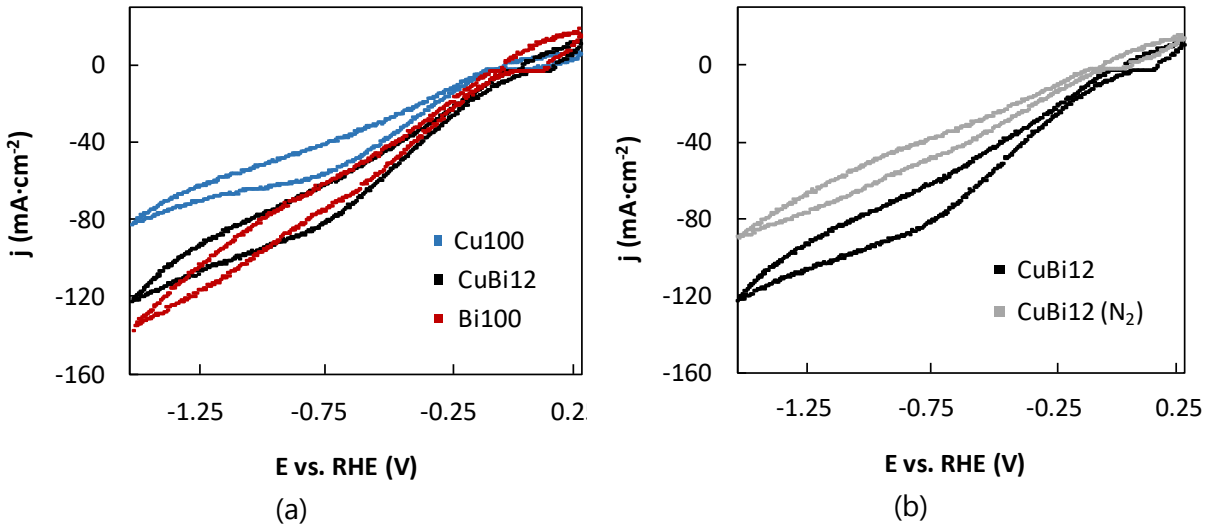

Figure 3.23. Cyclic voltammetry responses for (a) Cu100, CuBi12 and Bi100 in a CO_2 saturated 0.5 M $KHCO_3$ aqueous solutions and (b) CuBi12 in a media saturated with either CO_2 or N_2.

An oxidation-reduction contribution is observed between –0.2 V to 0.2 V vs. RHE, which seems to depend on Bi content. This could be initially related to the oxidation-reduction of the material with the potential scans, as found before for Bi-based electrocatalysts.[58,59] However, since the oxidative peak appears also in the reverse scan of Cu100 sample and it remains after the fifth scan, it can be also related to the formation of oxidized subproducts in the CO_2 reduction reaction. In any case, the main characteristic of the voltammograms is a reduction process starting at around –0.25 V vs. RHE, which can be initially associated with the reduction of CO_2, the formation of H_2 from HER and the partial formation/decomposition of oxides at the electrode surface. A similar curve with a slight shoulder at around –0.9 V vs. Ag/AgCl (–0.27 V vs. RHE) in a CO_2-saturated $KHCO_3$ aqueous solution was reported by Hori and co-workers. They suggested that the reduction peak can be attributed to the adsorbed intermediates during the CO_2 reduction reaction.[75] As can be also observed, the reduction wave is more pronounced for Bi-based samples, which might be initially assigned to an enhanced reduction of CO_2 to HCOOH commonly found at Bi-based surfaces.[51–60] Besides, mixing the Cu-based material with only 12% (atomic) of Bi (CuBi12) results in a notable activity close to Bi100 response, which may be indicative of CO_2 conversion by different reaction mechanisms than those at Cu100-based surfaces, denoting the synergic co-catalytic effect of copper and bismuth. As a rule, the higher current densities achieved at same voltage level required in the Cu-Bi co-catalyst systems should be consistent with the faster kinetics to produce reduced species from CO_2, although the HER competitive reaction should be also taken into account. Thus, the curve in the N_2 bubbled solution can be explained by the formation of H_2 from HER, while both reactions (*i.e.* CO_2 reduction and HER) occurs in parallel in the CO_2 saturated system. Figure 3.23b shows a significant increase in the cathodic current wave in the presence of CO_2, in comparison to that response in a N_2-saturated solution. This demonstrates that the material acts as a catalyst for CO_2 reduction and the response observed has more to do with CO_2 transformation rather than the oxidation-reduction of the catalytic material.

For a further comparison of the electrochemical activity for alcohols production, the semi-log Tafel relationship between partial current density for CH_3OH and C_2H_5OH and overpotential, η, in the kinetically controlled region is shown in Figure 3.24 for Cu100 and CuBi12 systems. No alcohols were detected with Bi100 material.

The Tafel slopes at the CuBi12-based GDE are 98.5 $mV \cdot dec^{-1}$ and 82.3 $mV \cdot dec^{-1}$ for CH_3OH and C_2H_5OH, respectively, which is about 30% lower than those results for Cu100. This indicates a faster kinetic reaction, which may be ascribed to the synergic effect of Cu and Bi in the electrochemical reduction of CO_2 to alcohols. The higher activity found at CuBi-based system agrees well with the enhanced activity found for

CO_2 electroreduction at nano-sized Bi-based catalyst electrodeposited on a Cu foil.[56] Besides, as previously stated, the rate-limiting step in the electroreduction of CO_2 at Cu-based materials involves a single electron transfer for the activation of CO_2 (to form $CO_2^{\cdot-}$) which is characterized with a Tafel slope of 120 mV·dec^{-1}.[76] CH_3OH and C_2H_5OH exhibited a Tafel slope close to this value with Cu100 (138.1 mV·dec^{-1} and 119.2 mV·dec^{-1}), implying that both products probably share the same rate-determining step which involves an initial one-electron transfer. The fact that the Tafel slopes are lower than 120 mV·dec^{-1} at CuBi12 suggests the lower kinetic barrier for CO_2 conversion to alcohols in contrast to the more sluggish reaction kinetics at Cu100, implying that the rate-determining step is probably a chemical step after a pre-equilibrium one-electron transfer.

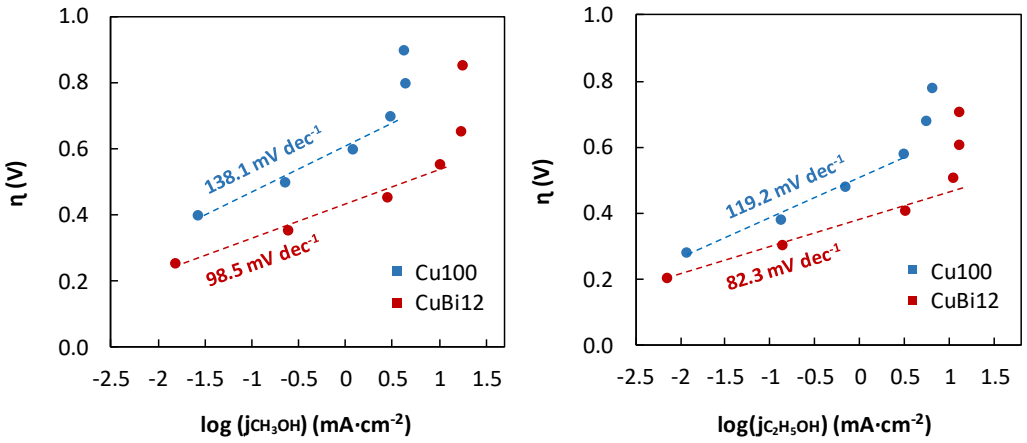

Figure 3.24. Tafel plots with linear fit for (a) CH_3OH and (b) C_2H_5OH at Cu100 and CuBi-12 based GDEs.

3.3.2.3. Continuous CO_2 electroreduction performance

Table 3.7 presents the reaction rates for liquid products (*i.e.* HCOOH, CH_3OH and C_2H_5OH), together with the cumulative CO_2 conversion rate to liquid products (r_{liq}) and selectivities, while Figure 3.25 depicts the evolution of the Faraday efficiency (FE) values (%) for all detected liquid and gas-phase reduction products in the filter press electrochemical cell equipped with homometallic (Cu100 and Bi100) and bimetallic (CuBi6-84) MOF modified GDEs. FEs are calculated assuming that 2 e^- are required per molecule of formic acid (HCOOH), hydrogen (H_2) and carbon monoxide (CO), 6 e^- per molecule of methanol (CH_3OH) and 12 e^- per molecule of ethanol (C_2H_5OH) and ethylene (C_2H_4). Trace amounts of methane (CH_4) were also detected. The cumulative FE was over 90% for all the materials applied. Besides, control experiments for the reduction of CO_2 conducted at the supporting neat carbon papers did not produce any measurable liquid product.

Table 3.7. CO_2 electroreduction performance to liquid products at CuBi6-84, Cu100 and Bi100-based electrodes. $Q_{g/A}$ = 10 ml·min^{-1}·cm^{-2}, $Q_{e/A}$ = 2 ml·min^{-1}·cm^{-2}, j = 20 mA·cm^{-2}.

Material	E (V vs. RHE)	r (μmol·m^{-2}·s^{-1})					S_{CH_3OH}	$S_{C_2H_5OH}$	$S_{alcohols}$
		r_{HCOOH}	r_{CH_3OH}	$r_{C_2H_5OH}$	$r_{alcohols}$	r_{liq}			
Cu100	–0.59	-	8.7	17.9	26.6	26.6	-	-	-
CuBi6	–0.42	128.3	28.4	26.6	55	183.3	0.15	0.14	0.29
CuBi9	–0.36	136.5	32.7	30.6	63.3	199.8	0.16	0.15	0.31
CuBi12	–0.21	162	29.7	48.8	78.5	240.5	0.12	0.2	0.32
CuBi15	–0.2	216.3	20.2	48	68.2	284.5	0.07	0.17	0.24
CuBi18	–0.2	222.6	11.4	50.7	62.1	284.7	0.04	0.18	0.22
CuBi21	–0.18	247.2	12.5	33.5	46	293.2	0.04	0.11	0.15
CuBi24	–0.17	356.7	8.84	30.5	39.3	396	0.02	0.18	0.2
CuBi60	–0.23	436	33.9	2.83	36.7	472.7	0.07	<0.01	0.07
CuBi84	–0.34	495.6	22.3	1.59	23.9	519.5	0.04	<0.01	0.04
Bi100	–0.32	435	-	-	-	435	-	-	-

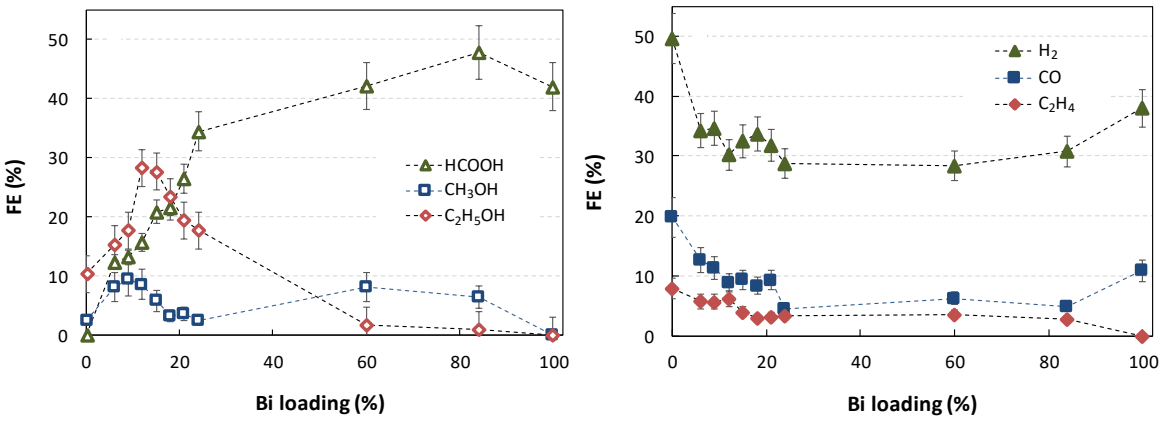

Figure 3.25. FE for the (a) liquid and (b) gas products obtained from CO_2 electroreduction at increasing Bi loadings. $Q_{g/A}$ = 10 mL·min^{-1}·cm^{-2}, $Q_{e/A}$ = 2 mL·min^{-1}·cm^{-2}, j = 20 mA·cm^{-2}.

As firstly observed, cumulative production rates for liquid products (r_{liq}) are enhanced as increasing Bi content in the bimetallic samples, going from r_{liq} =183.3 μmol·m^{-2}·s^{-1} to r_{liq} =519.5 μmol·m^{-2}·s^{-1} at CuBi6 and CuBi84-GDEs, respectively. The enhanced production rate is evident from comparison of the HCOOH obtained at CuBi84-based system (r_{HCOOH} = 495.6 μmol·m^{-2}·s^{-1}), which is approximately four times higher than r_{HCOOH} = 128.3 μmol·m^{-2}·s^{-1} for CuBi6-based GDEs. This is in agreement with the literature that demonstrated that Bi-based materials are able to promote the production of $HCOO^-$ (via $OCHO^*$), which is spontaneously released from the catalytic surface as HCOOH.[53–57] The production of

alcohols (*i.e.* r_{CH_3OH} and $r_{C_2H_5OH}$) is enhanced initially up to a Cu:Bi ratio of 88:12, after this point it decreases as the content of Bi increases since the reaction turns more selective to HCOOH production. It is also important to note that the r_{liq} values achieved at CuBi84 are higher than those obtained for Bi100, which may confirm the synergic co-catalytic effect of Cu and Bi. The same conclusion can be drawn when comparing GDEs modified with homometallic Cu sample and those containing lowest amounts of Bi, as inclusion of the latter boosts the alcohol formation. For instance, the reaction rates for alcohol production in CuBi12 system are r_{CH_3OH} = 29.7 $\mu mol \cdot m^{-2} \cdot s^{-1}$ and $r_{C_2H_5OH}$ = 48.8 $\mu mol \cdot m^{-2} \cdot s^{-1}$, while the Cu100 sample yield more inconspicuous values (r_{CH_3OH} = 8.7 $\mu mol \cdot m^{-2} \cdot s^{-1}$ and $r_{C_2H_5OH}$ = 17.9 $\mu mol \cdot m^{-2} \cdot s^{-1}$). All in all, the reaction selectivity to alcohols seems to find an optimum at 12% Bi content (S_{CH_3OH} = 0.12 and $S_{C_2H_5OH}$ = 0.2, $S_{alcohols}$ = 0.32).

The production of alcohols at HKUST-1-based electrodes can be also found in literature.[39,77,78] Zhao and coworkers synthesized different oxide derived Cu/C materials by a facile carbonization of HKUST-1. The electrocatalysts exhibited highly selective CO_2 reduction to alcohols (*i.e.* CH_3OH and C_2H_5OH) with a $FE_{alcohols}$ ranging from 45.2% to 71.2% at −0.1 to −0.7 V vs. RHE.[39] The production of alcohols, however, may be somehow unexpected attending at the formation of mainly HCOOH (FE = 91.3%) at nano-sized Bi-based catalyst electrodeposited on a Cu foil (non-MOF) at more negative potentials (–1.13 V vs. RHE),[56] which may also show the advantages of using MOF-based structures for the further electrochemical transformation of CO_2 to alcohols.

Moreover, the cathodic voltages are more positive in case of adding Bi to the sample than those results in its absence. This overpotential lowering follows the same trend observed from cyclic voltammetric analyses. For example, at an applied constant current of j = 20 $mA \cdot cm^{-2}$ (E = –0.21 V vs. RHE), an averaged $r_{alcohols}$ = 78.5 $\mu mol \cdot m^{-2} \cdot s^{-1}$ was observed with CuBi12. Significantly higher voltage (E = –0.59 V vs. RHE) was required under similar conditions and only a $r_{alcohols}$ =26.6 $\mu mol \cdot m^{-2} \cdot s^{-1}$ was achieved at Cu-based systems. Thus, it can be discerned that Cu/Bi-based MOFs ensemble is a much more active electrocatalyst than homometallic Cu-systems for CO_2 transformation to alcohols.

In line with the results presented in Table 3.7, the data from Figure 3.25 evidence that Bi has a marked effect on reaction selectivity. In particular, the results showed that a Bi atomic content between 6 to 12% (CuBi6-12) seems to be beneficial for CO_2 reduction to alcohols, reaching a maximum FE for alcohols at 12% of Bi ($FE_{alcohols}$ = 36.9%, $S_{alcohols}$ = 0.32). Exceeding this Bi content range, the system led primarily to

HCOOH in the liquid phase, which indicates that the amount of exposed Bi active sites in the GDE has a critical influence on alcohol production.

Besides, the analysis of gas-phase reduction products at the CuBi GDEs showed the formation of mainly H_2 (FE~ 30%) from the competitive HER, together with CO (FE from 10% to 3%) and small concentrations of C_2H_4, that seem to be negatively affected by the increase of Bi loading (from FE = 9.85% to FE = 2.76% for Cu100 and CuBi84, respectively). The literature demonstrated that the formation of C_2H_4 from CO_2 electroreduction at Cu-based MOFs is not unexpected.[79,80] In particular, Nam and coworkers were able to reach FEs as high as 45% for C_2H_4 at HKUST-1 (calcined at 250 ºC) spray-coated gas diffusion layers. The authors also reported a FE to C_2H_4 of around 10% for the as-prepared HKUST-1-based electrodes at –0.69 V vs. RHE.[79] Moreover, Figure 3.25 shows that the formation of H_2 and CO can be reduced at CuBi materials in comparison to those results at the homometallic MOFs. This has been explained before by a modulation of the electronic environment of Cu-Bi boundaries, resulting in an enhanced production of HCOOH via $OCHO^*$ intermediate that binds to the catalyst surface through an oxygen atom, hindering the formation of CO and partially suppressing the formation of H_2.[52]

It is generally recognized that the formation of CH_3OH from the electrochemical conversion of CO_2 proceeds through two different reaction pathways, implying CO and $HCOO^-$ intermediates.[2] In the case of C_2H_5OH, the first step involves a proton and electron transfer to give a $HCOO^-$ surface moiety that can dimerise/hydrogenate to C_2H_5OH and C_2H_4.[20,23,81,82] This C-C intermolecular coupling seems to be kinetically more favourable when the immediate reactants is CH_2O^*, rather than CO.[83] As the efficiency for HCOOH formation increases and CO decreases with Bi content, $HCOO^-$ may be acting as the main precursor for the formation of both alcohols at low Bi loadings. We therefore hypothesise that the enhanced production of alcohols at the CuBi MOF-based systems can be mainly ascribed to the formation of $HCOO^-$ at Bi sites (CAU-17), which is then transferred to neighbouring Cu actives sites (HKUST-1) where further conversion toward alcohols takes place. The diffusion pathways provided by the MOF-based structure would lengthen the permanence time, prompting further reduction to CH_3OH and C–C coupling reaction to C_2H_5OH. The results might be also explained by a simultaneous interaction between Cu-Bi boundaries and $HCOO^-$ intermediate as found in literature for Cu-Bi materials,[52] but considering the large micron-sized crystallites observed, it seems much less likely to be the main responsible for the significant increase in alcohols production. An in depth study on reaction mechanisms is certainly required in order to roundly assert the correlation among the reaction selectivity and the MOF-based electrodes.

To get deeper insights, Figure 3.26 gathers the influence of Bi loading and current density (j = 10 mA·cm^{-2} to j = 30 mA·cm^{-2}) on FE values for alcohols.

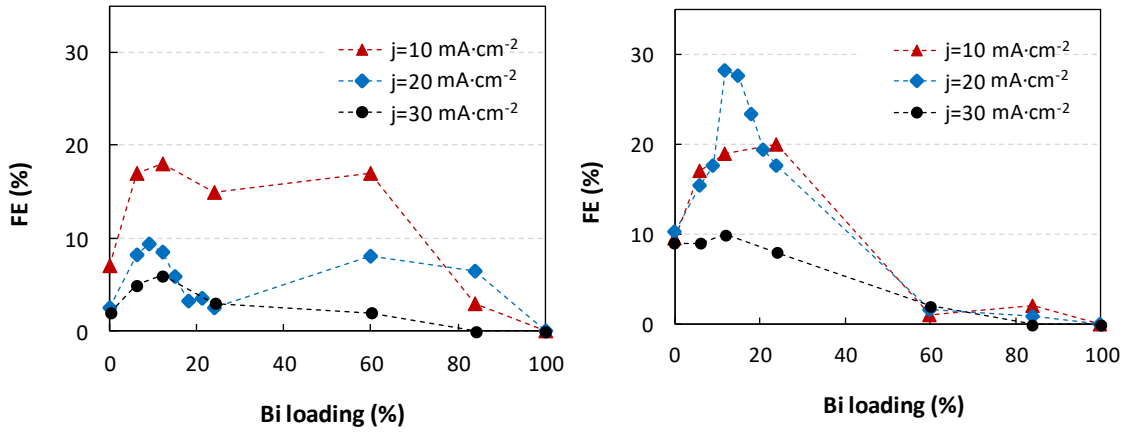

Figure 3.26. FE for (a) CH_3OH and (b) C_2H_5OH at increasing Bi loading and current density applied. $Q_{g/A}$ = 10 mL·min^{-1}·cm^{-2}, $Q_{e/A}$ = 2 mL·min^{-1}.

The figures show that product distribution and process efficiency are not uniquely correlated with Cu/Bi ratio but also with the current density applied to the system. At lower current densities, the reaction seems to be more selective for CO_2 reduction to CH_3OH over the CuBi electrocatalysts with a FE = 18.2% at j = 10 mA·cm^{-2}. As the current goes to j = 20 mA·cm^{-2}, C_2H_5OH seems to become the dominant CO_2 reduction alcohol (FE = 28.3%). Further increases in the applied current lead, in both cases, to a significant reduction in FE, which can be explained by an increased production of HCOOH and H_2, as can be seen at Bi and CuBi-based electrocatalyst for CO_2 conversion at more negative potentials.[52,53,59] Figure 3.26a also demonstrates that the CuBi GDEs prepared present an optimum selectivity for CH_3OH formation at j = 10 mA·cm^{-2}. The same can be said for C_2H_5OH formation, although its optimum is clearly at j = 20 mA·cm^{-2}, which may indicate that its formation follows a distinct reaction pathway as current increases.

It is also important to mention that the summation of reaction rates, $r_{alcohols}$, and efficiencies $FE_{alcohols}$ ($r_{alcohols}$ = 78.5 µmol·m^{-2}·s^{-1}, $FE_{alcohols}$ = 36.9%) at CuBi12-based surfaces at 90 min of operation and j = 20 mA·cm^{-2} are remarkably higher than those values previously obtained for the production of alcohols in the same experimental setup using a Cu plate (r = 23 µmol·m^{-2}·s^{-1}, FE = 3.6%)[18] and Cu_2O/ZnO (r = 50.8 µmol·m^{-2}·s^{-1}, FE = 31.4%) particles deposited onto carbon papers in a 0.5 M $KHCO_3$ aqueous solution and E= –1.3 V vs. Ag/AgCl (–0.67 V vs. RHE).[38] The results also enhanced the performance of the Cu-based MOFs materials tested before in our group (*i.e.* HKUST-1, CuAdeAce, CuDTA and CuZnDTA) for the electrochemical conversion of CO_2 to alcohols.[25] These values, however, are still far from the nearly 100% selectivity and FE of 77% to C_2H_5OH recently obtained at nitrogen (pyridinic

and pyrrolic type)-based mesoporous carbons,[84] which can be probably ascribed to the presence of Py-based co-catalysts able to act as electron shuttle and enhance reaction performance.[19]

3.3.2.4. Stability tests

Generally, the rapid deactivation of MOF-based electrodes (typically shorter than 2 h) is a major obstacle impeding their application in CO_2 electroreduction reactions. Accordingly, Figure 3.27 shows the time-dependence for the potential (E) and the cumulative FE for liquid products (FE_{liq}) achieved at CuBi12 in comparison with Cu100-GDEs at galvanostatic conditions (j = 20 mA·cm^{-2}) and gas and electrolyte flow rates of $Q_{g/A}$ = 10 mL·min^{-1}·cm^{-2} and $Q_{e/A}$ = 2 mL·min^{-1}·cm^{-2}, respectively. Besides, Figure 3.27b shows FE_{liq} with time in three consecutive runs (each lasting 1 h) for the same operating conditions.

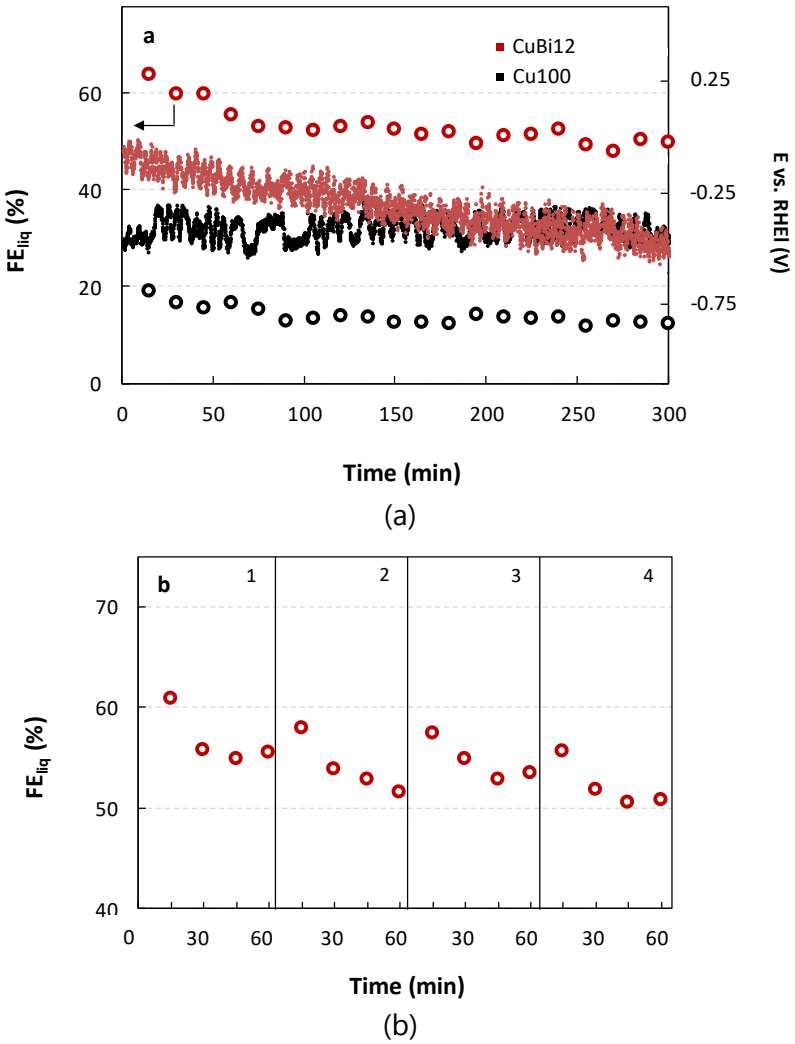

Figure 3.27. Time-dependence for (a) FE_{liq} and E at CuBi12-based electrodes in comparison to Cu100 and (b) CuBi12-GDEs after 4 consecutive runs. $Q_{e/A}$ = 2 mL·min^{-1}·cm^{-2}, $Q_{g/A}$ = 10 mL·min^{-1}·cm^{-2}, j = 20 mA·cm^{-2}.

As observed, the activity of CuBi12 and Cu100 GDEs decays progressively at first and then seems to stabilize after 90 min of operation. In general, the life of electrocatalytic materials may diminish due to the degradation produced by heterogeneity in the metal particle dispersion with time and poisoning or blocking of the active surface by intermediate species produced.[18] The catalytic material can also be gradually peeled off from the porous support, increasing the formation of H_2 due to an easy access of water to catalytic sites.[85] This is what is also observed in this case once we compared PXRD patterns and SEM micrographs taken on CuBi12-based fresh electrode and on electrodes subjected to 60 min and 300 min of operation at –0.37 V vs. RHE in the 0.5 M $KHCO_3$ solution (Figure 3.28). The GDE suffers a partial leaching during operating conditions and thus the efficiency to H_2 obtained after 15 min and 90 min of experimental time increases from 22% to 30.2%, respectively possibly due to this fact.

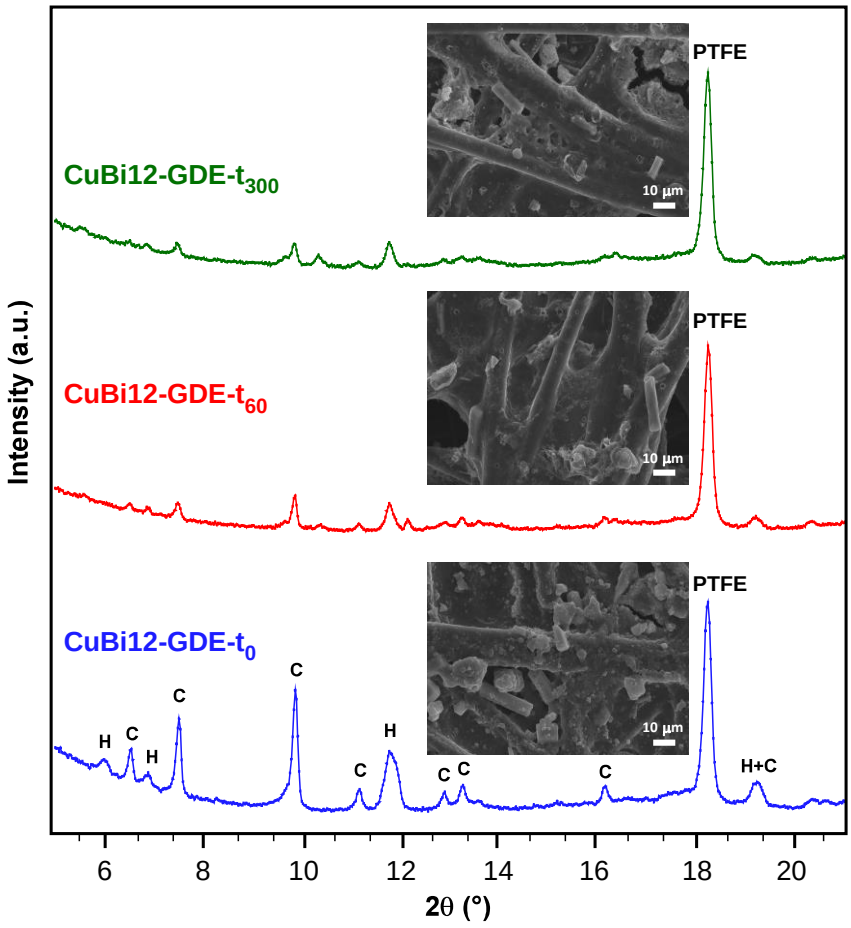

Figure 3.28. PXRD patterns and SEM micrographs at 1000 magnification for CuBi12-GDEs before and after the electrochemical process (t_0, t_{60}, t_{300} stand for GDE subjected to 0, 60 and 300 min, respectively). H and C stand for Bragg positions of HKUST-1 and CAU-17, respectively. PTFE stands for polytetrafluorethylene of the Nafion present in the catalytic ink.

According to PXRD patterns, both MOFs (HKUST-1 and CAU-17) retain the crystallinity. Nonetheless, the intensity of the diffraction peaks decay significantly from 0 (fresh electrode) to 60 min of operation, after which the decay seems to slow down up to 300 min. Such intensity decay in the diffraction peaks is in concordance with the leaching of catalytic material but it also fits the trend of the FE_{liq} values in long-term runs (Figure 3.27). The evolution of the homometallic electrodes was also evaluated (Figure 3.29), showing the same trend with a qualitative reduction of crystallinity and catalytic loading at the initial stage of the electrochemical process.

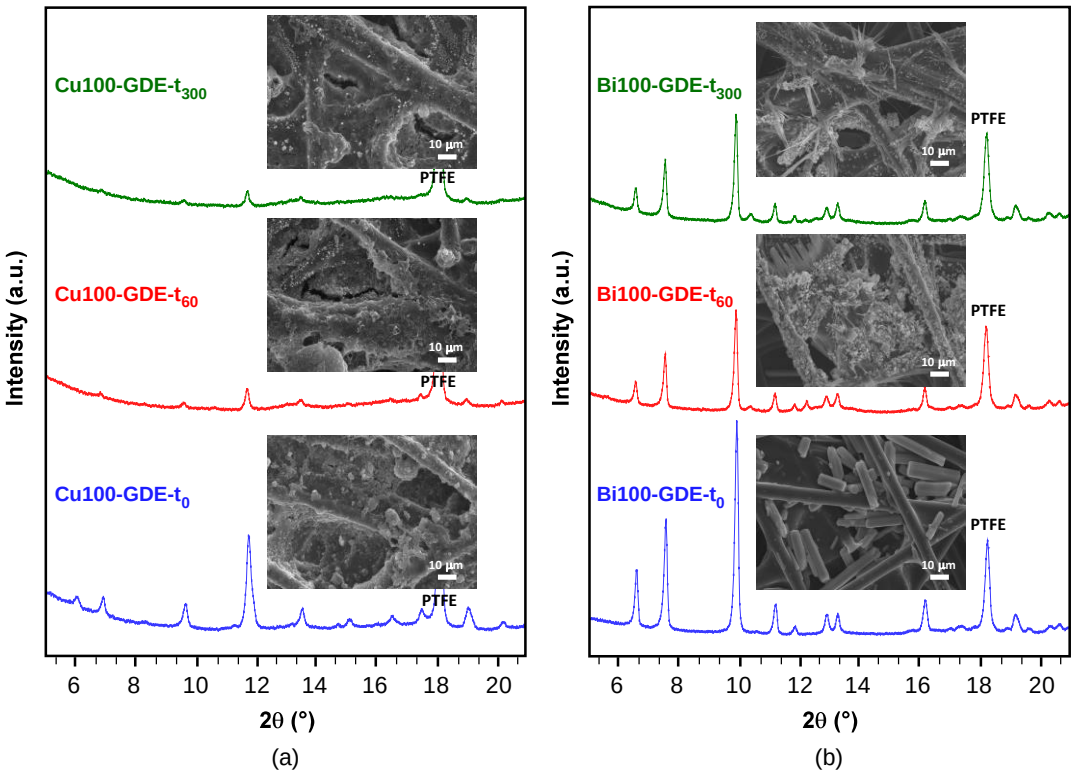

Figure 3.29. PXRD patterns and SEM micrographs at 1000 magnification for (a) Cu100-GDEs and (b) Bi100-GDE before and after the electrochemical process (t_0, t_{60}, t_{300} stand for GDE subjected to 0, 60 and 300 min, respectively). PTFE stands for polytetrafluorethylene of the Nafion present in the catalytic ink.

Furthermore, the XRF analysis carried out on the CuBi12-GDEs before and after the electrochemical process show that Bi:Cu ratio increased slightly from an initial value of 88:12 (Cu:Bi) to a stable value of 85:15 for running times of 60 min and 300 min. This fact indicates that the material leaching is somewhat higher for the Cu-MOF (HKUST-1), probably due to its smaller particle size. Figure 3.27b shows how the cumulative FE_{liq} remained after four successive runs of 60 min, indicating that only a slight observable deactivation occurred after testing the material repeatedly. Despite the overall efficiency loss along the cycles can be ascribed to the aforementioned material leaching, the relative increase at the initial stage of each cycle suggests that the long term activity loss shown in Figure 3.27a is also influenced by the poisoning

or blocking of the catalytic sites, that is mitigated from one cycle to the other upon washing of the material.

In any case, the relatively stable electrocatalytic activity of CuBi12 over time for liquid products, (FE_{liq}~50%) and in particular the cumulative efficiency for alcohols, CH_3OH and C_2H_5OH, ($FE_{alcohols}$~30%) in spite of the observed deactivation with time makes the materials appealing when considering requirements for the CO_2 electrochemical conversion towards alcohols.

3.4. CONCLUSIONS

In this chapter, we have presented two type of bimetallic MOF-based catalyst (*i.e.* HKUST-1(Cu,M_D) MOFs and HKUST-1/CAU-17 blends) and their performance into the electrochemical reduction of carbon dioxide into alcohols obtaining some interesting outcomes.

In first place, the solventless synthesis has demonstrated to be a suitable approach and facile route to afford HKUST-1(Cu,M_D) type MOFs, in such a way that the dopant (M_D) loading can be controlled by its ratio in the reagent mixture. Note that the extremely high reagent concentration that imply the reaction conditions can be a key issue making feasible the controllable doping of the MOFs. The products are obtained in high yields and good crystallinity as demonstrated by PXRD analysis and N_2 adsorption isotherms. The dopant causes a slight increase of the cell volume attributable to the smaller size of Cu(II) ion and to Jahn-Teller contraction implying the Cu–$O_{carboxylate}$ bonds. With regard to the microstructure, it must be emphasized that all the samples consist of sub-micrometric crystals which can be considered as an appealing feature since this fact increases the external surface area and prompts the reagent diffusion in catalytic processes. Regarding the electrocatalytic performance of HKUST-1(Cu,M_D)-GDEs, Ru(III) doping has a striking influence in the alcohol yield, reaching relatively high Faraday efficiencies (47.2%) comparable to those provided by nanosized inorganic catalysts. Unfortunately, its activity decays after 60 minutes of continuous reaction until reaching a similar performance to that of pristine HKUST-1(Cu). Nonetheless, in all cases, the increase of dopant loading promotes a selectivity increase towards ethanol, reaching values ranging from 93 to 100%. This trend might be explained by a favoured interplay between the dopant and reaction intermediates, which would lengthen the permanence time, prompting further C–C coupling reaction to ethanol.

Secondly, as the doping with Bi(III) of HKUST-1 resulted unsuccessful, the alternative approach based on the use of HKUST-1/CAU-17 blends, demonstrated the

remarkable benefits of using CuBi-based metal-organic frameworks supported in gas diffusion electrodes to reach enhanced rates and Faraday efficiencies in the electrochemical conversion of CO_2 to alcohols. The results firstly showed that including bismuth as co-catalyst lowered the overpotentials required, denoting a Cu-Bi synergic contribution in the reduction pathway of CO_2. The electrolysis product analyses show methanol and ethanol as liquid species obtained from CO_2 reduction, together with formic acid. The gas phase is mainly composed of hydrogen, together with carbon monoxide and small concentrations of ethylene. The maximum reaction rates for CO_2 conversion to methanol and ethanol are r_{CH_3OH} = 29.7 μmol·m^{-2}·s^{-1} (FE = 8.6%) and $r_{C_2H_5OH}$ = 48.8 μmol·m^{-2}·s^{-1} (FE= 28.3%), respectively, for the CuBi-based materials at j = 20 mA·cm^{-2}. These values enhance those obtained at homometallic Cu and Bi-based electrodes, which is associated with a favored interplay between Cu-Bi and reaction intermediates, prompting the formation of methanol and C–C coupling reaction to ethanol as observed also to doped HKUST-1 systems. The Cu/Bi metal ratio in the electrode surface as well as the current density applied to the system seems to be key parameters for controlling reaction selectivity. The optimum values for a more selective CO_2 reduction to alcohols can be set at a Bi atomic content of 12% and a current density of j = 20 mA·cm^{-2}. Besides, the mixed-metal systems remained pseudo-stable after 5 h of operation in liquid media (FE_{liq} ~50%, $FE_{alcohols}$~30%).

All in all, these results denote the potential of Cu-based bimetallic-based electrodes and expand the field of innovative electrocatalysts for the continuous conversion of CO_2 to alcohols, specially invigorating the electrochemical conversion by using MOF-based electrodes.

3.5. References

1 M. E. Boot-Handford, J. C. Abanades, E. J. Anthony, M. J. Blunt, S. Brandani, N. Mac Dowell, J. R. Fernández, M.-C. Ferrari, R. Gross, J. P. Hallett, R. S. Haszeldine, P. Heptonstall, A. Lyngfelt, Z. Makuch, E. Mangano, R. T. J. Porter, M. Pourkashanian, G. T. Rochelle, N. Shah, J. G. Yao and P. S. Fennell, Carbon capture and storage update, *Energy Environ. Sci.*, **2014**, 7, 130–189.

2 J. Albo, M. Alvarez-Guerra, P. Castaño and A. Irabien, Towards the electrochemical conversion of carbon dioxide into methanol, *Green Chem.*, **2015**, 17, 2304–2324.

3 M. Alvarez-Guerra, J. Albo, E. Alvarez-Guerra and A. Irabien, Ionic liquids in the electrochemical valorisation of CO_2, *Energy Environ. Sci.*, **2015**, 8, 2574–2599.

4 I. Merino-Garcia, E. Alvarez-Guerra, J. Albo and A. Irabien, Electrochemical membrane reactors for the utilisation of carbon dioxide, *Chem. Eng. J.*, **2016**, 305, 104–120.

5 A. Dominguez-Ramos, B. Singh, X. Zhang, E. G. Hertwich and A. Irabien, Global warming footprint of the electrochemical reduction of carbon dioxide to formate, *J. Clean. Prod.*, **2015**, 104, 148–155.

6 M. E. Royer, Réduction de l'acide carbonique en acide formique, *Compt. Rend*, **1870**, 1870, 731–732.

7 G. Centi and S. Perathoner, Opportunities and prospects in the chemical recycling of carbon dioxide to fuels, *Catal. Today*, **2009**, 148, 191–205.

8 J. Albo, M. Alvarez-Guerra and A. Irabien, Electro-, photo-, and photoelectro-chemical reduction of CO_2, in *Heterogeneous Catalysts: Advanced Design, Characterization and Applications*, eds. W. Y. Teoh, A. Urakawa, Y. H. Ng and P. Sit, WILEY-VCH GmbH, First Edit., 2021, pp. 649–669.

9 W. Zhang, Y. Hu, L. Ma, G. Zhu, Y. Wang, X. Xue, R. Chen, S. Yang and Z. Jin, Progress and Perspective of Electrocatalytic CO 2 Reduction for Renewable Carbonaceous Fuels and Chemicals, *Adv. Sci.*, **2018**, 5, 1700275.

10 J. Wu, Y. Huang, W. Ye and Y. Li, CO_2 reduction: From the electrochemical to photochemical approach, *Adv. Sci.*, **2017**, 4, 1–29.

11 J. Qiao, Y. Liu and J. Zhang, Eds., Electrochemical reduction of carbon dioxide. Fundamentals and technologies, *Electrochemical reduction of carbon dioxide. Fundamentals and technologies*, CRC Press, 2016.

12 R. Masel, Z. Liu, D. Zhao, Q. Chen, D. Lutz and L. Nereng, Chapter 10. CO_2 conversion to chemicals with emphasis on using renewable energy/resources to drive the conversion, 2015, pp. 215–257.

13 D. T. Whipple and P. J. A. Kenis, Prospects of CO2 utilization via direct heterogeneous electrochemical reduction, *J. Phys. Chem. Lett.*, **2010**, 1, 3451–3458.

14 J. I. Feldblyum, M. Liu, D. W. Gidley and A. J. Matzger, Reconciling the discrepancies between crystallographic porosity and guest access as exemplified by Zn-HKUST-1, *J. Am. Chem. Soc.*, **2011**, 133, 18257–18263.

15 D. D. Zhu, J. L. Liu and S. Z. Qiao, Recent advances in inorganic heterogeneous electrocatalysts for reduction of carbon dioxide, *Adv. Mater.*, **2016**, 28, 3423–3452.

16 D. Du, R. Lan, J. Humphreys and S. Tao, Progress in inorganic cathode catalysts for electrochemical conversion of carbon dioxide into formate or formic acid, *J. Appl. Electrochem.*, **2017**, 47, 661–678.

17 K. P. Kuhl, E. R. Cave, D. N. Abram and T. F. Jaramillo, New insights into the electrochemical reduction of carbon dioxide on metallic copper surfaces, *Energy Environ. Sci.*, **2012**, 5, 7050.

18 J. Albo, A. Sáez, J. Solla-Gullón, V. Montiel and A. Irabien, Production of methanol from CO_2 electroreduction at Cu_2O and Cu_2O/ZnO-based electrodes in aqueous solution, *Appl. Catal. B Environ.*, **2015**, 176–177, 709–717.

19 J. Albo, G. Beobide, P. Castaño and A. Irabien, Methanol electrosynthesis from CO_2 at Cu_2O/ZnO prompted by pyridine-based aqueous solutions, *J. CO2 Util.*, **2017**, 18, 164–172.

20 J. W. Maina, C. Pozo-Gonzalo, L. Kong, J. Schütz, M. Hill and L. F. Dumée, Metal-organic framework based catalysts for CO_2 conversion, *Mater. Horizons*, **2017**, 4, 345–361.

21 K. Sumida, D. L. Rogow, J. A. Mason, T. M. McDonald, E. D. Bloch, Z. R. Herm, T.-H. Bae and J. R. Long, Carbon dioxide capture in metal–organic frameworks, *Chem. Rev.*, **2012**, 112, 724–781.

22 L. Lu, X. Sun, J. Ma, D. Yang, H. Wu, B. Zhang, J. Zhang and B. Han, Highly efficient electroreduction of CO_2 to methanol on palladium-copper bimetallic aerogels, *Angew. Chemie Int. Ed.*, **2018**, 57, 14149–14153.

23 J. T. Feaster, C. Shi, E. R. Cave, T. Hatsukade, D. N. Abram, K. P. Kuhl, C. Hahn, J. K. Nørskov and T. F. Jaramillo, Understanding selectivity for the electrochemical reduction of carbon dioxide to formic acid and carbon monoxide on metal electrodes, *ACS Catal.*, **2017**, 7, 4822–4827.

24 S. Gulati, S. Vijayan, Mansi, S. Kumar, B. Harikumar, M. Trivedi and R. S. Varma, Recent advances in the application of metal-organic frameworks (MOFs)-based nanocatalysts for direct conversion of carbon dioxide (CO_2) to value-added chemicals, *Coord. Chem. Rev.*, **2023**, 474, 214853.

25 J. Albo, D. Vallejo, G. Beobide, O. Castillo, P. Castaño and A. Irabien, Copper-based metal-organic porous materials for CO_2 electrocatalytic reduction to alcohols, *ChemSusChem*, **2017**, 10, 1100–1109.

26 J. He, N. J. J. Johnson, A. Huang and C. P. Berlinguette, Electrocatalytic alloys for CO_2 reduction, *ChemSusChem*, **2018**, 11, 48–57.

27 M. K. Birhanu, M.-C. Tsai, A. W. Kahsay, C.-T. Chen, T. S. Zeleke, K. B. Ibrahim, C.-J. Huang, W.-N. Su and B.-J. Hwang, Copper and copper-based bimetallic catalysts for carbon dioxide electroreduction, *Adv. Mater. Interfaces*, **2018**, 5, 1800919.

28 D. A. Torelli, S. A. Francis, J. C. Crompton, A. Javier, J. R. Thompson, B. S. Brunschwig, M. P. Soriaga and N. S. Lewis, Nickel–gallium-catalyzed electrochemical reduction of CO_2 to highly reduced products at low overpotentials, *ACS Catal.*, **2016**, 6, 2100–2104.

29 M. Ma, K. Djanashvili and W. A. Smith, Controllable hydrocarbon formation from the electrochemical reduction of CO_2 over Cu nanowire arrays, *Angew. Chemie Int. Ed.*, **2016**, 55, 6680–6684.

30 C. Wang, M. Cao, X. Jiang, M. Wang and Y. Shen, A catalyst based on copper-cadmium bimetal for electrochemical reduction of CO_2 to CO with high faradaic efficiency, *Electrochim. Acta*, **2018**, 271, 544–550.

31 M. Karamad, V. Tripkovic and J. Rossmeisl, Intermetallic alloys as CO electroreduction catalysts—role of isolated active sites, *ACS Catal.*, **2014**, 4, 2268–2273.

32 A. Wuttig and Y. Surendranath, Impurity ion complexation enhances carbon dioxide reduction catalysis, *ACS Catal.*, **2015**, 5, 4479–4484.

33 Y. Hori, Electrochemical CO_2 reduction on metal electrodes, in *Modern Aspects of Electrochemistry*, Springer New York, New York, NY, pp. 89–189.

34 S. Ma, M. Sadakiyo, M. Heima, R. Luo, R. T. Haasch, J. I. Gold, M. Yamauchi and P. J. A.

Kenis, Electroreduction of carbon dioxide to hydrocarbons using bimetallic Cu–Pd catalysts with different mixing patterns, *J. Am. Chem. Soc.*, **2017**, 139, 47–50.

35 S. Lee, G. Park and J. Lee, Importance of Ag–Cu biphasic boundaries for selective electrochemical reduction of CO_2 to ethanol, *ACS Catal.*, **2017**, 7, 8594–8604.

36 D. Ren, B. S.-H. Ang and B. S. Yeo, Tuning the selectivity of carbon dioxide electroreduction toward ethanol on oxide-derived Cu_xZn catalysts, *ACS Catal.*, **2016**, 6, 8239–8247.

37 D. Kim, J. Resasco, Y. Yu, A. M. Asiri and P. Yang, Synergistic geometric and electronic effects for electrochemical reduction of carbon dioxide using gold–copper bimetallic nanoparticles, *Nat. Commun.*, **2014**, 5, 4948.

38 J. Albo and A. Irabien, Cu_2O-loaded gas diffusion electrodes for the continuous electrochemical reduction of CO_2 to methanol, *J. Catal.*, **2016**, 343, 232–239.

39 K. Zhao, Y. Liu, X. Quan, S. Chen and H. Yu, CO_2 electroreduction at low overpotential on oxide-derived Cu/carbons fabricated from metal-organic ramework, *ACS Appl. Mater. Interfaces*, **2017**, 9, 5302–5311.

40 S. S.-Y. Chui, S. M.-F. Lo, J. P. H. Charmant, A. G. Orpen and I. D. Williams, A Chemically functionalizable nanoporous material $[Cu_3(TMA)_2(H_2O)_3]_n$, *Science*, **1999**, 283, 1148–1150.

41 C. R. Groom, I. J. Bruno, M. P. Lightfoot and S. C. Ward, The Cambridge structural database, *Acta Crystallogr. Sect. B Struct. Sci. Cryst. Eng. Mater.*, **2016**, 72, 171–179.

42 M. P. Singh, N. R. Dhumal, H. J. Kim, J. Kiefer and J. A. Anderson, Influence of water on the chemistry and structure of the metal–organic framework Cu3 (btc)2, *J. Phys. Chem. C*, **2016**, 120, 17323–17333.

43 D. Sharma, S. Rasaily, S. Pradhan, K. Baruah, S. Tamang and A. Pariyar, HKUST-1 metal organic framework as an efficient dual-function catalyst: aziridination and one-pot ring-opening transformation for Formation of β-Aryl sulfonamides with C–C, C–N, C–S, and C–O bonds, *Inorg. Chem.*, **2021**, 60, 7794–7802.

44 J. Albo, D. Vallejo, G. Beobide, O. Castillo, P. Castaño and A. Irabien, Copper-Based Metal-Organic Porous Materials for CO2 Electrocatalytic Reduction to Alcohols, *ChemSusChem*, **2016**, 1–11.

45 G. Nickerl, U. Stoeck, U. Burkhardt, I. Senkovska and S. Kaskel, A catalytically active porous coordination polymer based on a dinuclear rhodium paddle-wheel unit, *J. Mater. Chem. A*, **2014**, 2, 144–148.

46 S. Schuster, E. Klemm and M. Bauer, The role of Pd2+/Pd0 in hydrogenation by [Pd(2-pymo)2]n: An X-ray absorption and IR spectroscopic study, *Chem. - A Eur. J.*, **2012**, 18, 15831–15837.

47 S. Opelt, V. Krug, J. Sonntag, M. Hunger and E. Klemm, Investigations on stability and reusability of $[Pd(2\text{-pymo})_2]_n$ as hydrogenation catalyst, *Microporous Mesoporous Mater.*, **2012**, 147, 327–333.

48 F. X. Llabrés i Xamena, A. Abad, A. Corma and H. Garcia, MOFs as catalysts: Activity, reusability and shape-selectivity of a Pd-containing MOF, *J. Catal.*, **2007**, 250, 294–

298.

49 J. Juan-Alcañiz, J. Ferrando-Soria, I. Luz, P. Serra-Crespo, E. Skupien, V. P. Santos, E. Pardo, F. X. Llabrés I Xamena, F. Kapteijn and J. Gascon, The oxamate route, a versatile post-functionalization for metal incorporation in MIL-101(Cr): Catalytic applications of Cu, Pd, and Au, *J. Catal.*, **2013**, 307, 295–304.

50 W. Zhang, M. Kauer, O. Halbherr, K. Epp, P. Guo, M. I. Gonzalez, D. J. Xiao, C. Wiktor, F. X. LIabrés i Xamena, C. Wöll, Y. Wang, M. Muhler and R. A. Fischer, Ruthenium metal-organic frameworks with different defect types: influence on porosity, sorption, and catalytic properties, *Chem. - A Eur. J.*, **2016**, 22, 14297–14307.

51 Y. Qiu, J. Du, C. Dai, W. Dong and C. Tao, Bismuth nano-flowers as a highly selective catalyst for electrochemical reduction of CO_2 to formate, *J. Electrochem. Soc.*, **2018**, 165, H594–H600.

52 M. Y. Zu, L. Zhang, C. Wang, L. R. Zheng and H. G. Yang, Copper-modulated bismuth nanocrystals alter the formate formation pathway to achieve highly selective CO_2 electroreduction, *J. Mater. Chem. A*, **2018**, 6, 16804–16809.

53 C. W. Lee, J. S. Hong, K. D. Yang, K. Jin, J. H. Lee, H.-Y. Ahn, H. Seo, N.-E. Sung and K. T. Nam, Selective electrochemical production of formate from carbon dioxide with bismuth-based catalysts in an aqueous electrolyte, *ACS Catal.*, **2018**, 8, 931–937.

54 P. Su, W. Xu, Y. Qiu, T. Zhang, X. Li and H. Zhang, Ultrathin bismuth nanosheets as a highly efficient CO₂ reduction electrocatalyst, *ChemSusChem*, **2018**, 11, 848–853.

55 J. H. Koh, D. H. Won, T. Eom, N.-K. Kim, K. D. Jung, H. Kim, Y. J. Hwang and B. K. Min, Facile CO_2 electro-reduction to formate via oxygen bidentate intermediate stabilized by high-index planes of Bi dendrite catalyst, *ACS Catal.*, **2017**, 7, 5071–5077.

56 W. Lv, J. Zhou, J. Bei, R. Zhang, L. Wang, Q. Xu and W. Wang, Electrodeposition of nano-sized bismuth on copper foil as electrocatalyst for reduction of CO_2 to formate, *Appl. Surf. Sci.*, **2017**, 393, 191–196.

57 H. Zhong, Y. Qiu, T. Zhang, X. Li, H. Zhang and X. Chen, Bismuth nanodendrites as a high performance electrocatalyst for selective conversion of CO_2 to formate, *J. Mater. Chem. A*, **2016**, 4, 13746–13753.

58 H. Zhang, Y. Ma, F. Quan, J. Huang, F. Jia and L. Zhang, Selective electro-reduction of CO_2 to formate on nanostructured Bi from reduction of BiOCl nanosheets, *Electrochem. commun.*, **2014**, 46, 63–66.

59 C.-C. Miao and G.-Q. Yuan, Morphology-Controlled Bi_2O_3 nanoparticles as catalysts for selective electrochemical reduction of CO_2 to formate, *ChemElectroChem*, **2018**, 5, 3741–3747.

60 N. Han, Y. Wang, H. Yang, J. Deng, J. Wu, Y. Li and Y. Li, Ultrathin bismuth nanosheets from in situ topotactic transformation for selective electrocatalytic CO_2 reduction to formate, *Nat. Commun.*, **2018**, 9, 1320.

61 S. Trasatti, Work function, electronegativity, and electrochemical behaviour of metals: III. Electrolytic hydrogen evolution in acid solutions, *J. Electroanal. Chem. Interfacial Electrochem.*, **1972**, 39, 163–184.

62 M. Köppen, A. Dhakshinamoorthy, A. K. Inge, O. Cheung, J. Ångström, P. Mayer and N. Stock, Synthesis, transformation, catalysis, and gas sorption investigations on the bismuth metal–organic framework CAU-17, *Eur. J. Inorg. Chem.*, **2018**, 2018, 3496–3503.

63 A. K. Inge, M. Köppen, J. Su, M. Feyand, H. Xu, X. Zou, M. O'Keeffe and N. Stock, Unprecedented topological complexity in a metal–organic framework constructed from simple building units, *J. Am. Chem. Soc.*, **2016**, 138, 1970–1976.

64 C. R. Groom, I. J. Bruno, M. P. Lightfoot and S. C. Ward, The Cambridge Structural Database, *Acta Crystallogr. Sect. B Struct. Sci. Cryst. Eng. Mater.*, **2016**, 72, 171–179.

65 M. Lanchas, S. Arcediano, A. T. Aguayo, G. Beobide, O. Castillo, J. Cepeda, D. Vallejo-Sánchez and A. Luque, Two appealing alternatives for MOFs synthesis: solvent-free oven heating vs. microwave heating, *RSC Adv.*, **2014**, 4, 60409–60412.

66 D. J. Morgan, Resolving ruthenium: XPS studies of common ruthenium materials, *Surf. Interface Anal.*, **2015**, 47, 1072–1079.

67 R. D. Shannon, Revised effective ionic radii and systematic studies of interatomic distances in halides and chalcogenides, *Acta Crystallogr. Sect. A*, **1976**, 32, 751–767.

68 J. Rodriguez-Carvajal, FULLPROF: a program for Rietveld refinement and pattern matching analysis, in *Satellite meeting on powder diffraction of the XV congress of the IUCr*, Tolouse, France, 1990, p. 127.

69 J. Rodriguez-Carvajal, FULLPROF 2000, version 2.5d, Laboratoire Léon Brillouin (CEA-CERS), 2003.

70 J. G. Santaclara, A. I. Olivos-Suarez, A. Gonzalez-Nelson, D. Osadchii, M. A. Nasalevich, M. A. van der Veen, F. Kapteijn, A. M. Sheveleva, S. L. Veber, M. V. Fedin, A. T. Murray, C. H. Hendon, A. Walsh and J. Gascon, Revisiting the incorporation of Ti(IV) in UiO-type metal–organic frameworks: Metal exchange versus grafting and their implications on photocatalysis, *Chem. Mater.*, **2017**, 29, 8963–8967.

71 J. Cepeda, S. Pérez-Yáñez, G. Beobide, O. Castillo, E. Goikolea, F. Aguesse, L. Garrido, A. Luque and P. A. Wright, Scandium/alkaline metal–organic frameworks: Adsorptive properties and ionic conductivity, *Chem. Mater.*, **2016**, 28, 2519–2528.

72 M. Thommes, K. Kaneko, A. V. Neimark, J. P. Olivier, F. Rodriguez-Reinoso, J. Rouquerol and K. S. W. Sing, Physisorption of gases, with special reference to the evaluation of surface area and pore size distribution (IUPAC Technical Report), *Pure Appl. Chem.*, **2015**, 87, 1051–1069.

73 A. Belsky, M. Hellenbrandt, V. L. Karen and P. Luksch, New developments in the Inorganic Crystal Structure Database (ICSD): accessibility in support of materials research and design, *Acta Crystallogr. Sect. B Struct. Sci.*, **2002**, 58, 364–369.

74 K. Okada, M. I. Kay, D. T. Cromer and I. Almodovar, Crystal structure by neutron diffraction and the antiferroelectric phase transition in copper formate tetrahydrate, *J. Chem. Phys.*, **1966**, 44, 1648–1653.

75 Y. Hori, O. Koga, H. Yamazaki and T. Matsuo, Infrared spectroscopy of adsorbed CO and intermediate species in electrochemical reduction of CO_2 to hydrocarbons on a

Cu electrode, *Electrochim. Acta*, **1995**, 40, 2617–2622.

76 W. Luc, C. Collins, S. Wang, H. Xin, K. He, Y. Kang and F. Jiao, Ag–Sn bimetallic catalyst with a core–shell structure for CO_2 reduction, *J. Am. Chem. Soc.*, **2017**, 139, 1885–1893.

77 H. Zhang, J. Li, Q. Tan, L. Lu, Z. Wang and G. Wu, Metal–organic frameworks and their derived materials as electrocatalysts and photocatalysts for CO_2 reduction: Progress, challenges, and perspectives, *Chem. – A Eur. J.*, **2018**, 24, 18137–18157.

78 F. N. Al-Rowaili, A. Jamal, M. S. Ba Shammakh and A. Rana, A review on recent advances for electrochemical reduction of carbon dioxide to methanol using metal–organic framework (MOF) and non-MOF catalysts: Challenges and future prospects, *ACS Sustain. Chem. Eng.*, **2018**, 6, 15895–15914.

79 D.-H. Nam, O. S. Bushuyev, J. Li, P. De Luna, A. Seifitokaldani, C.-T. Dinh, F. P. García de Arquer, Y. Wang, Z. Liang, A. H. Proppe, C. S. Tan, P. Todorović, O. Shekhah, C. M. Gabardo, J. W. Jo, J. Choi, M.-J. Choi, S.-W. Baek, J. Kim, D. Sinton, S. O. Kelley, M. Eddaoudi and E. H. Sargent, Metal–organic frameworks mediate Cu coordination for selective CO_2 electroreduction, *J. Am. Chem. Soc.*, **2018**, 140, 11378–11386.

80 Y.-L. Qiu, H.-X. Zhong, T.-T. Zhang, W.-B. Xu, P.-P. Su, X.-F. Li and H.-M. Zhang, Selective electrochemical reduction of carbon dioxide using Cu-based metal-organic framework for CO_2 capture, *ACS Appl. Mater. Interfaces*, **2018**, 10, 2480–2489.

81 D. Ren, Y. Deng, A. D. Handoko, C. S. Chen, S. Malkhandi and B. S. Yeo, Selective electrochemical reduction of carbon dioxide to ethylene and ethanol on copper(I) oxide catalysts, *ACS Catal.*, **2015**, 5, 2814–2821.

82 K. J. P. Schouten, Y. Kwon, C. J. M. van der Ham, Z. Qin and M. T. M. Koper, A new mechanism for the selectivity to C_1 and C_2 species in the electrochemical reduction of carbon dioxide on copper electrodes, *Chem. Sci.*, **2011**, 2, 1902.

83 J. H. Montoya, A. A. Peterson and J. K. Nørskov, Insights into C–C coupling in CO2 electroreduction on copper electrodes, *ChemCatChem*, **2013**, 5, 737–742.

84 Y. Song, W. Chen, C. Zhao, S. Li, W. Wei and Y. Sun, Metal-free nitrogen-doped mesoporous carbon for electroreduction of CO_2 to ethanol, *Angew. Chemie Int. Ed.*, **2017**, 56, 10840–10844.

85 H.-R. "Molly" Jhong, F. R. Brushett and P. J. A. Kenis, The effects of catalyst layer deposition methodology on electrode performance, *Adv. Energy Mater.*, **2013**, 3, 589–599.

Chapter 4

Zirconium(IV) and hafnium(IV)-based new MOFs for water adsorption and CO_2 electroreduction

4.1. INTRODUCTION

Among the extensive family of MOFs, as it has been commented, group 4 metal-based ones, including Ti-, Zr-, and Hf-based MOFs, are one of the most attractive families of MOFs owing to their superior chemical stability and structural tunability.[1] In this context, a remarkable step forward was achieved in 2008 with the discovery of the paradigmatic UiO-66[2] which boosted the development of group 4 metal-based MOFs.[3]

4.1.1. Synthesis of group 4 metal-based MOFs

The assembling of building blocks in MOFs is a dynamic process, which evolves from an initially disordered state towards an ordered stable state.[4] In this process, which can proceed through various pathways, the kinetic or thermodynamic control can lead to diverse structures. Usually, the thermodynamically driven structures are denser than the metastable ones, thus, obtaining the metastable products is a desirable challenge in the synthesis of MOFs, since it could enhance the porosity of these materials.[5–7] An example of this success can be considered the achievement of porous Co/Zn-imidazolate ZIFs by means of the controlled addition of structure directing agents,[8] since the thermodynamically obtained polymorphs lack of porosity.[9]

The use of modulators is widely extended in the synthesis of group 4-based MOFs and they have shown to improve the crystallinity of the samples, as it has been thoroughly demonstrated for the isoreticular family of UiO-66, UiO-67 and UiO-68.[10] Moreover, the modulator selection is also in the spotlight to control the number and nature of defect sites of Zr-MOFs, which tunes the pore properties for adsorption applications.[11,12] However, it is noteworthy that there are cases in which the modulator can also behave as a structure-directing agent, for example decreasing the connectivity of the Zr_6 octahedral secondary building units (SBUs) from twelve to eight in DUT-51.[13] For this structure directing effect to take place in M(IV) based MOFs, which are featured with a less reversible M–O bond, high modulator concentration is required.[14]

4.1.2. Water adsorption

Among the widespread applications of MOFs, their implementation in water adsorptive technologies has emerged during the last few years.[15] Water adsorption in porous materials is relevant for many applications such as dehumidification, thermal batteries, and delivery of drinking water in remote areas. Among them, the development of atmospheric water harvesting devices has recently stood out, which aim to mitigate water scarcity in arid and desert climates.[16–18] So far, zeolites have been commercially used for this purpose, since they can capture water at very low p/p° values with steep uptake behaviour. Nevertheless, these inorganic compounds possess an energetically demanding recyclability due to the strong interactions between water and the

framework. High water uptake capacity can also be achieved with large-pore materials, such as mesoporous silicas and carbons but, due to their hydrophobic nature, the water capture is restricted to the condensation at high relative pressure values, with these materials being difficult to be chemically manipulated in order to substantially modify their sorption profile.[19] This fact brings the need to design and study new porous materials in which the water adsorption behaviour meets the following criteria: (1) maintain its water capacity after a multitude of water uptake and release cycles, (2) exhibit a high water sorption working capacity under operational conditions, (3) have a low regeneration (removal of water molecules) temperature and (4) possess desirable dynamic water sorption properties.[15] During the last years, it has been demonstrated that some MOFs are particularly attractive for this purpose because of their water capture properties and chemical and structural tunability.[20,21] More specifically, zirconium-based MOFs are among the best performing ones, since they usually allow the formation of water clusters which are held by multiple hydrogen bonds in the cavities of the MOFs, suggesting that the number of intermolecular interactions between adsorbed water molecules and their geometry plays a key role in optimizing the adsorption process.[19]

Water adsorption properties of the well-known UiO-66 and its derivatives have been widely studied experimentally and computationally showing two interesting evidences: (1) almost all functionalized versions show enhanced interactions with water at relative humidity values below 25% (especially UiO-66-NH_2 and UiO-66-NO_2)[22] and (2) defects within the network can noteworthy make the MOF more hydrophilic, which is directly related to the relative humidity at which the pores fill with water.[23] This is of great interest because more hydrophilic materials usually start adsorbing water at lower humidity relative values, which may allow them to be used as adsorbents in arid regions.

4.1.3. Objectives

In this study we will develop a new family of Zr/Hf-MOFs (so-called EHU-30, EHU-30-NH_2 and EHU-30-NHR) through an alternative synthetic approach capable of modifying the framework topology retaining the SBU and chemical formula of UiO-66, using BDC and NH_2-BDC as linkers and different modulators as structure directing agents. In addition to the chemical and structural characterization, the adsorptive behaviour towards N_2, CO_2 and water vapour will be experimentally and computationally studied.

Furthermore, taking advantage of the higher chemical stability of group 4-based MOFs and knowing that copper-based materials are the most suitable to break the C–O bond of CO_2 and further convert CO to more reduced species, such as alcohols and

hydrocarbons, as analysed during Chapter 3, herein developed Zr-based new MOFs will be post-synthetically doped with Cu(II)-doping and assessed as catalyst in the electroreduction of carbon dioxide.

4.2. Zr(IV) AND Hf(IV)-BASED NEW MOFs AND THEIR PERFORMANCE IN WATER ADSORPTION

4.2.1. EXPERIMENTAL SECTION

In this section, synthetic procedure for obtaining Zr- and Hf- based MOFs is presented along with the characterization details of interest. Remaining data on the employed equipments and other characterization techniques are described in Section 2.2 of Chapter 2.

4.2.1.1. Synthetic procedure

Two different optimised solventless synthetic approaches are used to obtain so as called EHU-30(Zr) and EHU-30-X(Zr and Hf) (X = $–NH_2$ or NHR, R: 2-carboxypropyl) MOFs, respectively.

Synthesis of EHU-30. Zirconium(IV) propoxide, $Zr(OPr)_4$ (70% wt in 1-propanol, 2.25 mmol) was mixed under continuous stirring with methacrylic acid (9 mmol) and benzene-1,4-dicarboxylic acid, H_2BDC (2.25 mmol). Thereafter, to obtain the most crystalline sample 10 μL of water were added. Finally, the flask was sealed and the resulting doughy reaction mixture was heated at 140 °C for 90 minutes in a sand-bath with continuous stirring. The synthesis product was thoroughly washed with methanol and dried under ambient conditions. The resulting compound exhibited the aspect of a finely divided white powder.

Synthesis of EHU-30-NH_2 and EHU-30-NHR. The metal source (zirconium(IV) propoxide, $Zr(OPr)_4$, or hafnium(IV) isopropoxide, $Hf(OiPr)_4$, 2.25 mmol) was mixed under continuous stirring with a monocarboxylic acid (isobutyric or methacrylic acid, 15 and 16 mmol, for obtaining EHU-30-NH_2 or EHU-30-NHR, respectively) and 2-aminobenzene-1,4-dicarboxylic acid, H_2NH_2BDC (2.25 mmol) in a closed teflon vessel. Thereafter, to obtain the most crystalline samples, water was added at roughly stoichiometric ratios (see Table 4.1). As discussed below, the amount of added water plays a crucial role. The resulting reaction mixture was placed in a preheated oven at 140 °C for 4 hours. The synthesis product was thoroughly washed with methanol and dried under vacuum. The four resulting compounds named as EHU-30-NH_2(Zr), EHU-30-NH_2(Hf), EHU-30-NHR(Zr) and EHU-30-NHR(Hf) exhibited the aspect of a finely divided yellowish powder, with some differencies in yellow intensity (Figure 4.1).

Table 4.1 summarizes the quantities employed for preparing the five samples.

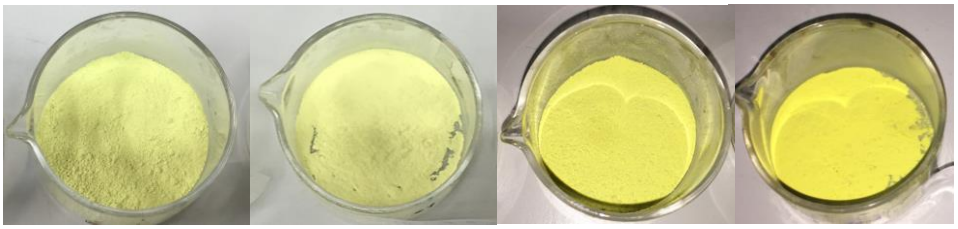

EHU-30-NH_2(Zr) EHU-30-NH_2(Hf) EHU-30-NHR(Zr) EHU-30-NHR(Hf)

Figure 4.1. Appearance of amino-based EHU-30 MOFs synthesised.

Table 4.1. Optimised synthetic conditions to obtain EHU-30, EHU-30-NH_2 and EHU-30-NHR MOFs based on zirconium(IV) and hafnium(IV).

Sample code	Metal source	Organic ligand	Modulator	Water
EHU-30(Zr)	1.0529 g of $Zr(OPr)_4$	0.3814 g of H_2BDC	771 μL of methacrylic acid	10 μL
EHU-30-NH_2(Zr)	1.0529 g of $Zr(OPr)_4$	0.4117 g of H_2NH_2BDC	1400 μL of isobutyric acid	10 μL
EHU-30-NH_2(Hf)	0.9343 g of $Hf(OiPr)_4$			ø
EHU-30-NHR(Zr)	1.0529 g of $Zr(OPr)_4$		1400 μL of methacrylic acid	50 μL
EHU-30-NHR(Hf)	0.9343 g of $Hf(OiPr)_4$			20 μL

4.2.1.2. Structural characterization

Synchrotron data collection and crystal structural elucidation of EHU-30. High resolution synchrotron X-ray diffraction pattern of polycrystalline EHU-30 was measured at I11 Beamline of Diamond Light Source.

The peak search algorithm implemented in Topas v5 program[24,25] was used to determine the angular positions of the first 42 reflections (up to about 20° 2θ). These positions were used to index the pattern using Topas v5 program into the hexagonal system. Inspection of systematic absences confirmed space group $P6_3/mmc$ as the correct one.

Crystal structure of EHU-30 was solved *ab initio* using Topas v5 program. Firstly, crystallographic position of heavy atom Zr was found by using the Charge–Flipping method.[26,27] Using only the Zr atom position, a preliminary Rietveld refinement[28] was carried out. This allowed calculating a difference Fourier map, which clearly showed electron density peaks, corresponding to atoms O1 and O2 of the Zr-based cluster. After including these two atoms in the Rietveld refinement, a subsequent different Fourier map already showed electron density clouds connecting the clusters, which corresponded to the organic linkers. These were then described in the refinement as semi-rigid body units.

Final Rietveld refinement of EHU-30 crystal structure was carried out in the 2θ range from 2.5 to 65° (about 0.77 Å in *d*-spacing) and atomic coordinates of all atoms were included. Different isotropic temperature factors were introduced for the organic linkers, O1 and O2 atoms and Zr atom in the structure refinement. The peak function used for fitting the experimental data was the Thompson–Cox–Hastings Pseudo–Voigt;[29] a 36 coefficients Chebyshev polynomial was used to model the background. On the final Rietveld fit, there were 90 different adjustable parameters (scale factor, zero shift, unit-cell parameters, peak-shape parameters, atomic coordinates and temperature factors). In Figure 4.2, the plot of the final Rietveld fit for EHU-30 compound is given. Table 4.2 reports crystallographic and refinement-related data, while atomic coordinates for non-H atoms are reported in Table 4.3. The crystallographic data of EHU-30 was deposited on the Cambridge Crystallographic Data Centre (CCDC) with the code 1894173.

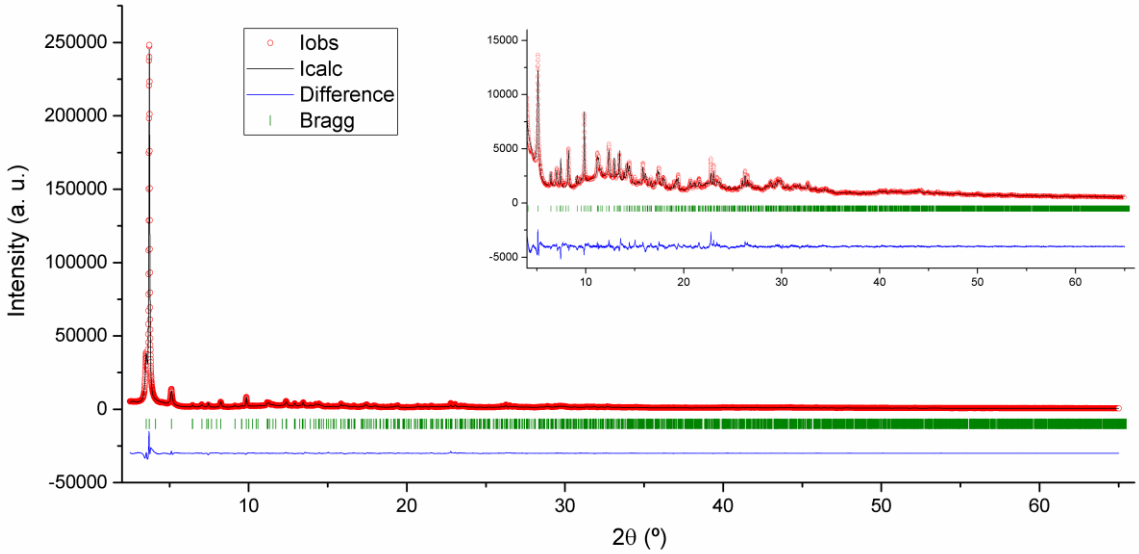

Figure 4.2. Final Rietveld refinement plot for EHU-30, showing the experimental (red circles), calculated (black line), and difference profiles (blue line); green tick marks indicate reflection positions. The inset shows a magnification of the peaks after the most intense one.

Table 4.2. Crystallographic data and Rietveld refinement summary for EHU-30.

Compound	**EHU-30**
Formula	$[Zr_6(C_8H_4O_4)_6(O)_4(OH)_4]_n$

Formula weight (g/mol)	1664.06
D_c (g/cm^3)	1.105
Crystal system	Hexagonal
Space group	$P6_3/mmc$
***a* (Å)**	14.6690(4)
***c* (Å)**	26.8478(19)
***V* (Å^3)**	5003.1(5)
Z	2
Radiation type	Synchrotron
Diffractometer	I11 Beamline, Diamond Light Source
Data collection mode	Transmission
Wavelength (Å)	0.82448
***R_p* (%)**	5.13
***R_{wp}* (%)**	7.00
***R_{exp}* (%)**	1.68
***R_B* (%)**	3.41
Goodness-of-fit	4.17

Table 4.3. Fractional atomic coordinates and isotropic displacement parameter (Å^2) of non-H atoms for EHU-30.

Atom	*x*	*y*	*z*	B_{iso}
Zr1	0.8400(3)	-0.08001(14)	0.05458(16)	1.29(7)
O1	0.8321(14)	-0.0840(7)	-0.0274(8)	0.5(4)
O2	1	0	0.0866(16)	0.5(4)
C1	0.5282(7)	-0.0392(12)	0.0414(9)	7.2(4)
C2	0.597(3)	0	0	7.2(4)
C3	0.699(3)	0	0	7.2(4)
O3	0.723(3)	-0.0350(12)	0.0371(10)	7.2(4)
C4	0.812(15)	-0.21(3)	0.2245(10)	7.2(4)
C5	0.8935(17)	-0.213(3)	0.199(2)	7.2(4)
C6	0.9019(17)	-0.196(3)	0.1454(19)	7.2(4)
O4	0.84(2)	-0.17(3)	0.124(4)	7.2(4)

Crystal structure elucidation of EHU-30-NH_2 samples. Crystal structures of both EHU-30-NH_2(Zr) and EHU-30-NH_2(Hf) were refined using Topas Academic v6 program.[25] The crystal structure of EHU-30(Zr) was taken as starting point, where an amino group was introduced, replacing one of the BDC hydrogen atoms.

Final Rietveld refinements of EHU-30-NH_2(Zr) and EHU-30-NH_2(Hf) crystal structures were carried out in the 2θ ranges 5-70° and 5-78° (up to about 1.34 and 1.22 Å in *d*-spacing), respectively, and atomic coordinates of all atoms were included. For each refinement, an isotropic atomic displacement parameter was applied for the metal atom, while an overall parameter was introduced for the light atoms (excluding the N atom). On the final fits, there were 90 and 83 different adjustable parameters, respectively (scale factor, zero shift, background, unit-cell parameters, peak-shape

parameters, atomic coordinates, and temperature factors). Figures 4.3 and 4.4 show the final Rietveld fits for EHU-30-NH_2(Zr) and EHU-30-NH_2(Hf), respectively. Table 4.4 summarizes the corresponding crystallographic and refinement-related data, while final atomic coordinates obtained for non-H atoms are reported in Tables 4.5 and 4.6. The crystallographic data of these structures was deposited with CCDC numbers 2097728 and 2097729 for EHU-30-NH_2(Zr) and EHU-30-NH_2(Hf), respectively.

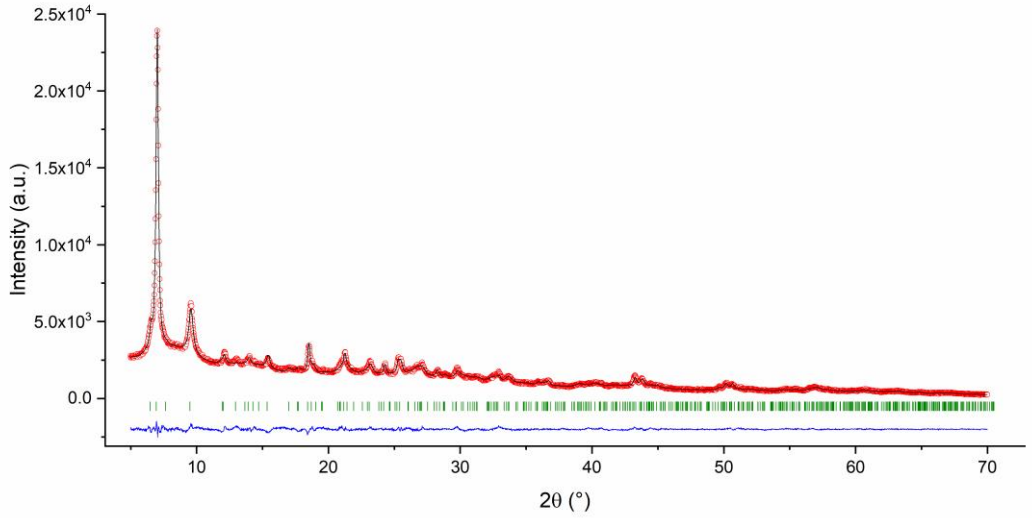

Figure 4.3. Final Rietveld refinement plot for EHU-30-NH_2(Zr), showing the experimental (red circles), calculated (black line), and difference profiles (blue line); green tick marks indicate reflection positions.

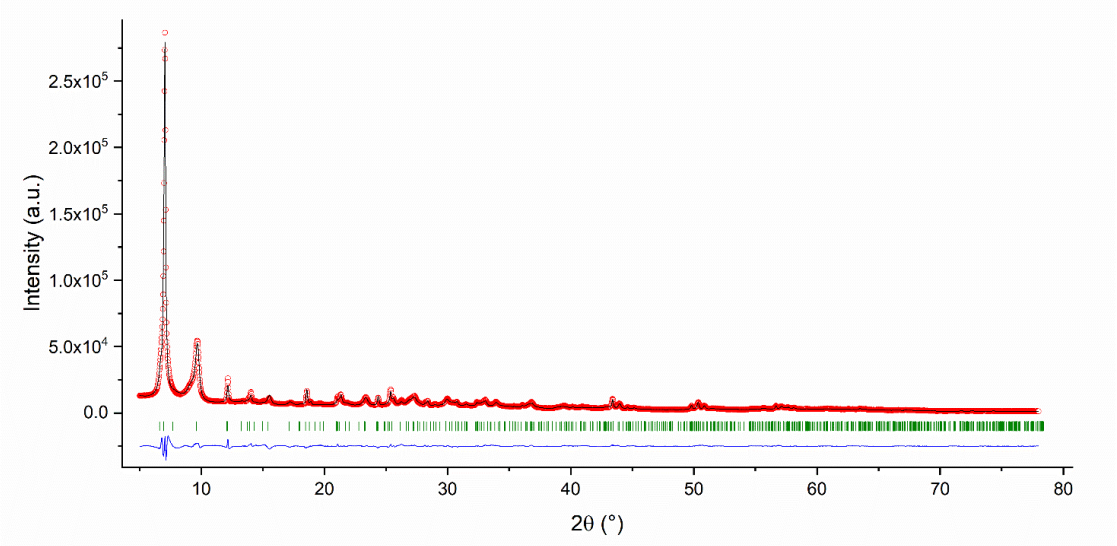

Figure 4.4. Final Rietveld refinement plot for EHU-30-NH_2(Hf), showing the experimental (red circles), calculated (black line), and difference profiles (blue line); green tick marks indicate reflection positions.

Table 4.4. Crystallographic data and Rietveld refinement summary for EHU-30-NH_2(Zr) and EHU-30-NH_2(Hf).

Compound	EHU-30-NH_2(Zr)	EHU-30-NH_2(Hf)
Formula	$[Zr_6(C_8H_5NO_4)_6(O)_4(OH)_4]$	$[Hf_6(C_8H_5NO_4)_6(O)_4(OH)_4]$
Formula weight (g/mol)	1750.1	2273.72
D_c (g/cm^3)	1.136	1.516
Crystal system	Hexagonal	Hexagonal
Space group	$P6_3/mmc$	$P6_3/mmc$
***a* (Å)**	14.7044(12)	14.6647(5)
***c* (Å)**	27.320(7)	26.744(7)
***V* (Å^3)**	5115.7(15)	4980.8(14)
Z	2	2
Radiation type	X-ray tube, Cu Kα_1	X-ray tube, Cu Kα_1
Diffractometer	Bruker D8 Advance	Bruker D8 Advance
Data collection mode	Reflection	Reflection
Wavelength (Å)	1.540596	1.540596
***R_p* (%)**	2.99	4.52
***R_{wp}* (%)**	3.92	5.94
***R_{exp}* (%)**	2.60	1.21
***R_B* (%)**	0.97	1.76
Goodness-of-fit	1.51	4.90

Table 4.5. Fractional atomic coordinates and isotropic displacement parameter (Å^2) of non-H atoms for EHU-30-NH_2(Zr).

Atom	*x*	*y*	*z*	B_{iso}	Occupancy
Zr1	0.8336(6)	-0.0832(3)	0.0505(5)	0.5(2)	1
O1	0.820(4)	-0.0901(18)	-0.032(4)	6.4(8)	1
O2	1	0	0.066(6)	6.4(8)	1
C1_1	0.515(3)	-0.063(5)	0.034(2)	6.4(8)	1
C3_1	0.5948(13)	0	0	6.4(8)	1
C4_1	0.696(3)	0	0	6.4(8)	1
O5_1	0.707(7)	-0.060(8)	0.033(2)	6.4(8)	1
N1_1	0.530(5)	-0.127(8)	0.070(3)	7.7(9)	0.25
C1_2	0.815(4)	-0.205(3)	0.2243(13)	6.4(8)	1
C3_2	0.898(3)	-0.205(6)	0.19857261(9)	6.4(8)	1
C4_2	0.907(6)	-0.186(12)	0.1461(3)	6.4(8)	1
O5_2	0.851(9)	-0.159(9)	0.123(4)	6.4(8)	1
N1_2	0.739(5)	-0.187(6)	0.1984(19)	7.7(9)	0.25

Table 4.6. Fractional atomic coordinates and isotropic displacement parameter (Å^2) of non-H atoms for EHU-30-NH_2(Hf).

Atom	*x*	*y*	*z*	B_{iso}	Occupancy
Hf1	0.8380(5)	-0.0810(2)	0.0551(5)	1.89(19)	1
O1	0.858(6)	-0.071(3)	-0.023(6)	8.1(11)	1
O2	1	0	0.071(9)	8.1(11)	1
C1_1	0.523(3)	-0.050(4)	0.039(2)	8.1(11)	1
C3_1	0.5958(14)	0	0	8.1(11)	1
C4_1	0.698(3)	0	0	8.1(11)	1
O5_1	0.717(8)	-0.046(9)	0.035(3)	8.1(11)	1
N1_1	0.546(5)	-0.102(8)	0.079(3)	9.7(13)	0.25
C1_2	0.816(4)	-0.201(3)	0.2237(16)	8.1(11)	1
C3_2	0.899(4)	-0.201(8)	0.197464259(6)	8.1(11)	1
C4_2	0.909(8)	-0.182(16)	0.1439(4)	8.1(11)	1
O5_2	0.853(11)	-0.156(11)	0.120(5)	8.1(11)	1
N1_2	0.740(6)	-0.184(6)	0.197(2)	9.7(13)	0.25

Location of water molecules by time-of-flight (TOF) neutron powder diffraction. TOF neutron powder diffraction measurements of polycrystalline EHU-30(Zr), D_2O@EHU-30(Zr), EHU-30-NH_2(Zr), and D_2O@EHU-30-NH_2(Zr) for understanding the mechanism and the nature of the host-guest interactions that determine the water adsorption were performed on GEM instrument of ISIS Neutron and Muon Source. Prior to measurements all the samples were conditioned by an outgassing procedure at 120 °C for 12 h and, after cooling down, they were immersed in deuterated water, which was lengthen for 3 days with fresh D_2O exchanges every 24 for obtaining D_2O@samples.

Crystal structures of all four samples were refined using Topas Academic v6 program.[25] For the case of water loaded samples, the preferred adsorption sites for D_2O molecules were revealed by means of subsequent difference Fourier map calculations and Rietveld refinements where the framework atomic positions were kept fixed. The final Rietveld refinements included the atomic coordinates of all atoms and GEM detectors banks 1 to 4, simultaneously. For each refinement, an isotropic atomic displacement parameter was applied for the metal atom, while an overall parameter was introduced for the light atoms, and H/D occupancies were refined for the hydrogen crystallographic sites on the frameworks. On the final fits, there were 93, 127, 95 and 111 different adjustable parameters, respectively (scale factor, background, unit-cell parameters, peak-shape parameters, atomic coordinates, and temperature factors). Figures 4.5 to 4.8 show the final Rietveld fits for EHU-30(Zr), D_2O@EHU-30(Zr), EHU-30-NH_2(Zr), and D_2O@EHU-30-NH_2(Zr), respectively. Table 4.7 summarises the corresponding crystallographic and refinement-related data, while obtained final atomic coordinates are reported in Tables 4.8 to 4.11.

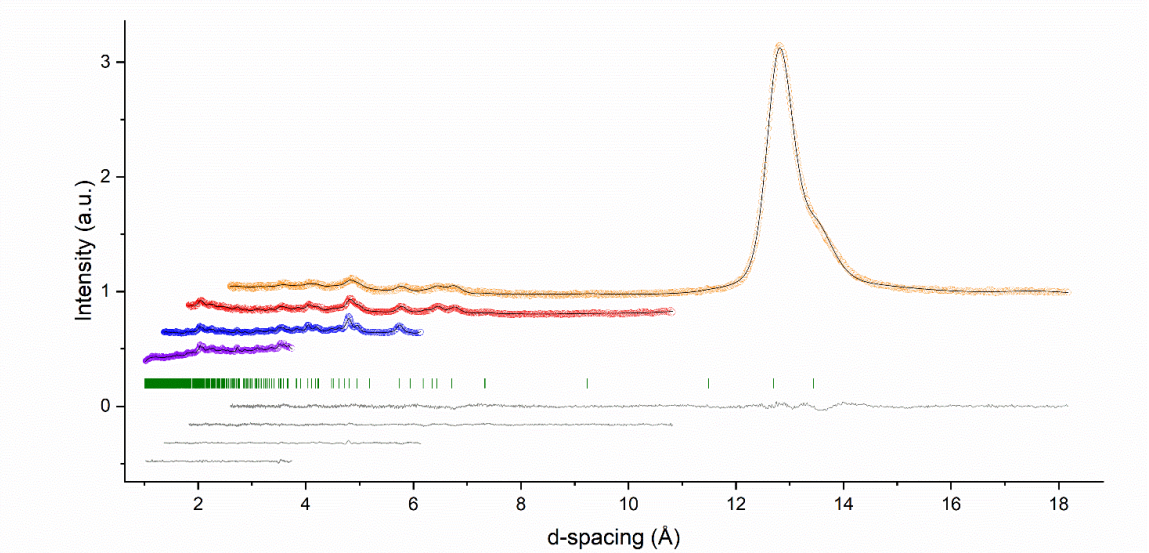

Figure 4.5. Final Rietveld refinement plot for EHU-30(Zr), showing the experimental (open circles) profiles for banks 1, 2, 3 and 4 (orange, red, blue and violet, respectively). Calculated and difference profiles are shown as black and grey lines, respectively, while green tick marks indicate reflection positions.

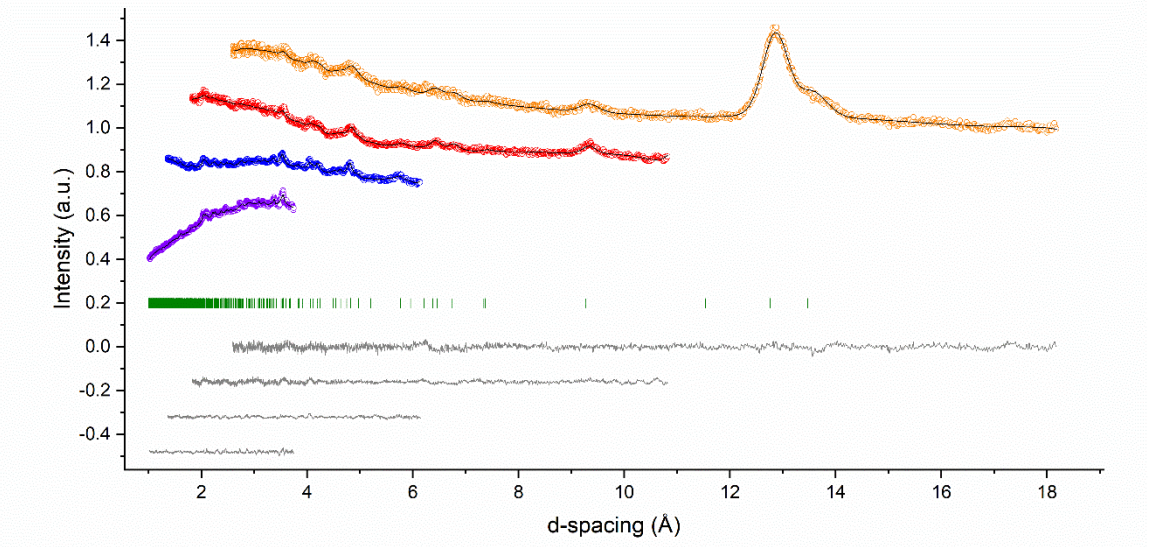

Figure 4.6. Final Rietveld refinement plot for D_2O@EHU-30(Zr), showing the experimental (open circles) profiles for banks 1, 2, 3 and 4 (orange, red, blue and violet, respectively). Calculated and difference profiles are shown as black and grey lines, respectively, while green tick marks indicate reflection positions.

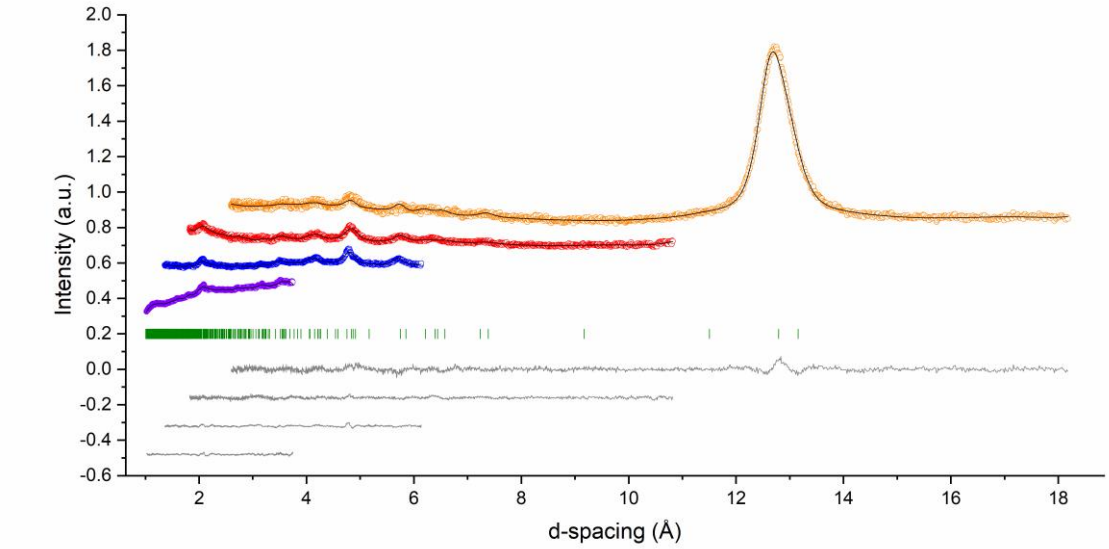

Figure 4.7. Final Rietveld refinement plot for EHU-30-NH_2(Zr), showing the experimental (open circles) profiles for banks 1, 2, 3 and 4 (orange, red, blue and violet, respectively). Calculated and difference profiles are shown as black and grey lines, respectively, while green tick marks indicate reflection positions.

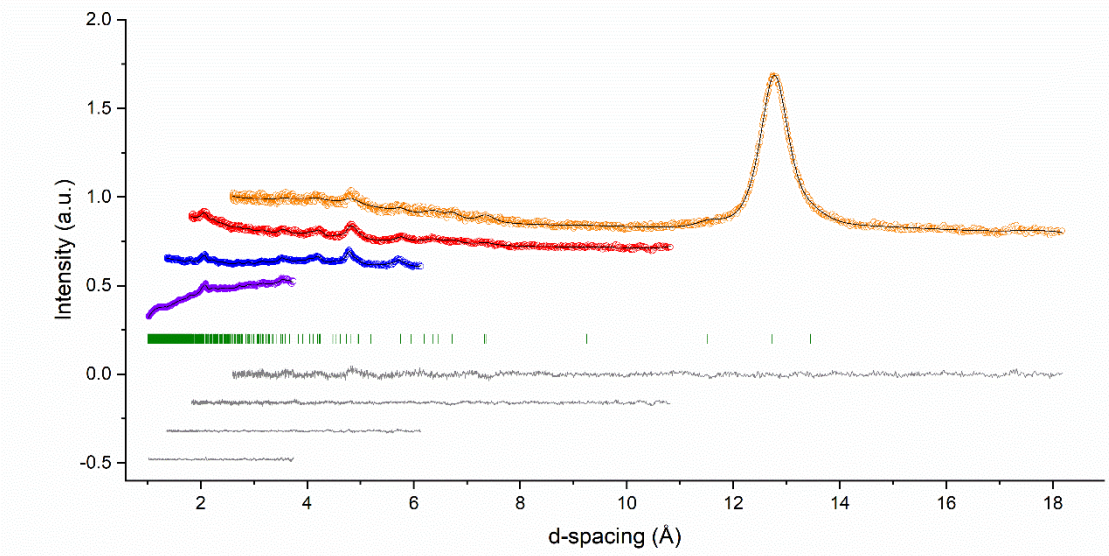

Figure 4.8. Final Rietveld refinement plot for D_2O@EHU-30-NH_2(Zr), showing the experimental (open circles) profiles for banks 1, 2, 3 and 4 (orange, red, blue and violet, respectively). Calculated and difference profiles are shown as black and grey lines, respectively, while green tick marks indicate reflection positions.

Table 4.7. Crystallographic data and Rietveld refinement summary for EHU-30(Zr), D_2O@EHU-30(Zr), EHU-30-NH_2(Zr) and D_2O@EHU-30-NH_2(Zr).

Compound	EHU-30(Zr)	D_2O@EHU-30(Zr)	EHU-30-NH_2(Zr)	D_2O@ EHU-30-NH_2(Zr)
Formula	$Zr_6(C_8H_3D_1O_4)_6O_8$	$Zr_6(C_8H_{0.54}D_{3.46}O_4)_6O_8 \cdot (D_2O)_{7.98}$	$Zr_6(C_8H_{4.18}D_{0.82}NO_4)_6O_8$	$Zr_6(C_8H_{1.28}D_{3.72}O_4)_6O_8 \cdot (D_2O)_{6.94}$
Formula weight (g/mol)	1664.979	1840.737	1765.434	1911.485
D_c (g/cm³)	1.10069	1.18231	1.16906	1.23250
Crystal system	Hexagonal	Hexagonal	Hexagonal	Hexagonal
Space group	$P6_3/mmc$	$P6_3/mmc$	$P6_3/mmc$	$P6_3/mmc$
a (Å)	14.669(4)	14.733(10)	14.772(14)	14.706(11)
c (Å)	26.879(8)	26.949(17)	26.31(3)	26.88(2)
V (Å³)	5009(3)	5066(7)	4972(11)	5034(9)
Z	2	2	2	2
Radiation type	Neutrons	Neutrons	Neutrons	Neutrons
Diffractometer	GEM, ISIS Facility	GEM, ISIS Facility	GEM, ISIS Facility	GEM, ISIS Facility
Data collection mode	Time-of-flight	Time-of-flight	Time-of-flight	Time-of-flight
R_p (%)	0.88	0.49	0.75	0.52
R_{wp} (%)	0.85	0.45	0.67	0.41
R_{exp} (%)	0.50	0.35	0.50	0.04
R_B (%)	0.23	0.18	0.48	0.07
Goodness-of-fit	1.70	1.29	1.34	1.03

Table 4.8. Fractional atomic coordinates and isotropic displacement parameter (Å²) of non-H atoms for EHU-30(Zr).

Atom	x	y	z	B_{iso}	Occupancy
Zr1	0.8386(13)	-0.0807(7)	0.0476(5)	7.2(6)	1
O1	0.8241(9)	-0.0880(4)	-0.0319(4)	0.5(4)	1
O2	1	0	0.0738(9)	0.5(4)	1
C1_1	0.5112(3)	-0.07200(19)	0.02999261	12.2(5)	1
H1_1	0.5199(5)	-0.1279(3)	0.0532609	14.6(6)	0.984(10)
D1_1	0.5199(5)	-0.1279(3)	0.0532609	14.6(6)	0.016(10)
C3_1b	0.59584(18)	0	0	12.2(5)	1
C4_1b	0.6782(3)	0	0	12.2(5)	1
O5_1	0.6924(13)	-0.0608(10)	0.02730(19)	12.2(5)	1
C1_2	0.8079(11)	-0.221(2)	0.22431(15)	12.2(5)	1
H1_2	0.7507(18)	-0.208(3)	0.2045(3)	14.6(6)	0.516(10)
D1_2	0.7507(18)	-0.208(3)	0.2045(3)	14.6(6)	0.484(10)
C3_2b	0.8893(10)	-0.221(2)	0.198598(3)	12.2(5)	1
C4_2b	0.8986(14)	-0.203(3)	0.14461(6)	12.2(5)	1
O5_2	0.843(2)	-0.176(3)	0.1208(7)	12.2(5)	1

Table 4.9. Fractional atomic coordinates and isotropic displacement parameter (Å^2) of non-H atoms for D_2O@EHU-30(Zr).

Atom	*x*	*y*	*z*	B_{iso}	Occupancy
Zr1	0.839(3)	-0.0805(17)	0.0516(15)	4.8(9)	1
O1	0.837(2)	-0.0813(11)	-0.0282(13)	0.5(8)	1
O2	1	0	0.075(3)	0.5(8)	1
C1_1	0.5318(6)	-0.0315(12)	0.0427(2)	5.0(5)	1
H1_1	0.5564(11)	-0.056(2)	0.0758(4)	6.0(6)	0.24(2)
D1_1	0.5564(11)	-0.056(2)	0.0758(4)	6.0(6)	0.76(2)
C3_1b	0.5953(5)	0	0	5.0(5)	1
C4_1b	0.6937(10)	0	0	5.0(5)	1
O5_1	0.720(2)	-0.029(2)	0.0389(5)	5.0(5)	1
C1_2	0.819(2)	-0.199(4)	0.2243(3)	5.0(5)	1
H1_2	0.762(3)	-0.186(6)	0.2046(5)	6.0(6)	0.03(2)
D1_2	0.762(3)	-0.186(6)	0.2046(5)	6.0(6)	0.97(2)
C3_2b	0.900(2)	-0.199(4)	0.198606(7)	5.0(5)	1
C4_2b	0.910(3)	-0.181(6)	0.14540(14)	5.0(5)	1
O5_2	0.852(4)	-0.155(5)	0.1248(14)	5.0(5)	1
O1_w1	0.212(3)	0.788(3)	0.491(3)	1.0(19)	0.46(2)
D1_w1	0.243(13)	0.847(7)	0.469(5)	1.0(19)	0.231(12)
D2_w1	0.137(4)	0.750(12)	0.488(7)	1.0(19)	0.231(12)
O1_w2	-0.022(6)	0.489(3)	0.849(2)	1.0(13)	0.57(3)
D1_w2	-0.01(5)	0.554(18)	0.862(11)	1.0(13)	0.286(14)
D2_w2	0.013(11)	0.50(2)	0.817(3)	1.0(13)	0.286(14)
O1_w3	⅔	⅓	0.0568(19)	1(2)	0.30(2)
D1_w3	0.61(5)	0.29(3)	0.08(2)	1(2)	0.101(7)
D2_w3	0.72(3)	0.396(16)	0.075(17)	1(2)	0.101(7)

Table 4.10. Fractional atomic coordinates and isotropic displacement parameter (Å^2) of non-H atoms for EHU-30-NH_2(Zr).

Atom	*x*	*y*	*z*	B_{iso}	Occupancy
Zr1	0.840(4)	-0.0799(18)	0.050(2)	15(2)	1
O1	0.8312(17)	-0.0844(9)	-0.0313(16)	0.5(7)	1
O2	1	0	0.0755(17)	0.5(7)	1
C1_1	0.5411(13)	-0.013(3)	0.04587(17)	15.4(12)	1
H1_1	0.573(2)	-0.023(5)	0.0815(3)	18.4(14)	0.75(4)
D1_1	0.573(2)	-0.023(5)	0.0815(3)	18.4(14)	0.00(4)
N1_1	0.582(5)	-0.025(5)	0.091(4)	18.4(14)	0.25
H5_1a	0.540(5)	-0.035(8)	0.127(4)	18.4(14)	0.16(3)
H5_1b	0.655(5)	-0.025(6)	0.091(4)	18.4(14)	0.16(3)
D5_1a	0.540(5)	-0.035(8)	0.127(4)	18.4(14)	0.09(3)
D5_1b	0.655(5)	-0.025(6)	0.091(4)	18.4(14)	0.09(3)
C3_1b	0.5951(7)	0	0	15.4(12)	1
C4_1b	0.6838(14)	0	0	15.4(12)	1
O5_1	0.724(3)	-0.011(4)	0.0396(7)	15.4(12)	1
C1_2	0.796(3)	-0.247(5)	0.2237(4)	15.4(12)	1
H1_2	0.739(4)	-0.234(7)	0.2035(7)	18.4(14)	0.75(7)
D1_2	0.739(4)	-0.234(7)	0.2035(7)	18.4(14)	0.00(7)

N1_2	0.722(12)	-0.230(8)	0.198(4)	18.4(14)	0.25
H5_2a	0.729(12)	-0.217(8)	0.157(4)	18.4(14)	0.13(4)
H5_2b	0.658(13)	-0.230(10)	0.218(4)	18.4(14)	0.13(4)
D5_2a	0.729(12)	-0.217(8)	0.157(4)	18.4(14)	0.12(4)
D5_2b	0.658(13)	-0.230(10)	0.218(4)	18.4(14)	0.12(4)
C3_2b	0.877(3)	-0.247(5)	0.197358(11)	15.4(12)	1
C4_2b	0.886(4)	-0.228(8)	0.1421(2)	15.4(12)	1
O5_2	0.832(5)	-0.201(8)	0.118(2)	15.4(12)	1

Table 4.11. Fractional atomic coordinates and isotropic displacement parameter (Å^2) of non-H atoms for D_2O@EHU-30-NH_2(Zr).

Atom	*x*	*y*	*z*	B_{iso}	Occupancy
Zr1	0.842(2)	-0.0790(12)	0.0420(14)	11.0(13)	1
O1	0.8138(13)	-0.0931(7)	-0.0308(9)	1.0(5)	1
O2	1	0	0.0741(14)	1.0(5)	1
C1_1	0.5316(10)	-0.0321(17)	0.0427(3)	23.6(11)	1
H1_1	0.5561(17)	-0.057(3)	0.0758(6)	28.3(13)	0.00(4)
D1_1	0.5561(17)	-0.057(3)	0.0758(6)	28.3(13)	0.75(4)
N1_1	0.563(5)	-0.064(6)	0.085(6)	28.3(13)	0.25
H5_1a	0.513(5)	-0.089(7)	0.118(6)	28.3(13)	0.15(3)
H5_1b	0.637(5)	-0.064(6)	0.085(6)	28.3(13)	0.15(3)
D5_1a	0.513(5)	-0.089(7)	0.118(6)	28.3(13)	0.10(3)
D5_1b	0.637(5)	-0.064(6)	0.085(6)	28.3(13)	0.10(3)
C3_1	0.5955(11)	0	0	23.6(11)	1
C4_1	0.689(2)	0	0	23.6(11)	1
O5_1	0.716(4)	-0.029(4)	0.0388(7)	23.6(11)	1
C1_2	0.803(2)	-0.228(4)	0.2239(4)	23.6(11)	1
H1_2	0.746(3)	-0.215(6)	0.2041(6)	28.3(13)	0.24(6)
D1_2	0.746(3)	-0.215(6)	0.2041(6)	28.3(13)	0.51(6)
N1_2	0.730(9)	-0.211(6)	0.198(3)	28.3(13)	0.25
H5_2a	0.737(9)	-0.198(7)	0.158(3)	28.3(13)	0.05(3)
H5_2b	0.665(9)	-0.211(8)	0.219(3)	28.3(13)	0.05(3)
D5_2a	0.737(9)	-0.198(7)	0.158(3)	28.3(13)	0.20(3)
D5_2b	0.665(9)	-0.211(8)	0.219(3)	28.3(13)	0.20(3)
C3_2	0.886(2)	-0.228(5)	0.197723(8)	23.6(11)	1
C4_2	0.896(3)	-0.209(7)	0.14364(16)	23.6(11)	1
O5_2	0.841(5)	-0.182(6)	0.1202(18)	23.6(11)	1
O1_w1	0.31(3)	0.707(19)	0.313(4)	9(3)	0.191(8)
D1_w1	0.29(4)	0.74(4)	0.288(5)	9(3)	0.191(8)
D2_w1	0.32(4)	0.74(3)	0.345(6)	9(3)	0.191(8)
O1_w2	0.940(4)	0.547(4)	0.2192(14)	5.0(11)	0.387(12)
D1_w2	0.966(17)	0.512(15)	0.1976(18)	5.0(11)	0.387(12)
D2_w2	0.948(8)	0.532(9)	0.2536(15)	5.0(11)	0.387(12)

4.2.1.3. Chemical and thermal characterization

Herein details about the chemical and thermal characterization performed on EHU-30, EHU-30-NH_2(Zr), EHU-30-NH_2(Hf), EHU-30-NHR(Zr) and EHU-30-NHR(Hf) are presented.

Proton nuclear magnetic resonance spectroscopy (^{1}H-NMR). To proceed with the ^{1}H-NMR spectrum (500 MHz), 70 mg of each sample were digested in 2 mL of a 1 M NaOH solution (in deuterated water, D_2O). The digestion was prolonged for 24 h, after which the solid residue corresponding to ZrO_2 or HfO_2 was filtered off and the NMR spectrum was taken on the liquid fraction. Figure 4.9 depicts spectrum for EHU-30, Figure 4.10 for EHU-30-NH_2(Zr) and EHU-30-NH_2(Hf) and Figure 4.11 for EHU-30-NHR(Zr) and EHU-30-NHR(Hf) with the label assignation of organic compounds present in each case. The residual signal of the solvent appears at 4.79 ppm in the five spectra. The rest of signals observed in each case are explained below.

In Figure 4.9 the singlet at 7.84 ppm is due to the aromatic signals of benzene-1,4-dicarboxylic acid. Extending the area around 5.0 ppm, the two characteristic singlets of the olefinic protons of methacrylic acid (5.61 and 5.30 ppm) are found, while methyl group appears at 1.84 ppm. The integration of the respective signals shows that the amount of methacrylic acid after the digestion of EHU-30 MOF is of a 4% relative to all carboxylic ligands (benzene-1,4-dicarboxylic acid plus methacrylic acid).

In Figure 4.10 the three signals with different multiplicity at around 7 ppm due to the aromatic protons of 2-aminobenzene-1,4-dicarboxylic acid are observed. Two additional signals (a multiplet at ~2 ppm that integrates to one proton and a doublet at ~1 ppm that integrates to six protons) are observed because of the presence of a small amount of isobutyric acid, the modulator used in these synthesis. The integration of the respective signals shows that the amount of isobutyric acid after the digestion of the MOFs is of a 9% relative to all carboxylic ligands (modulator plus 2-aminobenzene-1,4-dicarboxylic acid) in EHU-30-NH_2(Zr) and of a 12% in EHU-30-NH_2(Hf).

In Figure 4.11 six signals with different multiplicity at around 7 ppm due to the aromatic protons of 2-aminobenzene-1,4-dicarboxylic acid and to 2-((2-carboxypropyl)amino)benzene-1,4-dicarboxylic acid (coming from an Aza-Michael reaction between organic linker and methacrylic acid, that is further explained in Results and discussion section) are observed. The integration relation between them says that the 35% in Zr-based MOF and the 42% in Hf-based MOF of the total coordination positions occupied by a dicarboxylic ligand correspond to 2-((2-carboxypropyl)amino)benzene-1,4-dicarboxylic acid. Its presence is corroborated by

the signals (three multiplets and one singlet marked in pink) observed in the 1-4 ppm range that fit fairly well with the expected positions and with the integration respect to the aromatic signals of this species in both spectra. Three additional signals (two multiplets at ~5 ppm that integrates to one proton and a doublet at ~1 ppm that integrates to six protons) are also observed because of the presence of a small amount of methacrylic acid in both digested samples. The integration of the respective signals shows that the amount of methacrylic acid after the digestion of the MOF is of a 8% relative to all carboxylic ligands (modulator plus 2-aminobenzene-1,4-dicarboxylic acid and 2-((2-carboxypropyl)amino)benzene-1,4-dicarboxylic acid) in EHU-30-NHR(Zr) and of a 11% in EHU-30-NHR(Hf). Signals marked in green in the spectrum of Zr-based MOF digestion correspond to 1-propanol, which comes from zirconium reagent.

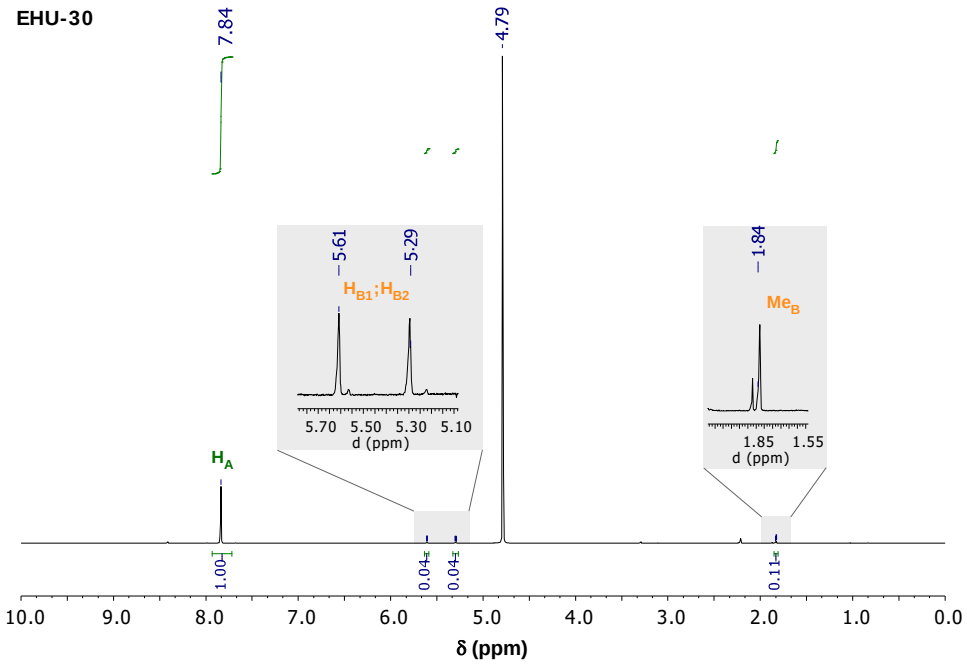

(a)

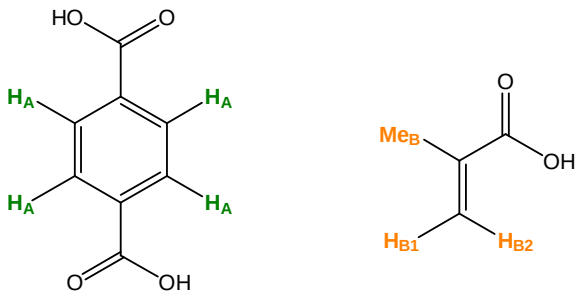

(b)

Figure 4.9. (a) ^{1}H-NMR spectrum of digested EHU-30 and (b) label assignation of organic compounds: benzene-1,4-dicarboxylic acid in green and methacrylic acid in orange.

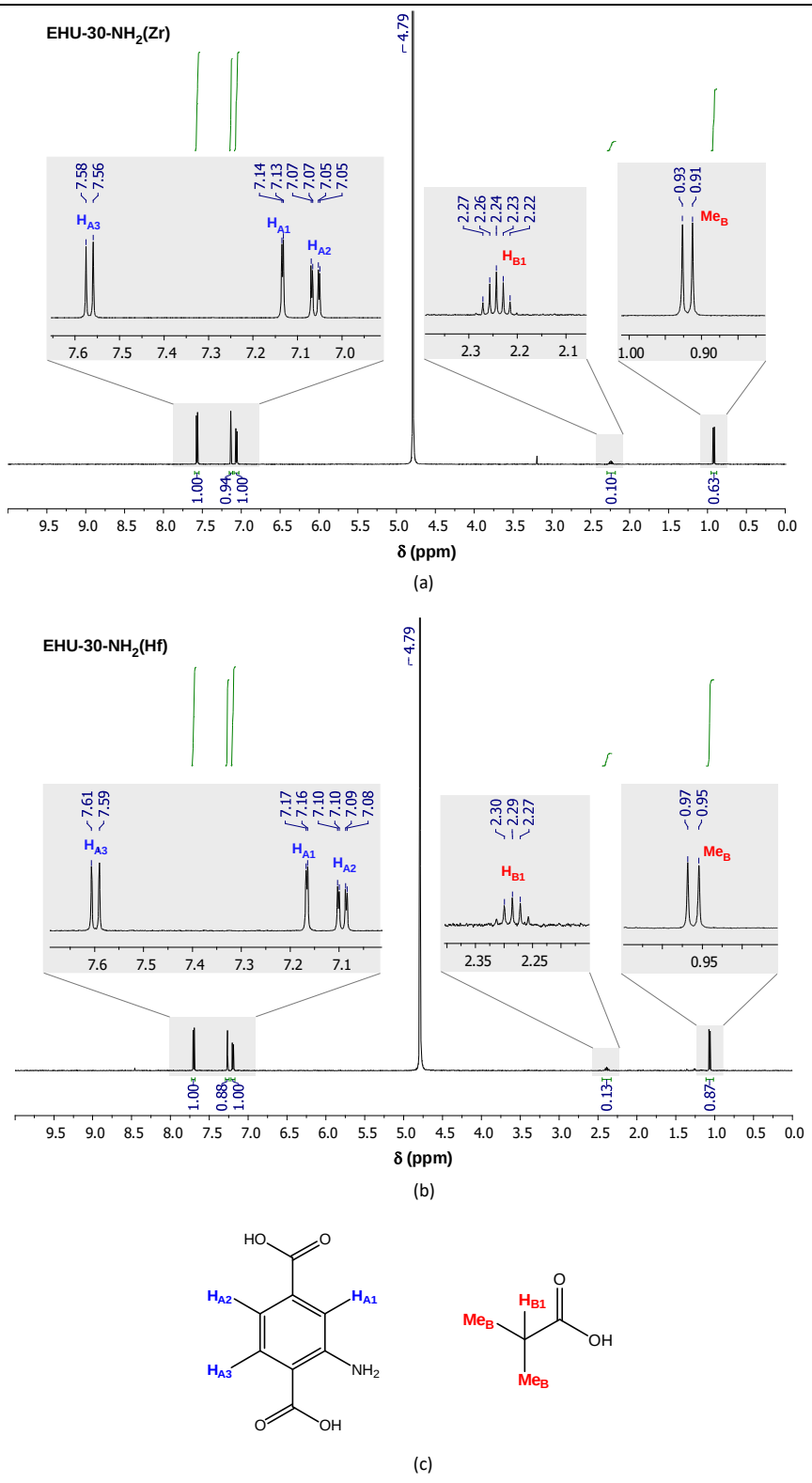

Figure 4.10. ^{1}H-NMR spectrum of digested (a) EHU-30-NH_2(Zr) and (b) EHU-30-NH_2(Hf). (c) Label assignation of organic compounds: 2-aminobenzene-1,4-dicarboxylic acid in blue and isobutyric acid in red.

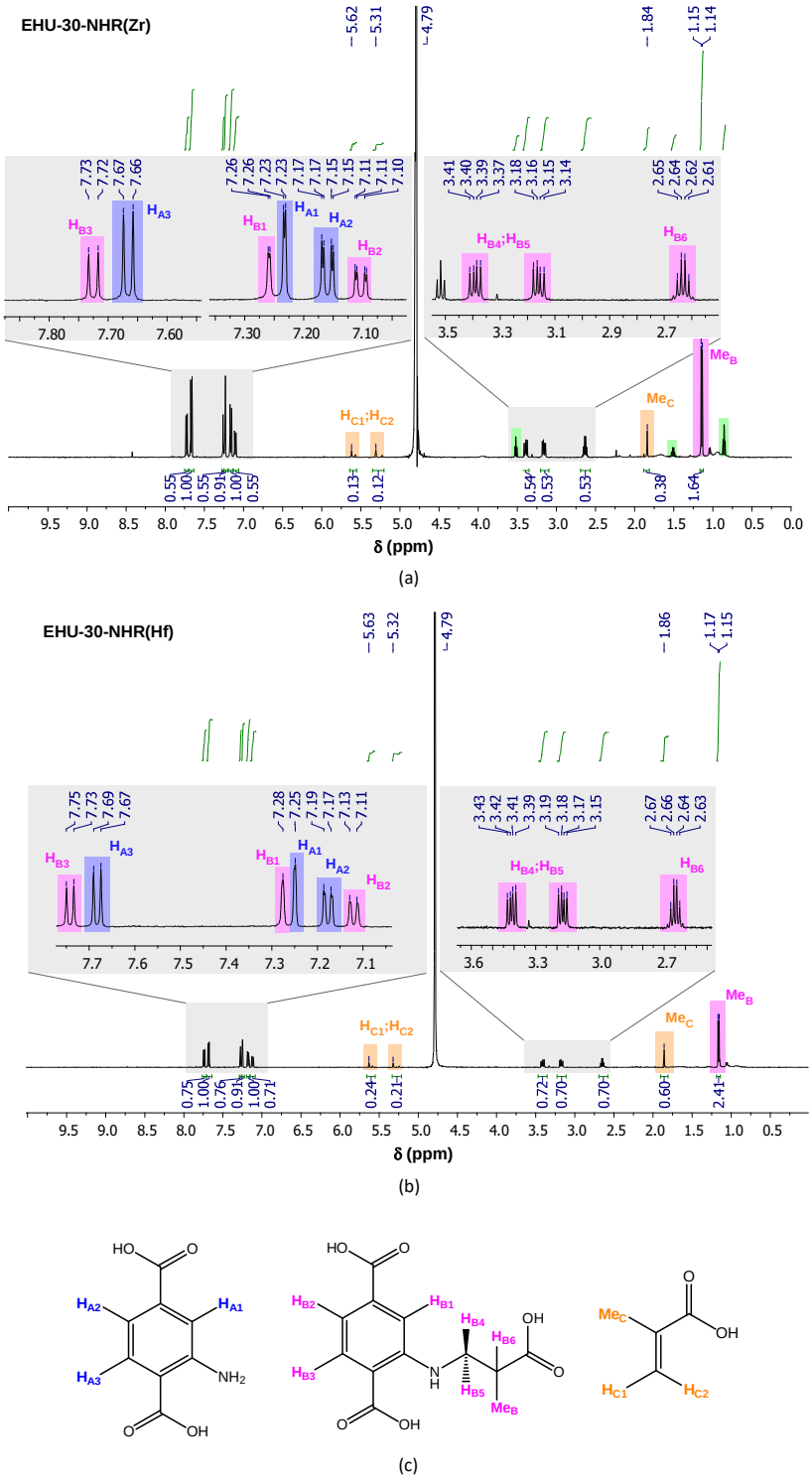

Figure 4.11. ^{1}H-NMR spectrum of digested (a) EHU-30-NHR(Zr) and (b) EHU-30-NHR(Hf). (c) Label assignation of organic compounds: 2-aminobenzene-1,4-dicarboxylic acid in blue, 2-((2-carboxypropyl)amino)benzene-1,4-dicarboxylic acid in pink and methacrylic acid in orange.

Fourier-transform infrared spectroscopy (ATR-FTIR). The infrared spectra taken on KBr pellets of the five synthesised MOFs and the assignation of the main vibrational bands are gathered in Figure 4.12. All of them are coincident with differences in intensity, except for characteristic bands of $–NH_2$ group that are only observed for EHU-30-NH_2 and EHU-30-NHR samples. The large O-H peaks in the IR spectrum is indicative of H_2O/OH^- pair replacing missing linkers in the structure (see further details in the Results and discussion section).

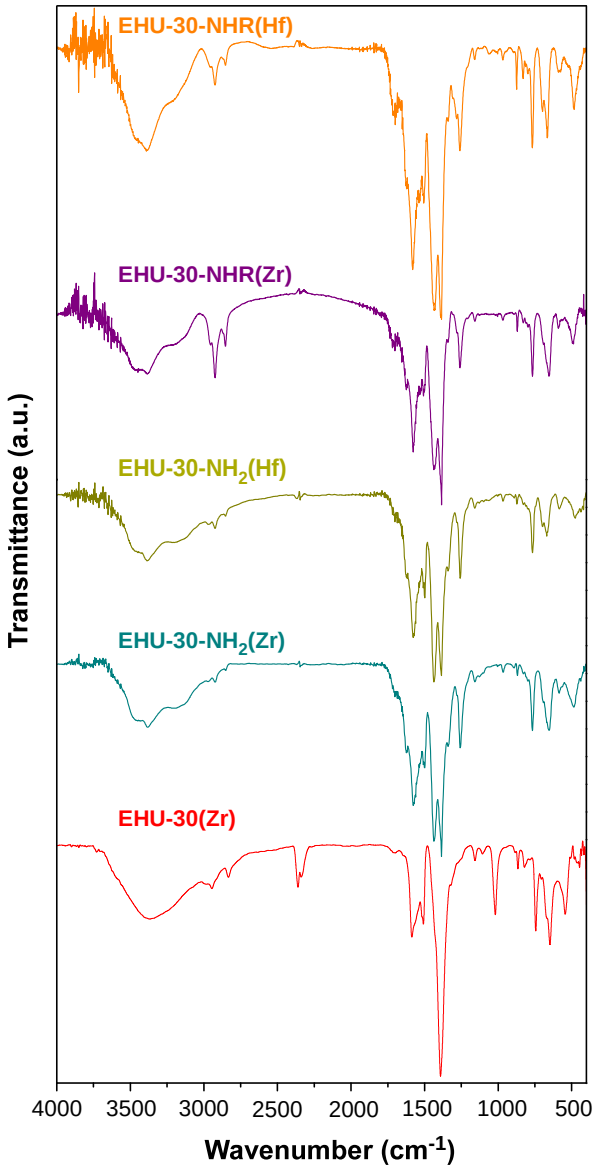

(a)

$\bar{\nu}$ (cm^{-1})	
3470, m	ν_{asym} (NH_2)
3380, m	ν_{sym} (NH_2)
3100-3500, m	ν (O–H)
3000 - 2850, w-m	ν (C–H)
1700, w	ν_{as} (COO)
1620, m	δ_{ip} (NH_2)
1575, s	ν (C_{ar}–C)
1500, m	ν_{ring} (C_{ar}–C_{ar})
1430, s	ν_s (COO) + ν (C-C)$_{ar}$
1385, s	ν (C_{ar}-N)
1336, sh	δ_{ip} (NH_2)
1255, m	δ_{oop}(NH_2)
1016, m	δ_{ip} (C-H)
760, s	δ_{oop} (C-H) + δ_{oop} (O-C-O)
650, m	ν (M–O_{oxide})
540, m	ν (M–$O_{carboxylato}$)
483, m	ν (M–$O_{hydroxide}$)

(b)

Figure 4.12. (a) FTIR spectra and (b) band assignments for EHU-30, EHU-30-NH_2 (Zr and Hf) and EHU-30-NHR (Zr and Hf) (s: strong, m: medium, w: weak and sh: shoulder signals; *sym*: symmetric, *asym*: asymmetric, *ip*: in plane, *ring*: ring stretching, *ar*: aromatic, *oop*: out of plane of stretching (ν) or bending (δ) modes).

Thermogravimetric analysis (TGA). Thermogravimetric analysis shows similar behaviour to that found for other zirconium- and hafnium-based MOFs. In all of thermograms (Figure 4.13), two main weight losses with differences in the temperature range can be observed. First, solvent and water molecules are released (30 – 100 °C). Thereafter, at 300 – 440 °C range for amino-functionalized samples and at 450-500 °C for EHU-30, the framework decomposition takes place. It is noteworthy how the amino group provides less thermal stability to the metal-organic frameworks.

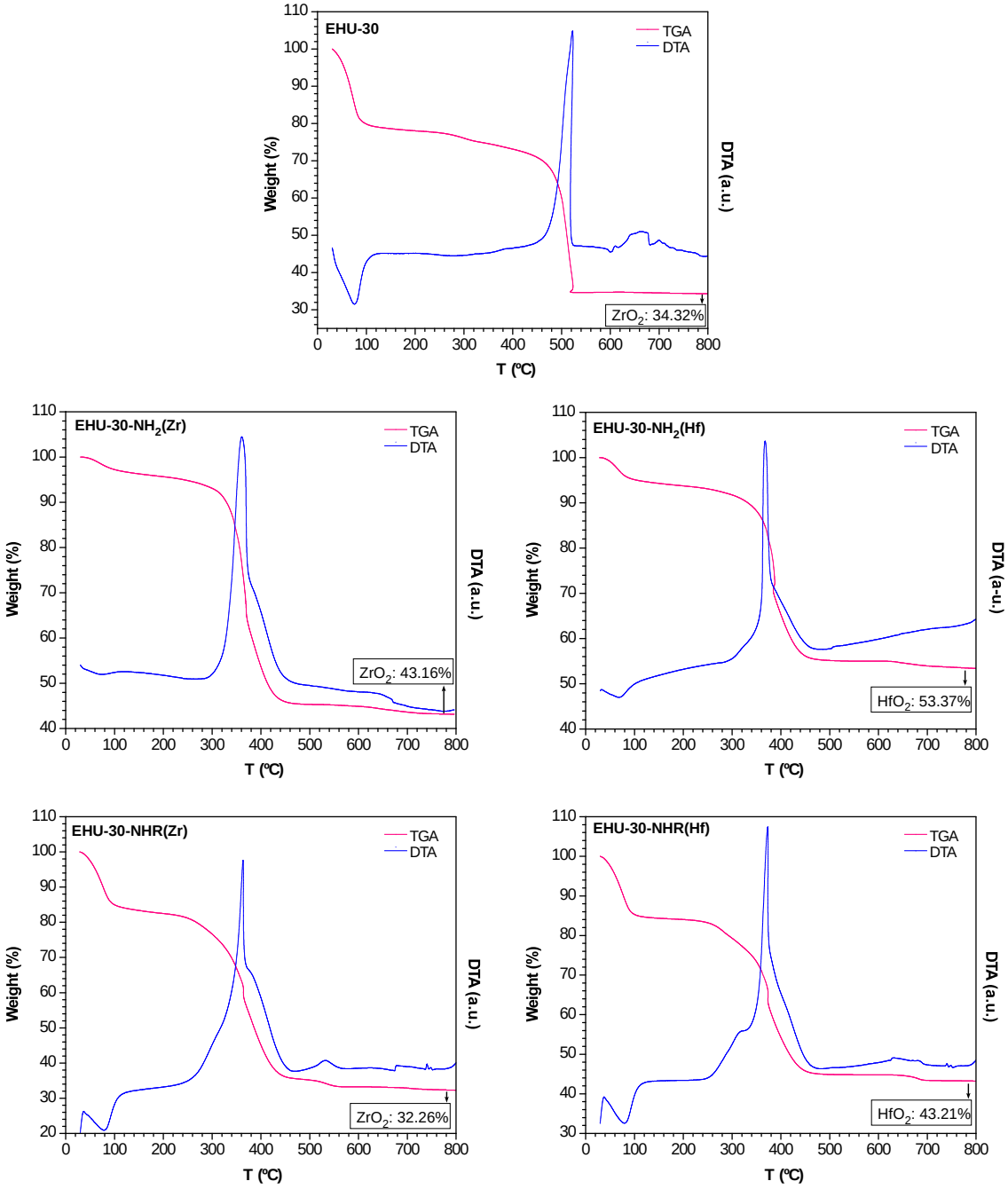

Figure 4.13. TGA-DTA curves for EHU-30, EHU-30-NH_2(Zr), EHU-30-NH_2(Hf), EHU-30-NHR(Zr) and EHU-30-NHR(Hf).

In order to provide a more precise formula, we calculated the number of linker vacancies per Zr_6 formula unit based on thermogravimetric and ^{1}H-NMR analysis, considering two possibilities of defect compensating ligands (OH^-/H_2O and monocarboxylates that come from the modulator). The general defective formula for each phase can be depicted as follows:

EHU-30: $[Zr_6(OH)_4O_4(C_8H_4O_4)_{6-x-y}(C_4H_5O_2)_{2x}(H_2O)_{2y}(OH)_{2y}]_n$,
EHU-30-NH_2(M): $[M_6(OH)_4O_4(C_8H_5NO_4)_{6-x-y}(C_4H_7O_2)_{2x}(H_2O)_{2y}(OH)_{2y}]_n$
EHU-30-NHR(M): $[M_6(OH)_4O_4(C_8H_5NO_4)_{6-x-y-z}(C_{12}H_{10}NO_6)_z(C_4H_5O_2)_{2x}(H_2O)_{2y}(OH)_{2y}]_n$.

where $C_8H_4O_4$ denotes for BDC, $C_8H_5NO_4$ for NH_2BDC, $C_{12}H_{10}NO_6$ for NHRBDC (R = 2-carboxypropyl), $C_4H_5O_2$ for methacrylato and $C_4H_7O_2$ for isobutyrato ligands.

Accordingly, the following formulas were obtained:

- **EHU-30:**
  $[Zr_6(OH)_4O_4(C_8H_4O_4)_{5.00}(C_4H_5O_2)_{0.32}(H_2O)_{1.68}(OH)_{1.68}]_n$
  MW: 1586.01 g/mol

- **EHU-30-NH_2(Zr):**
  $[Zr_6(OH)_4O_4(C_8H_5NO_4)_{4.76}(C_4H_7O_2)_{0.49}(H_2O)_{1.99}(OH)_{1.99}]_n$
  MW: 1644.40 g/mol

- **EHU-30-NH_2(Hf):** $[Hf_6(OH)_4O_4(C_8H_5NO_4)_{5.17}(C_4H_7O_2)_{0.71}(H_2O)_{0.95}(OH)_{0.95}]_n$
  MW: 2224.18 g/mol

- **EHU-30-NHR(Zr):**
  $[Zr_6(OH)_4O_4(C_8H_5NO_4)_{3.63}(C_{12}H_{10}NO_6)_{1.96}(C_4H_5O_2)_{0.47}(H_2O)_{0.35}(OH)_{0.35}]_n$
  MW: 1899.71 g/mol

- **EHU-30-NHR(Hf):**
  $[Hf_6(OH)_4O_4(C_8H_5NO_4)_{3.19}(C_{12}H_{10}NO_6)_{2.34}(C_4H_5O_2)_{0.69}(H_2O)_{0.25}(OH)_{0.25}]_n$
  MW: 2460.11 g/mol

In all of them a small fraction of dicarboxylato ligands have been replaced by methacrylato/isobutyrato ligands and OH^-/H_2O pairs, being the 5% for EHU-30, the 21% for EHU-30-NH_2(Zr) and the 14% for EHU-30-NH_2(Hf). In EHU-30-NHR(Zr) the 35% of dicarboxylato ligands has experienced an Aza-Michael reaction (further explained in the Results and discussion section) leading to the 2-carboxypropyl-amino derivative and 7% of the linker vacancies has been replaced by water/hydroxide pairs and methacrylato. In EHU-30-NHR(Hf) these values are 42% and 8%, respectively.

Variable temperature powder X-ray diffraction (TDX). According to temperature variable PXRD experiments upon heating EHU-30, EHU-30-NH_2(Zr and Hf) and EHU-30-NHR(Zr and Hf) samples, no polymorphic phase transition towards a

thermodynamically favoured phase was observed in any case, probably because the strength of the zirconium/hafnium–oxygen bond imposes a too high activation energy barrier on this transition.

As commented in TGA analysis, EHU-30 compound possesses the higher thermal stability, maintaining its crystalline structure up to *ca.* 450 °C, when a broad peak attributable to ZrO_2 starts to appear (Figure 4.14).

In the case of amino-functionalised samples (Figures 4.15 and 4.16), all of them exhibit a similar thermal stability being stable for up to *ca.* 300 °C after which it decomposes to yield ZrO_2/HfO_2, although on the range represented only the peak of ZrO_2 in Zr-based samples is observed. This trend when an $–NH_2$ is incorporated in the framework it has also been observed in UiO-66-NH_2 MOFs, with a thermal stability of *ca.* 300°C.[30]

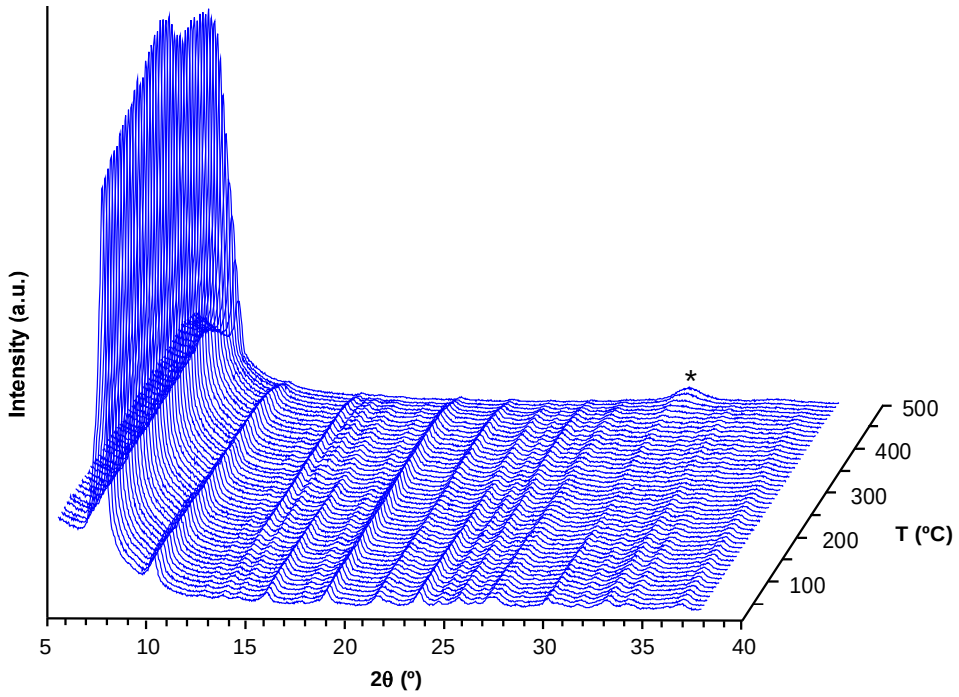

Figure 4.14. Variable-temperature PXRD patterns of EHU-30 measured from 20 to 500 °C each 10 °C at air atmosphere.

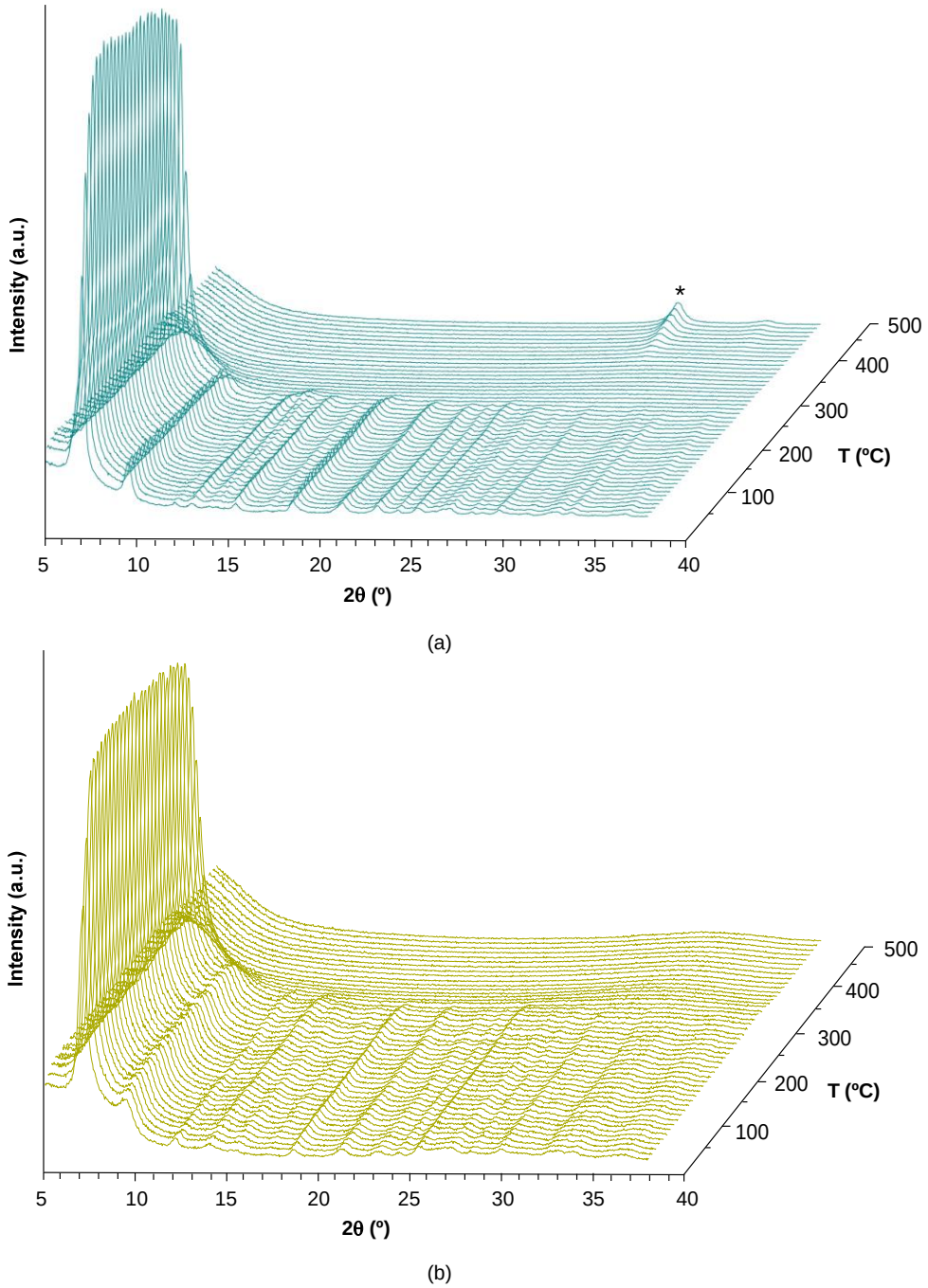

Figure 4.15. Variable-temperature PXRD patterns of (a) EHU-30-NH_2(Zr) and (b) EHU-30-NH_2(Hf) measured from 30 to 500 °C each 10 °C at air atmosphere.

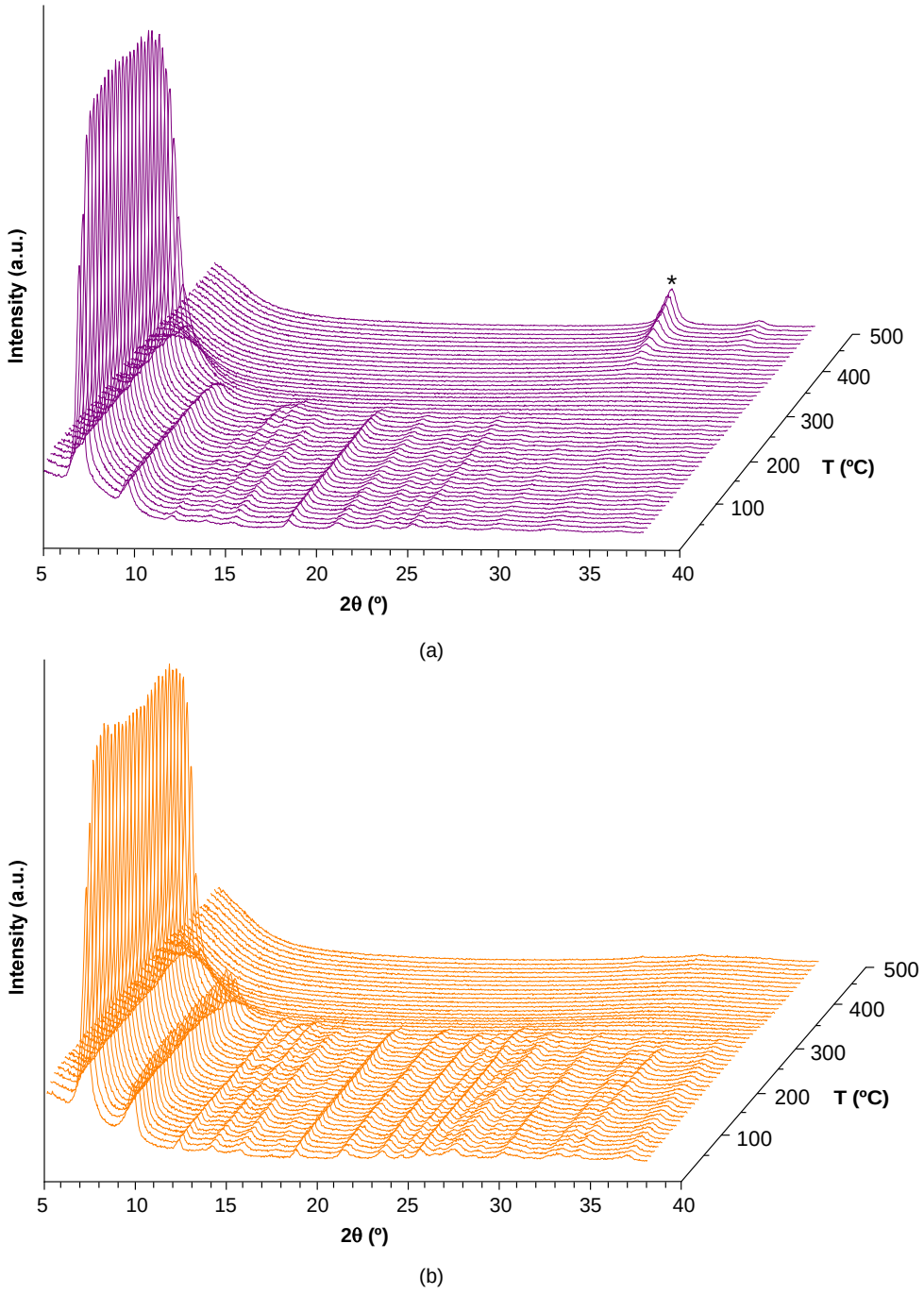

Figure 4.16. Variable-temperature PXRD patterns of (a) EHU-30-NHR(Zr) and (b) EHU-30-NHR(Hf) measured from 30 to 500 °C each 10 °C at air atmosphere.

4.2.1.4. Simulation of adsorption isotherms

Simulation of adsorption isotherms of pure components (CO_2 and N_2 for EHU-30, EHU-30-NH_2(Zr) and EHU-30-NH_2(Hf) MOFs) and binary mixtures (H_2O + N_2 for EHU-30, EHU-30-NH_2(Zr) and UiO-66(Zr)) were calculated using the software package RASPA. Details about the calculations are gathered in Section 2.4.3 of Chapter 2.

4.2.2. RESULTS AND DISCUSSION

4.2.2.1. Synthesis of the first polymorph of UiO-66

Herein, firstly, we present a new Zr-MOF, of formula $[Zr_6(\mu_3\text{-}O)_4(\mu_3\text{-}OH)_4(\mu_4\text{-}BDC)_6]_n$ (BDC: benzene-1,4-dicarboxylato) and named EHU-30 which was obtained through an alternative synthetic approach capable of modifying the framework topology of UiO-66 retaining its SBU and chemical formula. As a consequence we obtained the first polymorphic form of the referential UiO-66 MOF. EHU-30 is obtained as a white powder consisting on nanosized single-crystals of hexagonal prism shape (inset Figure 4.17), which differ from the cubic habit featuring UiO-66 crystals. Figure 4.17 compares the simulated powder X-ray diffraction pattern of UiO-66 with that of the new polymorph.

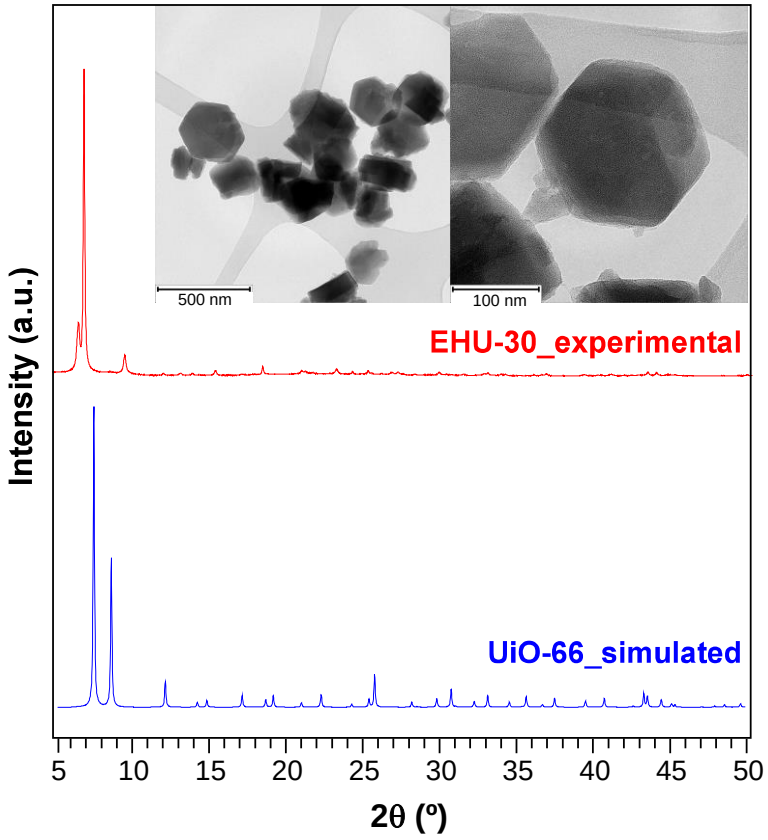

Figure 4.17. Experimental and simulated PXRD patterns for EHU-30 and UiO-66, respectively. Inset: TEM micrographs of EHU-30 nanosized crystals.

Previously reported synthesis of Zr-MOFs proceed under relatively diluted solvothermal conditions, using usually N,N-dimethylformamide as solvent.[31,32] On the contrary, EHU-30 is obtained under highly concentrated conditions, in which the modulator (methacrylic acid), apart from slowing down the nucleation and crystal growth,[31] exerts the template effect that directs the framework topology towards a kinetically favoured metastable structure (see discussion below). In fact, this is not the only critical point during the synthesis of EHU-30. It has also been observed that the amount of water during the synthesis plays a critical role in the formation of this polymorphic structure. Water (or hydroxide/oxide anions) is required for the formation of the zirconium cluster, as it has been previously described.[33,34] It can be added intentionally but it can also arise from ambient humidity or, as we have observed in this case, it can come from a side reaction involving the partial esterification of carboxylic acids with the propanol/propanoate contained in the Zr(IV) reagent. The presence of the esterification products, propyl methacrylate (propyl 2-methylprop-2-enoate) and propyl benzene-1,4-dicarboxylate, was verified by GC-MS measurements on the reaction media (Figure 4.18). It must be considered that previous works have demonstrated the capability of Zr(IV) complexes (including MOFs) to catalyse etherification reactions.[35] The formation of EHU-30 with no extra water was achieved, but the addition of 10 μL of water ensures the reproducibility of the synthesis in terms of crystallinity and adsorptive performance. Interestingly, the increase of the added water amount prompts the formation of low crystallinity UiO-66 phase, as can be seen in Figure 4.19, giving thus further evidence of the template effect of the modulator, as the addition of increasing amounts of water may dilute the reagents and have the ability to disrupt hydrogen bonding of the template, yielding as a consequence UiO-66 instead of EHU-30.

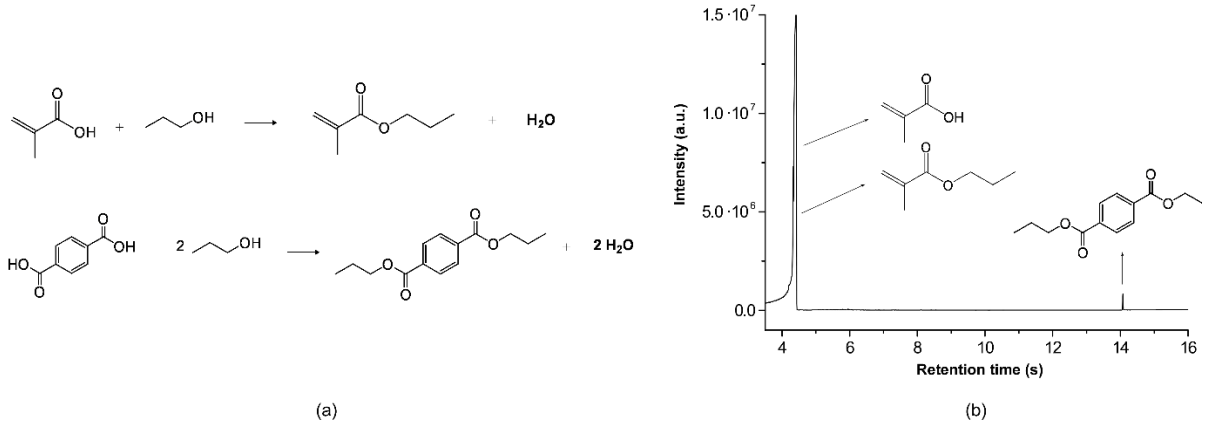

Figure 4.18. (a) Reaction schemes for the esterification of the carboxylic acids that take place during the synthesis process of EHU-30. (b) Chromatogram (GC-MS) taken on the leachate of the reaction product, in which the propyl esters of methacrylic acid and benzene-1,4-dicarboxylic acid were identified.

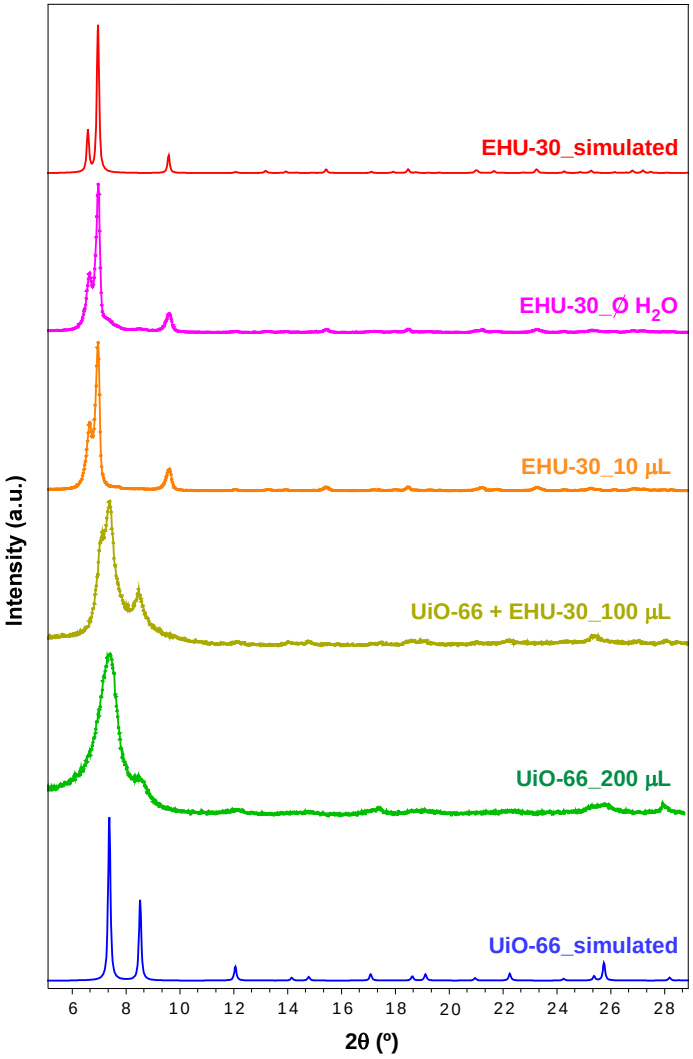

Figure 4.19. Experimental PXRD patterns for samples synthesised with varying amount of water and simulated PXRD patterns for EHU-30 and UiO-66.

Crystal structure

The hexagonal crystal structure of EHU-30 was determined *ab initio* from synchrotron X-ray powder diffraction data. The structural analysis shows how each $[Zr_6(\mu_3\text{-}O)_4(\mu_3\text{-}OH)_4(\mu\text{-}COO)_{12}]$ SBU is linked by means of twelve phenyl linkers to eight surrounding clusters, leading to an 8-connected uninodal three-dimensional net with hexagonal primitive topology (**hex**) and $(3^6{\cdot}4^{18}{\cdot}5^3{\cdot}6)$ point symbol,[36,37] while in UiO-66 each secondary building unit (SBU) is 12-connected into a **fcu**-type net. However, both polymorphs show a similar bidimensional hexagonal subnet (**hxl**) in which six of the BDC ligands are linking six coplanar Zr-SBUs (Figure 4.20a), and therefore the structural difference arises from the assembly of these layers. Accordingly, in UiO-66 each SBU is connected to three nodes of the upper layer and to another three of the lower layer, while in EHU-30 the SBU is linked to one each upper and lower layer SBUs by means of triple BDC pillars (Figure 4.20b). An additional feature of EHU-30 lies on a rather

unusual distortion observed for the BDC ligands comprising the triple pillar in which the carboxylate carbon atom lies out of the phenyl ring plane. This feature has been also observed in MOF-808 (M^{IV}: Zr, Hf).[38,39] The structural strain and the strength of the $Zr–O_{carboxylate}$ bond might be responsible for such distortion, but it must be taken with certain caution as the data arise from a PXRD Rietveld fitting.

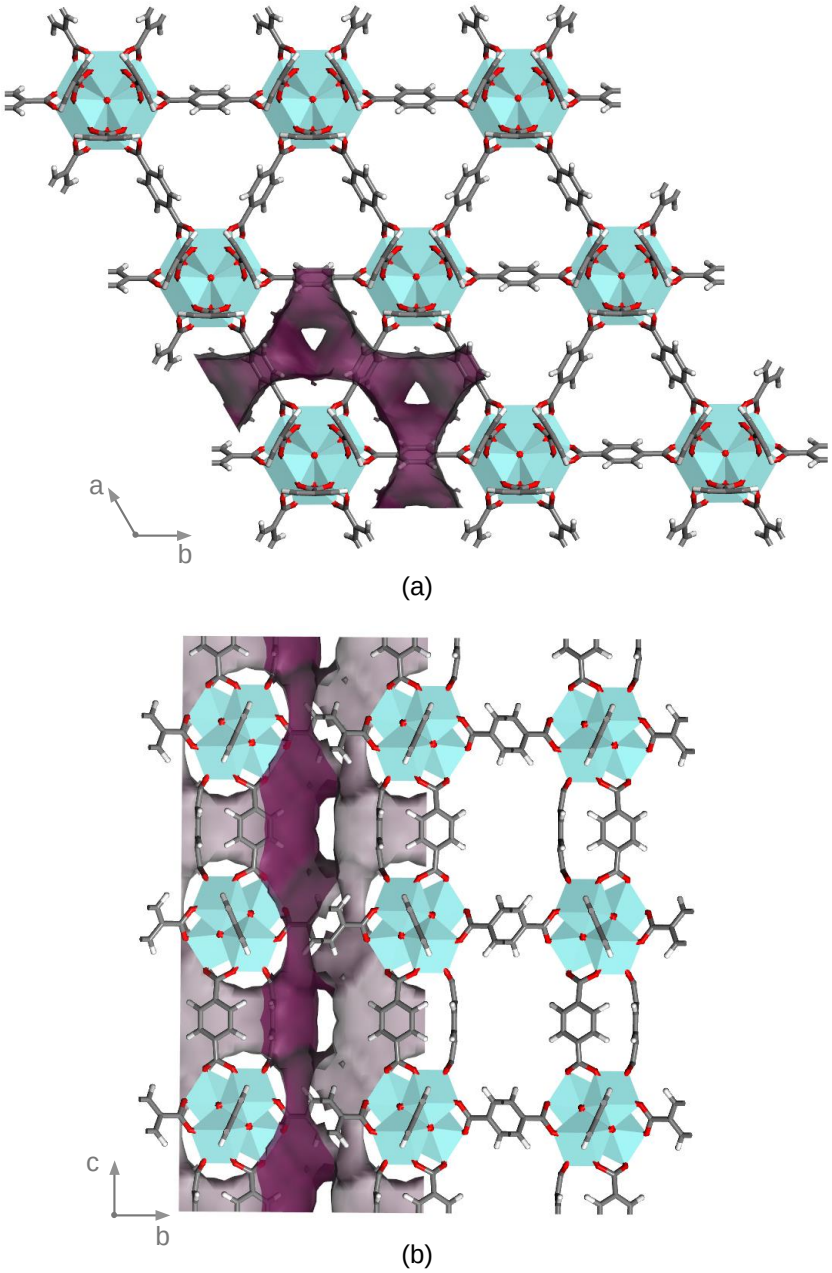

Figure 4.20. Crystal packing views of EHU-30 along (a) [001] and (b) [100] crystallographic directions within the computed accessible surface depicted in purple.

To get deeper insights into the fundamental differences between both polymorphs, periodic density functional theory (DFT) calculations were used to estimate the relative enthalpic stability. The structures were fully optimized (including atom coordinates and cell parameters) to yield total electronic energies. The more dense-packed UiO-66 is

more stable than EHU-30 by 30 kJ·mol^{-1}, which suggests a kinetic control upon the isolation of the new polymorph. Accordingly, recent experimental and quantum-chemical calculations on zeolitic imidazolate-frameworks have also evidenced a decrease in energy with increasing density, finding enthalpy differences ranging from 7 to 32 kJ·mol^{-1} within a polymorphic series.[40,41] The absence of previously reported UiO-66 polymorphs can be related to the strong Zr–O bond and to the resulting rigidity of the SBU/linker ensemble, which apparently hinders template effect to occur. Every framework modification done so far have implied to reduce the linker (BDC) to cluster ratio,[42,43] so obtained structures cannot be regarded as polymorphs. As aforementioned, the herein employed high reagent concentration enables the methacrylic acid to act both as modulator and structure template. In EHU-30, this template effect, that may be based on hydrogen-bonding interactions, implies a distortion of the arrangement of the BDC ligands around the hexanuclear cluster: two triplets of BDC ligands located on opposite triangular faces of the SBU would be forced to get closer by the interacting methacrylic acid (Figure 4.21) and therefore they would direct the growth of the crystalline structure in a substantially different way to that taking place in UiO-66.

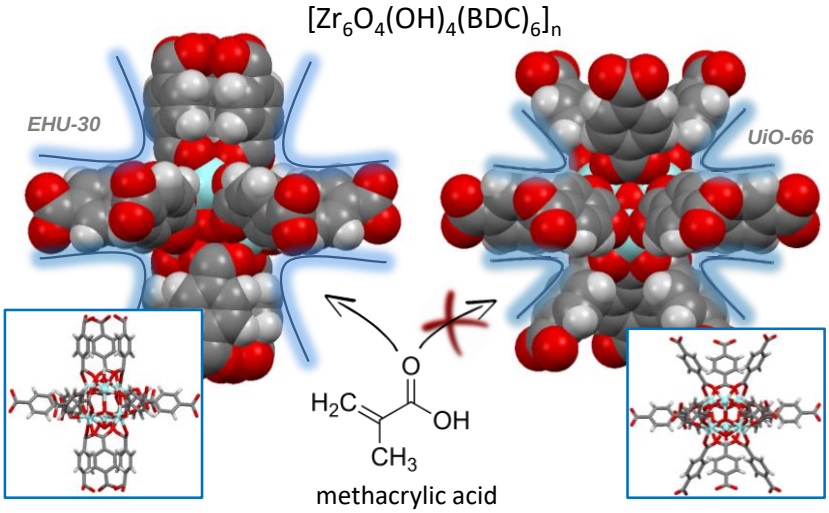

Figure 4.21. Detail of the structural differences around the cluster that leads to the formation of EHU-30 and UiO-66.

4.2.2.2. Zr- and Hf-based amino-functionalised family of EHU-30

Following a similar strategy to that of EHU-30 synthesis, we were able to obtain two types of amino-functionalised isomorphous series of EHU-30 (Scheme 1 and Figure 4.22). Isobutyric acid as both modulator and template conducts the growth of the isostructural amino-functionalised EHU-30 MOFs based on zirconium and hafnium and

denoted as EHU-30-NH_2(M) ($[M_6O_4(OH)_4(NH_2BDC)_6]_n$; M: Zr, Hf, NH_2BDC: 2-amino-benzene-1,4-dicarboxylato). In this case, the use of methacrylic acid in the presence of NH_2BDC linkers also has the ability to yield the targeted framework, but the propenylic group provides an additional functionalization of the linker by anchoring a 2-carboxypropyl substituent (R) into the exo-cyclic amino group, via an Aza-Michael reaction. In fact, this Aza-Michael reaction has been previously employed as a post-synthetic modification reaction in UiO-66-NH_2 for intentionally including different functional groups in the framework by means of the reaction with acrylonitrile, acrylic acid, methyl acrylate and methyl vinyl ketone.[44] As a result, the isomorphous series named as EHU-30-NHR(M) was obtained, in which around 40% of the amino sites were functionalized: $[M_6O_4(OH)_4(NH_2BDC)_{3.6}(NHRBDC)_{2.4}]_n$ (M: Zr, Hf).

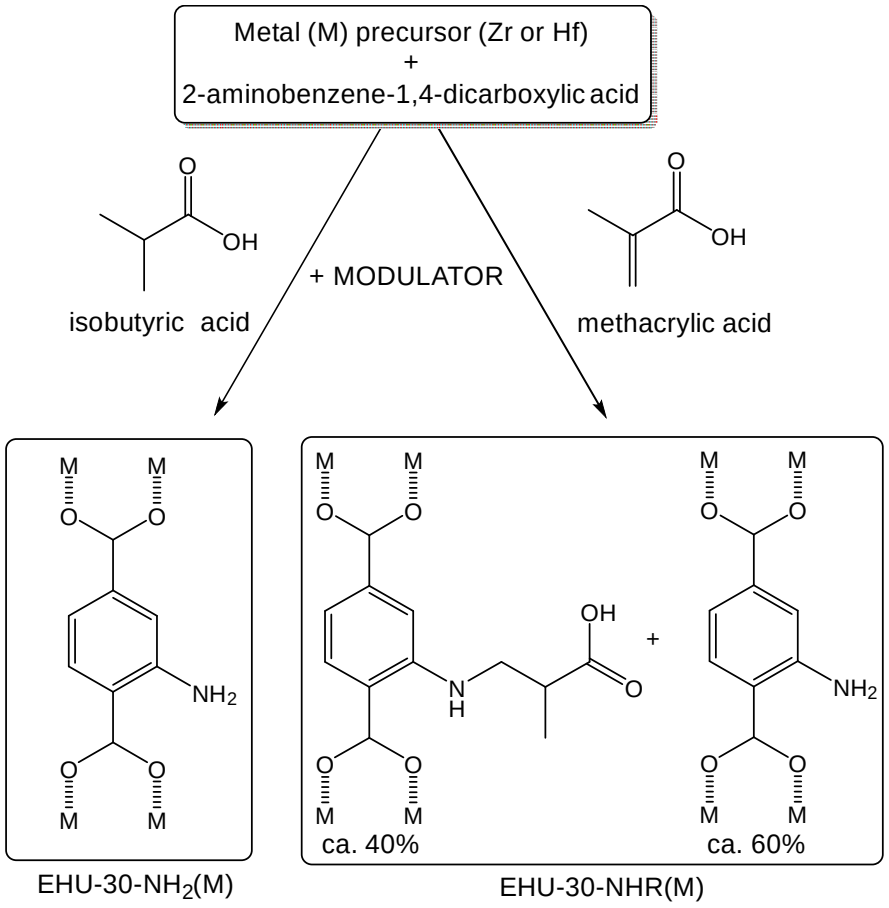

Scheme 4.1. Synthesis details for EHU-30-NH_2 and EHU-30-NHR depicting the influence of the modulator (monocarboxylic acid).

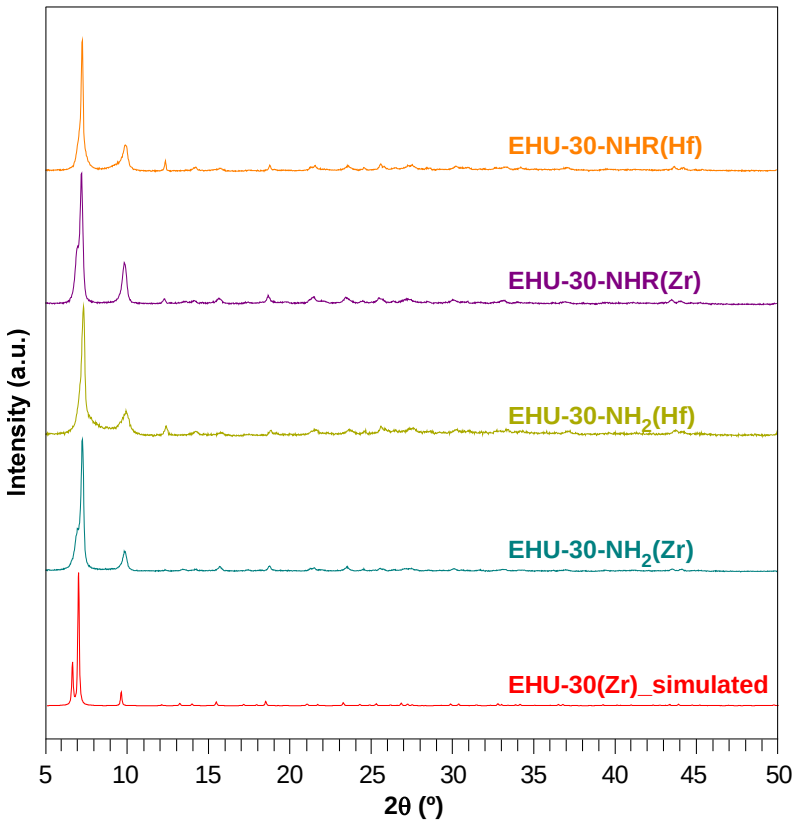

Figure 4.22. Experimental diffraction patterns for EHU-30-NH_2 and EHU-30-NHR based on Zr and Hf in comparison to simulated pattern of parent EHU-30.

Structure-directing capability of modulators

We analysed the influence of using templates with slight topological and size differences by replacing isobutyric acid with butyric acid, propionic acid and acetic acid in the synthesis of EHU-30-NH_2. In all cases, the target phase was obtained but the powder X-ray diffraction (PXRD) patterns revealed an overall lowering of the crystallinity and the presence of UiO-66 as an impurity (Figure 4.23). Two main peaks of parent EHU-30 are observed in every sample, (1 0 0) and (1 0 2), but some impurities that correspond to UiO-66 are also observed as emerging peaks (marked with asterisks and reference in the image) when using these other monocarboxylic acids as modulators. Furthermore, full width at half maximum (FWHM) of peak (1 0 0) of EHU-30-NH_2(Zr) is calculated in the samples where this reflection peak is well defined, showing that a greater crystallinity is obtained in the sample prepared with isobutyric acid. Thus, the topological resemblance of isobutyric acid and methacrylic acid probably makes the former the most suitable template to yield the targeted framework without the additional functionalization that the latter gives.

The influence of water presence during the synthesis process was also studied as for EHU-30. Regarding the synthesis of EHU-30-NH_2 and EHU-30-NHR, in general terms, we observed that addition of water ranging stoichiometric amounts (up to 1-2 mmol

of H_2O per metal ion mmol) is also beneficial as it improves the crystallinity and purity of the samples. However, greater amounts of water give rise to the formation of UiO-66-NH_2/NHR impurities together with EHU-30-NH_2/NHR (Figure 4.24). Thus, it is corroborated again that the excess of water interferes with the modulator, inhibiting its ability to template the growth of the target framework, and allowing consequently, the formation of the favoured thermodynamically coordination structures. The optimum amount of water is different depending on the modulator and on the metal ion employed, as it can be observed in the synthesis procedures detailed above.

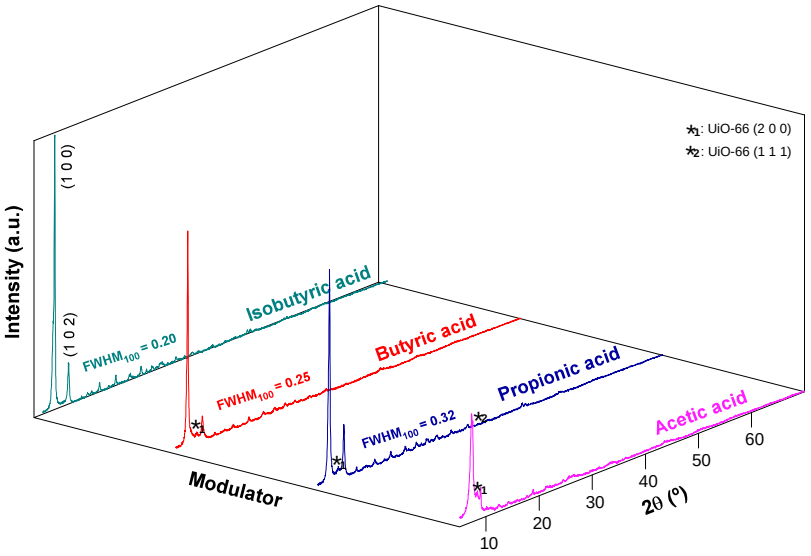

Figure 4.23. Experimental PXRD patterns for EHU-30-NH_2(Zr) samples synthesised varying the modulator. Isobutyric acid resulted the best option to obtain EHU-30-NH_2 phases.

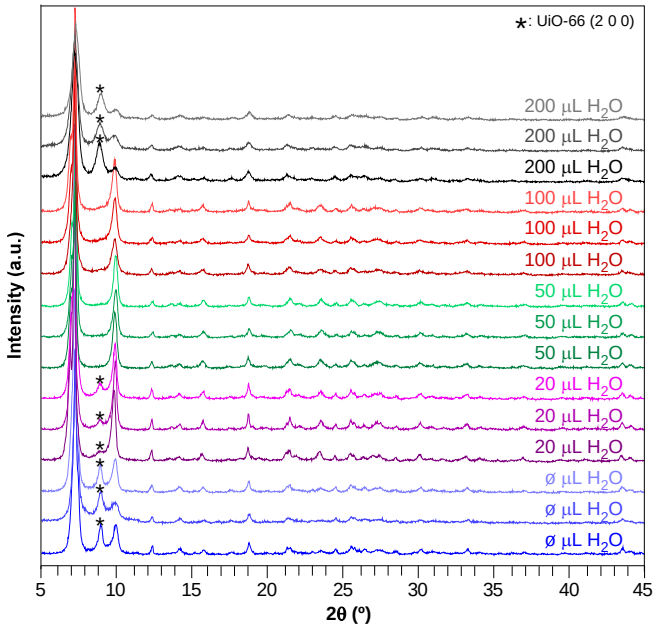

Figure 4.24. PXRD patterns of the samples resulting from the optimization process of water amount in the synthesis of EHU-30-NHR(Zr). Done in triplicate for each amount of added water.

Crystal structure and microstructure

The crystal structures of EHU-30-NH_2(M) (M: Zr, Hf) were determined from high resolution X-ray powder diffraction data using the parent EHU-30 structure as starting point. Refinement of the experimental PXRD patterns are gathered in the previous section (Section 4.2.1.2, Figures 4.3 and 4.4, respectively). Refined crystal structure parameters are comparable to those reported for the unfunctionalised EHU-30 (Section 4.2.1.2, Table 4.4). As in EHU-30, the metal-organic framework of EHU-30-NH_2 is built by 8-connected [$M_6(\mu_3\text{-}O)_4(\mu_3\text{-}OH)_4(\mu\text{-}COO)_{12}$] SBUs, linked by twelve aminophenyl rings into an uninodal three-dimensional net with hexagonal primitive topology (**hex**) (Figure 4.25). Bidimensional hexagonal subnets (**hxl**) in which each M_6-cluster is 6-connected by NH_2BDC ligands (equatorial linkers) (Figure 4.25a) are connected between them through SBUs by means of triple ligand pillars (axial linkers) to one each upper and lower layers SBUs (Figure 4.25b). Interestingly, the formation of the triple pillar is not inhibited by the insertion of NH_2 or NHR groups as demonstrated by powder X-ray diffraction.

The TEM and SEM analysis of EHU-30-NH_2 and EHU-30-NHR shows that the polycrystalline samples are comprised by hexagonal plates (Figures 4.25c and 4.26 to 4.28). The crystal growth is influenced by the type of modulator and metal centre as can be better analysed in SEM micrographs, in such a way that the methacrylic acid (*i.e.* EHU-30-NHR samples) and hafnium give rise to greater crystallite sizes. Interestingly, the amount of structural defects is related with the latter as greater crystals are less faulty (linker vacancies: EHU-30-NH_2(Zr), 21% ; EHU-30-NH_2(Hf), 14% EHU-30-NHR(Zr), 8%; EHU-30-NHR(Hf), 7%; see Section 4.2.1.3). The rather small height ratio of the plates indicates that the crystal growth is favoured along the equatorial linkers, leading to **hxl**-layers, while the assembling through the tightened triple NH_2BDC-pillar takes place more awkwardly. Note that crystals oriented perpendicularly to the [001] direction reveal a layered structure with an interlayer distance (~14 Å) fitting reasonably well to that observed in the crystal structure between pillared **hxl**-subnets ($d_{(002)}$ = 13.4 Å) (see Figure 4.25b and c).

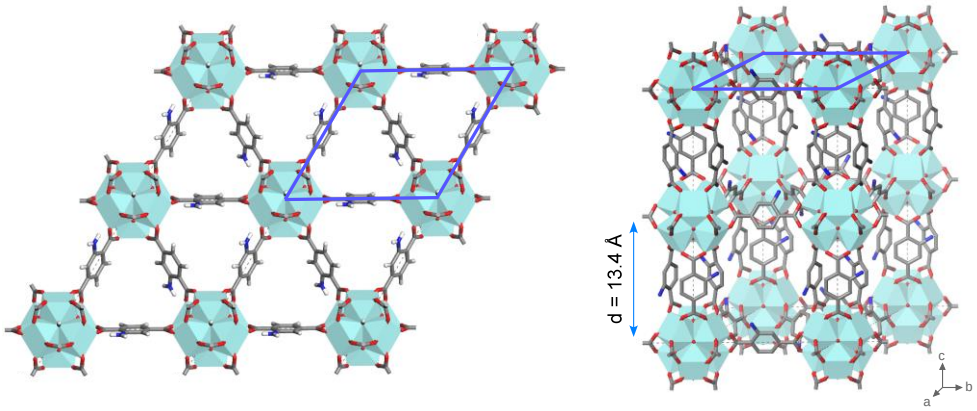

(a) (b)

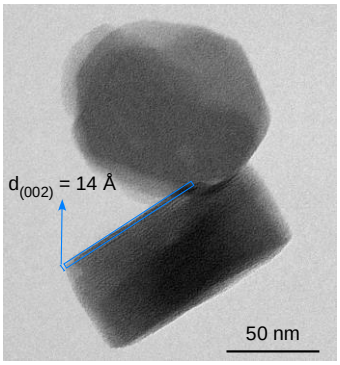

(c)

Figure. 4.25. (a) Upper view of the hexagonal 2D subnet of EHU-30-NH_2. (b) View of the crystal structure of EHU-30-NH_2(Zr) along [110] direction (H-atoms were omitted for clarity). (c) TEM image of the nanosized crystals. Highlighted area shows a set of crystallographic planes with the corresponding Miller index and spacing.

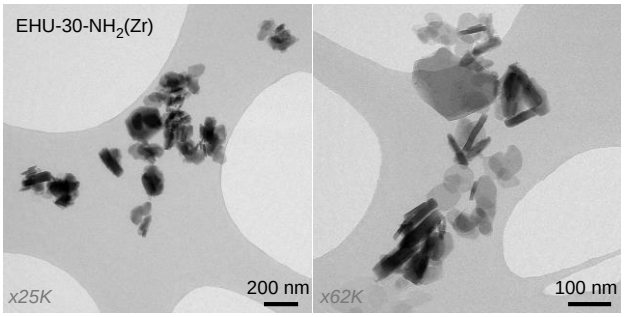

(a)

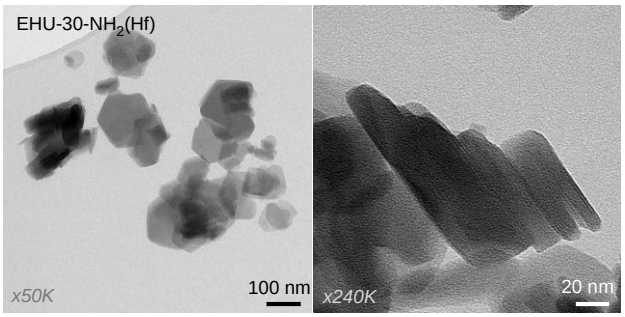

(b)

Figure 4.26. Transmission electron microscopy images taken on (a) EHU-30-NH_2(Zr) and (b) EHU-30-NH_2(Hf).

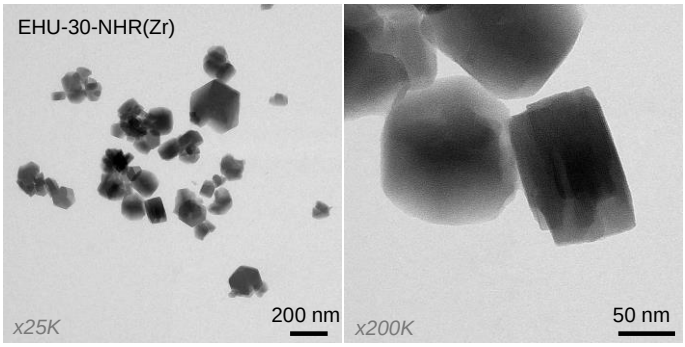

(a)

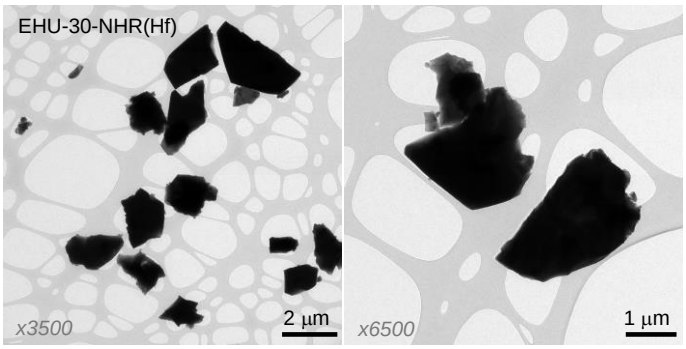

(b)

Figure 4.27. Transmission electron microscopy images taken on (a) EHU-30-NHR(Zr) and (b) EHU-30-NHR(Hf).

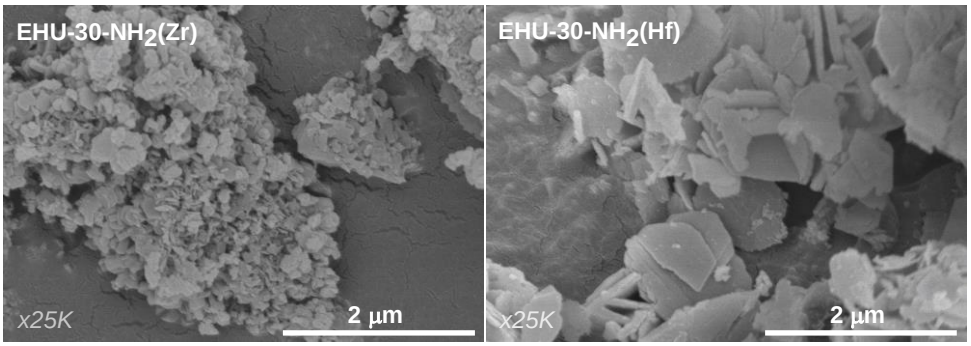

(a) (b)

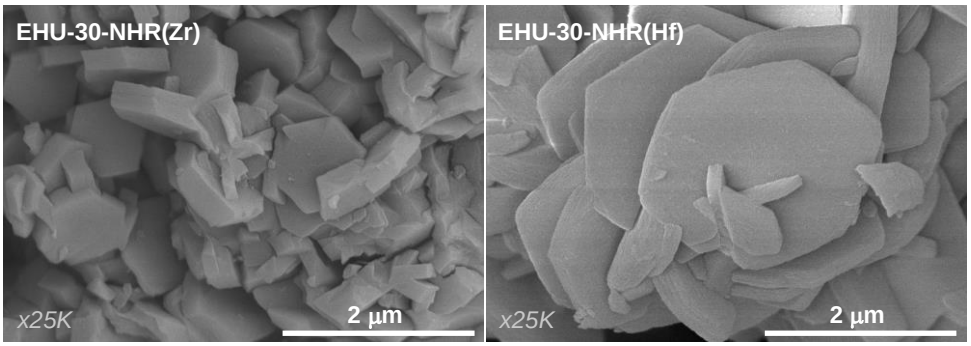

(c) (d)

Figure 4.28. Scanning electron microscopy images taken at 25K magnification on (a) EHU-30-NH_2(Zr), (b) EHU-30-NH_2(Hf), (c) EHU-30-NHR(Zr) and (d) EHU-30-NHR(Hf).

4.2.2.3. Porous structure of EHU-30 family

In order to analyse the underlying pore networks of EHU-30 family and compare it to UiO-66-type structures, it has been computed their geometric pore size distribution (Figure 4.29a) by means of a Monte Carlo procedure (calculation details in Section 2.4.1). Porous structure of EHU-30 and EHU-30-NH_2 is comprised of a 3D channel system in which 8.3 Å and 8.2 Å -sized prismatic cages, respectively, are connected by means of narrower necks along [0 0 1] (neck-*t*: ~5.5 Å) and along [-1 1 0], [1 ½ 0] and [-1 -½ 0] (neck-*r*: ~6.5 Å) crystallographic directions (Figure 4.29b). Neck-*t* is limited by the triangular windows formed by the equatorial linkers of the **hxl**-subnet, while neck-*r* shows a rectangular shaped window enclosed by two bunches of pillars and two equatorial linkers from neighbouring **hxl**-layers. Interestingly, in EHU-30-NH_2 the amino-substituents from both axial and equatorial BDC ligands are pointing towards the cage, which as explained below implies meaningful differences on the absorption behaviour and mechanism. Accordingly, the comparison of the computed geometric pore size distribution shows how the inclusion of the NH_2 group diminishes somewhat the pore volume of the wide cage but it increases the contribution of necks connecting them. As a result, the total pore volume and porosity are slightly diminished (He probe volume: 0.534 and 0.466 $cm^3 \cdot g^{-1}$; porosity: 59 vs. 54%, for EHU-30(Zr) and EHU-30-NH_2(Zr), respectively). The results also show how the prismatic pore cage size of EHU-30 (mode: 8.3 Å) surpasses the mean dimensions of the octahedral and tetrahedral cages of UiO-66 (mode: 7.1 and 7.9 Å). As a result, EHU-30 presents a greater accessible pore volume and thus, a lighter structure than UiO-66 (He probe volume: 0.428 $cm^3 \cdot g^{-1}$,porosity: 53%). Similarly, UiO-66-NH_2(Zr) structure is featured by a bimodal pore distribution in which the cavities (mode: 5.9 and 7.3 Å) are below the size of the wide cage of EHU-30-NH_2 and computed total pore volume and porosity (0.384 $cm^3 \cdot g^{-1}$ and 50 %) lie below that of EHU-30-NH_2.

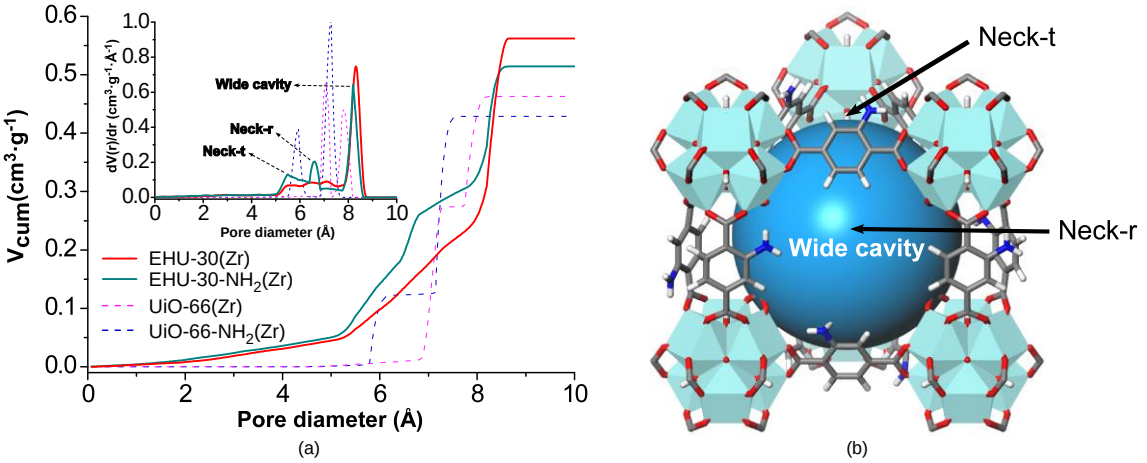

Figure 4.29. (a) Comparison of cumulative and derivative (inset) pore size distribution plots between EHU-30, EHU-30-NH_2, UiO-66 and UiO-66-NH_2 (Zr-based) and (b) immediate environment around the main pore of EHU-30-NH_2.

4.2.2.4. Gas physisorption experiments

The porosity of EHU-30, EHU-30-NH_2(M) and EHU-30-NHR(M) (M: Zr, Hf) was further assessed by the measurement of dinitrogen and carbon dioxide adsorption isotherms.

According to the microporous nature of the samples, all the N_2 (77 K) adsorption curves resemble a type I[45] isotherm with a sharp knee at low relative pressures ($p/p° < 0.04$). (Figure 4.30). The monotonic increase at intermediate pressures and the condensation at relative high pressures ($p/p° > 0.93$) in EHU-30 and EHU-30-NH_2 compounds is related to the contribution of inter-particle porosity of the nanosized crystals comprising the samples. Due to the greater crystal size of EHU-30-NHR, the isotherms are featured by a rather stable plateau after the micropore filling. Table 4.12 shows the surface area values obtained from the BET fitting of the experimental isotherms and simulated isotherms computed by means of GCMC (*Grand Canonical Monte Carlo*) calculations (for EHU-30, EHU-30-NH_2(Zr and Hf), Figure 4.31). In all cases, the experimental surface area values lie somewhat below those obtained from the GCMC simulations. Similarly, the micropore volume is also below the crystallographic values above described. The probed lower porosity can be ascribed to the defective crystal structure of these compounds, as it has been previously stated. The formation of linker defects induced by the presence of modulators in the synthesis of group-4 MOFs has also been reported for UiO-66.[46,47]

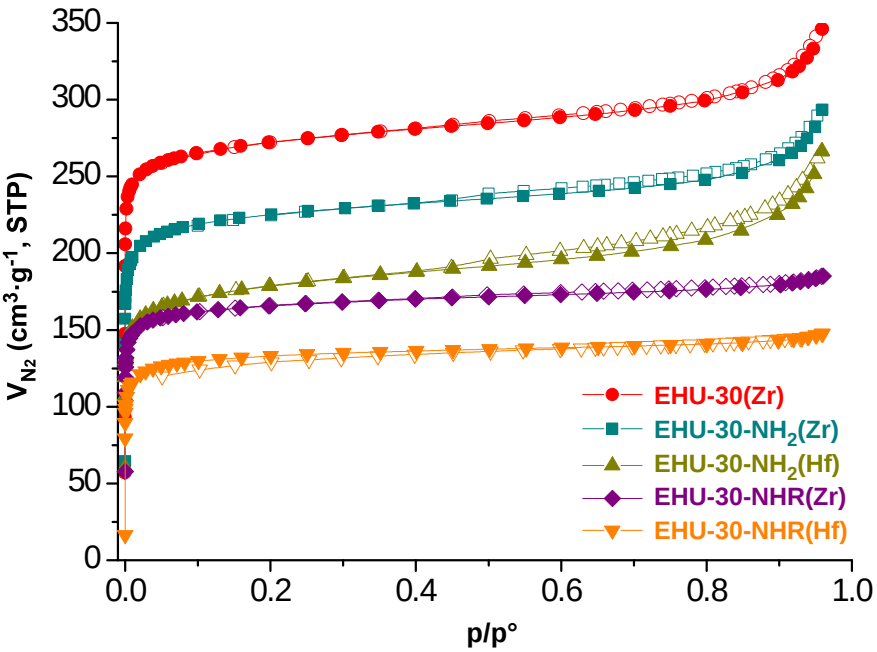

Figure 4.30. Experimental N_2 (77 K) adsorption isotherms for EHU-30, EHU-30-NH_2 and EHU-30-NHR based on zirconium and hafnium. Closed symbols, adsorption; open symbols, desorption.

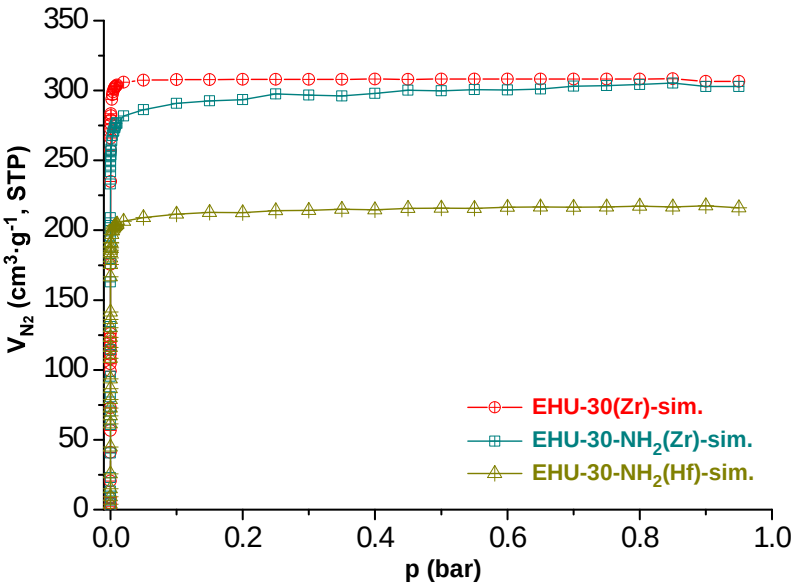

Figure 4.31. Simulated N_2 adsorption isotherms at 77 K for EHU-30(Zr), EHU-30-NH_2(Zr) and EHU-30-NH_2(Hf).

Figure 4.32 shows the consistency plot [V(1-p/p°) vs. p/p°] for experimental and simulated N_2 isotherms that allow us to select the proper pressure range to calculate the BET surface area following the criteria proposed by Roquerol et al. as explained in Section 2.2.6 of Chapter 2. Note that the BET surface area calculated from a type I isotherm must not be considered as a real accessible surface area, but it must be taken as an apparent surface area.[48] In any case, this criteria allows to estimate an area that can be regarded as an useful adsorbent "fingerprint", as it avoids a doubtful selection of the fitting range. In fact, this procedure is commonly applied to calculate the BET surface area values of MOFs.[49–52]

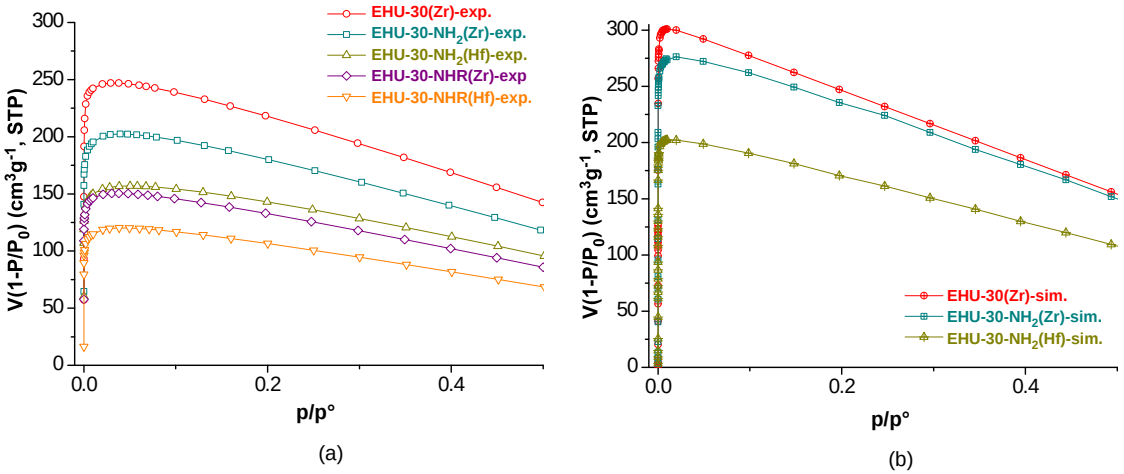

Figure 4.32. Consistency plot [V(1 – p/p°) vs. p/p°] for experimental and simulated N_2 isotherms represented in Figures 4.30 and 4.31.

Table 4.12. Surface area, micropore volumes and isosteric heats of adsorption obtained from simulated and experimental the gas adsorption isotherms.[a]

Sample	S_{exp} ($m^2 \cdot g^{-1}$)	S_{sim} ($m^2 \cdot g^{-1}$)	V_{micro} ($cm^3 \cdot g^{-1}$)	Q_{st-0} ($kJ \cdot mol^{-1}$)	Q_{st-i} ($kJ \cdot mol^{-1}$)
EHU-30(Zr)	1083	1320	0.388	28.0	21.0
EHU-30-NH_2(Zr)	891	1204	0.321	26.7	23.2
EHU-30-NH_2(Hf)	691	888	0.241	30.7	27.0
EHU-30-NHR(Zr)	662	-	0.242	30.1	24.9
EHU-30-NHR(Hf)	531	-	0.196	33.0	26.6

[a]: S_{exp} and S_{sim}: BET surface area values calculated from experimental and GCMC-simulated N_2 isotherms. V_{micro}: micropore volume. Q_{st-0}: isosteric heat of adsorption for CO_2 at near-zero coverage. Q_{st-i}: isosteric heat of adsorption at CO_2:M_6-cluster uptake ratio of 3:1.

CO_2 adsorption isotherms were measured at 273 and 298 K (Figure 4.33) to calculate the isosteric heats of adsorption (Q_{st}) (Figure 4.34.and Table 4.12). The Q_{st} values corresponding to near-zero coverage range from 27 to 33 $kJ \cdot mol^{-1}$ and they decay to values within 21-27 $kJ \cdot mol^{-1}$ when the gas uptake reaches a ratio of *ca*. three CO_2 per metal cluster. The comparison of the isotherms shows how the CO_2 uptake at intermediate pressures of less porous EHU-30-NH_2 series overpass the uptake shown by parent EHU-30. Such behaviour can be explained by the trend of Q_{st} values and it provides a clue on the adsorption mechanism related to the involvement of different adsorption-sites. At near zero loading the Q_{st} value is somewhat lower for EHU-30-NH_2(Zr) with regard to EHU-30 (26.7 *vs.* 28.0 $kJ \cdot mol^{-1}$), while at intermediate loadings the Q_{st} values of EHU-30-NH_2(Zr) surpass the ones corresponding to EHU-30 (23.2 *vs.* 21.0 $kJ \cdot mol^{-1}$), leading to higher CO_2 uptake in the former. In this sense, it can be inferred that in EHU-30-NH_2 the adsorption at intermediate pressures might occur in the vicinity of amino groups, providing a stronger interaction with CO_2. Furthermore, it must be emphasized that hafnium derivative of EHU-30-NH_2 exhibits greater isosteric heats than its zirconium analogue, which suggests that at early stages the CO_2 adsorption is also dominated by the interaction with the metal cluster. Note that EHU-30-NHR shows the same trend in Q_{st} regarding the type of metal, however the reduction of the pore volume caused by the 2-carboxypropyl substituents leads to a lower CO_2 uptake.

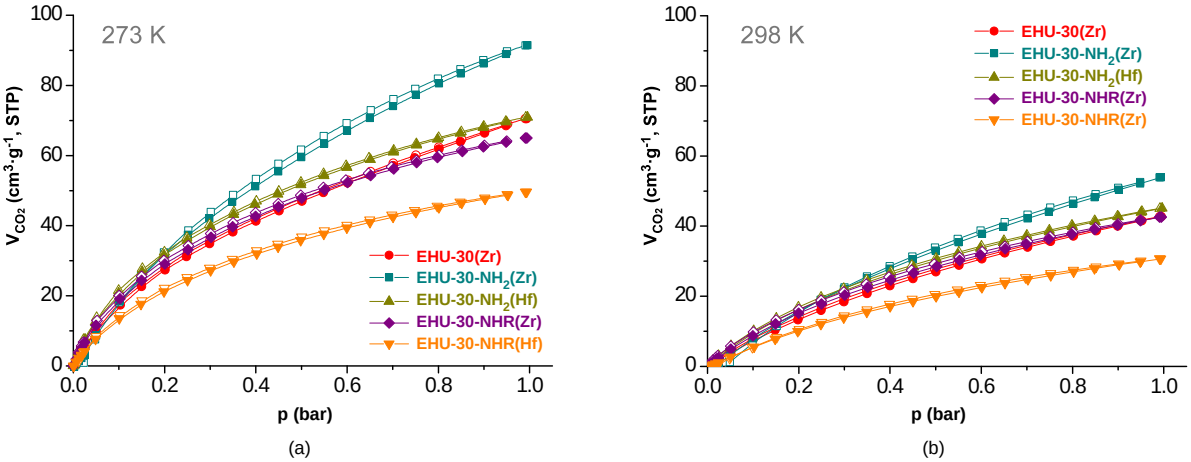

Figure 4.33. Experimental CO_2 adsorption isotherms at (a) 273 K and (b) 298 K for EHU-30, EHU-30-NH_2 and EHU-30-NHR based on zirconium and hafnium. Closed symbols, adsorption; open symbols, desorption.

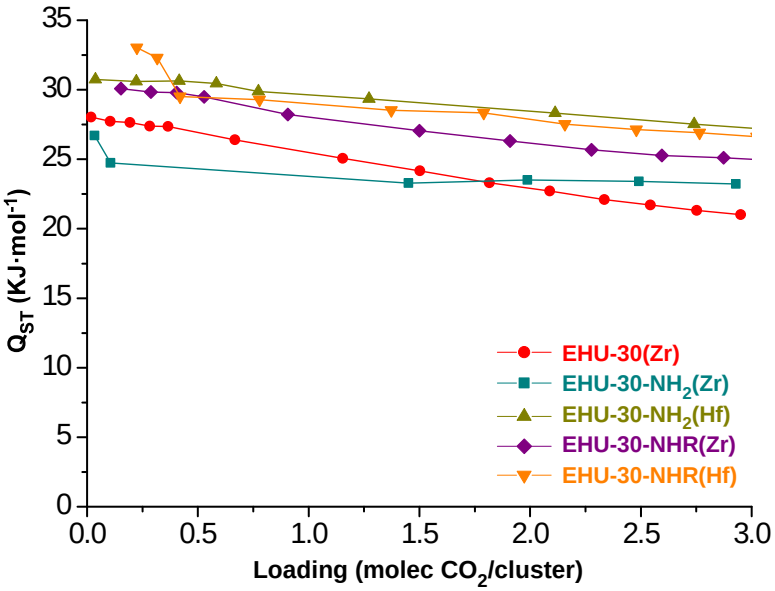

Figure 4.34. Calculated isosteric heats of adsorption for CO_2 using isotherms measured at 273 and 298 K for EHU-30, EHU-30-NH_2 and EHU-30-NHR.

To get a deeper insight, we have inspected the probability density maps resulting from the GCMC simulations of CO_2 adsorption isotherms (Figure 4.35). Accordingly, in EHU-30, the adsorption takes place preferentially at the corners of the wide cavity, in the vicinity of the metal clusters and faced to bridging μ_3-O/OH groups. This type of interaction is influenced by the metal comprising the cluster and can explain the differences found for zirconium and hafnium derivatives. In EHU-30-NH_2, apart from the aforementioned site, a second adsorption site arises enclosed within the triangular window of neck-*t*, where the interaction of CO_2 with the surrounding non-bonding electron pairs of –NH_2 groups is favourable and supports the higher Q_{st} values and CO_2 uptake at intermediate pressures values.

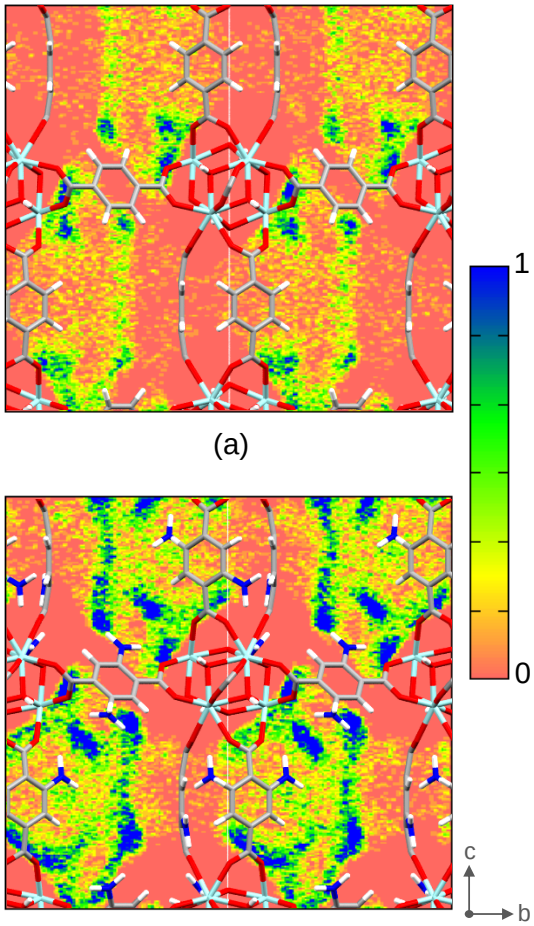

Figure 4.35. Probability density maps for CO_2 physisorbed at 0.7 bar and 273 K for (a) EHU-30(Zr) and (b) EHU-30-NH_2(Zr).

4.2.2.5. Water-vapour adsorption experiments

Water adsorption capability of zirconium-based EHU-30, EHU-30-NH_2 and EHU-30-NHR was tested assessing the influence of the temperature and cyclability on the uptake behaviour. Figure 4.36 shows the comparative of the first cycle of water sorption isotherms measured at 25 °C and Table 4.13 summarizes the threshold value from where the sorption of water starts and the water uptake value at 50% and 95% of relative humidity (RH) for the three samples.

The features of the water adsorption isotherm of EHU-30 show a threshold at 35% of relative humidity, after which a very rapid filling of the structural voids takes place up to a 380 $cm^3 \cdot g^{-1}$ (30% wt of water content). The whole process of structural void filling takes place between 35-40% of relative humidity. Once this step is completed, a slow monotonical increase takes place due to the condensation of water in the inter-particulate space. Conversely, the water adsorption isotherms for amino-functionalized structures present a more progressive adsorption behaviour, where the

initial water adsorption takes place at values of relative humidity lower than 15%, which remarks their more hydrophilic pore environments caused by the presence of the amino group,[22] presenting both inferior total water uptake capacity than EHU-30, at 95% RH, not surpassing 350 $cm^3 \cdot g^{-1}$ in any case.

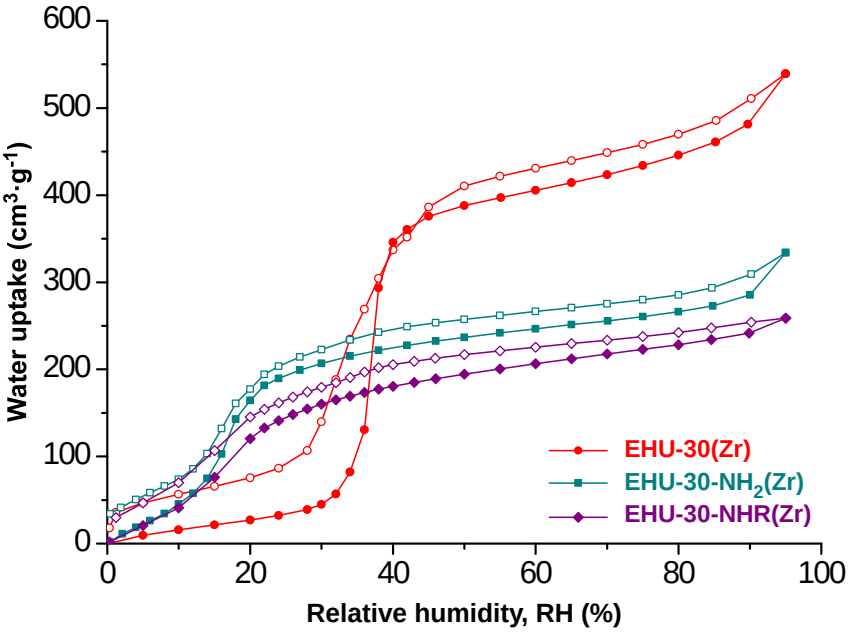

Figure 4.36. Experimental water vapour adsorption isotherms measured at 250 °C for EHU-30, EHU-30-NH_2 and EHU-30-NHR based on zirconium. Closed symbols, adsorption; open symbols, desorption.

Table 4.13. Referential values extracted from water vapour isotherms measured at 25 °C for EHU-30, EHU-30-NH_2 and EHU-30-NHR.

	Threshold (%, RH)	Water uptake 50% RH (cm^3g^{-1} / %, wt)	Water uptake 95% RH (cm^3g^{-1} / %, wt)
EHU-30	35	388 / 31	539 / 43
EHU-30-NH_2(Zr)	< 15	237 / 19	334 / 27
EHU-30-NHR(Zr)	< 15	195 / 16	259 / 21

Looking into the desorption process it is remarkable that desorption curve of EHU-30 does not fit the adsorption curve, leading to a hysteresis cycle. This disparity is more noteworthy when analysing the isotherms measured at different temperatures (Figure 4.37). The hysteresis cycle shows the expected features at 15 °C, while a crossing between the adsorption and desorption curves takes place for the remaining temperatures (25 °C, 35 °C and 45 °C), being more pronounced with the increasing temperature. This behaviour is quite unusual, although it has been previously reported for some other MOFs but without providing an explanation (DUT-52(Zr)[53] and MOF-808(Zr)[19]) or blaming it to a partial decomposition of the framework (DUT-4(Al))[54]. It is worth noting that this behaviour has not been observed for the thermodynamically

favoured UiO-66 counterpart, which has been classified as highly stable at high humidity conditions.[20] A plausible explanation for this behaviour is that the structure in the adsorption branch and the one on the desorption branch somehow differ, the latter being less hydrophilic. Anyway, the material remains functional for water adsorption after five consecutive cycles (Figure 4.38). The second cycle underperformed a 7% of the maximum capacity of water uptake and then this loss lies below 2% for the last three cycles. The desorption curve also does not close at zero humidity, with a 3-4% of adsorbed water being retained. This amount of irreversibly captured water molecules corresponds to occupation of the coordination defective positions within the Zr_6 cluster and indicate that around one in six of the bridging benzene-1,4-dicarboxilato ligands are missing, which matches with the vacant ligand positions estimated by chemical analysis presented above.

The following cycles roughly start at this water capture percentage and, interestingly, they show conventional hysteresis curves with a lower threshold (*i.e.* RH value at which compound start to adsorb water vapour abruptly) and without the previously observed crossing feature and completing closed adsorption/desorption cycles. The adsorption step starts at lower humidity values (RH: 30%) in the second and successive cycles as the irreversibly coordinated water molecules provide a more hydrophilic pore surface. In addition to that, their steps present a less pronounced slope than that of the first cycle, which could indicate a greater diversity of adsorption sites. All of the cycles match within the low relative humidity region but differ at higher humidity values, probably due to a greater sample compaction during the water adsorption/desorption cycling.

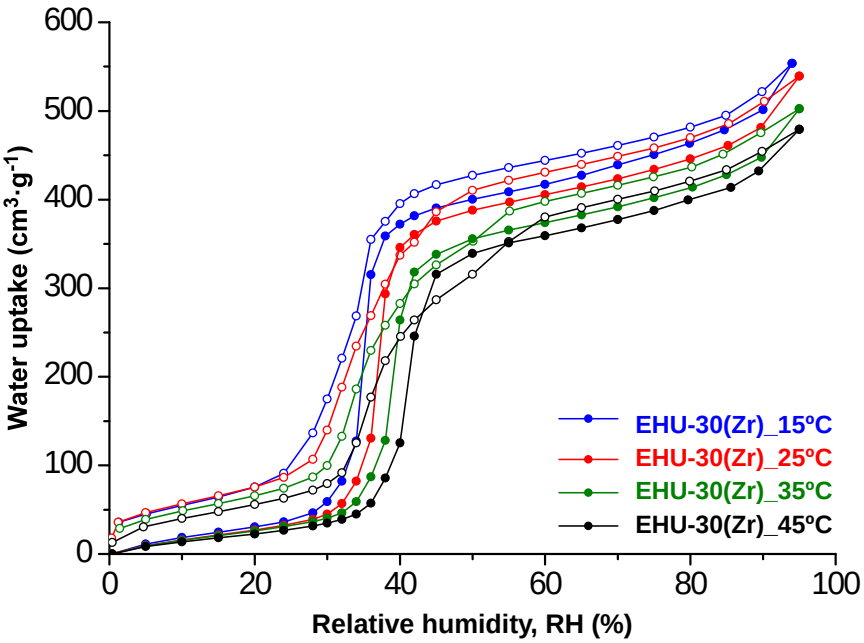

Figure 4.37. Experimental water vapour adsorption isotherms of EHU-30(Zr) measured at 15°C, 25°C, 35°C and 45°C. Closed symbols, adsorption; open symbols, desorption.

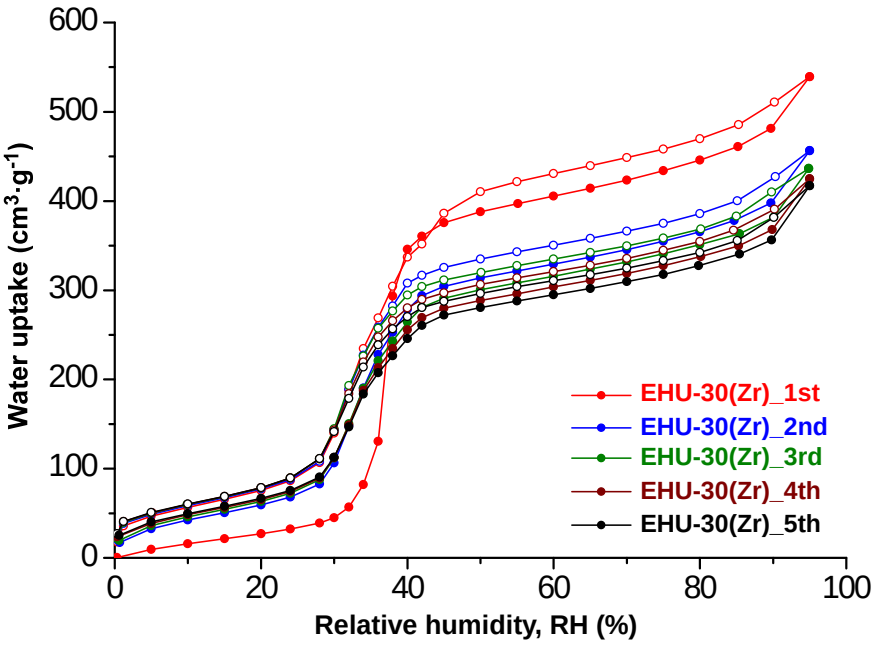

Figure 4.38. Cyclability of water vapour adsorption of EHU-30(Zr) measured at 25°C. Closed symbols, adsorption; open symbols, desorption.

Overall, the best option to provide an explanation to these features would come from the coordination of the sorbed water molecules in the outgassed Zr_6 SBU defective positions and the partial transition of the metastable EHU-30(Zr) structure into the thermodynamically preferred UiO-66(Zr). As it will be explained below, both phenomena are related.

After the coordination of these water molecules has taken place, the nature of the interaction between the host and the releasable water changes. However, this modification would lead to an, in principle, more hydrophilic nature of the porous internal walls implying a widening of the hysteresis cycle around the threshold humidity value, not a crossing as it is observed, which in fact seems to be more related with a less hydrophilic material coming back in the desorption curve.

As previously stated, there is a clear consensus that these retained water molecules belong to the benzene-1,4-dicarboxilate lacking defects that are replaced by water molecules in the coordination sphere of the zirconium metal centres.[55] The Zr–O bond strength prevents their release unless moderate temperature and ultrahigh vacuum is applied, as it happens during the initial outgassing procedure. Therefore, the amount of water molecules still retained at 0% relative humidity value provides a way to estimate the amount of defects within the crystal structure. However, taking into account that these compounds are not the thermodynamically preferred polymorphs, it cannot be ruled out a structural transformation, probably linked to the energy released during the first adsorption cycle, which includes that corresponding to the coordination of the water molecules to the defective positions of the SBU. The

activation energy required for a structural transformation on the ideal, non-defective structures is probably too high to allow a transformation at close to room temperature. In fact, a recent publication highlighted the complete structural transformation from the EHU-30 to the UiO-66 polymorph under solvothermal conditions.[56]

However, in a defective structure the activation energy for the structural rearrangements can be reduced, depending on the defects accumulated in each Zr_6 SBU. The energy released during the first adsorption cycle implies not only that related to the physisorption of water molecules but also their chemisorption into the vacant coordination positions and it could be enough to overpass some of these activation energies. On the other hand, the energy put in place during the following adsorption cycles, physisorption only, seems to be insufficient to prompt further rearrangements among the SBUs. The explained structural transformation would account why the crossing increases with the temperature, as it would provide further energy to accomplish it. This structural rearrangement would imply a change from the 8-connected structure of EHU-30 to a 12-connected one in UiO-66. In fact, simulated water adsorption computed on the basis of the ideal EHU-30(Zr) and UiO-66(Zr) structures (Figure 4.39), although do not satisfactorily fit the experimental data (probably because of the unaccounted influence of the defects on the adsorption properties), clearly indicates the more hydrophobic nature of UiO-66(Zr), which would agree with the crossing observed on the first cycle. As further structural transitions do not take place on the following cycles, their adsorption/desorption cycles are more conventional without the presence of any crossing phenomena.

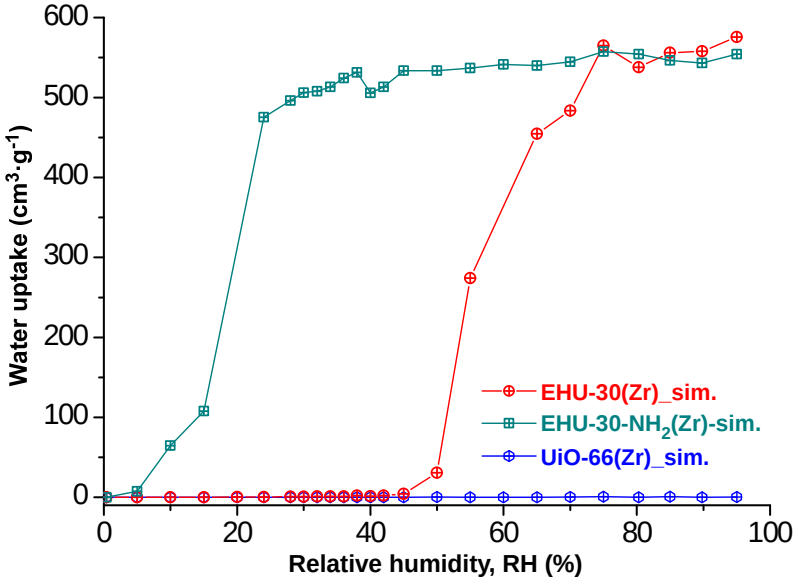

Figure 4.39. Simulated water vapour adsorption isotherms of EHU-30(Zr), EHU-30-NH_2(Zr) and UiO-66(Zr) measured at 25°C.

Evidence of this transformation has been found by comparing the diffraction patterns of an outgassed EHU-30 sample (140 °C, 6 h) before and after the exposure to water vapour at 35 °C (24 h). In the latter, a lowering on the intensity of the EHU-30 diffraction peaks is observed, together with a broadening of the (102) peak due to the emergence of the symmetry-forbidden (003) reflection. Also broad peaks and shoulder appear at the expected positions for the more intense reflections of UiO-66(Zr), (111) and (200) (Figure 4.40). The emergence of the EHU-30(Zr) symmetry-forbidden diffraction peak, not observed in the initial sample, may arise from stacking faults resulting from the mismatch on the distance between the hexagonal subnets, common to both structures and depicted in Figure 4.20a (EHU-30(Zr): 13.42 Å *vs.* UiO-66(Zr): 11.98 Å). This structural rearrangement from an 8-conectivity of the nodes in EHU-30 to a 12-conectivity in UiO-66 necessarily implies multiple successive steps. It means that several SBUs are going to be trapped in an intermediate transformation stage, which contributes to the background raise on the diffraction patterns and also to the emergence of broader signals. Interestingly, stability experiments in liquid water (24h and 20 °C) with activated samples (140 °C, 6h) clearly indicate that these transformations do not occur under these conditions, probably because liquid water is very efficient dissipating the energy released during the adsorption process, leaving the crystal structure unaltered (Figure 4.41).

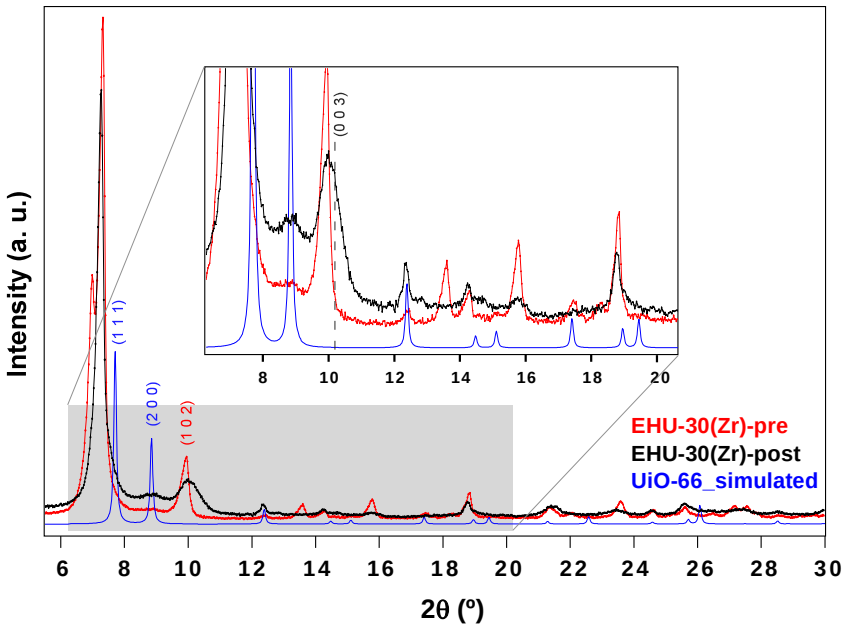

Figure 4.40. PXRD of EHU-30 pre and post treatment with water vapour, compared to UiO-66 simulated pattern.

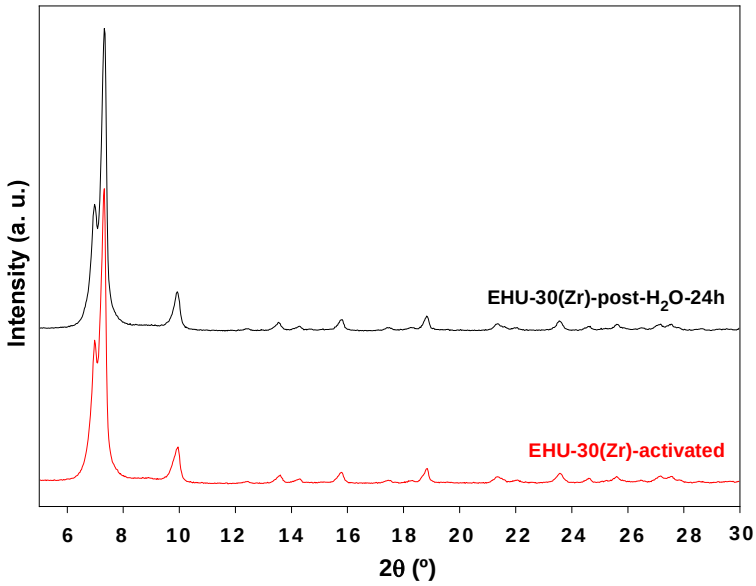

Figure 4.41. PXRD patterns of EHU-30(Zr) before and after exposure to liquid water during 24h.

Furthermore, solid state ^{13}C-NMR measurements indicate a partial transition of the spectra from the pristine EHU-30(Zr) towards UiO-66(Zr) in the sample exposed to water vapour (Figure 4.42). This indicates that small regions in the material have their original crystal structure altered (it would explain the decrease on the adsorption capacity within the sharp adsorption region and a less steep filling of the pores, as now the local environment is more diverse) and even the presence of very small domains with a proto-UiO-66 structure (Figure 4.43).

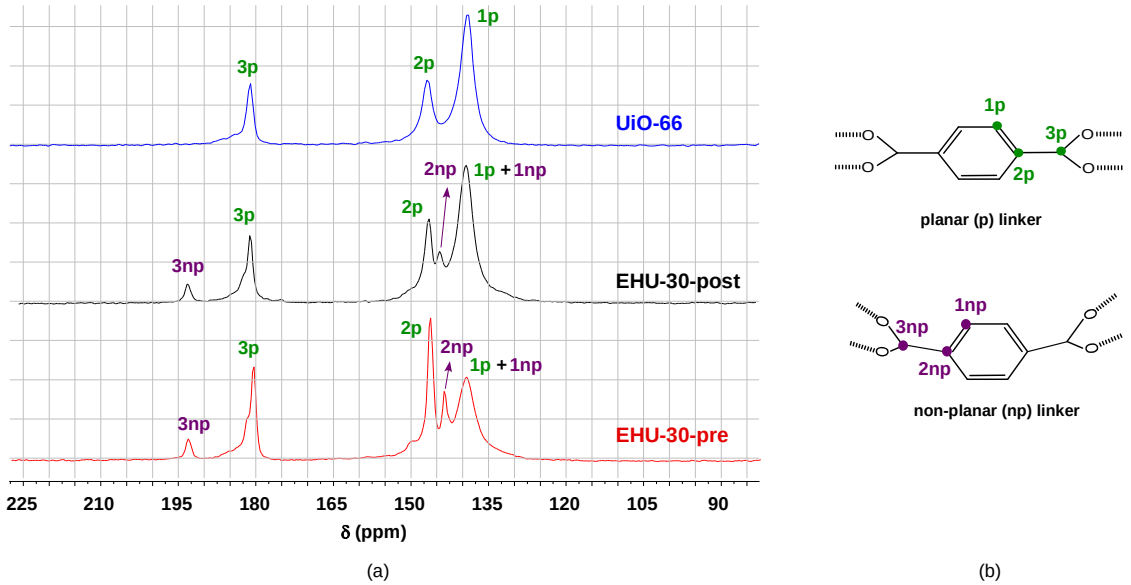

Figure 4.42. (a) ^{13}C-NMR spectra of EHU-30 pre and post treatment with water vapour compared to UiO-66 and (b) planar (common to EHU-30 and UiO-66) and non-planar (from the triple pillars of EHU-30) benzene-1,4-dicarboxilato ligands with the signal assignment labels.

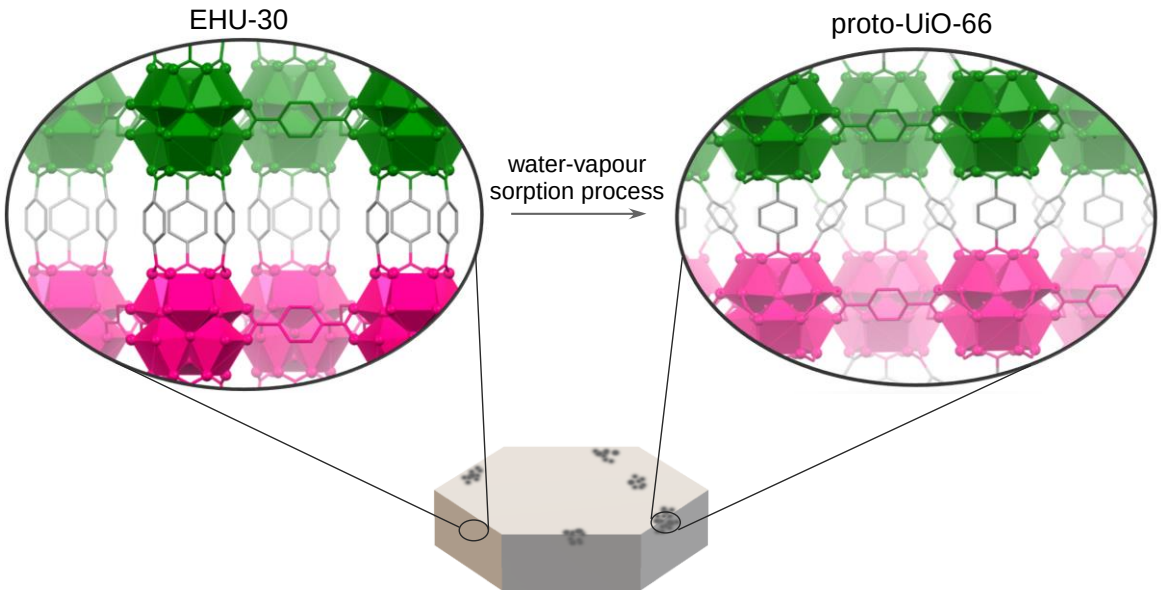

Figure 4.43. Schematic illustration of local transformation from 8-connected EHU-30 into 12-connected UiO-66, taking place in small regions of the crystal during the water-vapour adsorption process. In green and pink, consecutive **hxl** layers.

EHU-30-NHR provides a further evidence for this hypothesis as it shows conventional water adsorption/desorption curves, likely because the residues anchored to the amino group and placed on the voids of the structure hinder the required structural rearrangement for the transformation (Figure 4.44 and 4.45). EHU-30-NH_2 could be found in between, in which a narrowing of the hysteresis curve is observed, but not a crossing even after the increase on the temperature (Figure 4.46). At this point, the amino group increases the difficulty for the structural rearrangement to take place in such a way that only very few SBUs complete all the transformation steps into the UiO-66 connectivity and the X-ray diffraction patterns show a background increase, but not observable emergence of UiO-66-NH_2 peaks (Figure 4.48). In any case, it is important to realize that these transformations affect only to a small fraction of the material, as it can be deduced after four water adsorption cycles (Figure 4.47).

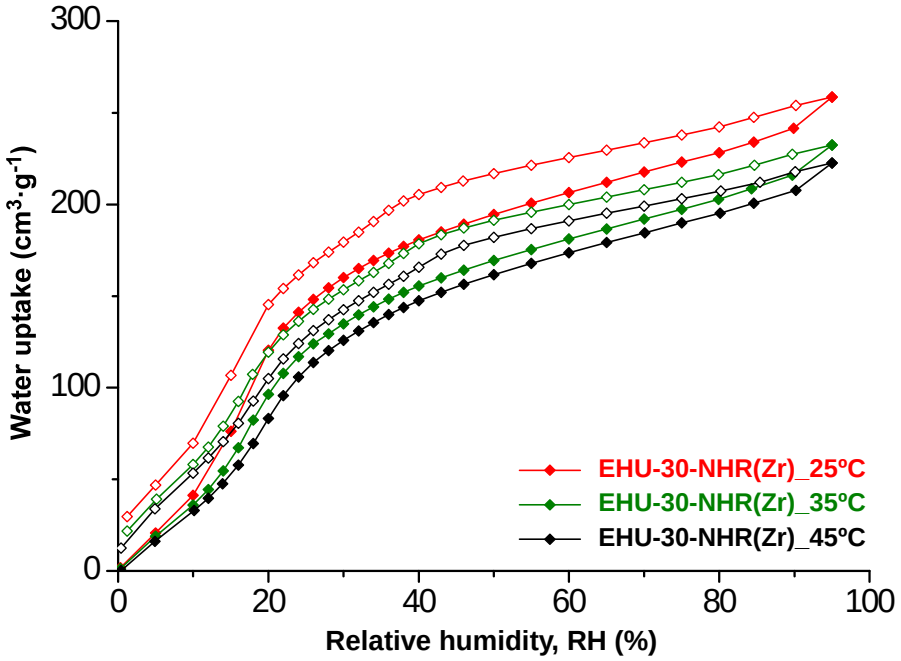

Figure 4.44. Water vapour adsorption isotherms of EHU-30-NHR(Zr) measured at 25°C, 35°C and 45°C. Closed symbols, adsorption; open symbols, desorption.

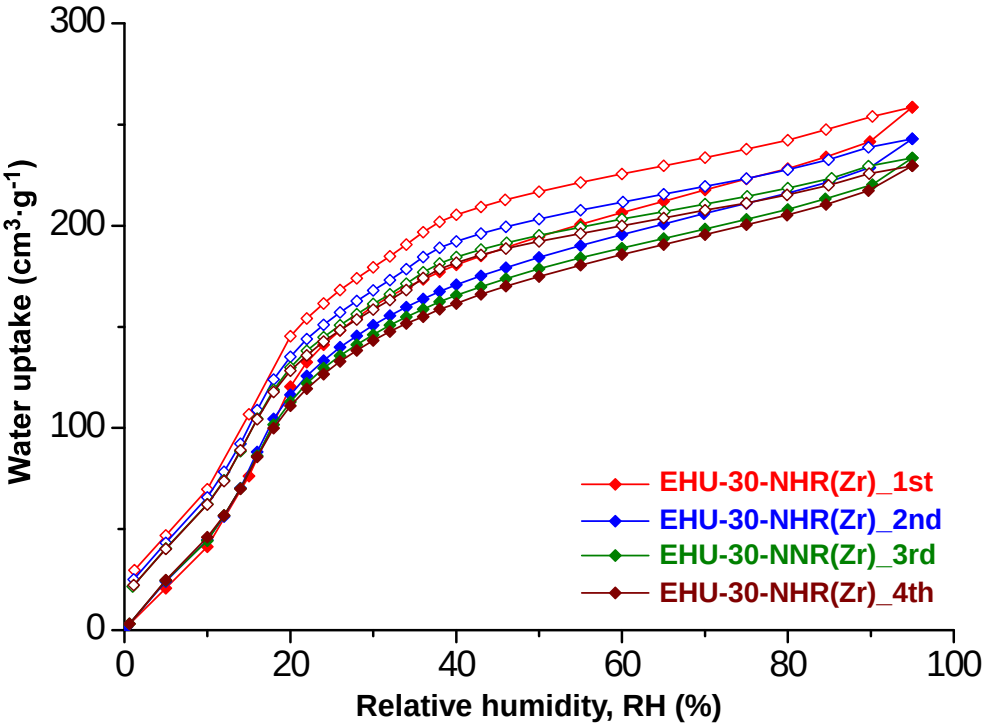

Figure 4.45. Cyclability of water vapour adsorption of EHU-30-NHR(Zr) measured at 25°C. Closed symbols, adsorption; open symbols, desorption.

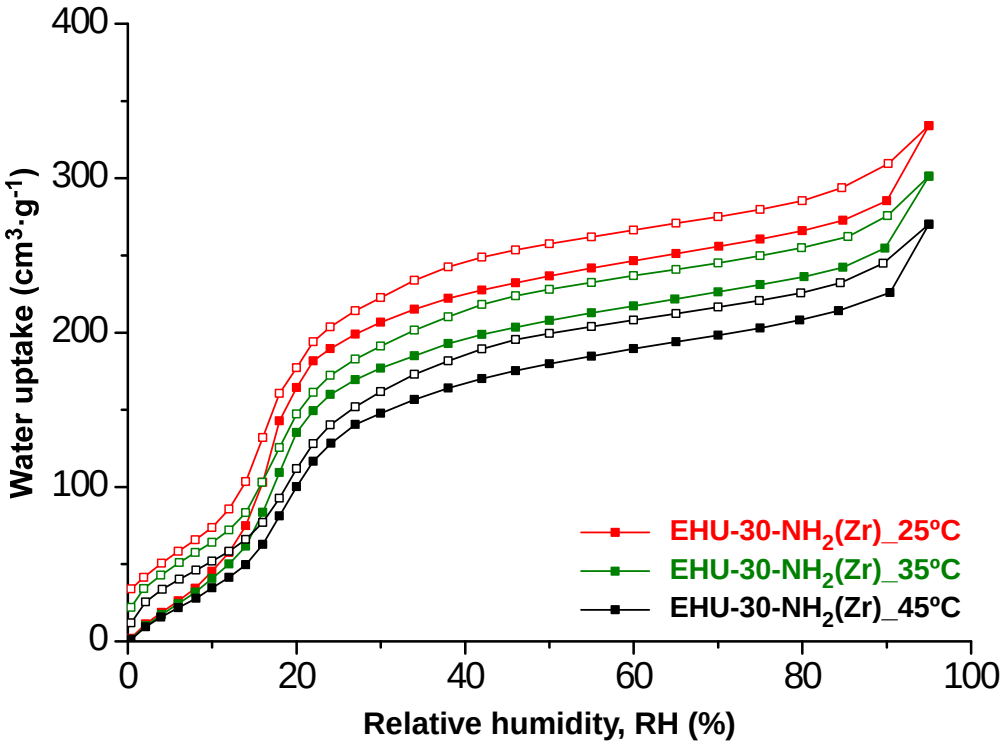

Figure 4.46. Water vapour adsorption isotherms of EHU-30-NH_2(Zr) measured at 25°C, 35°C and 45°C. Closed symbols, adsorption; open symbols, desorption.

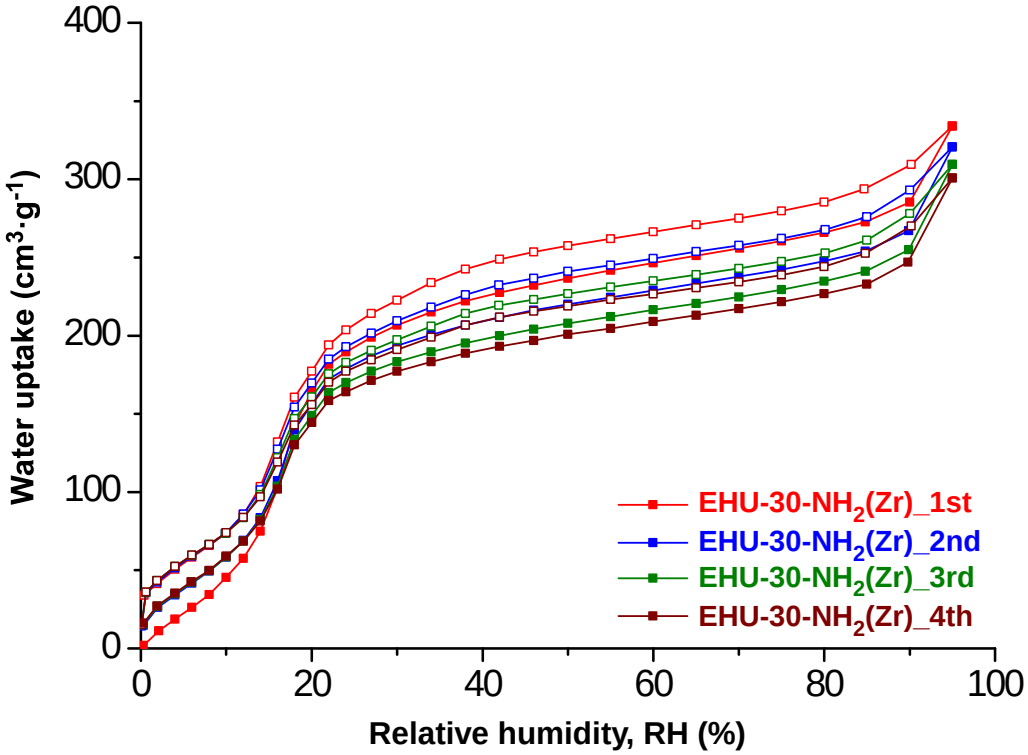

Figure 4.47. Cyclability of water vapour adsorption of EHU-30-NH_2(Zr) measured at 25°C. Closed symbols, adsorption; open symbols, desorption.

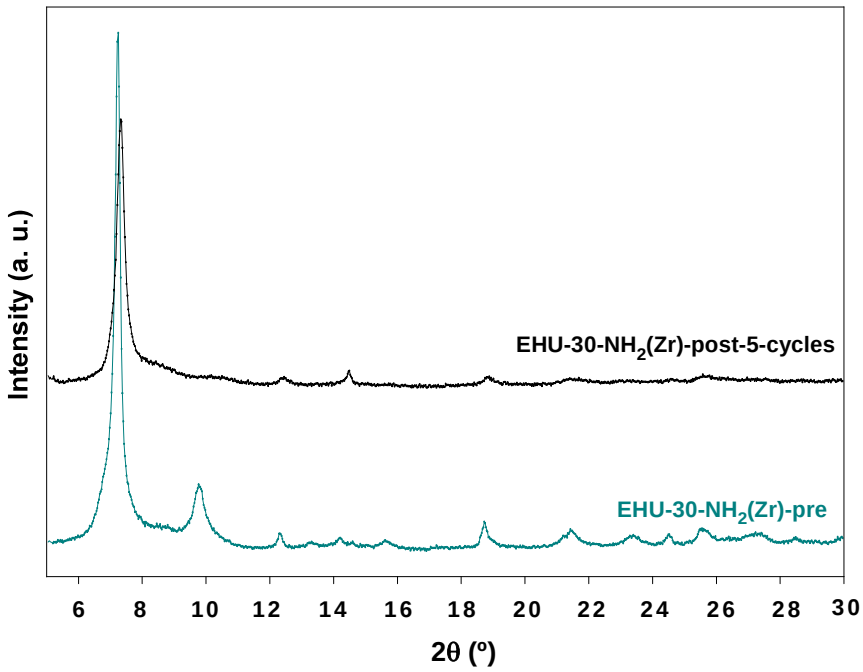

Figure 4.48. PXRD patterns of EHU-30-NH_2(Zr) before and after exposure to 5 cycles of water vapour adsorption at 25 °C

4.2.2.6. Location of water molecules by TOF neutron diffraction

The preferred adsorption sites for water molecules in EHU-30(Zr) and EHU-30-NH_2(Zr) were determined from TOF neutron powder diffraction data collected at room temperature. Rietveld refinement of the data fit well to the afore described pristine crystal structures (see Section 4.2.1.2), while difference Fourier analysis allowed to locate the position of the adsorbed water molecules. In the case of EHU-30, three preferred sites are identified and labelled as site-I, -II and III (Figure 4.49a). Site-I is in the vicinity of neck-*r* and confined within the rectangular window limited by two sets of triple-pillar and two equatorial linkers. The water molecule located at site-I is at hydrogen bonding distance from the aromatic H-atoms of equatorial linker (C-H···O: 2.417 Å). Site-II lies within neck-*t* (limited by the triangular window of hexagonal subnet) and exhibits distances of 2.6–3.5 Å to O-atoms comprising the SBU. Site-III is located at the centre of the triangular window of neck-*t* and it seems to be stabilised by the interaction with the water molecules of site-II (O3w···O2w: 3.568 Å).

EHU-30-NH_2 exhibits two crystallographically distinguishable sites: site-I and site-IV (Figure 4.49b). Similarly to the unfunctionalized counterpart, site-I is located in neck-*r*, enclosed by the pillar ligands. Site-IV is at the wide pore cavity, where the water molecules are stabilised by the hydrogen bonding established with amino groups of the equatorial linkers, which in fact point towards the cavity. It is worth to note that both of the analysed crystal structures correspond to partial hydration states that sum up 7.98 and 6.94 water molecules per formula for EHU-30 and EHU-30-NH_2

respectively, which is below the saturation estimated from water adsorption isotherms at 50% RH (28.79 and 18.59 water molecules per formula, respectively).

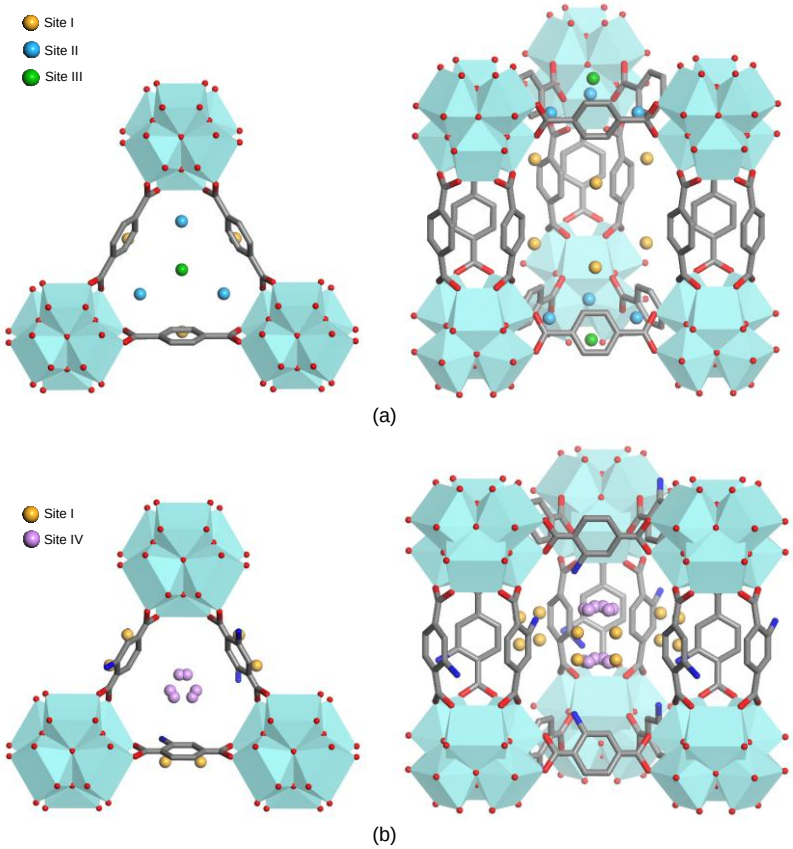

Figure 4.49. Physisorbed water molecules in (a) EHU-30 and (b) EHU-30-NH_2 located by TOF neutron diffraction data. O-atoms of crystallographically independent water molecules have been coloured in orange, blue, green and purple to highlight each distinguishable adsorption site. H-atoms have been omitted for clarity.

4.3. Cu(II)-DOPED EHU-30 MOFs FOR THE CONTINUOUS ELECTROREDUCTION OF CO_2

In this section, we have synthesised EHU-30 and EHU-30-NH_2 (Zr-based) and doped them with copper(II) to analyse their performance in the electroreduction of CO_2.

4.3.1. EXPERIMENTAL SECTION

4.3.1.1. Synthetic procedure

EHU-30(Zr) and EHU-30-NH_2(Zr) samples were prepared as explained in Section 4.2.1.1.

Doping process. Copper(II) nitrate (0.017g, 0.072 mmol) was dissolved in 7 mL of MeOH while stirring. Then, EHU-30 or EHU-30-NH_2 (0.072 mmol) were added and

the suspension was stirred at room temperature for 2 hours in a close vessel. Consecutively, the powdered sample was collected by vacuum filtration and washed with MeOH (7 mL) while stirring for 10 minutes to remove unreacted copper(II) salt. Finally, the obtained precipitate was collected again by vacuum filtration and dried at 80 °C for 1 h. For comparative purposes, the doping process was also performed for other metal transition metal ions on EHU-30(Zr) following the same procedure but using instead copper(II) nitrate, manganese(II) nitrate, iron(II) chloride, cobalt(II) nitrate, nickel(II) nitrate or zinc nitrate.

4.3.1.2. Physico-chemical characterization

Doped samples. The chemical analysis performed by X-ray fluorescence (XRF) on EHU-30 samples doped with different metal ions reveals that the doping is more efficient for copper(II), since it allows to include a noticeably greater amount of this metal into the structure. Figure 4.50 shows the M/Zr ratios (M(II): Mn, Fe, Co, Ni, Cu and Zn) for each doped sample.

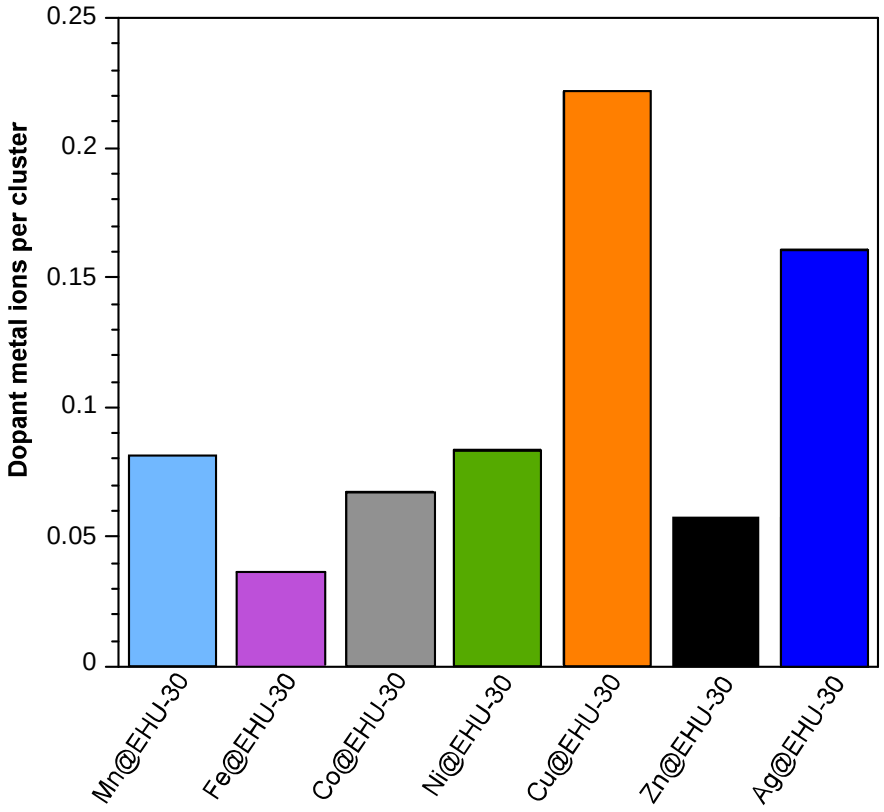

Figure 4.50. Amount of divalent transition metal ions included during the doping of EHU-30, referred as M/Zr ratio (M(II): Mn, Fe, Co, Ni, Cu, and Zn).

Powder X-ray diffraction (PXRD) analysis. The crystallinity and purity of the samples was assessed by powder X-ray diffraction. Figure 4.51 gathers the experimental PXRD patterns of parent and doped MOFs. The pattern-matching analysis of all Cu-doped samples (Figure 4.52), performed using the space group and cell parameters of EHU-

30 and EHU-30-NH_2 shows a good agreement as it can be inferred from the similar cell parameters and low disagreement factors (Table 4.14 to 4.17). According this, the Cu-doping does not exert any meaningful change in the crystal structure parameters which consistent with robustness of the Zr-MOF.

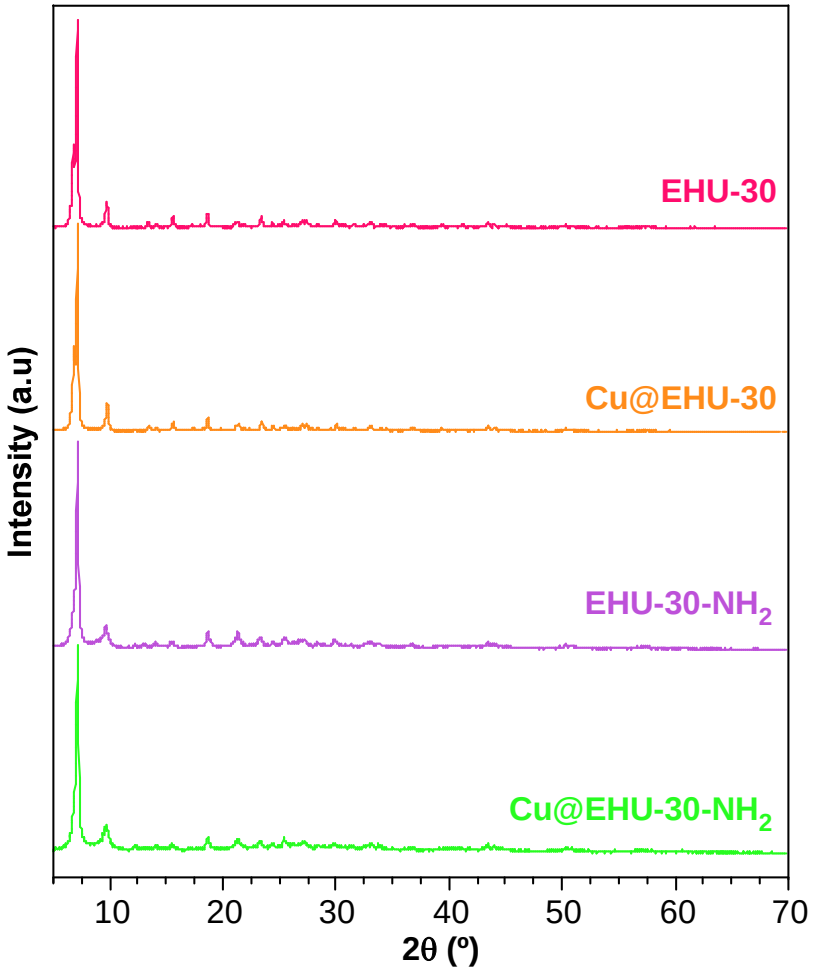

Figure 4.51. PXRD patterns of Cu(II)-doped metal-organic frameworks in comparison with diffractograms of EHU-30 and EHU-30-NH_2

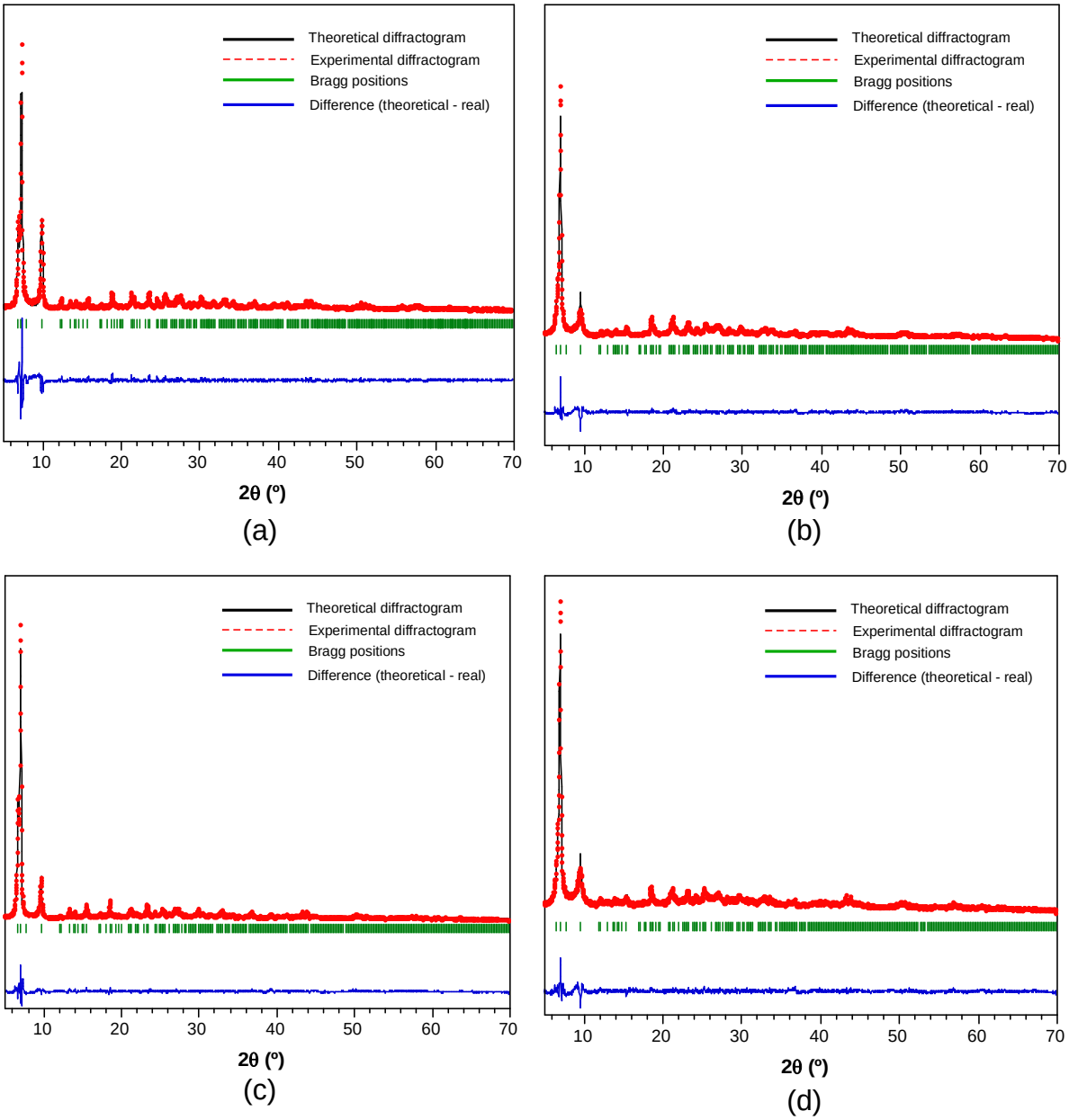

Figure 4.52. Pattern-matching analysis for (a) EHU-30, (b) EHU-30-NH_2, (c) Cu@EHU-30 and (d) Cu@EHU-30-NH_2 synthesized.

Table 4.14. Cell parameters and factors obtained by pattern-matching analysis made on EHU-30.

Reported for EHU-30		**Experimental profile fitting**	
Space group	*P*6$_3$/*mmc*	Space group	*P*6$_3$/*mmc*
a (Å)	14.6690(4)	a (Å)	14.666(3)
c (Å)	26.8478(1)	c (Å)	26.883(8)
V (Å^3)	5003.10	V (Å^3)	5008.07
		R_p	11.3
		R_{wp}	14.4
		R_{exp}	7.72
		χ^2	3.48

$R_p=100\cdot(\sum_{i=I,n}|y_i - y_{c,i}|)/(\sum_{i=I,n} y_i)$; $R_{wp}= \sqrt{[(\sum w_i(y_i(obs)-y_i(calc)^2)/ (\sum w_i y_i^2(obs))]}$; $R_{exp}= \sqrt{[(N-P-C)/ \sum w_i y_i^2(obs)]}$ and $\chi^2= [R_{wp}/R_{exp}]$.

Table 4.15. Cell parameters and factors obtained by pattern-matching analysis made on EHU-30-NH_2.

Reported for EHU-30-NH_2		**Experimental profile fitting**	
Space group	*P6₃/mmc*	Space group	*P6₃/mmc*
a (Å)	14.7044(12)	a (Å)	14.6741(4)
c (Å)	27.320(7)	c (Å)	27.363(1)
V (Å^3)	5115.71	V (Å^3)	5102.77
		R_p	9.60
		R_{wp}	13.8
		R_{exp}	7.10
		χ^2	3.79

$R_p=100\cdot(\sum_{i=I,n}|y_i - y_{c,i}|)/(\sum_{i=I,n} y_i)$; $R_{wp}= \sqrt{[(\sum w_i(y_i(obs)-y_i(calc)^2)/ (\sum w_i y_i^2(obs))]}$; $R_{exp}= \sqrt{[(N-P-C)/ \sum w_i y_i^2(obs)]}$ and $\chi^2= [R_{wp}/R_{exp}]$.

Table 4.16. Cell parameters and factors obtained by pattern-matching analysis made on Cu@EHU-30.

Reported for EHU-30		**Experimental profile fitting**	
Space group	*P6₃/mmc*	Space group	*P6₃/mmc*
a (Å)	14.6690(4)	a (Å)	14.6630(2)
c (Å)	26.8478(1)	c (Å)	26.6305(6)
V (Å^3)	5003.10	V (Å^3)	4958.59
		R_p	9.28
		R_{wp}	12.9
		R_{exp}	6.97
		χ^2	3.41

$R_p=100\cdot(\sum_{i=I,n}|y_i - y_{c,i}|)/(\sum_{i=I,n} y_i)$; $R_{wp}= \sqrt{[(\sum w_i(y_i(obs)-y_i(calc)^2)/ (\sum w_i y_i^2(obs))]}$; $R_{exp}= \sqrt{[(N-P-C)/ \sum w_i y_i^2(obs)]}$ and $\chi^2= [R_{wp}/R_{exp}]$.

Table 4.17. Cell parameters and factors obtained by pattern-matching analysis made on Cu@EHU-30-NH_2.

Reported for EHU-30-NH_2		**Experimental profile fitting**	
Space group	*P6₃/mmc*	Space group	*P6₃/mmc*
a (Å)	14.7044(12)	a (Å)	14.6955(3)
c (Å)	27.320(7)	c (Å)	27.305(1)
V (Å^3)	5115.71	V (Å^3)	5106.84
		R_p	8.87
		R_{wp}	11.9
		R_{exp}	7.52
		χ^2	2.52

$R_p=100\cdot(\sum_{i=I,n}|y_i - y_{c,i}|)/(\sum_{i=I,n} y_i)$; $R_{wp}= \sqrt{[(\sum w_i(y_i(obs)-y_i(calc)^2)/ (\sum w_i y_i^2(obs))]}$; $R_{exp}= \sqrt{[(N-P-C)/ \sum w_i y_i^2(obs)]}$ and $\chi^2= [R_{wp}/R_{exp}]$.

Fourier-transform infrared specta (FTIR). The infrared spectra of Cu@EHU-30 and Cu@EHU-30-NH_2 in comparison to EHU-30 and EHU-30-NH_2 samples and the assignation of the mian vibrational modes are shown in Figure 4.53. The large O–H peaks in the IR spectra are indicative of H_2O/OH^- pairs that replace the missing linkers in the structure.

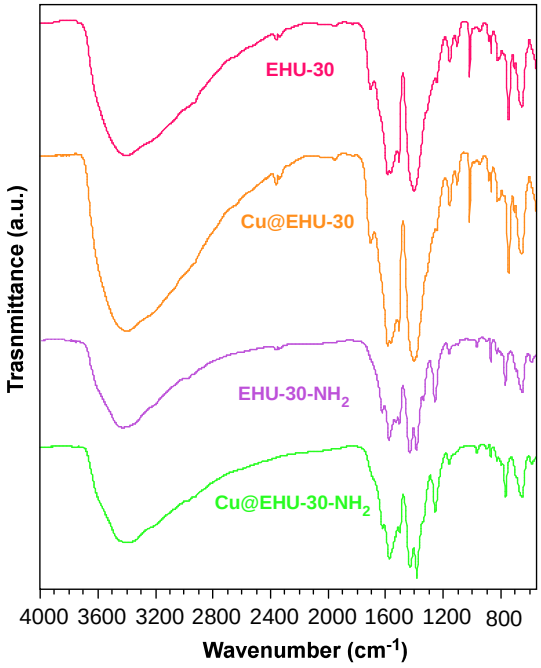

(a)

$\bar{\nu}$ (cm^{-1})	EHU-30 Cu@EHU-30	EHU-30-NH_2 Cu@EHU-30-NH_2
ν (OH)	3000-3700, m	3000-3700, m
ν_{asym} (NH_2)	--	3400-3500, m
ν (C–H)	3000-2850, w-m	3000 - 2850, w-m
ν_{asym} (COO)	1700 m	1700 m
ν (C_{ar}–C)	1575, s	1575, s
ν_{ring} (C_{ar}–C_{ar})	1500, m	1500, m
ν_s (COO)	1425, s	1430, s
ν (Car-N)	--	1380, s
δ_{ip} (NH_2)	1336, sh	1336, sh
δ_{oop} (NH_2)	1255, m	1255, m
δ_{oop} (C-H)	750, s	770, s
ν (M–O_{oxide})	650, m	650, m
ν (M–O_{coo})	550, m	580, m
ν (M–O_{OH})	490, m	490, m

(b)

Figure 4.53. (a) FTIR spectra and (b) band assignments for parent and doped MOFs (s: strong, m: medium, w: weak and sh: shoulder signals; *sym*: symmetric, *asym*: asymmetric, *ip*: in plane, *ring*: ring stretching, *ar*: aromatic, *oop*: out of plane of stretching (ν) or bending (δ) modes).

N_2 adsorption isotherms (77 K) are gathered in Figure 4.54. Figure 4.55 gathers the consistency plot for BET surface calculations while Table 4.18 summarised the extracted data from isotherms.

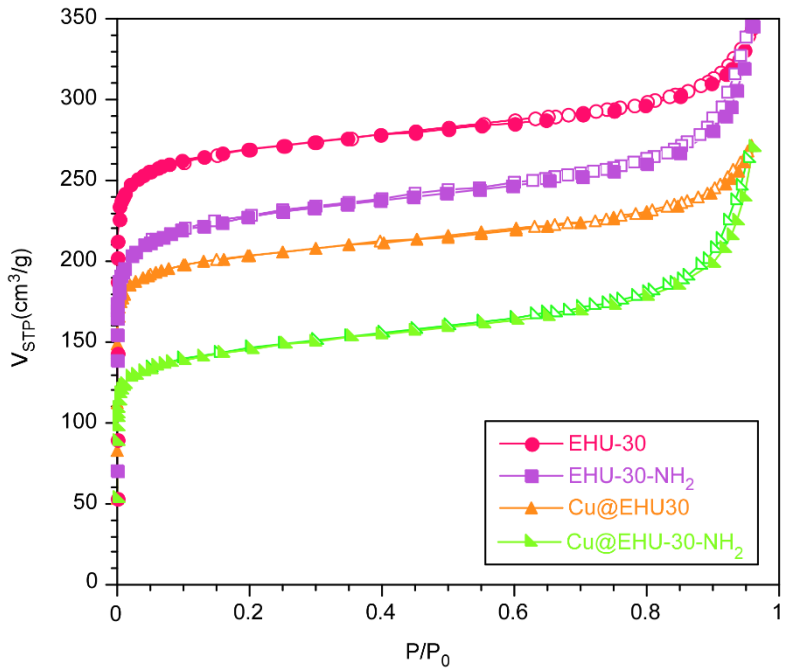

Figure 4.54. Nitrogen adsorption isotherm for EHU-30, Cu@EHU-30, EHU-30-NH_2 and Cu@EHU-30-NH_2.

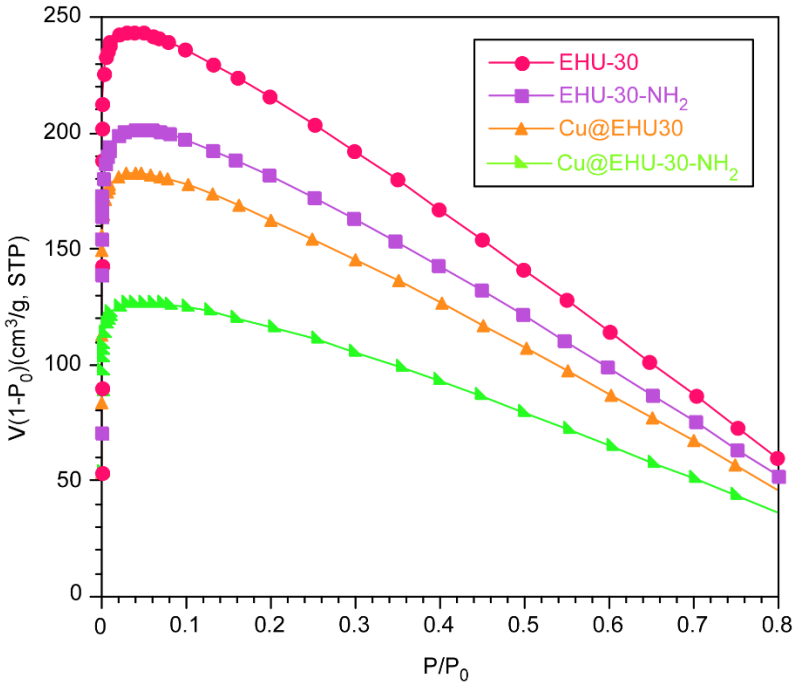

Figrue 4.55. Consistency plot [$V(1 - P/P_0)$ vs. P/P_0] for experimental N_2 isotherms represented in Figures 4.54.

Table 4.18. BET fitting details for experimental N_2 isotherms.

Code	P/P₀ range	S_{BET} (m^2/g)	R^2	C	V_m (cm^3/g)	P/P₀ for V_m (interpolation)
EHU-30	0.0009–0.0304	1065	0.99999	5838.8	233.10	0.01368
Cu@EHU-30	0.00201–0.0397	801	0.99999	3242.2	183.95	0.01831
EHU-30-NH_2	0.0006–0.0206	885	0.99997	2489.2	203.11	0.01053
Cu@EHU-30-NH_2	0.0041–0.0048	558	0.99999	2281.3	128.13	0.02113

CO_2 adsorption isotherms were measured at 273 and 298 K (Figure 4.55). The lowering of CO_2 uptake capacity at medium-high pressures follows the same trend to that observed for N_2 isotherms.

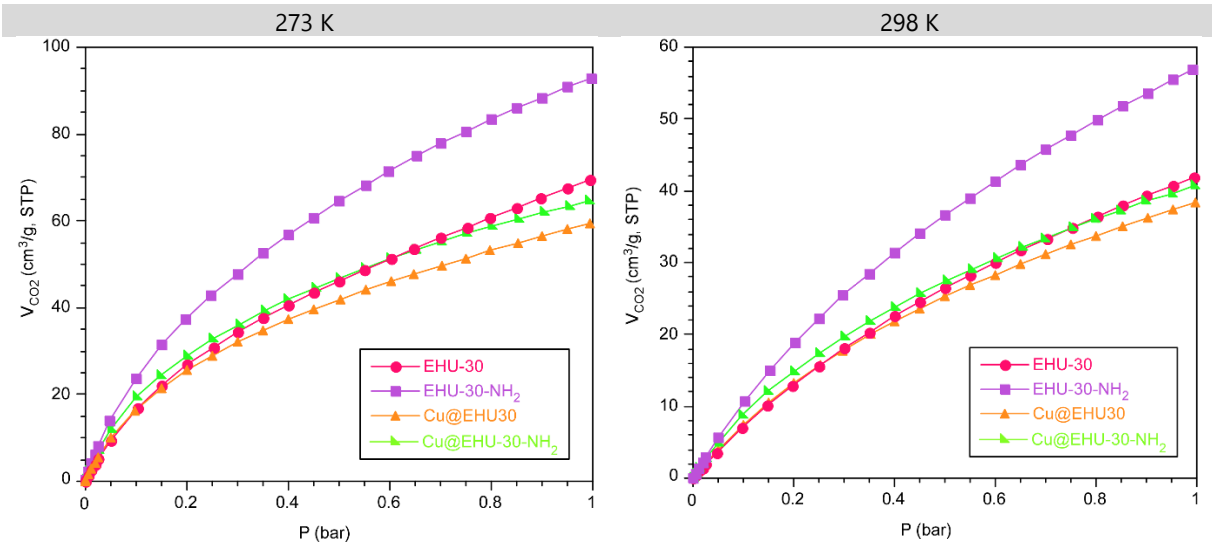

Figure 4.56. CO_2 adsorption isotherms at 273 and 298 K for EHU-30, Cu@EHU-30, EHU-30-NH_2 and Cu@EHU30-NH_2.

With the aim of estimating CO_2 adsorption enthalpies, the isotherms were fitted to modified Clausius-Clapeyron equation.[57] Figure 4.57 shows the calculated isosteric heats of adsorption (Q_{st}).

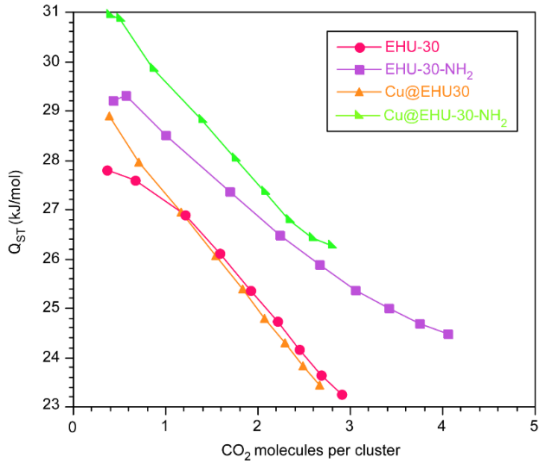

Figure 4.57. Calculated isosteric heats of adsorption for CO_2.

4.3.2. Continuous CO_2 reduction experiments

Preparation of MOF-GDEs and electrochemical experiments were performed following the procedure gathered in Section 3.2.1 of Chapter 3.

In this case, the continuous CO_2 electroredution performance was performed using a current density of j= 10 mA·cm^{-2}, a CO_2 flow/area ratio of $Q_{g/A}$= 20 mL·min^{-1}·cm^{-2} and a flow rate of anolyte and catholyte of $Q_{e/A}$= 2 mL·min^{-1}·cm^{-2}. The experimental time was 90 min, except for the stability test where the material was evaluated for 400 min. Liquid samples were taken every 15 min from the catholyte tank. Besides, gas-phase reduction products were analysed every 5 min. The concentration of every product was averaged from at least three replicates with a maximum standard deviation of 15.6 %.

Table 4.19 and 4.20 summirised the Faradaic efficiencies (FE) and their time-dependence evolution with respect to the potential employed.

Table 4.19. FEs for the continuous electroreduction of CO_2 and hydrogen evolution using EHU-30-based GDEs (j = 10 mA·cm^{-2}; $Q_{e/A}$ = 2 mL·min^{-1}·cm^{-2}, $Q_{g/A}$ = 20 mL·min^{-1}·cm^{-2}).[a]

Material	***E* (V vs. Ag/AgCl)**	***FE (%)***						
		CO	HCOOH	*CH_3OH*	*C_2H_4*	*TOTAL (CO_2 products)*	*H_2*	***TOTAL***
EHU-30	-2.01	3.3±0.8	8.4±1.1	-	-	11.7	77.5	**89.2**
EHU-30-NH_2	-1.82	5.6±1.1	10.5±1.8	-	-	16.1	71.6	**87.7**
Cu@EHU-30	-1.54	5.1±0.4	7.9±0.8	2.9±0.7	4.1±0.5	20.1	63.6	**83.7**
Cu@EHU-30-NH_2	**-1.46**	**7.6±0.6**	**9.6±1.4**	**6.1±2.1**	**7.5±1**	**30.9**	**51.8**	**82.7**

[a]: Traces of ethanol were detected.

Table 4.20. Time-dependence on total FE (CO_2 products) with Cu@EHU-30-NH_2 (j = 10 mA·cm^{-2}; $Q_{e/A}$= 2 mL·min^{-1}·cm^{-2}, $Q_{g/A}$= 20 mL·min^{-1}·cm^{-2}).

Time (min)	**E (V vs. Ag/AgCl)**	***FE_{TOTAL}* (%)**
15	-1.59	21.2±2
30	-1.62	26.6±2.9
45	-1.51	28.5±1.8
60	-1.48	30.9±2.2
75	-1.46	30.9±3
90	-1.46	30.8±3.1
120	-1.48	31.2±1.9
150	-1.49	32.4±2.2
220	-1.51	30.7±1.4
250	-1.55	29.6±2
280	-1.56	29.9±1
400	-1.60	27.7±0.9

Post-CO_2-reduction GDEs characterization. SEM, FTIR, and ^{1}H-NMR analyses were performed for the GDE containing Cu@EHU-30-NH_2 catalyst before and after the CO_2 reduction reaction. The results are shown in Figures 4.58–4.60. SEM images show microcrystallites of Cu@EHU-30-NH_2 dispersed in Nafion. Note that not all the material can be observed as part is masked by the Nafion. The comparison of the images suggests that some material is leached during the reaction. The FTIR spectra collected by attenuated total reflectance (ATR) mode show that the main vibration modes of the metal-organic framework persist indicating that the overall molecular structure is retained. Furthermore, the ^{1}H-NMR spectra show that the signals corresponding to the aromatic ring of NH_2BDC ligand remain invariable, ensuring the stability of the amino group during the reaction.

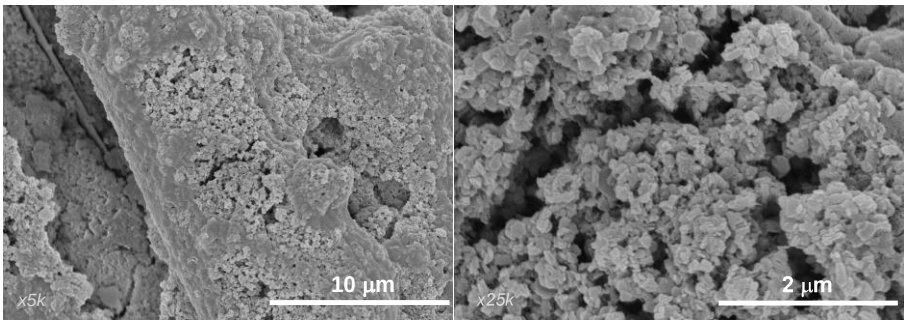

(a)

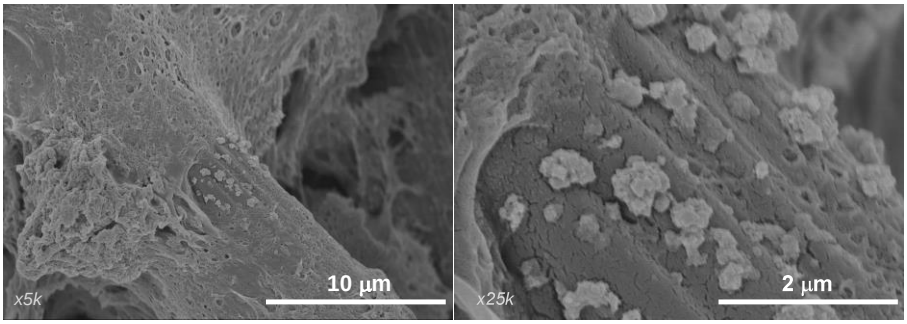

(b)

Figure 4.58. SEM images taken on GDEs containing Cu@EHU-30-NH_2 catalyst (a) before and (b) after the CO_2 reduction reaction.

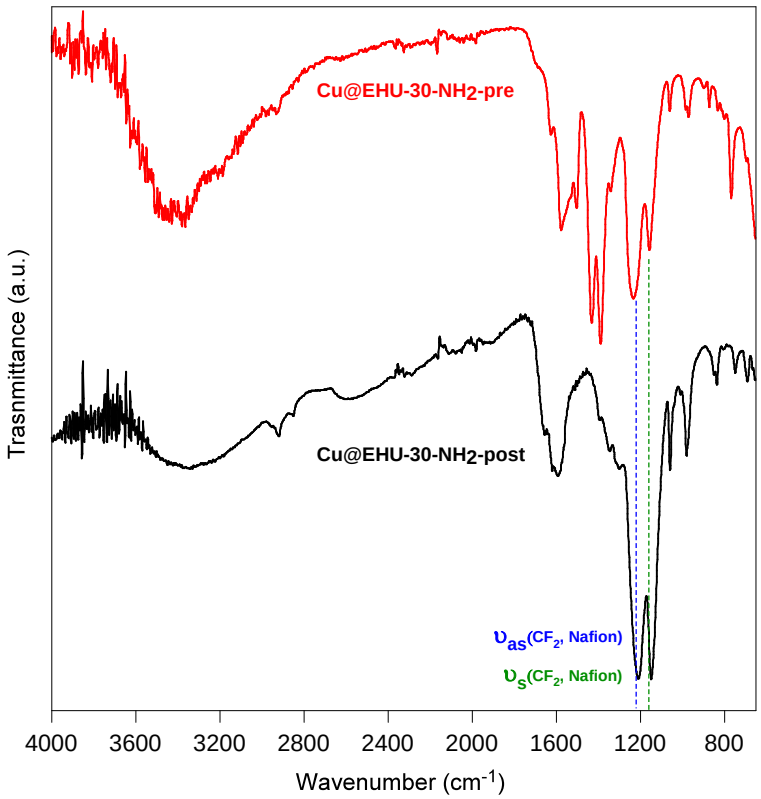

Figure 4.59. FTIR-ATR spectra taken on GDEs containing Cu@EHU-30-NH_2 catalyst before (black) and after (red) the CO_2 reduction reaction.

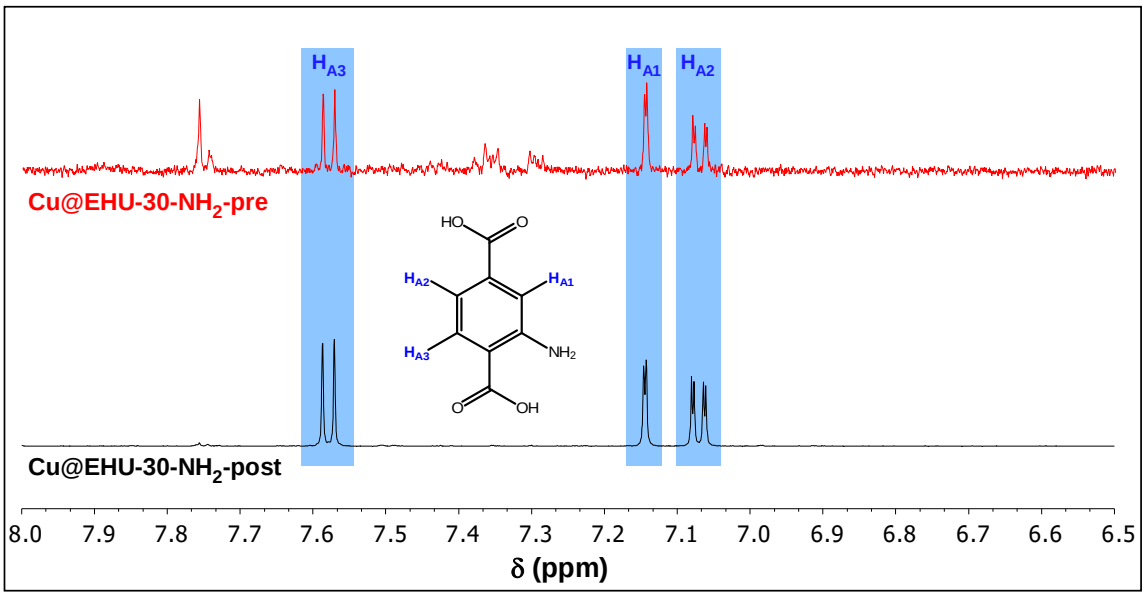

Figure 4.60. ^{1}H-NMR spectra collected for Cu@EHU-30-NH_2 before and after the CO_2 reduction reaction**.**

4.3.3. RESULTS AND DISCUSSION

As a result of doping process, a Cu/Zr ratio determined by X-ray fluorescence (XRF) of 0.04 and 0.05 was achieved for each MOF (Cu@EHU-30 and Cu@EHU-30-NH_2), while no traces of nitrate remained in the doped frameworks. Transmission electron microscopy (TEM) images show a homogeneous distribution of the dopant metal over the hexagonal prism shaped crystallites of the MOFs (Figure 4.61), while the comparison of powder X-ray diffraction (PXRD) patterns with those of pristine MOFs ensures the phase purity of the samples after doping process (see previous section). According to the profile fitting performed on the PXRD data, the Cu-doping does not exert any meaningful change in the crystal structure parameters which is consistent with robustness of the zirconium coordination framework.

Pair distribution function analysis (PDF) of synchrotron total scattering data of EHU-30 and Cu@EHU-30 (Figure 4.62a) show almost coincident profiles, with some subtle differences in the intensity of the signal after normalisation to chemical composition. The simulated PDF data show a decay of the intensity for the atom-atom correlations corresponding to Zr···Zr, Zr–O and Zr···O distances, which suggests that the inclusion of copper takes place through a transmetalation reaction. The absence of new peaks in the PDF profile of Cu@EHU-30 compared to that of the pristine material allows to disregard a chemical anchoring to the cluster or nucleation of copper in the pore cavity.

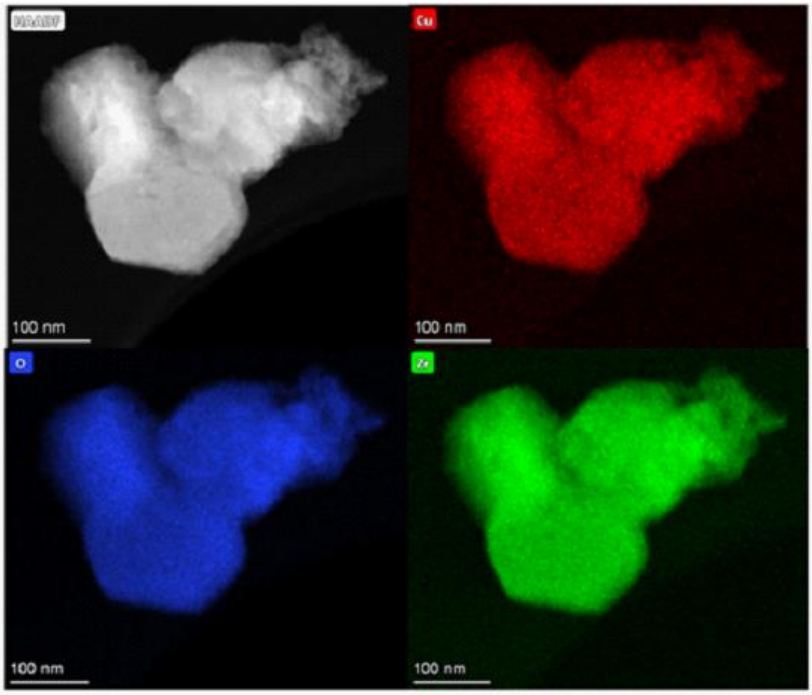

Figure 4.61. HAADF-TEM and elemental mapping (EDXRF) taken on Cu@EHU-30.

Furthermore, the chemical balance analysis (Figure 4.62b) performed in the digested sample solution and in the post-doping solution fits the expectations for a

transmetalation reaction in which each incorporated copper atom replaces a zirconium atom of the hexanuclear cluster. Note that the high ratio of linker vacancies in EHU-30 series and the stress accumulated on the triple bunch of linkers can facilitate the replacement of Zr from the SBU. In fact, upon similar doping conditions, the metalation with Cu(II) of the polymorphic UiO-66 series takes place through chemical anchorage at the SBU, which seems to support the relevance of the unique structural features of EHU-30 series into the transmetalation reaction. We also observed that upon same doping conditions other divalent first row transition metal ions (Mn, Fe, Co, Ni, Zn) led to markedly smaller metalation (M/Zr ratio: 0.006–0.014, previous section) than that achieved for copper, which can be related to the plasticity of the coordination sphere of Cu(II) that can ease its inclusion.

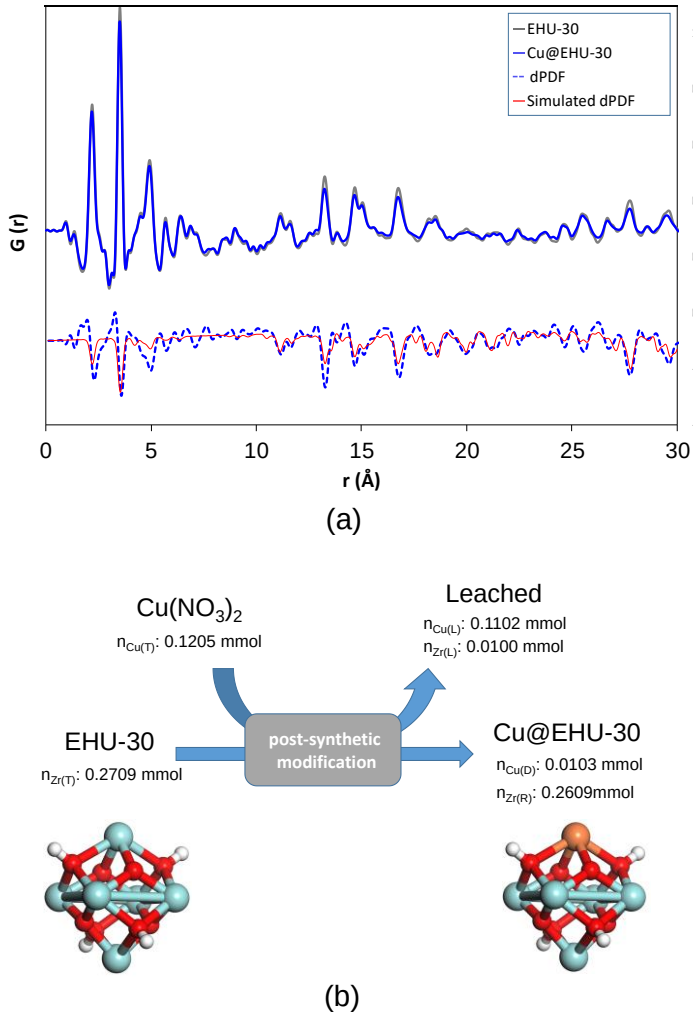

Figure 4.62. (a) Total PDF data of EHU-30 and Cu@EHU-30, and differential PDF signal to highlight changes in intensity. (b) Molar balance resulting from the post-synthetic metalation of EHU-30 depicting a representative image of the transmetalation within the inorganic core $\{Zr_6O_4(OH)_4\}$.

Prior to the electrochemical transformation experiments, the porosity of the pristine and doped samples was assessed by the measurement of dinitrogen and carbon dioxide adsorption isotherms (previous section). All the N_2 (77 K) adsorption curves resemble a type I isotherm with a sharp knee at low relative pressures ($p/p° < 0.04$), as expected for microporous samples. The slight progressive increase at intermediate pressures and the condensation at relative high pressures ($p/p° > 0.94$) is explained by the interparticle porosity of the nanosized crystallites. The estimated BET surface area was smaller for doped samples (Cu@EHU-30 and Cu@EHU-30-NH_2: 801 and 558 $m^2 \cdot g^{-1}$) than for parent compounds (EHU-30 and EHU-30-NH_2: 1065 and 885 $m^2 \cdot g^{-1}$), which probably could be related to a slight crystallinity decrease led by the post-synthetic modification, as inferred from the increase of full width at half maximum (FWHM) values of the PXRD reflections (13 and 21% increase of FWHM for Cu@EHU-30 and Cu@EHU-NH_2, respectively). The isosteric heats of adsorption (Q_{st}) derived from CO_2 isotherms show values ranging from 27 to 31 $kJ \cdot mol^{-1}$ at near-zero coverage, which decay to 23–26 $kJ \cdot mol^{-1}$ when the gas uptake reaches a ratio of 2.5 CO_2 per metal cluster. At low coverage, the Q_{st} values of EHU-30-NH_2 (29.2 $kJ \cdot mol^{-1}$) overpasses those provided by EHU-30 (27.8 $kJ \cdot mol^{-1}$), which can be explained by the enhanced interacting capacity provided by the amino-group upon the CO_2 adsorption.[58] Besides, the inclusion of Cu(II) seems to improve also the affinity towards CO_2 as it also yields somewhat higher Q_{st} values (Cu@EHU-30 and Cu@EHU-30-NH_2: 28.9 and 30.9 $kJ \cdot mol^{-1}$) than those exhibited by the parent compounds.

Table 4.21 gathers the data for the continuous transformation of CO_2 at galvanostatic conditions in a filter press electrochemical cell obtained for the GDEs prepared. The analysis is performed in terms of reaction rates for CO, HCOOH, CH_3OH and C_2H_4 formation, as well as the total rate and cell potential (E). The corresponding Faradaic efficiency (FE) values were calculated considering that 2 e^- are required per molecule of CO and HCOOH, 6 e^- for CH_3OH and 12 e^- for C_2H_4 (Figure 4.63a). The rest of the efficiency is related to H_2 evolution (see previous section) and energy losses of the cell (ohmic resistance). No other liquid products were detected, except non-quantifiable traces of ethanol. Control experiments for neat carbon papers did not produce any measurable product, so the performance can be ascribed to the catalytic activity of the selected materials.

Neat zirconium MOFs exhibit moderate reaction rates and efficiencies for the CO_2 conversion into CO and HCOOH. The FE_{HCOOH} values are higher (8.4 and 10.5% for EHU-30 and EHU-30-NH_2, respectively) than those achieved with other zirconium metal-organic materials (2.3–4.2%) in equal operating conditions.[59] Besides, the amino-function in EHU-30-NH_2 boosts the yield toward both CO and HCOOH, reaching higher total reaction rates and FE values than the not functionalised EHU-30

(61.9 vs 47.9 μmol·m^{-2}·s^{-1}; 16.1 vs 11.7 %). This improvement might be related with the greater affinity towards CO_2 uptake provided by the amino-functionalization, as demonstrated by the measured isosteric heats of adsorption. In fact, previous works have stated that the inclusion of amino functional groups favours the CO_2 adsorption and as a consequence, CO_2 reduction reaction is favoured with respect HER.[60] This trend is also observed in the series of MOF herein analysed. Note that as below described, the inclusion of copper(II) seems to have the same effect and therefore, the overall performance could be ascribed to a dual active site system.

As it was aimed, the inclusion of copper(II) promotes a further conversion of CO_2 into more reduced species, *i.e.* methanol and ethylene, while the CO and HCOOH yields are almost retained. As a result, the total reaction rates and Faradaic efficiency experience a meaningful enhancement doubling the performance of pristine MOFs (Cu@EHU-30: 74.0 μmol·m^{-2}·s^{-1}and 20.1%; Cu@EHU-30-NH_2: 109.3 μmol·m^{-2}·s^{-1} and 30.9%).

Considering the results for homometallic Cu^{II}-MOFs and heterometallic Cu^{II}/M-MOFs (M: Zn^{II}, Ru^{III}, Pd^{II}) presented in Chapter 3 the herein prepared materials provide a similar yield of the most reduced products (alcohols and alkanes) and a greater performance when considering all products, despite of the relative low amount of copper(II) used in the doped samples (Cu@EHU-30 and Cu@EHU-30-NH_2: 9.1 and 11 mg Cu/g MOF; Chapter 3 presented copper-based MOFs: 123–350 mg Cu/g MOF). Such behaviour can be ascribed to a synergic relation implying both zirconium and copper metal centres. In this sense, formic acid can be considered an intermediate product in the formation of alcohols and alkanes. Thus, its concentration in the reaction media limits the yield toward the more reduced species that Cu containing MOFs can yield. Since Cu^{II}-MOFs lead to rather low formation of formic acid and zirconium based materials yields formic acid as the mayor product, the simultaneous presence of both metal centres invigorates the overall performance of the reaction. Similar results were observed for the physical mixture of polycrystalline MOFs of Cu(II) and Bi(III) also presented in Chapter 3, but using greater amounts of copper (52–289 mg Cu/g MOF).

To assess the long term stability of the neat and Cu-doped zirconium MOFs, the continuous transformation of CO_2 was monitored for 400 minutes. The resulting time dependence for the total FE for Cu@EHU-30-NH_2 is plotted in Figure 4.63b along with the current/density potential over time. The results show a slight increase of the performance during the first 90 minutes to get into a roughly steady conversion of CO_2. Such stable conversion is related to the stability provided by the zirconium-based coordination framework and implies a considerable advantage with respect to Cu-based MOF for which the performance decays at reaction times shorter than 1 hour. Consider that Cu-based MOFs imply a framework built by the assembly of Cu-SBUs

and carboxylate linkers, which provide a feebler structure than that based on zirconium-carboxylate bonding.[61]

Table 4.21. Reaction rates (r) for the electroreduction of CO_2 using EHU-30-based GDEs.[a]

Material	*E* (V)	r (μmol·m^{-2}·s^{-1})				
		CO	HCOOH	*CH_3OH*	*C_2H_4*	*TOTAL*
EHU-30	-2.01	4.2	43.7	-	-	47.9
EHU-30-NH_2	-1.82	7.2	54.7	-	-	61.9
Cu@EHU-30	-1.54	6.6	40.9	5.1	21.4	74.0
Cu@EHU-30-NH_2	-1.46	9.8	49.8	10.6	39.1	109.3

[a] The cell potential (E) was measured using Ag/AgCl reference electrode. Current density (j) was set to 10 mA·cm^{-2}, while electrolyte ($Q_{e/A}$) and CO_2 gas flow ($Q_{g/A}$) were maintained 2 and 20 mL·min^{-1}·cm^{-2}, respectively. The data correspond to 90 min of reaction.

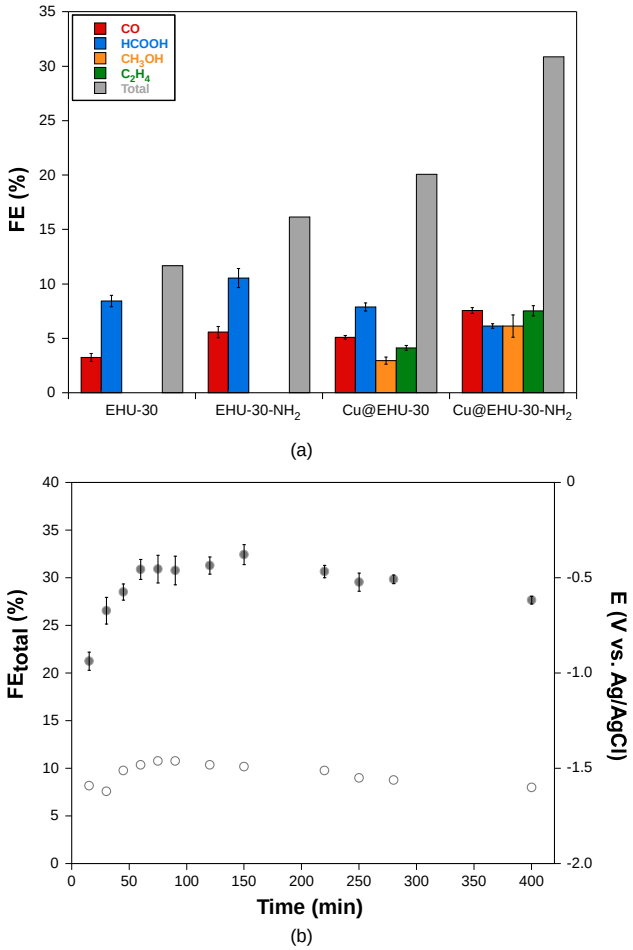

Figure 4.63. (a) FE as a function of the electrocatalytic material applied. (b) Time-dependence of total FE (filled circles) and current density/potential (empty circles) for all CO_2 reduction products using Cu@EHU-30-NH_2.

4.4. CONCLUSIONS

The careful selection of the structure directing agents and the use of solvent-less synthesis conditions allowed to isolate five new isoreticular compounds. The so-called Zr-based EHU-30, that could be consider the first strict polymorph of well known UiO-66 and its amino functionalised family based on group 4 metal centres: EHU-30-NH_2(M) and EHU-30-NHR(M) (M: Zr, Hf; R: 2-carboxypropyl). The analysis of the crystal structure of these new materials discloses a framework with **hex**-type topology in which wide pore cavities (~8 Å) are connected by means of narrower necks whose size is limited by the linkers connecting the SBUs (neck-*t*: 5.5 Å; neck-*r*: 6.5 Å). With this regard, the adsorption properties were meaningfully influenced by both amino-substituent of the linker and the type of metal comprising the SBU. As expected, the amino-functionalized and hafnium-containing MOFs exhibited lower specific surface area values than the parent EHU-30(Zr). Contrarily, the isosteric heats of CO_2 adsorption increase with the functionalization of the linker and with the replacement of zirconium by hafnium. Such behaviour can be rationalized on the basis of the probability density maps obtained from the GCMC simulations, which reveal two preferred adsorption sites. The first site is enclosed within the linkers of neck-*t* and its occupation is boosted by the presence of the amino substituent in the linker. The second one is found in the vicinity of the μ_3-O/OH groups and it is influenced by the type of metal comprising the SBU.

Likewise, the threshold for the water vapour adsorption occurred at lower relative humidity values for the functionalized compounds (EHU-30-NH_2/NHR: < 15%; EHU-30: 35%), as a result of the greater hydrophilicity provided by the amino group. Interestingly, the water adsorption and desorption branches of the isotherms show an uncommon crossing which was found to be sensible to the temperature, sorption cycles and functionalization of the linker. This behaviour has been rationalized on the basis of PXRD and solid-state ^{13}C-NMR measurements and attributed to a local and partial structural transformation from the metastable EHU-30 to UiO-66. This structural rearrangement is probably eased by the meaningful linker vacancies found in EHU-30, which render free edges in the SBU ready to admit incoming ligands. In any case, upon the water vapour adsorption conditions the range of the transformation process was least and the overall structure of EHU-30 was retained.

Furthermore, EHU-30 and EHU-30-NH_2 zirconium-based MOFs were doped with Cu(II) at Cu/Zr ratios of 0.04 and 0.05, displaying a homogenous distribution of copper over the MOF nanoscopic crystallites. The chemical balance and PDF analysis suggest a transmetalation reaction in such a way that each incorporated copper atom replaces a zirconium atom of the metal cluster that comprises the SBU of the MOF. When comparing the results of the CO_2 electroreduction reactions, the MOFs containing the

amino functional group (EHU-30-NH_2 and Cu@EHU-30-NH_2) led to a better performance than their not functionalised analogous materials (EHU-30 and Cu@EHU-30), probably, due to the favoured CO_2 adsorption of the formers. Besides, while neat zirconium MOFs produce CO and HCOOH as the major products, doping them with copper turns the product selectivity toward more reduced species (methanol and ethylene) but also enhances markedly the overall performance doubling the total reaction rates and Faradaic efficiencies of neat zirconium MOFs. Apart from that, the inclusion of copper as dopant into a zirconium metal-organic framework provides a roughly stable continuous transformation of CO_2 into value-added products and thus, it precludes the rapid deactivation reported for Cu-based MOFs, which is a major obstacle for the application of this kind of materials in CO_2 electroreduction reactions.

4.5. References

1 S. Yuan, J.-S. Qin, C. T. Lollar and H.-C. Zhou, Stable Metal–Organic Frameworks with Group 4 Metals: Current Status and Trends, *ACS Cent. Sci.*, 2018, **4**, 440–450.

2 J. H. Cavka, S. Jakobsen, U. Olsbye, N. Guillou, C. Lamberti, S. Bordiga and K. P. Lillerud, A New Zirconium Inorganic Building Brick Forming Metal Organic Frameworks with Exceptional Stability, *J. Am. Chem. Soc.*, 2008, **130**, 13850–13851.

3 Y. Bai, Y. Dou, L.-H. Xie, W. Rutledge, J.-R. Li and H.-C. Zhou, Zr-based metal–organic frameworks: design, synthesis, structure, and applications, *Chem. Soc. Rev.*, 2016, **45**, 2327–2367.

4 S. Whitelam and R. L. Jack, The Statistical Mechanics of Dynamic Pathways to Self-Assembly, *Annu. Rev. Phys. Chem.*, 2015, **66**, 143–163.

5 H. Su, Y. Du, J. Zhang, P. Peng, S. Li, P. Chen, M. Gozin and S. Pang, Stabilizing Metastable Polymorphs of Metal–Organic Frameworks via Encapsulation of Graphene Oxide and Mechanistic Studies, *ACS Appl. Mater. Interfaces*, 2018, **10**, 32828–32837.

6 S. L. Anderson, A. Gładysiak, P. G. Boyd, C. P. Ireland, P. Miéville, D. Tiana, B. Vlaisavljevich, P. Schouwink, W. van Beek, K. J. Gagnon, B. Smit and K. C. Stylianou, Formation pathways of metal–organic frameworks proceeding through partial dissolution of the metastable phase, *CrystEngComm*, 2017, **19**, 3407–3413.

7 A. K. Cheetham, G. Kieslich and H. H.-M. Yeung, Thermodynamic and Kinetic Effects in the Crystallization of Metal–Organic Frameworks, *Acc. Chem. Res.*, 2018, **51**, 659–667.

8 M. Lanchas, D. Vallejo-Sánchez, G. Beobide, O. Castillo, A. T. Aguayo, A. Luque and P. Román, A direct reaction approach for the synthesis of zeolitic imidazolate frameworks: template and temperature mediated control on network topology and crystal size, *Chem. Commun.*, 2012, **48**, 9930–9932.

9 E. C. Spencer, R. J. Angel, N. L. Ross, B. E. Hanson and J. A. K. Howard, Pressure-Induced Cooperative Bond Rearrangement in a Zinc Imidazolate Framework: A High-Pressure Single-Crystal X-Ray Diffraction Study, *J. Am. Chem. Soc.*, 2009, **131**, 4022–4026.

10 A. Schaate, P. Roy, A. Godt, J. Lippke, F. Waltz, M. Wiebcke and P. Behrens, Modulated synthesis of Zr-based metal-organic frameworks: From nano to single crystals, *Chem. - A Eur. J.*, 2011, **17**, 6643–6651.

11 H. Wu, Y. S. Chua, V. Krungleviciute, M. Tyagi, P. Chen, T. Yildirim and W. Zhou, Unusual and Highly Tunable Missing-Linker Defects in Zirconium Metal–Organic Framework UiO-66 and Their Important Effects on Gas Adsorption, *J. Am. Chem. Soc.*, 2013, **135**, 10525–10532.

12 F. Vermoortele, B. Bueken, G. Le Bars, B. Van de Voorde, M. Vandichel, K. Houthoofd, A. Vimont, M. Daturi, M. Waroquier, V. Van Speybroeck, C. Kirschhock and D. E. De Vos, Synthesis Modulation as a Tool To Increase the Catalytic Activity of Metal–Organic Frameworks: The Unique Case of UiO-66(Zr), *J. Am. Chem. Soc.*, 2013, **135**, 11465–11468.

13 V. Bon, V. Senkovskyy, I. Senkovska and S. Kaskel, Zr(iv) and Hf(iv) based metal–organic frameworks with reo-topology, *Chem. Commun.*, 2012, **48**, 8407–8409.

14 Y.-F. Zhang, Q. Wang, D.-X. Xue and J. Bai, Single-crystal synthesis and diverse topologies of hexanuclear Ce^{IV}-based metal–organic frameworks, *Inorg. Chem.*, 2020, **59**, 11233–11237.

15 N. Hanikel, M. S. Prévot and O. M. Yaghi, MOF water harvesters, *Nat. Nanotechnol.*, 2020, **15**, 348–355.

16 S. Kim, Hyunho, Yang, S. R. Rao, S. Narayanan, E. A. Kapustin, H. Furukawa, A. S. Umans, O. M. Yaghi and E. N. Wang, Water harvesting from air with metal-organic frameworks powered By Natural Sunlight, *Science.*, 2017, **356**, 430–434.

17 F. Fathieh, M. J. Kalmutzki, E. A. Kapustin, P. J. Waller, J. Yang and O. M. Yaghi, Practical water production from desert air, *Sci. Adv.*, 2018, **4**, 1–10.

18 H. Kim, S. R. Rao, E. A. Kapustin, L. Zhao, S. Yang, O. M. Yaghi and E. N. Wang, Adsorption-based atmospheric water harvesting device for arid climates, *Nat. Commun.*, 2018, **9**, 1–8.

19 H. Furukawa, F. Gándara, Y. B. Zhang, J. Jiang, W. L. Queen, M. R. Hudson and O. M. Yaghi, Water adsorption in porous metal-organic frameworks and related materials, *J. Am. Chem. Soc.*, 2014, **136**, 4369–4381.

20 N. C. Burtch, H. Jasuja and K. S. Walton, Water stability and adsorption in metal-organic frameworks, *Chem. Rev.*, 2014, **114**, 10575–10612.

21 X. Liu, X. Wang and F. Kapteijn, Water and Metal-Organic Frameworks: From Interaction toward Utilization, *Chem. Rev.*, 2020, **120**, 8303–8377.

22 G. E. Cmarik, M. Kim, S. M. Cohen and K. S. Walton, Tuning the adsorption properties of UiO-66 via ligand functionalization, *Langmuir*, 2012, **28**, 15606–15613.

23 P. Ghosh, Y. J. Colón and R. Q. Snurr, Water adsorption in UiO-66: The importance of defects, *Chem. Commun.*, 2014, **50**, 11329–11331.

24 A. A. Coelho, TOPAS-Academic V5, Coelho software, Brisbane, Australia, http://www.topas-academic.net/, (Accessed: January 2019).

25 A. A. Coelho, TOPAS and TOPAS-Academic: An optimization program integrating computer algebra and crystallographic objects written in C++, *J. Appl. Crystallogr.*, 2018, **51**, 210–218.

26 G. Oszlányi and A. Sütő, Ab initio structure solution by charge flipping, *Acta Crystallogr. Sect. A*, 2004, **60**, 134–141.

27 A. A. Coelho, Tangent formula, symmetry consideration, determination of origin, atom picking and assignment, *Acta Crystallogr.*, 2007, **A36**, 400–406.

28 H. M. Rietveld, A profile refinement method for nuclear and magnetic structures, *J. Appl. Crystallogr.*, 1969, **2**, 65–71.

29 P. Thompson, D. E. Cox and J. B. Hastings, Rietveld refinement of Debye–Scherrer synchrotron X-ray data from Al 2 O 3, *J. Appl. Crystallogr.*, 1987, **20**, 79–83.

30 M. Kandiah, M. H. Nilsen, S. Usseglio, S. Jakobsen, U. Olsbye, M. Tilset, C. Larabi, E. A. Quadrelli, F. Bonino and K. P. Lillerud, Synthesis and stability of sagged UiO-66 Zr-MOFs, *Chem. Mater.*, 2010, **22**, 6632–6640.

31 Y. Bai, Y. Dou, L.-H. Xie, W. Rutledge, J.-R. Li and H.-C. Zhou, Zr-based metal–organic frameworks: design, synthesis, structure, and applications, *Chem. Soc. Rev.*, 2016, **45**, 2327–2367.

32 G. Liu, Z. Ju, D. Yuan and M. Hong, In situ construction of a coordination zirconocene tetrahedron, *Inorg. Chem.*, 2013, **52**, 13815–13817.

33 M. Taddei, J. A. van Bokhoven and M. Ranocchiari, Influence of Water in the Synthesis of the Zirconium-Based Metal–Organic Framework UiO-66: Isolation and Reactivity of [ZrCl(OH)2(DMF)2]Cl, *Inorg. Chem.*, 2020, **59**, 7860–7868.

34 V. V Butova, A. P. Budnyk, K. M. Charykov, K. S. Vetlitsyna-Novikova, C. Lamberti and A. V Soldatov, Water as a structure-driving agent between the UiO-66 and MIL-140A metal–organic frameworks, *Chem. Commun.*, 2019, **55**, 901–904.

35 F. G. Cirujano, A. Corma and F. X. Llabrés i Xamena, Zirconium-containing metal organic frameworks as solid acid catalysts for the esterification of free fatty acids: Synthesis of biodiesel and other compounds of interest, *Catal. Today*, 2015, **257**, 213–220.

36 Topos Main Page http://www.topospro.com (Accessed: January 2019)., .

37 V. A. Blatov, A. P. Shevchenko and D. M. Proserpio, Applied topological analysis of crystal structures with the program package ToposPro, *Cryst. Growth Des.*, 2014, **14**, 3576–3586.

38 H. Furukawa, F. Gándara, Y.-B. Zhang, J. Jiang, W. L. Queen, M. R. Hudson and O. M. Yaghi, Water adsorption in porous metal–organic frameworks and related materials, *J. Am. Chem. Soc.*, 2014, **136**, 4369–4381.

39 L. H. T. Nguyen, T. T. Nguyen, H. L. Nguyen, T. L. H. Doan and P. H. Tran, A new superacid hafnium-based metal–organic framework as a highly active heterogeneous catalyst for the synthesis of benzoxazoles under solvent-free conditions, *Catal. Sci. Technol.*, 2017, **7**, 4346–4350.

40 Z. Akimbekov, A. D. Katsenis, G. P. Nagabhushana, G. Ayoub, M. Arhangelskis, A. J. Morris, T. Friščić and A. Navrotsky, Experimental and theoretical evaluation of the stability of true MOF polymorphs explains their mechanochemical interconversions, *J. Am. Chem. Soc.*, 2017, **139**, 7952–7957.

41 A. K. Cheetham, G. Kieslich and H. H.-M. Yeung, Thermodynamic and kinetic effects in the crystallization of metal–organic frameworks, *Acc. Chem. Res.*, 2018, **51**, 659–667.

42 S. Yuan, W. Lu, Y.-P. Chen, Q. Zhang, T.-F. Liu, D. Feng, X. Wang, J. Qin and H.-C. Zhou, Sequential linker installation: Precise placement of functional groups in multivariate metal–organic frameworks, *J. Am. Chem. Soc.*, 2015, **137**, 3177–3180.

43 V. Bon, I. Senkovska, I. A. Baburin and S. Kaskel, Zr- and Hf-based metal–organic frameworks: Tracking down the polymorphism, *Cryst. Growth Des.*, 2013, **13**, 1231–1237.

44 H. Amer Hamzah, T. S. Crickmore, D. Rixson and A. D. Burrows, Post-synthetic modification of zirconium metal–organic frameworks by catalyst-free aza-Michael additions, *Dalt. Trans.*, 2018, **47**, 14491–14496.

45 M. Thommes, K. Kaneko, A. V. Neimark, J. P. Olivier, F. Rodriguez-Reinoso, J. Rouquerol and K. S. W. Sing, Physisorption of gases, with special reference to the evaluation of surface area and pore size distribution (IUPAC Technical Report), *Pure Appl. Chem.*, 2015, **87**, 1051–1069.

46 G. C. Shearer, S. Chavan, S. Bordiga, S. Svelle, U. Olsbye and K. P. Lillerud, Defect Engineering: Tuning the Porosity and Composition of the Metal − Organic Framework UiO-66 via Modulated Synthesis, 2016, **28**, 37493761.

47 M. J. Katz, Z. J. Brown, Y. J. Colón, P. W. Siu, K. A. Scheidt, R. Q. Snurr, J. T. Hupp and O. K. Farha, A facile synthesis of UiO-66, UiO-67 and their derivatives, 2013, **49**, 9449–9451.

48 D. A. Gómez-Gualdrón, P. Z. Moghadam, J. T. Hupp, O. K. Farha and R. Q. Snurr, Application of consistency criteria to calculate BET areas of micro- and mesoporous metal–organic frameworks, *J. Am. Chem. Soc.*, 2016, **138**, 215–224.

49 O. K. Farha, A. Özgür Yazaydın, I. Eryazici, C. D. Malliakas, B. G. Hauser, M. G. Kanatzidis, S. T. Nguyen, R. Q. Snurr and J. T. Hupp, De novo synthesis of a metal–organic framework material featuring ultrahigh surface area and gas storage capacities, *Nat. Chem.*, 2010, **2**, 944–948.

50 H. Furukawa, N. Ko, Y. B. Go, N. Aratani, S. B. Choi, E. Choi, A. Ö. Yazaydin, R. Q. Snurr, M. O'Keeffe, J. Kim and O. M. Yaghi, Ultrahigh Porosity in Metal-Organic Frameworks, *Science*, 2010, **329**, 424–428.

51 O. K. Farha, I. Eryazici, N. C. Jeong, B. G. Hauser, C. E. Wilmer, A. A. Sarjeant, R. Q. Snurr, S. T. Nguyen, A. Ö. Yazaydın and J. T. Hupp, Metal–organic framework materials with ultrahigh surface areas: Is the sky the limit?, *J. Am. Chem. Soc.*, 2012, **134**, 15016–15021.

52 K. S. Walton and R. Q. Snurr, Applicability of the BET method for determining surface areas of microporous metal−organic frameworks, *J. Am. Chem. Soc.*, 2007, **129**, 8552–8556.

53 V. Bon, I. Senkovska, M. S. Weiss and S. Kaskel, Tailoring of network dimensionality and porosity adjustment in Zr- and Hf-based MOFs, *CrystEngComm*, 2013, **15**, 9572–9577.

54 P. Küsgens, M. Rose, I. Senkovska, H. Fröde, A. Henschel, S. Siegle and S. Kaskel, Characterization of metal-organic frameworks by water adsorption, 2009, **120**, 325–330.

55 C. A. Trickett, K. J. Gagnon, S. Lee, F. Gándara, H. B. Bürgi and O. M. Yaghi, Definitive Molecular Level Characterization of Defects in UiO-66 Crystals, *Angew. Chemie - Int. Ed.*, 2015, **54**, 11162–11167.

56 S. J. Lee, J. L. Mancuso, K. N. Le, C. D. Malliakas, Y. S. Bae, C. H. Hendon, T. Islamoglu and O. K. Farha, Time-Resolved in Situ Polymorphic Transformation from One 12-Connected

Zr-MOF to Another, *ACS Mater. Lett.*, 2020, **2**, 499–504.

57 H. Pan, J. A. Ritter and P. B. Balbuena, Isosteric heats of adsorption on carbon predicted by density functional theory, *Ind. Eng. Chem. Res.*, 1998, **37**, 1159–1166.

58 L. A. Darunte, K. S. Walton, D. S. Sholl and C. W. Jones, CO2 capture via adsorption in amine-functionalized sorbents, *Curr. Opin. Chem. Eng.*, 2016, **12**, 82–90.

59 J. Santos-Lorenzo, R. San José-Velado, J. Albo, G. Beobide, P. Castaño, O. Castillo, A. Luque and S. Pérez-Yáñez, A straightforward route to obtain zirconium based metal-organic gels, *Microporous Mesoporous Mater.*, 2019, **284**, 128–132.

60 M. Abdinejad, A. Seifitokaldani, C. Dao, E. H. Sargent, X. Zhang and H. B. Kraatz, Enhanced electrochemical reduction of CO_2 catalyzed by cobalt and iron amino porphyrin complexes, *ACS Appl. Energy Mater.*, 2019, **2**, 1330–1335.

61 S. Yuan, J.-S. Qin, C. T. Lollar and H.-C. Zhou, Stable metal–organic frameworks with group 4 metals: Current status and trends, *ACS Cent. Sci.*, 2018, **4**, 440–450.

Chapter 5

Titanium(IV)-based metal-organic gels for the photocatalytic carbon dioxide reduction and hydrogen production

5.1. INTRODUCTION

Since the first report on the photoassisted electro-splitting of water on a titanium dioxide electrode[1] by Fujishima and Honda in 1972 followed by the seminar work of Inoue et al. in 1979 about the photocatalyzed reduction of carbon dioxide,[2] the research community has been attempting to mimic nature and chase the spontaneous transformation of atmospheric CO_2 and H_2O to chemicals using sunlight as the sole energy input. The development of this approach is understandable since its effective application would allow transforming solar energy into chemical energy, obtaining carbon-neutral/free fuels, such as high energy-density alcohols from CO_2 reduction or hydrogen (H_2) from the hydrogen evolution reaction (HER).[3]

5.1.1. Photocatalysis

As the name itself indicates, a photocatalytic process implies a reaction mediated by a catalyst when is exposed to light irradiation. For inorganic semiconductors, photons of adequate energy (equal to or higher than their bandgap, E_g) excite electrons (e^-) from the valence band (VB) to the conduction band (CB) generating electron (e^-)/hole (h^+) pairs (charge carriers).[4] These species can suffer recombination leading to a total/partial null process or can be separated and transferred to the surface, being there capable to perform reduction and oxidation reactions, respectively. The challenge in photocatalysis lies on the fact that the catalyst employed should be able to perform adequately both light harvesting, formation and separation of e^-/h^+ pairs and catalyse a specific reaction. Therefore these are the three major features that will define the efficiency in photocatalysis.[5]

The band alignment is also crucial for the overall redox reactions to succeed. The CB edge must be more negative than the desired reduction redox potential, and the VB edge should be more positive than the oxidation potential.[6] The light-driven reduction reactions that takes place for CO_2 and H_2O (*i.e.* H^+ reduction) are the same depicted in Section 3.1.1 of Chapter 3. In parallel, and to make the process catalytic, an e^- donor must be provided to scavenge h^+ in the VB, preclude charge recombination and close the redox cycle reactions on the catalyst. Since the 4 e^- water oxidation is also a challenging process (OER, oxygen evolution reaction: $2H_2O \rightarrow O_2 + 4H^+ + 4e^-$, $E = -82$ V vs NHE at pH = 7), various organic or inorganic sacrificial agents, denominates as hole scavengers, have been used for this role (e.g. methanol and triethanolamine).[7] In the case of H_2 production from "pure" water, the process is called water splitting (HER and OER occurring simultaneously), but when organic substances, such as carbohydrates, are used as sacrificial agents, the process is conventionally defined as photoreforming.[8]

Although photocatalytic H_2 production and CO_2 reduction did both started developing at the same period, the CO_2 reduction has supposed more challenging compared with H_2 production due to the high energy input required for breaking the C=O bonds, as explained in Section 3.1.1. Furthermore, the formation of products more reduced than CO (*i.e.* those containing C–H bonds) implies that a synergy of proton and multi-electron transfer steps takes place for CO_2 reduction and, therefore, not only the thermodynamic criteria must be met but also kinetic barriers exist. On the other hand, in aqueous media, both H^+ and CO_2 (multi electron) reduction make use of CB e^- and as their thermodynamic reduction occurs at similar potentials, the two reactions are in competition.[9]

5.1.2. MOFs in photocatalysis

Photocatalytic processes started to be investigated as effective tools to solve environmental problems using mainly TiO_2 as catalyst due to its excellent optical and electronic properties, high chemical stability, low cost, and eco-friendliness.[10] In this sense, during the past decade, much effort has been devoted to modifying TiO_2 via anion/cation doping[11,12] or combining with other metal/semiconductors for better light utilization.[5,13] More recently, due to its large surface area, well-ordered porous structure and tunable organic linkers/metal clusters, which endow promising photophysical/chemical properties, metal–organic frameworks (MOFs) have received much attention in this field as they also show photocatalytic activity under UV and/or visible irradiation.[14–18] To date, several MOFs (such as MOF-5, UiO-66(Zr), and MIL-125(Ti)) have been described as photocatalysts, in which the organic linkers serve as antennas to absorb light and transfer the photoexcited charge carriers to the central metal clusters upon light excitation, namely the linker-to-metal-cluster charge transfer (LMCT) mechanism.[17] Thus, the photocatalytic process in so that considered semiconducting MOFs could be explained through a similar charge-separation process as for conventional semiconductors, but in which the VB and CB are defined as the highest occupied molecular orbital (HOMO) located in the organic linker and the lowest unoccupied molecular orbital (LUMO) in the metal-oxo cluster, respectively, according to the molecular orbital theory (Figure 5.1).[18] Therefore, oxidation reactions generally take place in organic linkers, while reduction reactions in metal–oxo clusters. What is especially interesting in metal-organic porous materials is that the high-density metal nodes provide abundant catalytic active sites and at the same time, their high porosity enables reactants to become close to the catalytic active sites, which are spaced by organic linkers. As a result, the photoinduced electrons migrate as commented from the photoexcited organic linkers to the adjacent metal nodes rather than to the external surface of the whole semiconducting MOFs, suggesting that a low bulk recombination of photoexcited electron/hole pairs occurs in the migration process.[19]

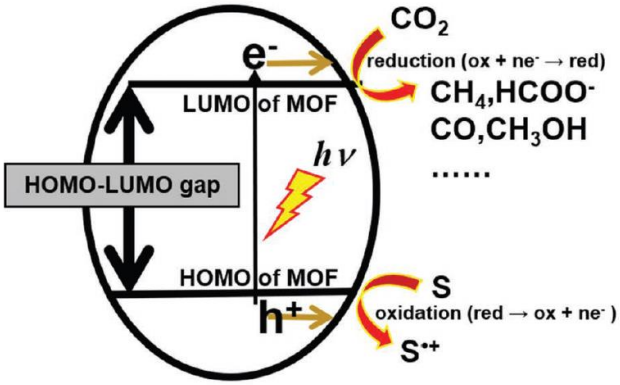

Figure 5.1. Schematic diagram of the photocatalytic CO_2 reduction over MOF photocatalysts. S: hole scavenger, $S^{\cdot+}$: oxidised hole scavenger. Reproduced from reference 19.

Due to the fact that the ultraviolet (UV) radiation ($\lambda < 400$ nm) accounts for only about 4% of the whole solar energy, while visible light (400 nm $< \lambda <$ 800 nm) reaches about 53%,[20] under natural sunlight illumination, visible light active materials are expected to produce the maximum amount of charges to mediate the pursued reaction. In this respect, there are mainly two approaches to obtain visible-light responsive MOFs. One is to select ligands or metal centres with visible-light response and the other is post-synthetic functionalization.[21] For example, amino-functionalized MIL-125(Ti)[22] and UiO-66(Zr)[23] exhibited photocatalytic activities under visible-light for CO_2 reduction. MIL-125-NH_2 can also be used to produce hydrogen by using a Pt cocatalyst[24] while UiO-66-NH_2 could degrade organic dyes under visible-light.[25] Copper-based or functionalized MOFs have been also of interest, as an example Cu-doped ZIF-67 (Co(II)/2-methylimidazolate MOF) are photoactive under visible-light for degradation of organic dyes,[26] while copper(II)-porphyrin MOFs have been used in combination with TiO_2 for highly improved the photocatalytic CO_2 reduction.[27]

In this regard, porphyrins are also versatile functional molecules useful for light harvesting due to their aromatic macrocycle consisting of four pyrrole units connected though methine bridges. They participate in several important biological processes such as light harvesting of photosynthesis through a complex composed of porphyrin-derivative-associated protein arrays[28] and, for this reason, their optical properties have been widely studied.[29] Once again trying to mimic nature, they have been recently implemented in metal-organic frameworks to obtain visible-light photoactive catalyst for H_2 production,[30] CO_2 reduction[31] and decontamination processes,[32] among others.[33,34] The number of porphyrin derivatives is quite extensive depending on the substituents of the macrocycle, although the one used in MOFs preparation is mainly the one attached to four carboxyphenyl substituents, the *meso*-tetra(4-carboxyphenyl)porphine (H_4TCPP), that allows to link it to the metal-clusters though the four carboxylate groups (Figure 5.2a). Furthermore, as the porphyrin is present in

its free-base form (*i.e.* nitrogen of macrocycle link to hydrogens), it can also be considered as a versatile platform framework allowing pre- and post-synthetic chemical modifications by porphyrin metalation, forming the so call metaloporphyrins (Figure 5.2b), of great interest too for different applications, such as the enhancement of solar energy conversion.[35]

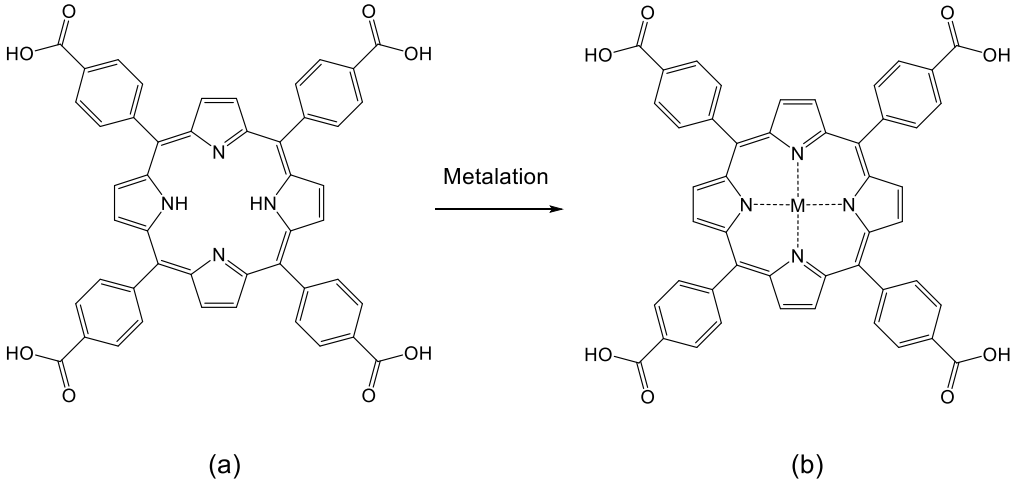

Figure 5.2. Schematic representation of *meso*-tetra(4-carboxyphenyl)porphine in its (a) free-base form $H_4TCPP(H_2)$ and (b) metalation form $H_4TCPP(M)$.

More recently, meso/macroporous metal-organic aerogels (MOAs) comprised by Ti(IV) oxo-clusters and aromatic dicarboxylic linkers, as an alternative to microporous MIL-125 and MIL-125-NH_2, have significantly overcome the performance in the continuous visible-light-driven photocatalytic CO_2 reduction into alcohols of the latter ones. This is attributed in part to a better diffusion of reagents and products in the meso/macroporous microstructure in contrast to the intrinsic microporosity of MOFs.[36]

5.1.3. Objectives

Taking all of these precedents into account, the present study sought to prepare, characterize and evaluate a series of metal-organic aerogels (MOAs) and gels (MOGs) in the photocatalytic reduction of CO_2 and H_2 production, respectively, as follows:

- In first place, MOAs based on titanium oxo-clusters and 2-aminobenzene-1,4-dicarboxylato ligands are going to be prepared including different ratios of *meso*-tetra(4-carboxyphenyl)porphine for a subsequent post-synthetic Cu-doping process with the aim of enhancing the performance and selectivity towards alcohols production in the continuous visible-light-driven photocatalytic reduction of carbon dioxide.
- Secondly, the as prepared MOGs based also in Ti(IV) oxo-cluster and benzene-1,4-dicarboxyalto ligands with different ratios in the presence of amino-functionalized linker are going to be prepared and tested in the hydrogen evolution reaction (HER) under simulated solar illumination.

5.2. Cu(II)-doped porphyrin based titanium(IV) MOGs for photocatalytic CO_2 reduction

5.2.1. Experimental section

Herein it is presented the synthetic procedure used to obtain the Cu(II) doped porphyrin-based titanium(IV) metal-organic gels (MOGs). The MOGs are initially prepared by an optimized sol-gel procedure and afterwards, a post-synthetic modification is carried out to get the Cu(II)-doped MOGs. Additionally, post-handling techniques to produce xerogels and aerogels are also explained. All the chemicals employed were of reagent grade and are gathered in Table 2.1 of Chapter 2. Finally, the conditions for their chemical characterization and for the CO_2 photoreduction experiments are also presented.

5.2.1.1. Synthetic procedure

Synthesis of metal-organic gels. Firstly, 1114 µL of titanium(IV) n-butoxide (3.18 mmol) were added to 10 mL of 2-butanol and after 5 min of mixing 118 µL of HCl 0.29 M dissolved in 4 mL of 2-butanol were added dropwise. The resulting clear solution was stirred for an hour in a sealed vessel. Afterwards, a DMF/2 butanol (10 mL/2 mL) solution containing 2-aminobenzene-1,4-dicarboxylic acid (H_2NH_2BDC, 0.4355 g, 2.38 mmol) and different amounts of *meso*-tetra(4-carboxyphenyl)porphine (H_4TCPP) (Table 5.1) were added obtaining stable sols. The total amount of dicarboxylic ligand was set to achieve a titanium:linker molar ratio of 1:0.75, according to the ideal ratio found in MIL-125-NH_2 MOF.[37]

Table 5.1. Sample coding and amounts of H_4TCPP ligand and copper(II) employed during the synthesis and doping of Ti/NH_2BDC/TCPP gels.[a]

Sample code	MOGs synthesis			Cu-doping process	Post-doping code
	H_4TCPP amount		Ti:TCPP ratio	$Cu(NO_3)_2{\cdot}2.5H_2O$ solution (mM)	
	g	mmol			
TCPP_0.01	0.0032	0.0040	8:0.01	0.008	**Cu@TCPP_0.01**
TCPP_0.1	0.0324	0.0397	8:0.1	0.119	**Cu@TCPP_0.1**
TCPP_1	0.3235	0.3969	8:1	0.768	**Cu@TCPP_1**

[a] The number provided in the sample codes indicates the synthesis ratio of TCPP per Ti_8O_8 core.

Finally, the mixture was introduced in a preheated oven within a closed vessel and maintained at 80 °C for 6h. As a result, well-formed reddish metallogels were obtained. The gels were robust enough to maintain the shape of the content vessel and to be processed as monolithic shapes using cutting tools (Figure 5.3). The remaining reagents were removed exchanging the solvent trapped in the gels with a mixture of

2-butanol/DMF (2:1), followed by a mixture of 2-butanol/DMF/absolute ethanol (1:1:1) and finishing with three exchanges of absolute ethanol to obtain the alcogels.

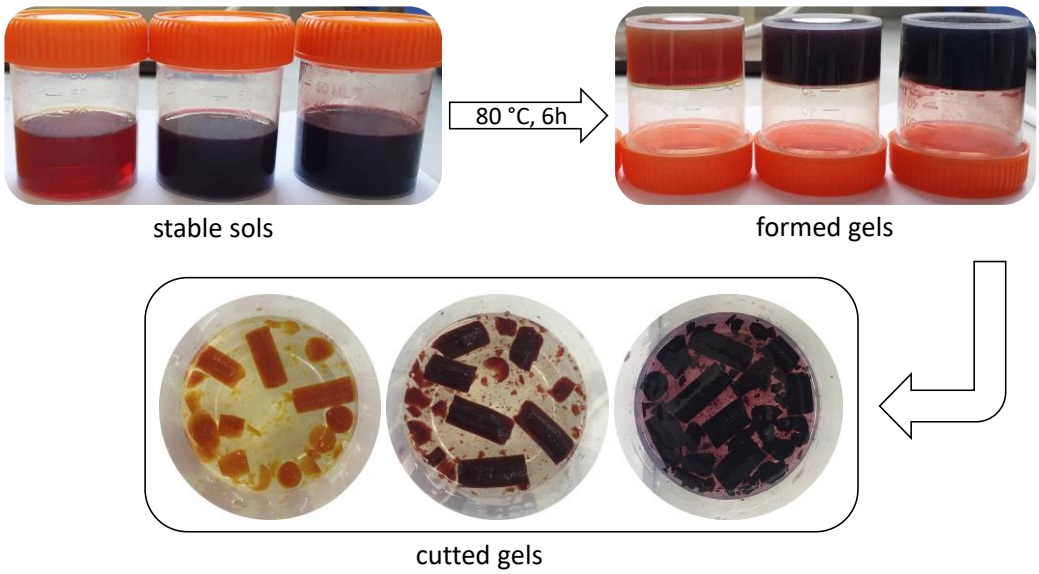

Figure 5.3. Appearance of synthesized MOGs: TCPP_0.01 (left), TCPP_0.1 (medium) and TCPP_1 (right).

Cu-doping of metal-organic gels. The three porphyrin-based MOGs were subjected to a copper(II)-doping process. For this purpose, 5 g of the alcogels were placed in a closed vessel within 100 mL of a copper(II) nitrate solution in absolute ethanol. The Cu(II) concentrations were varied depending on the TCPP real content of the gels to provide one copper for each porphyrinic ligand (Table 5.1). The process was prolonged for 12 h in a closed vessel. Afterwards, the MOGs were recovered and exchanged with absolute ethanol three times.

Preparation of MOXs and MOAs. Metal-organic xerogels (MOXs) were prepared drying the alcogels in an oven for 2 h at 150 °C. Thereafter, the xerogels were outgassed under vaccum at 150 °C during 4 h to ensure the removal of any remaining solvent molecule, prior to the chemical characterization of the material. This was performed prior to the Cu-doping process to obtain the real composition/ratios of the material. Furthermore, in order to get the metal-organic aerogels (MOAs) a supercritical drying was performed. This procedure was performed using a E3100 critical point dryer from Quorum Technologies and it allowed to replace the ethanol with air without destroying the nanostructured pore network. First, the MOGs were immersed in liquid CO_2 at 20 °C and 50 bar for one hour to exchange the ethanol. Afterwards, the exchanged alcohol was removed through the purge valve and the process was repeated three times. Then, they were dried under supercritical conditions by increasing the temperature and pressure to 40 °C and 85 bar (above carbon dioxide critical point: 31 °C and 74 bar) and finally, under constant temperature (40 °C), the chamber was slowly vented up to

atmospheric pressure. Figure 5.4 shows the aspect of the cut monoliths after the two different drying processes with respect to the original MOGs. MOAs maintain almost the same shape and similar size due to a lower contraction (≤ 25%) that takes place in the supercritical drying, whereas MOXs greatly reduce their size and suffer some cracks due to the collapse of the porous structure during the conventional drying.

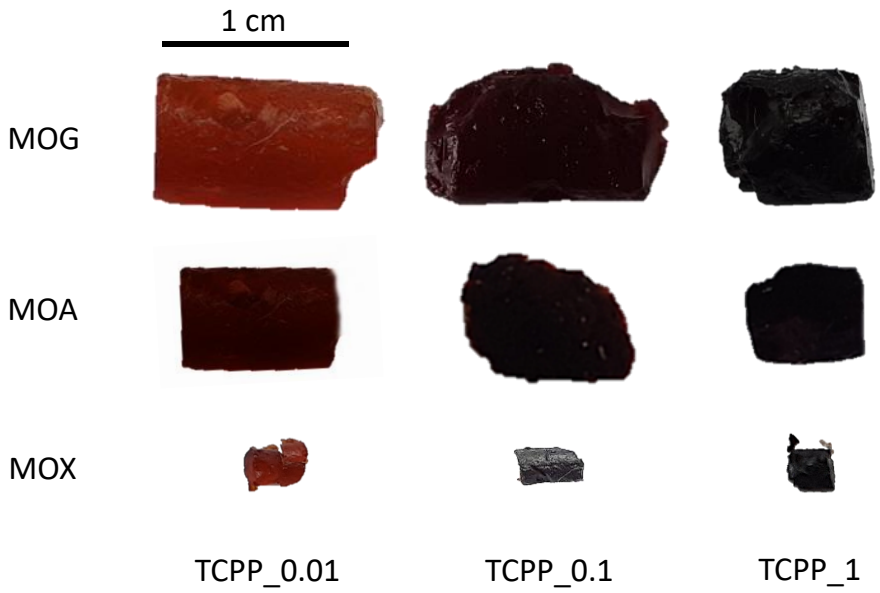

Figure 5.4. Comparison between MOGs, MOAs and MOXs monoliths after the different drying process.

5.2.1.2. Chemical characterization

Herein specific conditions employed in certain chemical characterization techniques are included, which can aid the comprehension of the results described below. Remaining data on the employed equipment and other characterization techniques are described in Section 2.2 of Chapter 2.

Electrospray ionization mass spectrometry (ESI-MS). ESI(+)-MS analysis were performed in duplicate by injecting the reaction mixtures (diluted in 2-butanol) prior and after the addition of the carboxylic ligand solution at a flow rate of 20 $\mu L \cdot min^{-1}$. Results are presented and explained in Results and discussion section.

Proton nuclear magnetic resonance spectroscopy (^{1}H-NMR). To proceed with the ^{1}H-NMR spectrum (500 MHz), 50 mg of each MOX (prior to doping process) were digested in 2 mL of a 1 M NaOH solution (in deuterated water, D_2O). The digestion was prolonged for 1 h, after which fumaric acid (*trans*-butenedioic acid, 20 mg) were added as internal standard and the solid residue corresponding to TiO_2 was filtered off. The NMR spectra were taken on the liquid fraction. Figure 5.5 shows the label assignation

of the species identified in the NMR spectra (Figures 5.6– 5.8). In all of them, the singlet at 8.39 ppm corresponds to the formic acid C–H atoms, whereas the three chemically distinguishable H-atoms of 2-aminobenzene-1,4-dicarboxylic acid are featured by three set of signals at 7.63 ppm (doublet), 7.20 ppm (doublet) and 7.12 ppm (double doublet). The singlet at 6.45 ppm is related to the two vinylic H-atoms of fumaric acid. The not assigned signals observed roughly in Figure 5.8 correspond to *meso*-tetra(4-carboxyphenyl)porphine which gives broad peaks not possible to be suitable for its quantification by ^{1}H-NMR. Further details of its characterization are provided in the following section.

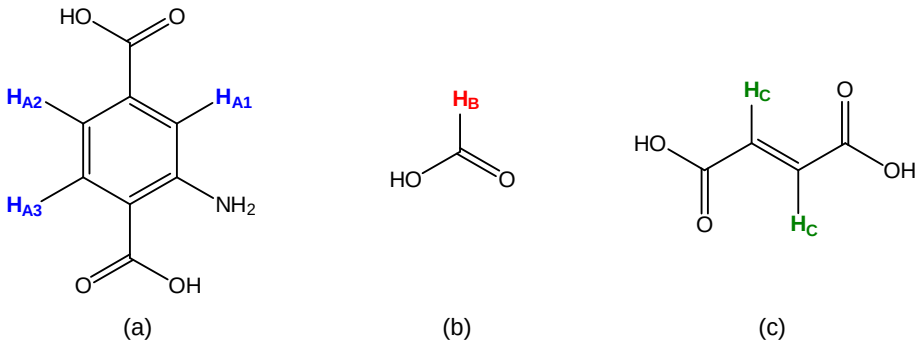

(a) (b) (c)

Figure 5.5. Proton label assignation of (a) 2-aminobenzene-1,4-dicarboxylic acid, (b) formic acid and (c) fumaric acid for ^{1}H-NMR spectra in Figures 5.6 – 5.8.

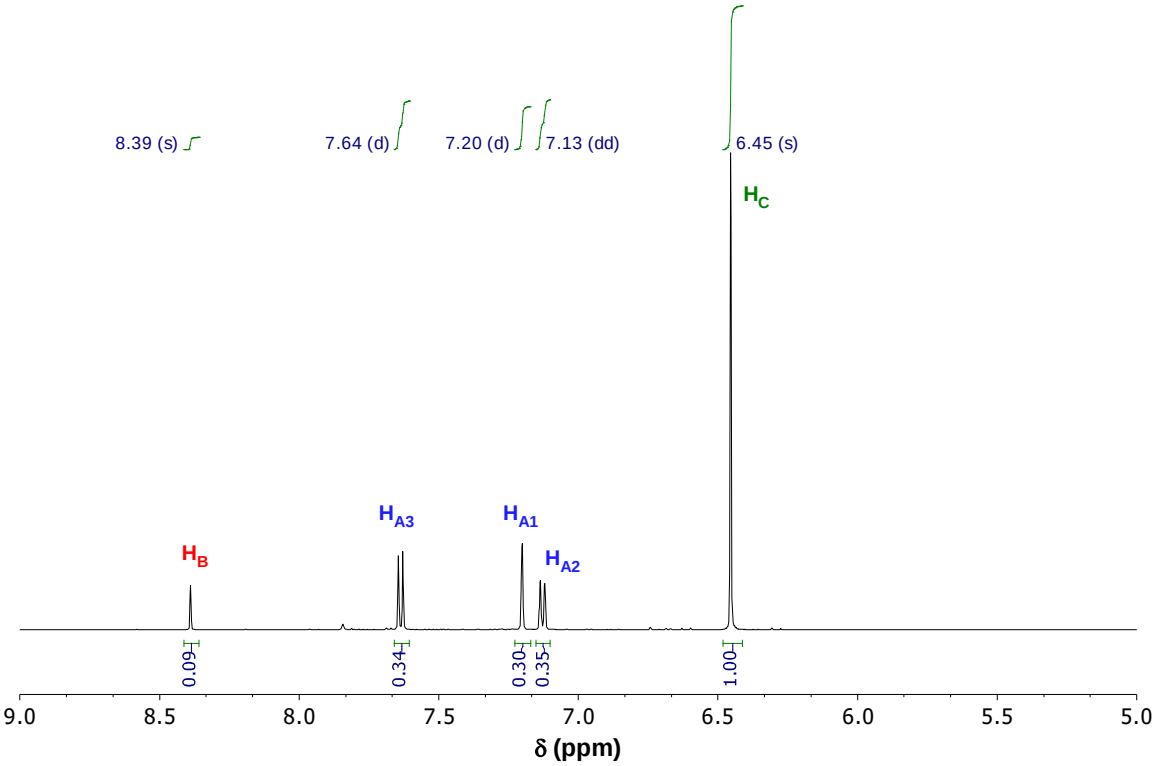

Figure 5.6. ^{1}H-NMR spectrum of digested TCPP_0.01 sample with the proton label assignation, chemical shifts (δ) with multiplicity of signals and relative integration values.

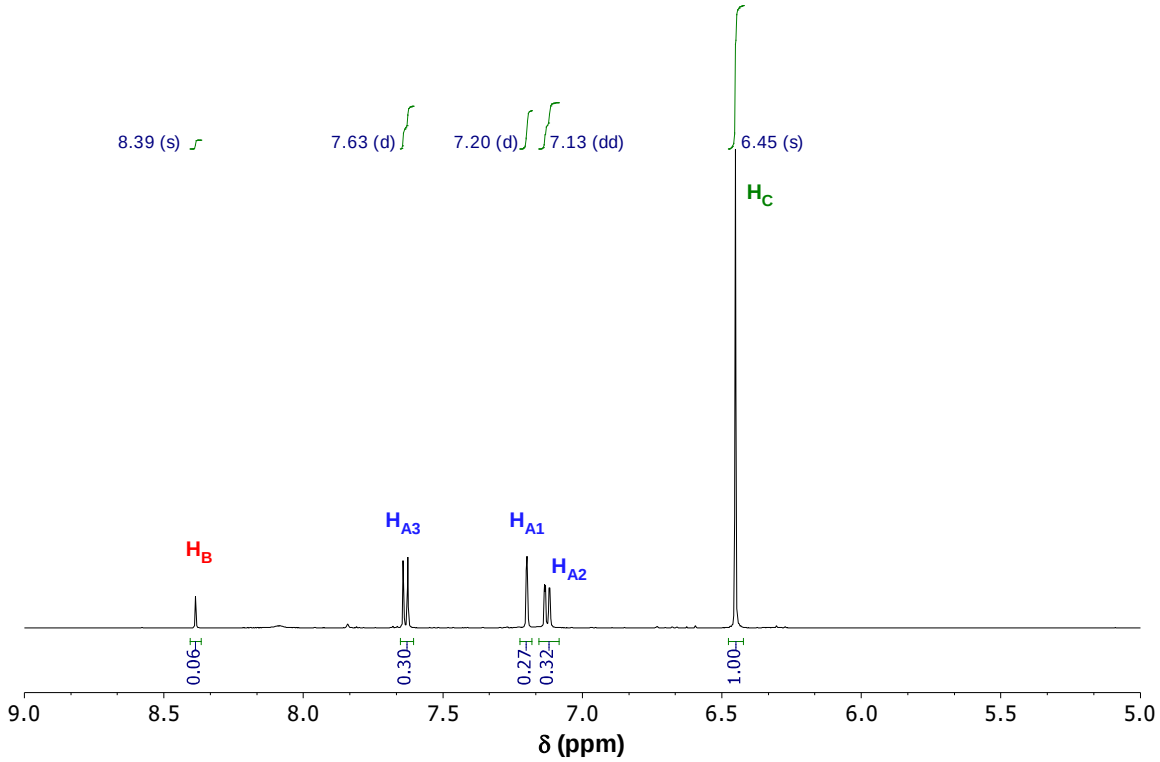

Figure 5.7. ^{1}H-NMR spectrum of digested TCPP_0.1 sample with the proton label assignation, chemical shifts (δ) with multiplicity of signals and relative integration values.

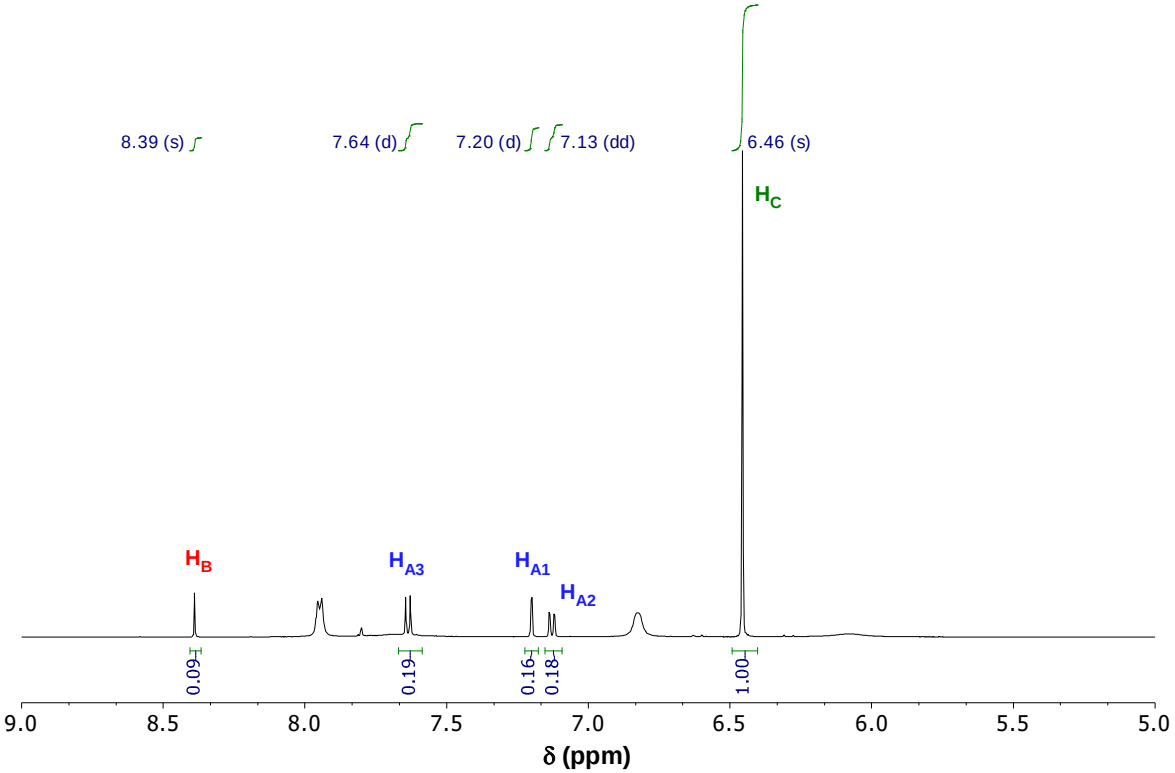

Figure 5.8. ^{1}H-NMR spectrum of digested TCPP_1 sample with the proton label assignation, chemical shifts (δ) with multiplicity of signals and relative integration values.

Ultraviolet-visible spectroscopy (UV-Vis). To determine the *meso*-tetra(4-carboxyphenyl)porphine (TCPP) content in the metal-organic gels, an UV-Vis absorption calibration curve was built using 1 M NaOH solutions with different content of TCPP (Figure 5.9). Afterwards, suitable amount of MOXs (to accomplish with the calibration range) were digested in a 1 M NaOH solution for 12 h. After this time, the solution was filtered off and the absorbance was measured in the filtered part (Table 5.2).

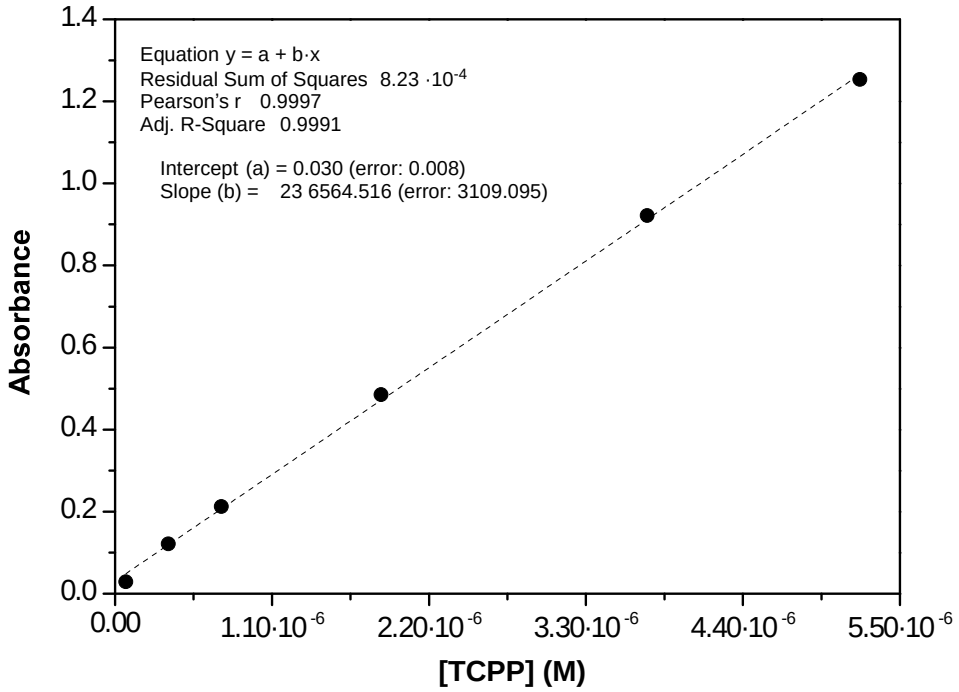

Figure 5.9. Calibration curve for TCPP concentration determined by UV-Vis spectroscopy.

Table 5.2. Data summary for TCPP content determination using UV-Vis spectroscopy.

Smaples	Mass (g)	V_{tot} (mL)	Abs	[TCPP] (M)	Experimental Ti:TCPP ratio
TCPP_0.01	0.0156	25	0.729	$2.95 \cdot 10^{-6}$	8:0.006
TCPP_0.1	0.0057	100	0.913	$3.73 \cdot 10^{-6}$	8:0.09
TCPP_1	0.0034	250	1.260	$5.20 \cdot 10^{-6}$	8:0.70

Thermogravimetric analysis (TGA). Thermogravimetric analysis of MOXs were performed in synthetic air from 30 °C to 800 °C (Figure 5.10). In all compounds, the thermograms show three main stages of weight loss. First, solvent molecules are released (30 – 150 °C). Thereafter, at intermediate temperature values (150 – 350 °C), dehydroxylation of titanium cluster takes place releasing coordinated water molecules that come from the condensation of hydroxide groups and formic acid. Besides, at this temperature range, the amino group is pyrolytically released, which is further discussed in the TGA analysis of Section 5.3.1.2. Finally, the framework decomposition takes place (*ca.* 350 – 500 °C) in an exothermic process forming TiO_2 as final residue, which was

determined by PXRD (crystalline phase: rutile in TCPP_0.01 and TCPP_0.1, and a mixture of rutile with a small amount of anatase in TCPP_1). Note that for TCPP_1, the sample with the higher amount of porphyrinic ligand, the framework decomposition starts slightly before (300 °C) and it prolongs until *ca.* 550 °C.

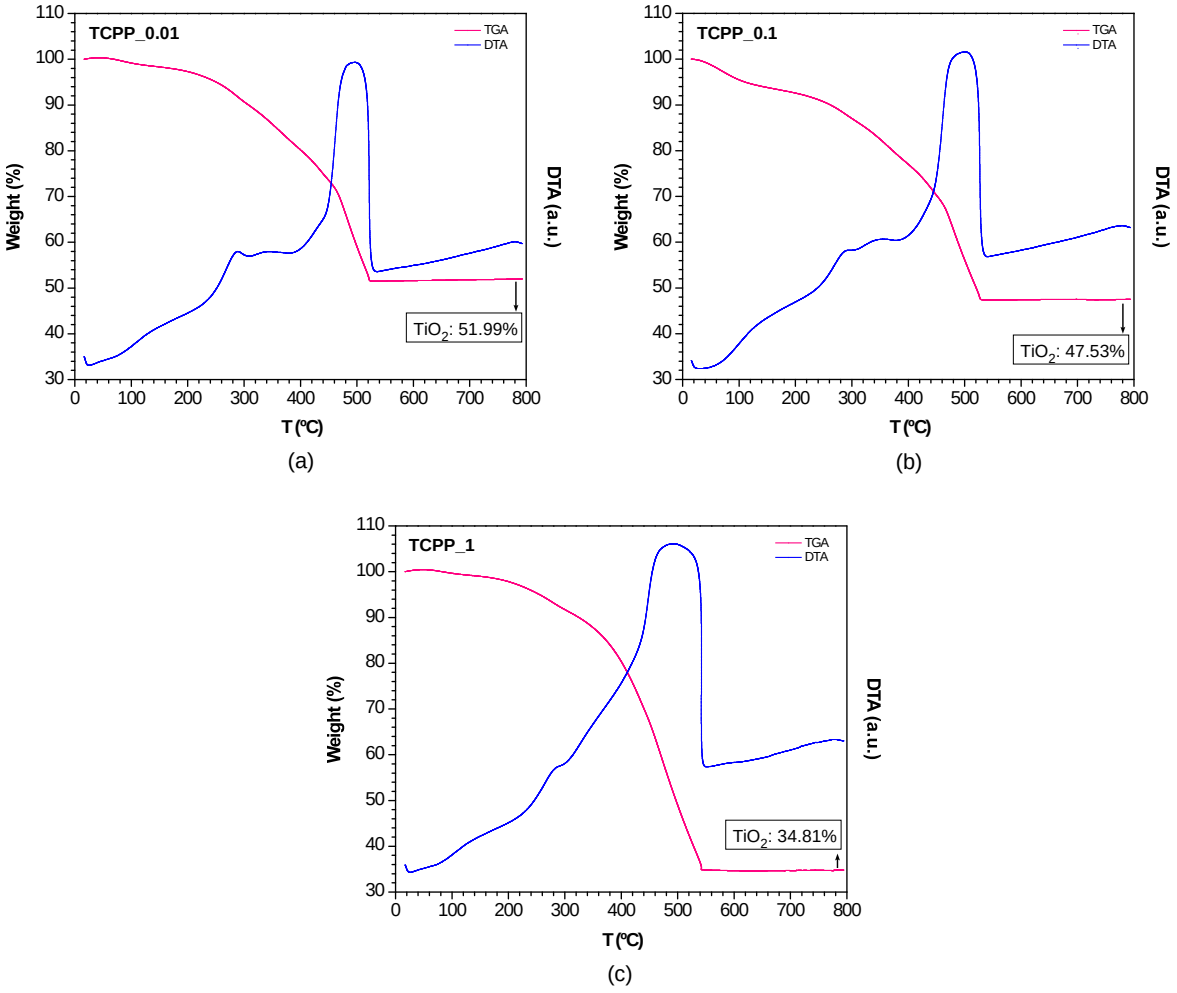

Figure 5.10. TGA-DTA curves of (a) TCPP_0.01, (b) TCPP_0.1 and (c) TCPP_1.

Attenuated total reflectance - Fourier-transform infrared spectroscopy (ATR-FTIR). The infrared spectra of metallogels prior and after Cu(II)-doping process and the assignation of the main vibration modes are gathered in Figure 5.11. All the spectra show the main bands of the NH_2BDC ligand which have been analysed in previous chapters for Zr-based metal-organic materials. The inclusion of the TCPP ligand promotes some changes in the spectra including peak width and relative intensity of the peaks which can be ascribed to the contribution of analogous vibration modes to that of the main ligand (NH_2BDC). Furthermore, those samples with a greater TCPP content (TCPP_0.1 and TCPP_1) exhibit an additional peak at 3318 and 965 cm^{-1} which can be attributed to ν(N–H) and δ(NH) vibrations of the pyrrole ring.[38]

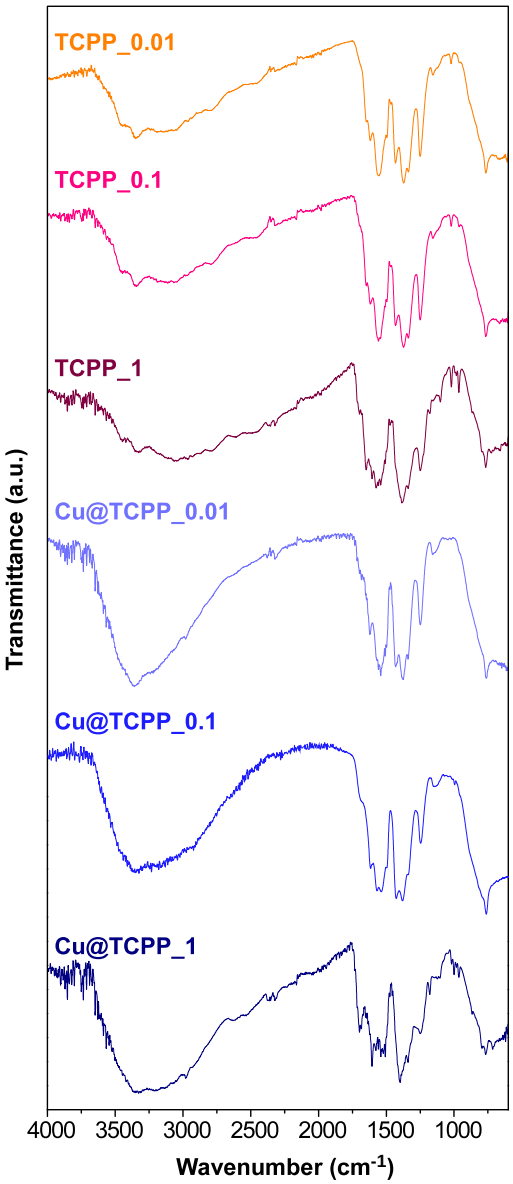

(a)

Wavenumber (cm^{-1})	Band assignation
3460, m	ν_{asym} (NH_2)
3340, m	ν_{sym} (NH_2)
3318	ν (N–H)
3000-3500, m	ν (O–H)
1645, sh	ν_{asym} (COO)
1620, m	δ_{ip} (NH_2)
1560, s	ν (C_{ar}–C)
1500, sh	ν_{ring} (C_{ar}–C_{ar})
1420, s	ν (C_{ar}-N)
1370, s	ν_{sym} (COO)
1335, sh	δ_{ip} (NH_2)
1250, m	δ_{oop} (NH_2)
1020, w	δ (C-H)
965, w	δ (N-H)
760, s	δ_{oop} (C-H) + δ_{oop} (O-C-O)
650, m	ν (M–O_{oxide})

(b)

Figure 5.11. (a) FTIR spectra and (b) band assignments for neat and Cu(II)-doped TCCP-based MOAs (s: strong, m: medium, w: weak and sh: shoulder signals; *sym*: symmetric, *asym*: asymmetric, *ip*: in plane, *ring*: ring stretching, *ar*: aromatic, *oop*: out of plane of stretching (ν) or bending (δ) modes).

5.2.1.3. Light-driven CO_2 reduction experiments

Preparation of the light-responsive supports. All metal-organic aerogels were outgassed at 150 °C under vacuum for 4 h prior to their use as catalysts. The light-responsive surfaces were prepared by airbrushing a catalytic ink onto a teflonated porous carbon paper (Toray TGP-H-60) covered by a paper mask with a hole of 1 cm^2. This ink includes the MOAs, a 5 wt% Nafion dispersion as binder and isopropanol as a vehicle, with a 70/30 catalyst/Nafion mass ratio and a 3% solids (catalyst + Nafion) percentage. This mixture was sonicated for 30 min to obtain a homogeneous slurry that was subsequently airbrushed on the surface of the porous carbon paper. The airbrushing process is carried out at 100 ºC to ensure the complete evaporation of the solvent during the accumulation of photocatalytic layers. The total mass loading per photoelectrode was set to 2 $mg \cdot cm^{-2}$, which is experimentally determined by continuous weighing.[39]

Optofluidic microreactor and experimental conditions. The porous carbon papers containing the MOAs were assembled in a planar optofluidic microreactor equipped with a reaction microchamber of 1 cm^2 and 75 µL and home-made designed microchamber and irradiated with LED lights (peak at 450 nm) with a light intensity of E = 5 $mW \cdot cm^{-2}$ for the continuous light-driven transformation of CO_2 into alcohols. A full description of the experimental setup and photoreactor details can be found in Section 2.3.2. A CO_2 saturated 0.5 M $KHCO_3$ aqueous solution (pH = 7.38 ± 0.03) was supplied to the microchamber with a peristaltic pump at a flow rate of Q_L = 100 $\mu L \cdot min^{-1}$. The photochemical CO_2 reduction tests for each photoactive material were carried out by duplicate (desviation < 15%) in continuous mode for 180 min, when a pseudo-stable performance is reached. The concentration of alcohols in each sample was analysed by duplicate in a headspace gas chromatograph. An average concentration was obtained for each point. The performance of the process is analysed in terms of reaction rates (r), *i.e.* product yield per gram of photocatalyst and time. The apparent quantum yield (AQY) is defined as $(n_e/n_p) \cdot 100$, where n_e represents the rate of electrons transferred towards CH_3OH and C_2H_5OH, defined as the number of molecules evolved (mol) multiplied by the number of reacted electrons (6 and 12 e^- for CH_3OH and C_2H_5OH, respectively) and the Avogadro´s number (mol^{-1}). On the contrary, n_p is the rate of incident photons on the surface, calculated according to the equation 5.2:

$$n_p = \frac{E \cdot A \cdot t \cdot \lambda}{h \cdot c} \qquad \text{equation 5.2}$$

where E is the light intensity ($W \cdot m^{-2}$), A represents the irradiation area (m^2), t is the reaction time (s), λ corresponds to the wavelength peak (m), h is the Planck's constant ($6.626 \cdot 10^{-34}$ J·s) and c represents the speed of light ($2.998 \cdot 10^8$ $m \cdot s^{-1}$), respectively.

Three reference measurements considered as blanks were performed with one of the samples using the same abovementioned conditions but changing the following:

(1) without light irradiation
(2) without CO_2 saturation in the 0.5 M $KHCO_3$ solution (pH = 8.29 ± 0.04)
(3) without light irradiation and without CO_2 saturation in the 0.5 M $KHCO_3$ solution (pH = 8.29 ± 0.04)

5.2.2. RESULTS AND DISCUSSION

5.2.2.1. Chemical characterization

First of all, in order to prove the nuclearity of the titanium oxo-clusters present in the metal-organic network, electrospray ionization mass spectrometry (ESI-MS) was performed in the stable solutions obtained prior the addition of hydrochloric acid and after the addition of carboxylic ligands. The peaks found in the spectra have allowed to identify the formula of the species formed using *ChemCalc* platform,[40] while *MassLynx software* was employed to simulate the spectra of each identified species. The collation of the measured and simulated spectra is shown in Figure 5.12 and the corresponding m/z values and other agreement figures are gathered in Table 5.3. Both ESI(+)-MS measurements evidence the presence of a series of Ti_8O_8 clusters with differences in the amount of water and solvent molecules that affect directly to the position of the peaks. The addition of the carboxylic ligands to the reaction media affects to the relative intensity of the peaks in the spectrum, which is related to concentration changes of complexes in solution. This change seems to be related to the extra water added with the DMF solution, as those peaks that disappear or reduce their intensity are related to species with a lower relative water content. Note that the intensity of the computed peaks are all the same and normalized to the maximum intensity as the simulation cannot deal with the concentration of the species.

Besides, the absence of both, changes in peak shape and emergence of new peaks upon the addition of the bridging linker, seems to indicate that the carboxylic ligand is not coordinated at the initial stage of the reaction. Thus, once the reaction media is subjected to the heating process (80 °C, 6h) the carboxylic ligands (NH_2BDC and TCPP) substitute some of the molecules coordinated to the Ti_8O_8 core interconnecting them and triggering the polymerization until the gelation process takes place, trapping most of the solvent within the network. These octanuclear clusters are observed in Ti-based MOFs, including the well-known MIL-125 family,[41] but are also commonly found among reported discrete Ti(IV) oxo-clusters containing carboxylic ligands.[42]

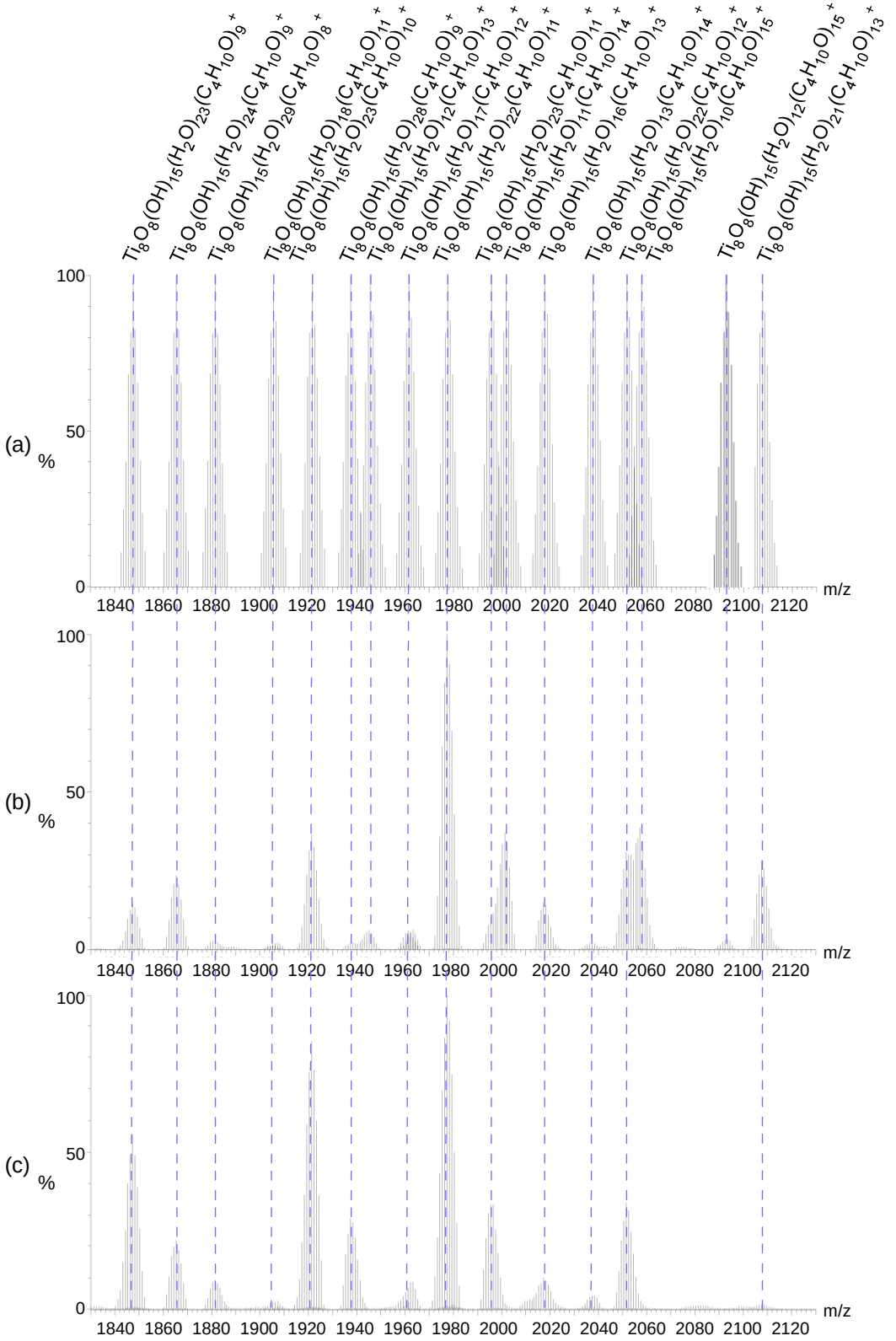

Figure 5.12. Comparison of the (a) simulated ESI-MS spectrum with the experimental ones for the reaction solution (b) prior to the addition of HCl and bridging ligand and (c) after the addition of bridging ligands.

Table 5.3. Peak maximum ($(m/z)_{max}$) and peak width ($\Delta_{m/z}$) values subtracted from the experimental ESI(+)-MS spectra for the reaction mixtures compared to the values of the simulated isotopic distribution for the octanuclear species.[a,b]

SIMULATED (a)			EXPERIMENTAL (b)		EXPERIMENTAL (c)	
$(m/z)_{max}$	**$\Delta_{m/z}$**	**Formula**	**$(m/z)_{max}$**	**$\Delta_{m/z}$**	**$(m/z)_{max}$**	**$\Delta_{m/z}$**
1847.52	1844.52–1850.52	$Ti_8O_8(OH)_{15}(H_2O)_{23}(C_4H_{10}O)_9^+$	1847.33	1844.34 – 1850.33	1847.33	1844.34 – 1850.32
1865.53	1862.53 – 1868.53	$Ti_8O_8(OH)_{15}(H_2O)_{24}(C_4H_{10}O)_9^+$	1865.34	1862.35 – 1868.34	1865.33	1862.34 – 1868.333
1881.51	1878.51 – 1884.51	$Ti_8O_8(OH)_{15}(H_2O)_{29}(C_4H_{10}O)_8^+$	1880.35	1878.36 – 1884.32	1881.33	1878.35 – 1884.32
1905.61	1902.61 – 1908.61	$Ti_8O_8(OH)_{15}(H_2O)_{18}(C_4H_{10}O)_{11}^+$	1905.21	1902.21 – 1908.19	1905.31	1902-23 – 1908.35
1921.60	1918.60 – 1924.60	$Ti_8O_8(OH)_{15}(H_2O)_{23}(C_4H_{10}O)_{10}^+$	1921.40	1918.41 – 1924.40	1921.40	1918.40 – 1924.39
1937.58	1934.58 – 1940.58	$Ti_8O_8(OH)_{15}(H_2O)_{28}(C_4H_{10}O)_9^+$	1937.40	1935.42 – 1940.37	1937.39	1935.40 – 1940.38
1945.70	1942.70 – 1948.70	$Ti_8O_8(OH)_{15}(H_2O)_{12}(C_4H_{10}O)_{13}^+$	1945.27	1942.28 – 1947.27	–	–
1961.68	1958.68 – 1964.68	$Ti_8O_8(OH)_{15}(H_2O)_{17}(C_4H_{10}O)_{12}^+$	1961.27	1958.27 – 1964.26	1961.27	1958.28 – 1964.34
1977.66	1974.66 – 1980.66	$Ti_8O_8(OH)_{15}(H_2O)_{22}(C_4H_{10}O)_{11}^+$	1977.46	1974.47 – 1980.46	1977.45	1974.46 – 1980.45
1995.67	1992-67 – 1997.67	$Ti_8O_8(OH)_{15}(H_2O)_{23}(C_4H_{10}O)_{11}^+$	1995.46	1992.47 – 1998.45	1995.46	1993.47 – overlap
2001.76	1998.76 – 2004.76	$Ti_8O_8(OH)_{15}(H_2O)_{11}(C_4H_{10}O)_{14}^+$	2001.33	1998.36 – 2004.32	–	–
2017.74	2014.74 – 2020.74	$Ti_8O_8(OH)_{15}(H_2O)_{16}(C_4H_{10}O)_{13}^+$	2017.32	2014.33 – 2020.32	2017.31	2014.33 – 2020.31
2037.78	2034.78 – 2040.78	$Ti_8O_8(OH)_{15}(H_2O)_{13}(C_4H_{10}O)_{14}^+$	2037.51	2034.51 – 2040.39	2037.50	2034.50 – 2040.48
2051.73	2048.73 – 2054.73	$Ti_8O_8(OH)_{15}(H_2O)_{22}(C_4H_{10}O)_{12}^+$	2051.52	2048.53 – overlap	2051.51	2048.52 – 2054.51
2057.82	2054.82 – 2060.82	$Ti_8O_8(OH)_{15}(H_2O)_{10}(C_4H_{10}O)_{15}^+$	2057.38	overlap – 2060.38	–	–
2093.84	2090.84 – 2096.84	$Ti_8O_8(OH)_{15}(H_2O)_{12}(C_4H_{10}O)_{15}^+$	2093.55	2090.54 – 2095.54	–	–
2107.79	2104.79 – 2110.79	$Ti_8O_8(OH)_{15}(H_2O)_{21}(C_4H_{10}O)_{13}^+$	2107.57	2105.58 – 2110.57	small with noise	

[a] Width at half height ($\Delta_{m/z}$) with respect to the maximum peak of the species isotopic distribution pattern (measured as the peak closest to that value).

[b] *SIMULATED (a)* corresponds to the simulated spectrum of Figure 5.12a and *EXPERIMENTAL (b)* and *EXPERIMENTAL (c),* to the spectra of Figure 5.12b and c, respectively.

Chemical analysis combining ^{1}H-NMR and UV-Vis characterization of digested samples and TGA analysis of xerogels (see previous section) helped us to get bigger insight into the chemical composition of the network. We estimated a chemical formula per Ti_8O_8 unit based on thermogravimetric analysis (that gathers titanium content), ^{1}H-NMR (to get the amount of 2-aminobenzene-1,4-dicarboxylate and formate ions) and UV-Vis analysis (contributing with TCPP content), considering two possibilities of defect compensating ligands: OH^-/H_2O and formate ($HCOO^-$ that comes from DMF decomposition). Accordingly, the formulas shown in Table 5.4 were obtained.

Table 5.4. Chemical formula estimated for synthesized porphyrin-based MOGs.

Sample[a]	Formula
TCPP_0.01	$Ti_8O_8(OH)_4(NH_2BDC)_{2.71}(HCOO)_{0.68}(TCPP)_{0.006}(H_2O)_{5.876}(OH)_{5.876}$
TCPP_0.1	$Ti_8O_8(OH)_4(NH_2BDC)_{2.90}(HCOO)_{0.53}(TCPP)_{0.09}(H_2O)_{5.31}(OH)_{5.31}$
TCPP_1	$Ti_8O_8(OH)_4(NH_2BDC)_{2.13}(HCOO)_{0.71}(TCPP)_{0.70}(H_2O)_{4.23}(OH)_{4.23}$

[a] The number provided in the sample codes indicate the targeted ratio of TCPP per Ti_8O_8 core.

As it can be observed, each MOG is comprised by 2-3 NH_2BDC linkers per Ti_8O_8 cluster and the content of TCPP is near the targeted one. Formate and OH^-/H_2O pairs would complete the coordination sphere of the octanuclear clusters to compensate the linker vacancies, as commented before and as usually occurs in defective MOFs of group IV metals.[43] Furthermore, the PXRD patterns of MOXs (Figure 5.13) reveal a short range ordering broad peak at 2θ = 6 – 7° which is fairly close to the maximum intensity peak present in MIL-125-NH_2 pattern (2θ = 6.8°) that corresponds to the interplanar distance set by NH_2BDC linker between titanium cluster arrays from the combined contributions of (101) and (110) reflections (d_{101} = 12.0 Å; d_{110} = 13.2 Å).[44] Interestingly, when the TCPP content increases a second broad maximum emerges at 2θ = 3 – 4° as it is observed in TCPP_1 sample. This maximum corresponds to a spacing of 22.1 - 29.4 Å which approaches to range of distances set by TCPP ligand among titanium oxo-clusters (centroid – centroid distances: 23.27 – 27.57 Å)[45–47] in metal-organic structures corresponds to distances around 20 Å due to the interconnection of the clusters through porphyrinic ligands that present a higher size near to this value.

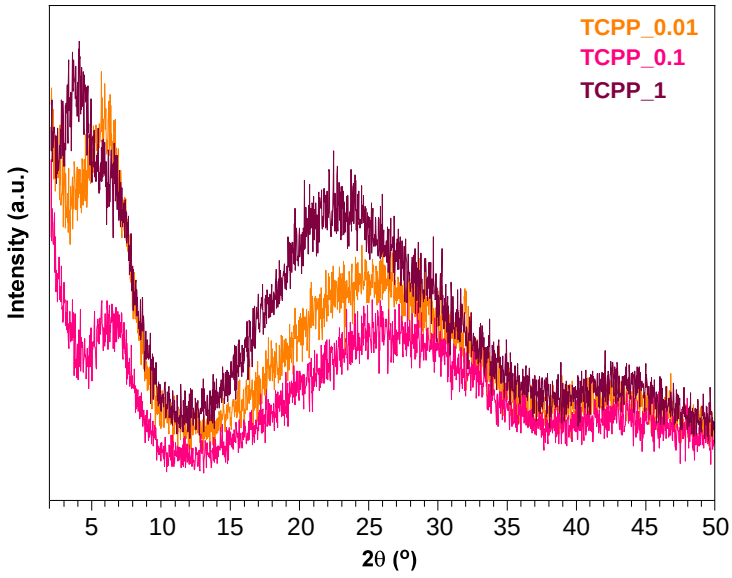

Figure 5.13. PXRD patterns of TCPP_0.01, TCPP_0.1 and TCPP_1.

Once the Cu(II)-doping process was performed, copper content was determined by X-ray fluorescence measurements (XRF). Results are summarized in Table 5.5. Taking into account these data, all the tetrapyrrole rings may have been occupied by copper ions in samples Cu@TCPP_0.01 and Cu@TCPP_0.1, whereas in Cu@TCPP_1 50% of the

available positions might be occupied. To corroborate that effectively copper ions were inserted in TCPP ligands, fluorescence spectroscopy measurements were performed (Figure 5.14). In this analysis, it can be observed that the increase of TCPP content produces itself a self-quenching in the fluorescence emission of the samples (prior to copper insertion), as it can be inferred from the progressive reduction in maximum relative intensity of fluorescence emission as TCPP ratio of the pristine materials increases. After the doping process, the two fluorescence bands present at 650 and 718 nm (excitation wavelength: 420 nm) fall down to almost zero in Cu@TCPP_0.01 and disappear in other two samples. This means that, effectively, copper ions were coordinated to TCPP macrocycle during doping process as Cu(II)-porphyrin complexes are featured by a quenching of the fluorescence due to the unpaired electron present in the $3d_{x^2-y^2}$ orbital of copper, which enables an intramolecular charge transfer between the levels $^2S_1$ and $^2T_1$, responsible of the total absence of fluorescence. This phenomena also affects to the phosphorescence properties of the organic ligand.[48]

Table 5.5. Titanium and copper content (wt_M, % of total metal) of doped MOGs and relative TCPP:Cu content.

Sample	Relative Ti content (wt_M, %)	Relative Cu content (wt_M, %))	TCPP:Cu ratio
Cu@TCPP_0.01	99.85	0.15	1:1.51
Cu@TCPP_0.1	98.15	1.85	1:1.26
Cu@TCPP_1	94.82	5.18	1:0.47

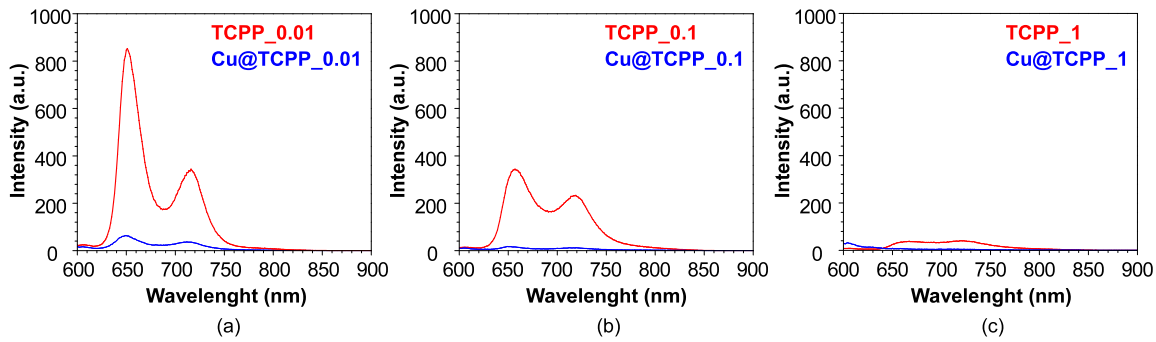

Figure 5.14. Comparison of fluorescence spectra of MOXs prior and after doping process (excitation wavelength 420 nm).

Further evidence of the copper(II)-porphyrine complex was provided by the UV-Vis diffuse reflectance spectroscopy (DRS) measurements performed in the metal-organic samples. The Kubelka-Munk function, $F(R) = (1-R_\infty)^2/2 \cdot R_\infty$ ($R_\infty = R_{sample} / R_{standard}$, is the reflectance),[49] was used for the data treatment to represent the UV-Vis absorption spectra. The collected and treated data for neat MOXs prior to doping process are gathered in Figure 5.15.

As porphyrins are extended aromatic systems, their absorption bands involve $\pi \rightarrow \pi^*$ electronic transitions, and in their UV-Vis absorption spectra two main regions are

distinguished: the area of the so called Soret or B band (380 – 500 nm) and the Q band region (500 – 700 nm). In free-base neutral porphyrins (*i.e.* nothing coordinated to the tetrapyrrol macrocycle → TCPP(H_2)) with a D_{2h} point group, the Q bands arise from two possible electronic transitions (HOMO → LUMO and HOMO –1 → LUMO) in where two different vibrational modes are involved and appear separately in the spectrum, giving as a result four characteristic Q bands. The Soret band instead corresponds to electronic transitions to a higher energy unoccupied orbital (LUMO +1) and is usually more intense. The position of these bands shifts depending on the substituents of the porphyrinic ring.[29,50,51]

Accordingly, the absorption spectra of the samples prior to the addition of copper show the four characteristic Q-bands (651 nm, 594 nm, 559 nm and 520 nm) with a higher relative absorption when the TCPP(H_2) content in the sample increases. At lower wavelength values, in 450-500 nm range, the spectra shows a steep rise of the absorption which is ascribed to the π → π* transitions of the amino-functionalized BDC linker (see the referential spectrum in Figure 5.15b for the metal-organic material lacking of TCPP ligand). As consequence, the Soret band is not well-defined but its maximum can be located in the lower edge of visible region (420 nm for TCPP_0.01 and TCPP_0.1; 390 and 450 nm for TCPP_1).

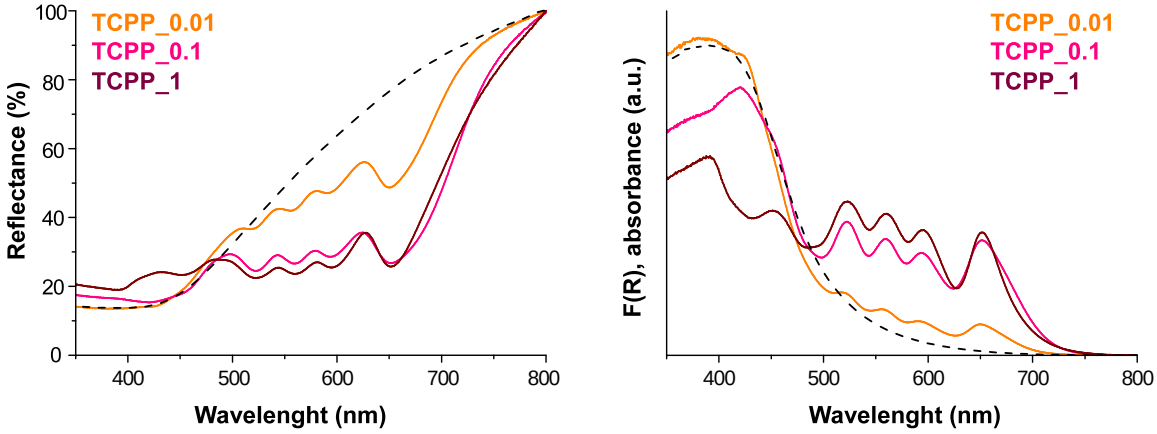

Figure 5.15. UV-Vis diffuse reflectance spectroscopy of TCPP-based xerogels (a) as measured (R,%) and (b) transformed to absorbance using the Kubelka-Munk function (F(R)). Dashed line corresponds to Ti(IV)/NH_2-BDC sample prepared and analysed in Section 5.3.

A comparison of the UV-Vis spectra of Cu-doped and neat samples is depicted in Figure 5.16. As previously reported, the coordination of a metal to the tetrapyrrolic ring leads to a change in molecular symmetry from D_{2h} to D_{4h} and therefore, the allowed electronic transitions in the Q band region change from two to one, which in turn, gives rise to two bands instead of four, according to the contribution of two vibrational energy levels.

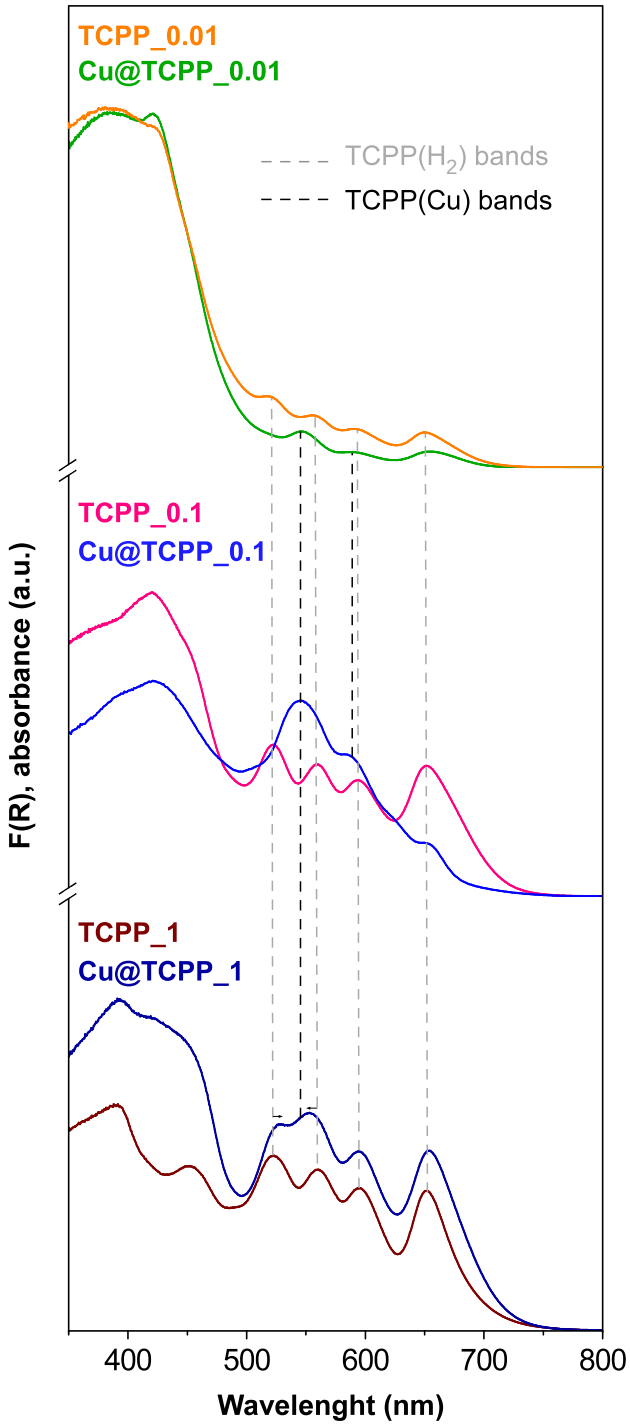

Figure 5.16. Absorbance (F(R)) comparison of neat and Cu-doped xerogels. Q-band maxima of free-base porphyrin bands and Cu(II)-coordinated porphyrin are depicted by grey and black dashed lines, respectively.

For Cu@TCPP_0.01 and Cu@TCPP_0.1 samples, three Q bands are observed: two new signals at 545 and 590 nm that can be related to the copper porphyrin complex, and a third band at 650 nm that matches with the band that appears in the free-base spectrum. It may arise from the fact that a minor percentage of porphyrins are not coordinated to copper and thus transition remains visible, as the metalloporphyrin bands do not mask it. This conclusion is in agreement with the aforementioned partial

quenching in the fluorescence spectra. In the case of Cu@TCPP_1, the shape, number and position of the Q bands depict an intermediate situation in which a meaningful amount of both free porphyrin and Cu-porphyrin is present in the sample. Note that since the most intense Q band of TCPP(Cu) lies between the higher in energy two Q bands of TCPP(H_2), their merging in the spectra of Cu@TCPP_1 sample leads to two maximum slightly shifted to higher and lower energies (552 nm and 526 nm). The other two maintain the position (651 and 594 nm) with respect to free-porphyrin containing sample. These results agree with the chemical analysis of Cu@TCPP_1 in which the Cu:TCPP ratio is *ca*. 0.5.

To end up with the chemical characterization, X-ray photoelectron spectroscopy (XPS) measurements of Cu@TCPP_1 are presented in Figure 5.17. The full spectrum is shown in Figure 5.17a, whereas b to f figures present the high resolution spectrum of each of the elements observed with their characteristic components. This analysis allowed to identify the distinctive 2p peaks of titanium(IV) ($2p_{3/2}$ and $2p_{1/2}$ at 458.9 and 464.6 eV, respectively) and their three satellite peaks, that fit well with the data available in the literature for MOFs with Ti_8O_8-type clusters with a hexacoordinated TiO_6 environment.[52,53] Furthermore, the peak observed at 935.2 eV is attributable to Cu $2p_{3/2}$ level and it lies within the common range for Cu(II) compounds.[54] In fact, the binding energy of this signal matches well with that found for Cu(II)-metalloporphyrins-based materials.[55] The intensity of this band is small due to the amount of copper present in the sample in terms of atomic %, for that reason the other characteristic band of Cu^{2+}, Cu $2p_{1/2}$, of less intensity, is barely observed (mixed with noise) and in consequence, is not presented. Finally, expected C 1s, O 1s and N 1s bands coming from the organic linkers are observed. In the case of carbon, two C 1s bands at 288.4 eV and 284.6 eV are ascribed to O–C=O and C–C/C–H carbon-type, respectively. Two different environments are also observed for nitrogen, with bands at 398.7 and 401.4 eV, that can be attributed to the $–NH_2$ group of BDC linker and to the nitrogen of the porphyrinic ligand, respectively. The band at 531.1 eV for O 1s comes from the contribution of carboxylic, oxide and hydroxide ligands.[56,57]

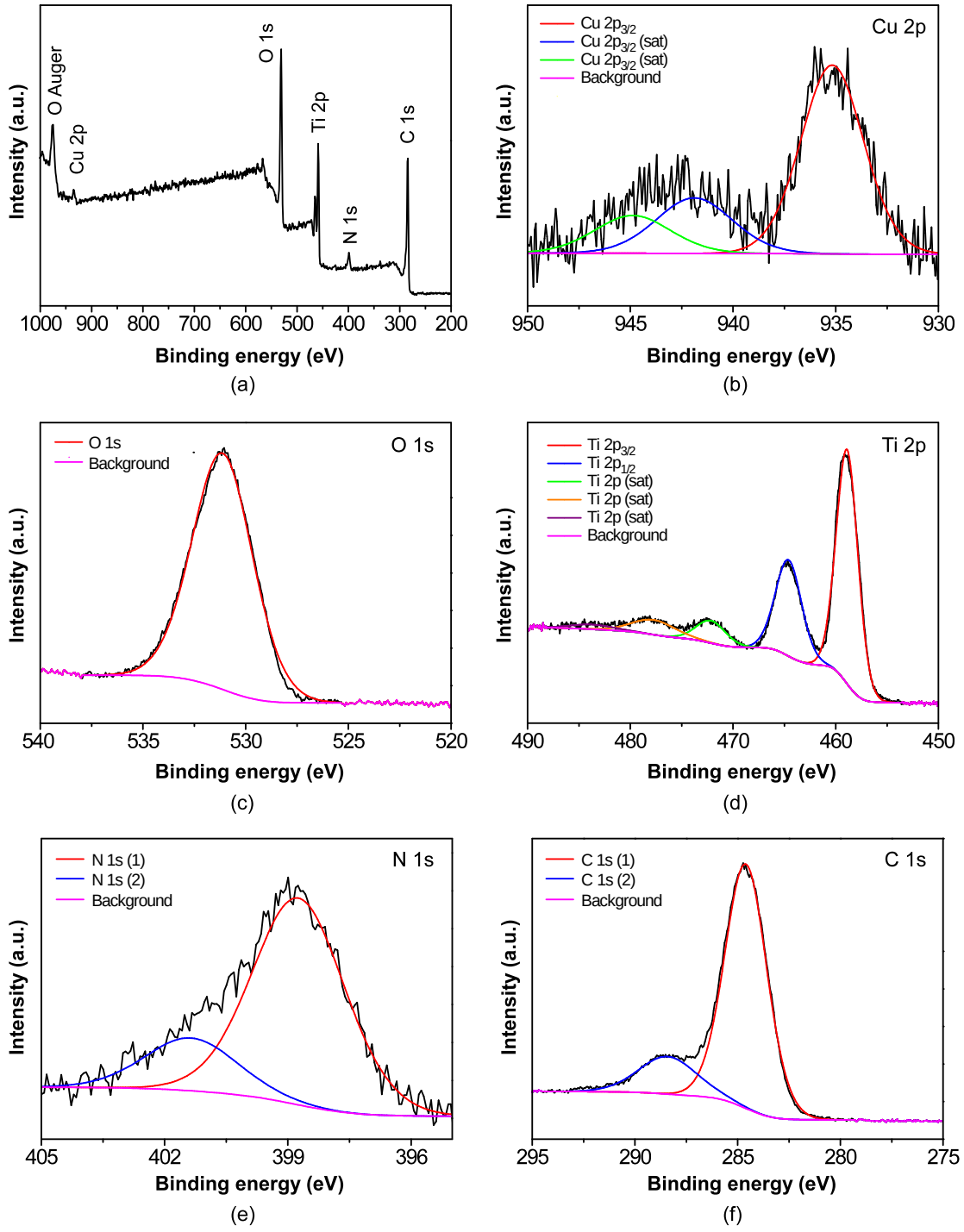

Figure 5.17. (a) XPS full spectrum and high resolution spectrum for (b) Cu 2p, (c) O 1s, (d) Ti 2p, (e) N 1s and (f) C 1s peaks of Cu@TCPP_1 sample. "Sat" refers for characteristic satellite peaks.

5.2.2.2. Microstructural characterization

Microstructure of the obtained materials was firstly studied by transmission electron microscopy (TEM) carried out on dry samples (aerogels). In this study, we observed that every system was comprised by partially sintered small nanoparticles of *ca.* 5-10 nm (Figure 5.18). The random sinterization between them leaves in the system meso- and macropores with a polydisperse size distribution.

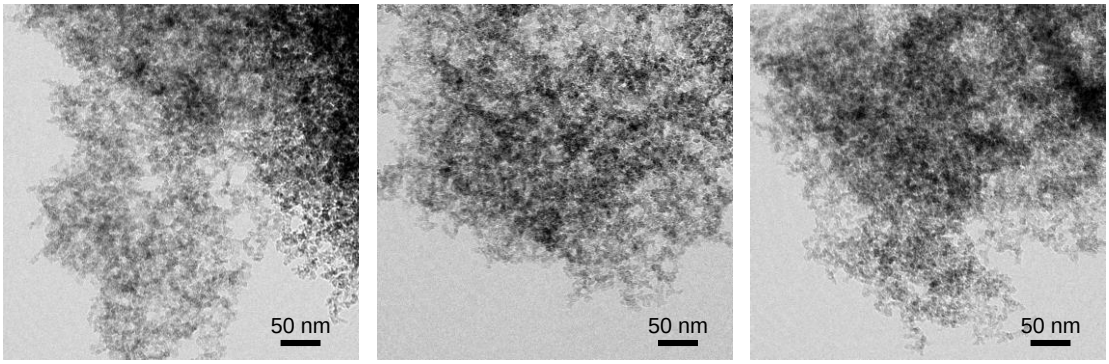

Figure 5.18. TEM micrographs of (a) TCPP_0.01, (b) TCPP_0.1 and (c) TCPP_1 taken at 100k magnifications.

The microstructure of the MOAs after copper doping is retained. HAADF-TEM images and element mapping analysis (Figure 5.19) show a fine and homogeneous distribution of copper thorough all the metal-organic gel, which is consistent with a situation in which copper is coordinated to the metal-organic network instead clustered within the aerogel microstructure.

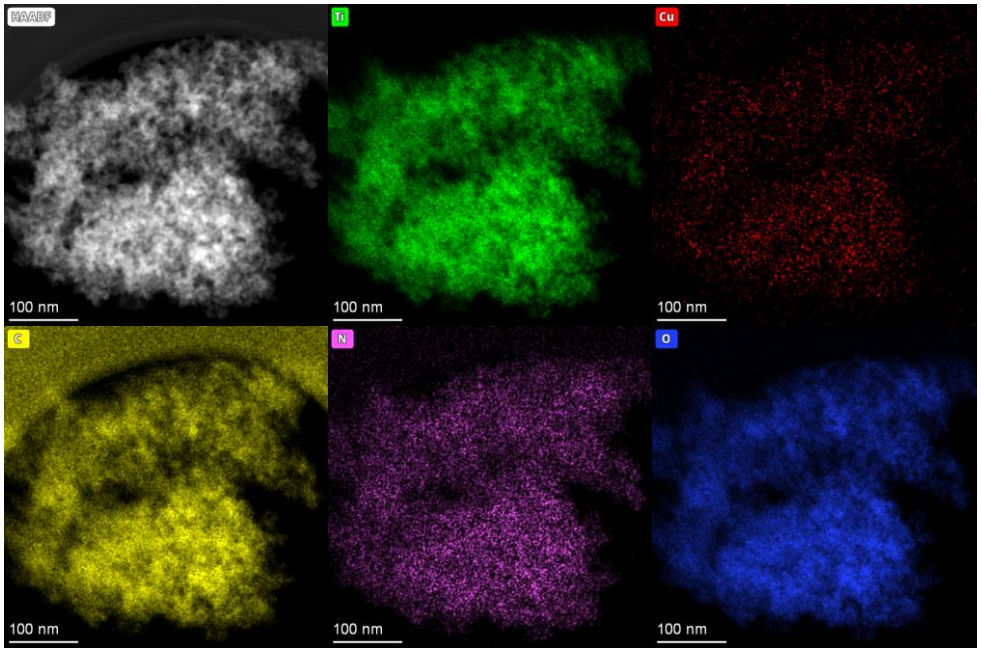

Figure 5.19. HAADF-TEM micrograph and element mapping taken on Cu@TCPP_0.1 sample.

Furthermore, SEM images were also taken on aerogels prior and after the doping process. In all of the cases, we observed a granular uniform surface with aggregations of nanoparticles of around 50 – 80 nm. Figure 5.20 shows micrographs taken at 25 000 magnifications.

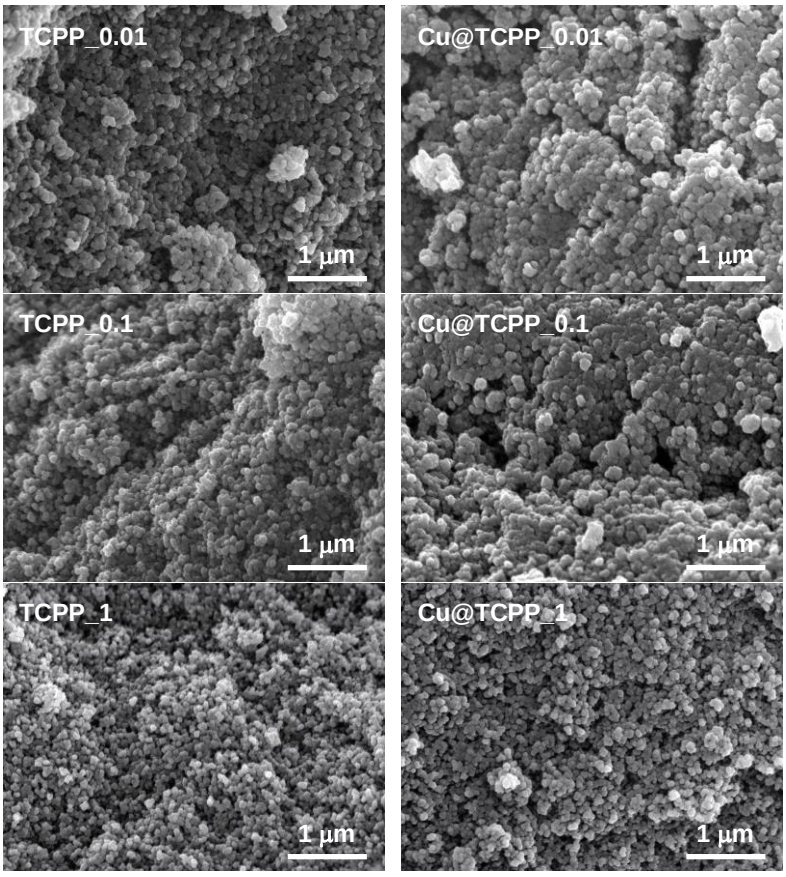

Figure 5.20. SEM images at 25 kX magnifications taken on (a) neat MOAs and (b) Cu-doped MOAs.

Gas physisorption measurements

To get further details of the porosity of the prepared MOAs, N_2 adsorption isotherms at 77 K were measured (Figure 5.21). All samples exhibit type II/IV adsorption isotherms following the IUPAC criteria[58] with a narrow hysteresis loop at relative high pressures ($p/p° > 0.85$) as a result of the combination of macropores and mesopores. The data subtracted from the numerical analysis of the curves is gathered in Table 5.6. The BET surface area of the pristine aerogels ranges from 613 to 822 $m^2 \cdot g^{-1}$.[36] Despite these values are lower than those found for the crystalline Ti(IV)-based MOFs of similar linker,(1300 – 3800 $m^2 \cdot g^{-1}$)[59] can be considered relatively high due to the small particle size and lightness of titanium. In fact, these values overpass those found for analogous zirconium(IV) MOAs (52 – 377 $m^2 \cdot g^{-1}$)[60]. The pore volume analysis of the samples demonstrates a major contribution of macropores (79 – 86% of the total porosity) accompanied by a meaningful presence of mesopores (14 – 21%) and a minor

contribution of micropores (< 1%). Interestingly, *t*-plot method analysis of the data reveals that the sample with the greatest porphyrin content (TCPP_1) has significantly greater contribution of micropores (see S_{micro} and V_{micro} values), which explains its notably greater surface area with respect to the aerogels with less TCPP content (TCPP_0.01 and TCPP_0.1). Since non-meaningful microstructural changes were observed in TEM analysis, the origin of this difference in microporosity can be related to the intrinsic porosity of the particles provided by the large porphyrinic spacer, which, despite of the lack of crystallinity, it allows to retain certain interconnection between the cavities hold within the polymeric coordination framework. The doping with copper(II) produces a slight lowering of the specific surface area and pore volume values which can be attributed to the increase of the mass of the framework after the doping. The exception to this statement is the macropore volume whose value is largely influenced by the p/p° value resulting from the equilibration of the last point of the isotherm. In this sense, small changes in p/p° can probe notably greater or smaller pore ranges.

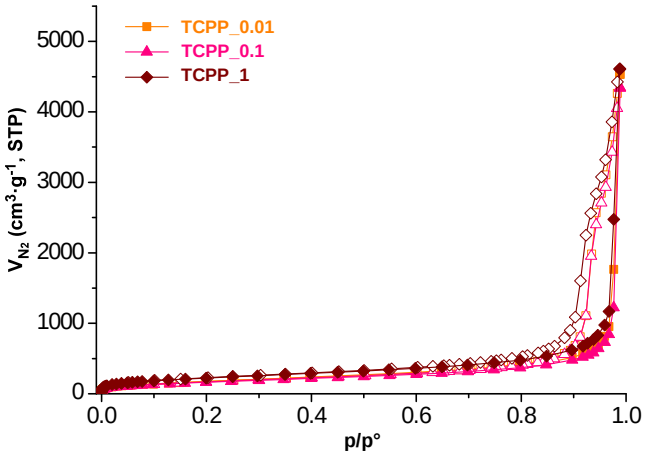

Figure 5.21. Nitrogen adsorption isotherms (77 K) for (a) neat and (b) Cu(II)-doped MOAs. Close symbols for adsorption curves and open symbols for desorption.

Table 5.6. Porosity data for neat and Cu(II)-doped MOAs.[a]

Sample	S_{BET} ($m^2 \cdot g^{-1}$)	S_{micro} ($m^2 \cdot g^{-1}$)	S_{ext} ($m^2 \cdot g^{-1}$)	V_{micro} ($cm^3 \cdot g^{-1}$)	V_{meso} ($cm^3 \cdot g^{-1}$)	V_{macro} ($cm^3 \cdot g^{-1}$)	D_{probed} (nm)
TCPP_0.01	651	41	610	0.010	1.248	5.725	≤ 170
TCPP_0.1	613	39	574	0.009	1.123	6.584	≤ 174
TCPP _1	822	119	703	0.046	1.462	5.623	≤ 163
Cu@TCPP_0.01	512	0	512	0	0.961	5.786	≤175
Cu@TCPP_0.1	564	0	564	0	1.069	5.863	≤ 176
Cu@TCPP_1	686	86	600	0.033	1.323	6.782	≤ 175

[a] S_{BET} stands for BET specific surface area. Micropore surface area (S_{micro}) and volume (V_{micro}) are estimated from the t-plot calculation. External surface area is calculated by subtracting the microporous contribution from the total area ($S_{ext} = S_{BET} - S_{micro}$), V_{meso} is the extracted pore volume for pores ≤ 50 nm subtracting the contribution of micropore volume and V_{macro} is the calculated by subtracting V_{micro} and V_{meso} to the total void volume for pores below the maximum probed pore-size (D_{probed}).

5.2.2.3. Photocatalytic conversion of carbon dioxide

The alcohol production rates (r_{CH_3OH} and $r_{C_2H_5OH}$) and apparent quantum yields (AQY) provided by MOAs in the CO_2 photoreduction reaction under visible led light are gathered in Table 5.7. Blank test performed in absence of CO_2 and/or light did not produce any measurable product. The sample TCPP_0.1 produces methanol as the major product (r_{CH_3OH} = 331 $\mu mol \cdot g^{-1} \cdot h^{-1}$, AQY_{CH_3OH} = 6%), but also ethanol was detected in the liquid fraction ($r_{C_2H_5OH}$ = 36 $\mu mol \cdot g^{-1} \cdot h^{-1}$, $AQY_{C_2H_5OH}$ = 1%). The previously reported titanium(IV)-NH_2BDC aerogel performed somewhat better in terms of total alcohol reaction rate (422 $\mu mol \cdot g^{-1} \cdot h^{-1}$) and apparent quantum yield (AQY = 11%),[36] which implies that the inclusion of neat porphyrin did not provide any benefit. However, the inclusion of copper (Cu@TCPP_0.1) led to a meaningful increase of the total alcohol production (642 $\mu mol \cdot g^{-1} \cdot h^{-1}$) with an apparent quantum yield of 20%. Besides, the presence of copper produces a change in the product selectivity in such a way that ethanol reaction rate (491 $\mu mol \cdot g^{-1} \cdot h^{-1}$) overpasses notably that of methanol (151 $\mu mol \cdot g^{-1} \cdot h^{-1}$). This favoured formation of ethanol respect methanol is also observed in the remaining copper-doped samples (Cu@TCPP_0.01 and Cu@TCPP_1), but both reaction rate and AQY values are below that of Cu@TCPP_0.1.

Table 5.7. Continuous photoreduction of CO_2 at prepared MOAs-based surfaces under visible light (5 $mW \cdot cm^{-2}$). Operating conditions: 100 $\mu L \cdot min^{-1}$ (CO_2 sat. 0.5 M $KHCO_3$), 2 $mg \cdot cm^{-2}$.

Sample	**CO_2 gas**	**Light rradiation**	CH_3OH	C_2H_5OH	CH_3OH	C_2H_5OH
			r ($\mu mol \cdot g^{-1} \cdot h^{-1}$)		**AQY (%)**	
TCPP_0.1	Yes	**No**	-	-	-	-
TCPP_0.1	No	Yes	-	-	-	-
TCPP_0.1	**No**	**No**	-	-	-	-
TCPP_0.1	Yes	Yes	331	36	6	1
Cu@TCPP_0.01	Yes	Yes	89	266	2	10
Cu@TCPP_0.1	Yes	Yes	151	491	3	17
Cu@TCPP_1	Yes	Yes	143	295	3	10

Electrodes after the CO_2 reduction reaction (continuous for 180 min) were characterized by HAADF-TEM elemental mapping (Figure 5.22), that showed the preservation of metal-organic network after the process. Catalytic surfaces suffered from partial material leaching, nevertheless most of the catalytic ink sprayed onto de carbon paper is retained after the photocatalytic reaction process (Figure 5.23).

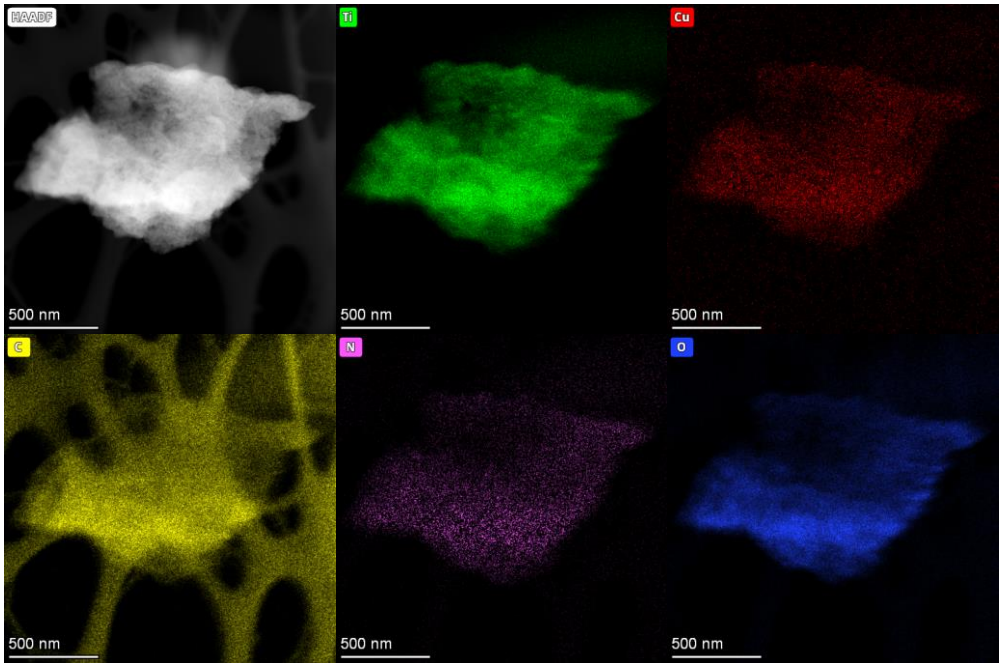

Figure 5.22. HAADF-TEM micrograph and elemental mapping taken on Cu(II)-doped TCPP_0.1-based surface (electrode) after de CO_2 photoreduction experiments.

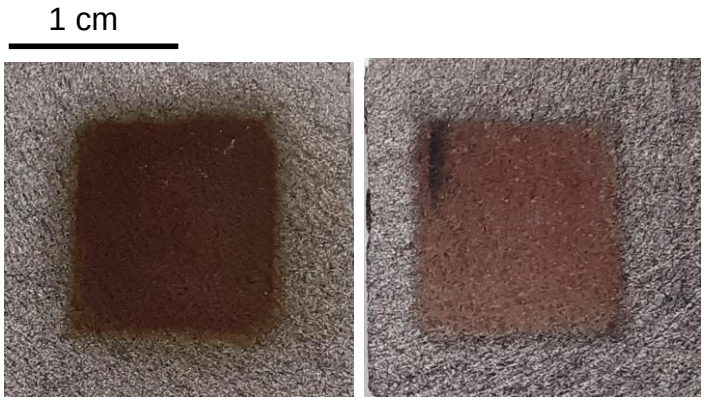

Figure 5.23. Appearance of Cu@TCPP_0.1 electrode (a) before and (b) after the catalytic reaction.

5.3. Ti(IV)-BASED MOGS FOR PHOTOCATALYTIC HYDROGEN PRODUCTION

5.3.1. EXPERIMENTAL SECTION

This section describes the synthetic procedure used to obtain the metal-organic gels based on titanium(IV) and rigid dicarboxylic ligands (BDC: benzene-1,4-dicarboxylato and/or NH_2BDC: 2-aminobenzene-1,4-dicarboxylato), and analysed their performance in the photocatalytic hydrogen evolution reaction (HER). The MOGs are prepared using the optimized sol-gel procedure before described for TCPP-based systems. Afterwards, a post-synthetic modification is carried out to get platinum(IV)-doped MOGs. Same post-handling techniques explained in the last part of Section 5.2.1.1 are used to obtain the xerogels (conventional drying) and aerogels (supercritical drying). Chemical characterization of the materials was carried out on xerogels samples, while for microstructural analysis gel and aerogel samples were employed. All the chemicals employed were of reagent grade and are gathered in Table 2.1 of Chapter 2. Finally, the conditions for the light-driven hydrogen evolution reaction experiments are explained.

5.3.1.1. Synthetic procedure

Synthesis of metal-organic gels. First, titanium(IV) n-butoxide (1114 μL, 3.18 mmol) was mixed under continuous stirring with 10 mL of 2-butanol and subsequently,118 μL of HCl 0.29 M dissolved in 4 mL of 2-butanol were added dropwise. The resulting clear solution was stirred for an hour in a closed vessel. Afterwards, a DMF/2-butanol (10 mL/2 mL) solution containing the ligands (benzene-1,4-dicaboxylic acid (H_2BDC) and /or 2-aminobenzene-1,4-dicarboxylic acid (H_2NH_2BDC)) was mixed with the Ti(IV) solution obtaining clear and stable sol. The total ligand amount (2.38 mmol) was set to achieve a titanium:linker molar ratio of 1:0.75, according to the ideal ratio found in MIL-125 and MIL-125-NH_2.[37] The sample coding and the ligand quantities employed are gathered in Table 5.8. Finally, the mixture was introduced in a preheated oven within a closed vessel and maintained at 80 °C for 6h.

As a result, well-formed translucent metallogels were obtained which acquired a yellow-orangish colour when NH_2BDC ligand is introduced (Figure 5.24). The remaining regaents were removed exchanging the solvent trapped in the gels with a mixture of 2-butanol/DMF (2:1), followed by a mixture of 2-butanol/DMF/ethanol (1:1:1) and finishing with three exchanges of absolute ethanol to get the alcogels suitable for drying process and chemical/microstructural characterization. Finally, gels were also conditioned in

water using deionized H_2O (3 times) to get the hydrogels for the hydrogen evolution reaction (HER) experiments.

Table 5.8. Sample coding and amounts of ligand employed during the synthesis of Ti-BDC/NH_2BDC gels.

Sample[a]	Ligand employed (g, mmol)		BDC:NH_2BDC ratio
	H_2BDC	H_2NH_2BDC	
B100	0.4035, 2.205	–	100:0
B50A50	0.2017, 1.102	0.2177, 1.284	50:50
A100	–	0.4355, 2.569	0:100

[a] B and A stand for BDC and NH_2BDC, respectively, and numeric characters represent the targeted ligand ratio.

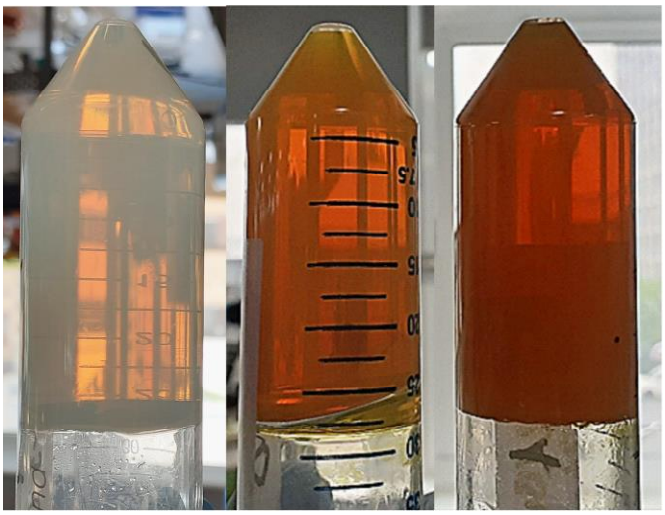

(a) (b) (c)

Figure 5.24. Appearance of as-synthesized (a) B100, (b) B50A50 and (c) A100 gels.

Pt-doping of metal-organic gels. The three Ti(IV)-based MOGs were subjected to a platinum(IV)-doping process. For this purpose, 4 g of the alcogels were placed in a closed vessel containing 30 mL of a 0.26 mM hexachloroplatinic(IV) acid solution in absolute ethanol. The platinum content was stablished to reach 1 wt% of Pt respect to the amount of dried gels. The doping process was prolonged for 12 h at room temperature. Then, the MOGs were recovered and exchanged with absolute ethanol three times (alcogels for drying processes and characterization) and finally, conditioned in water (hydrogels) for HER measurements.

5.3.1.2. Chemical characterization

Same procedures explained in Section 5.2.1.2 were performed to accomplish chemical characterization in Ti(IV) and BDC/NH_2BDC-based MOGs.

Proton nuclear magnetic resonance spectroscopy (^{1}H-NMR). Figure 5.25 shows the label assignation of the species identified in the NMR spectra (Figures 5.26–5.28). In all of them, the singlet at 8.39 ppm corresponds to the formic acid C–H atom

and the singlet at 6.45 ppm is related to the two vinylic H-atoms of fumaric acid (internal standard). The singlet present at 8.31 ppm corresponds to the four aromatic H-atoms of benzene-1,4-dicarboxilic acid (Figures 5.26 and 5.27) while the three chemically distinguishable H-atoms of 2-aminobenzene-1,4-dicarboxylic acid are featured by three set of signals at 7.63 ppm (doublet), 7.20 ppm (doublet) and 7.12 ppm (double doublet) (Figures 5.27 and 5.28). Further details of its characterization in the following section.

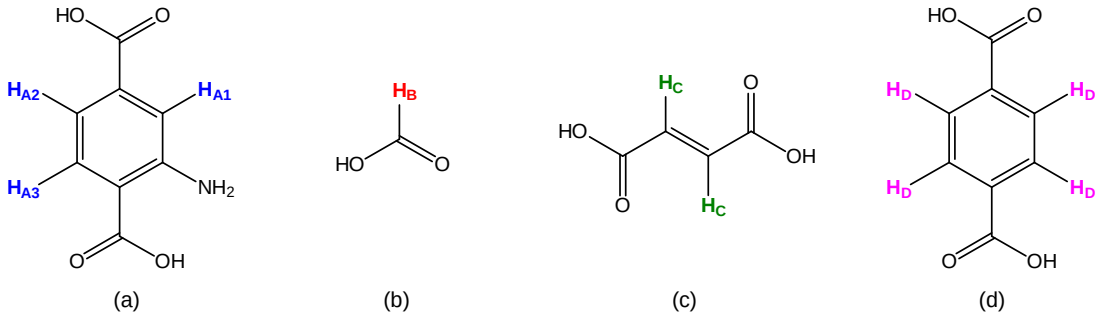

Figure 5.25. Proton label assignation for (a) 2-aminobenzene-1,4-dicarboxylic acid, (b) formic acid, (c) fumaric acid and (d) benzene-1,4-dicarboxylic acid for ^{1}H-NMR spectra in Figures 5.26 – 5.28.

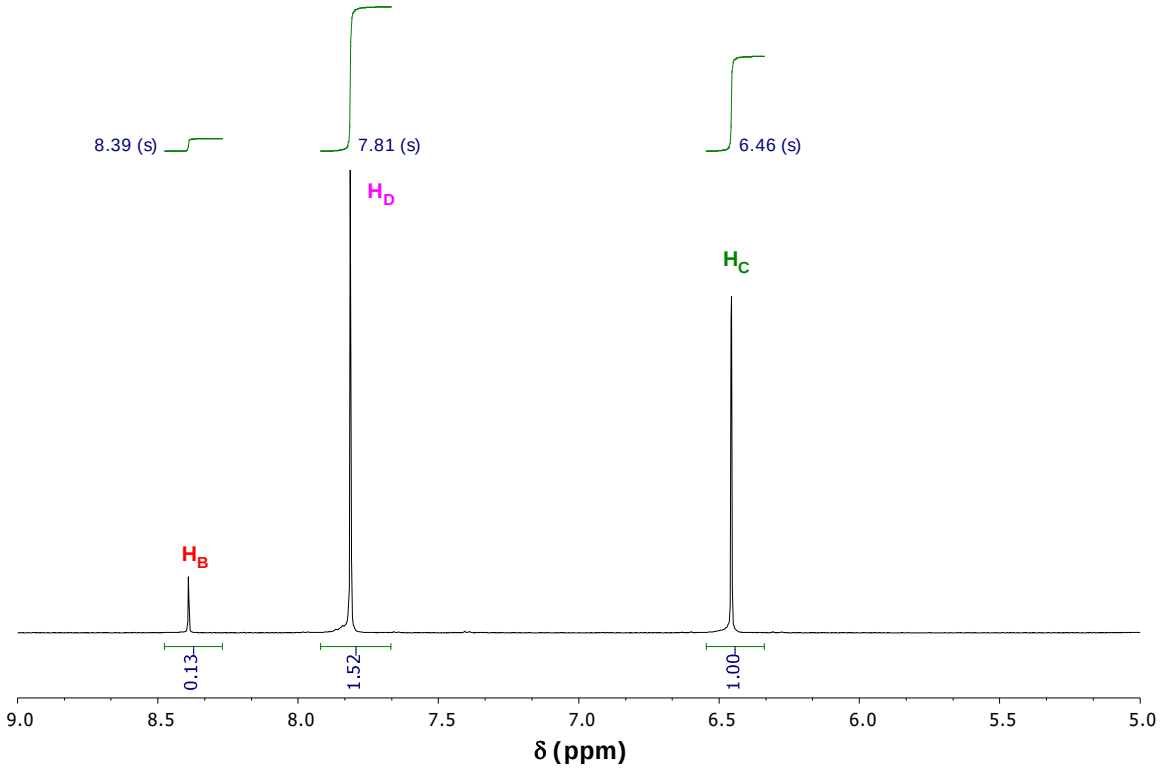

Figure 526. ^{1}H-NMR spectrum of digested B100.

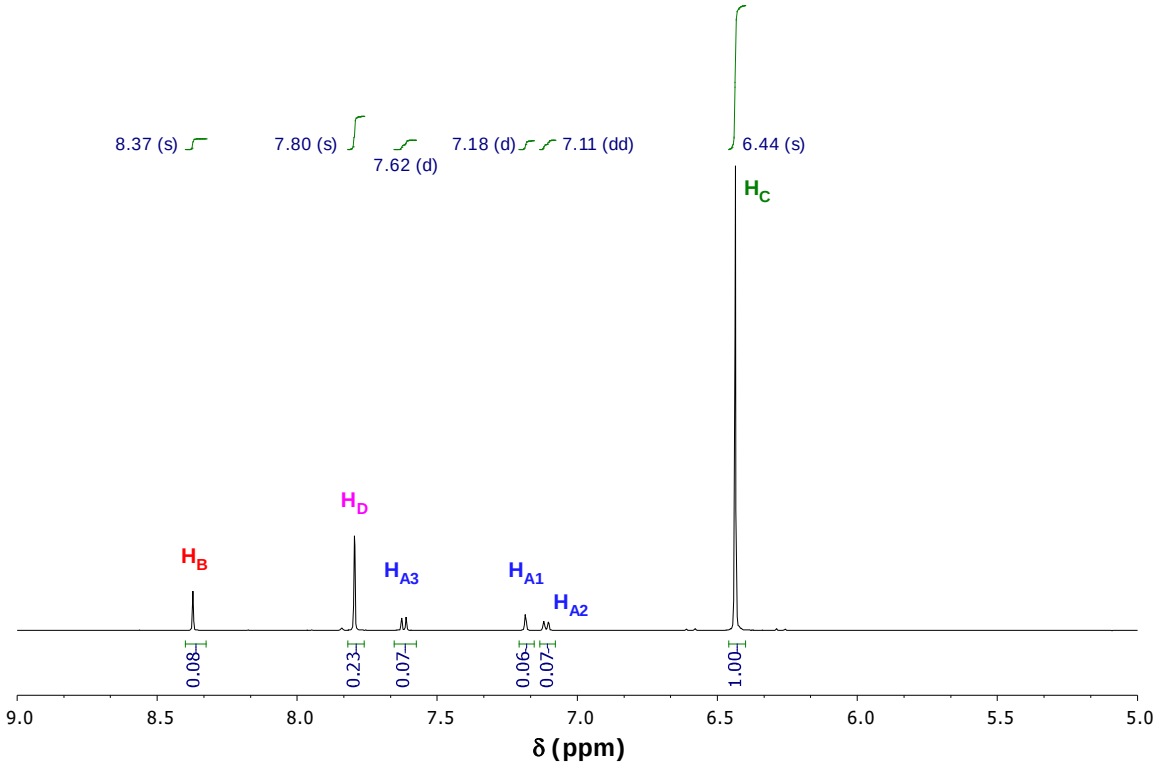

Figure 5.27. ^{1}H-NMR spectrum of digested B50A50.

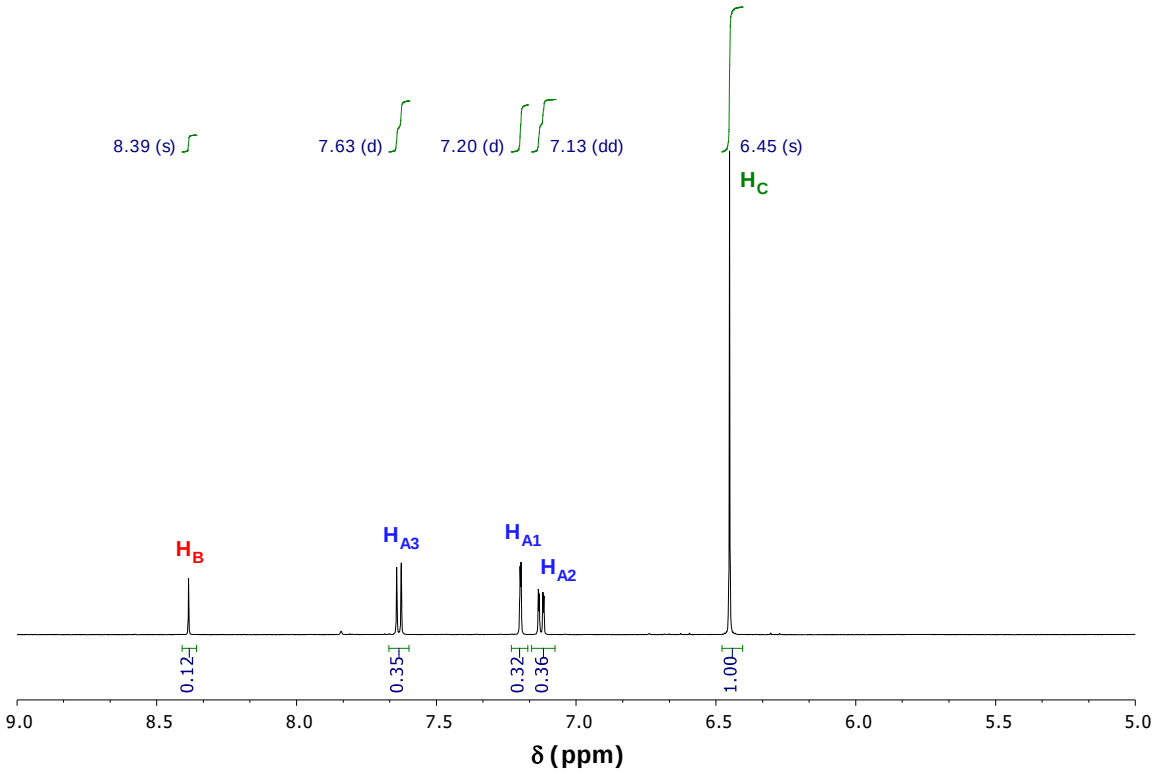

Figure 5.28. ^{1}H-NMR spectrum of digested A100.

Thermogravimetric analysis (TGA). Figure 5.29 shows the thermogravimetric analysis of MOXs performed in synthetic air from 30 °C to 800 °C. The thermograms show three main stages of weight loss. First, solvent molecules contained within the pores are released (30 – 150 °C). Thereafter, at intermediate temperature values (150 – 300 °C), coordinated water molecules that come from the condensation of hydroxide groups and formic acid are released. Finally, the framework decomposition takes place (300 – 500 °C). In the case of B100 sample the framework decomposes exothermically in a single step that starts roughly at 400 °C. The samples containing NH_2BDC ligand (B50A50 and A100) exhibit a mass loss close to 300 °C probably related to the pyrolytic release of the $–NH_2$ group. This type of decompositions are usually endothermic, however the sensitivity of the DTA signal was not enough to observe a clear peak in this region. Thereafter, around 400 °C the remaining material decomposes again exothermically. In all cases, TiO_2 was formed as final residue, which was identified by PXRD (rutile phase).

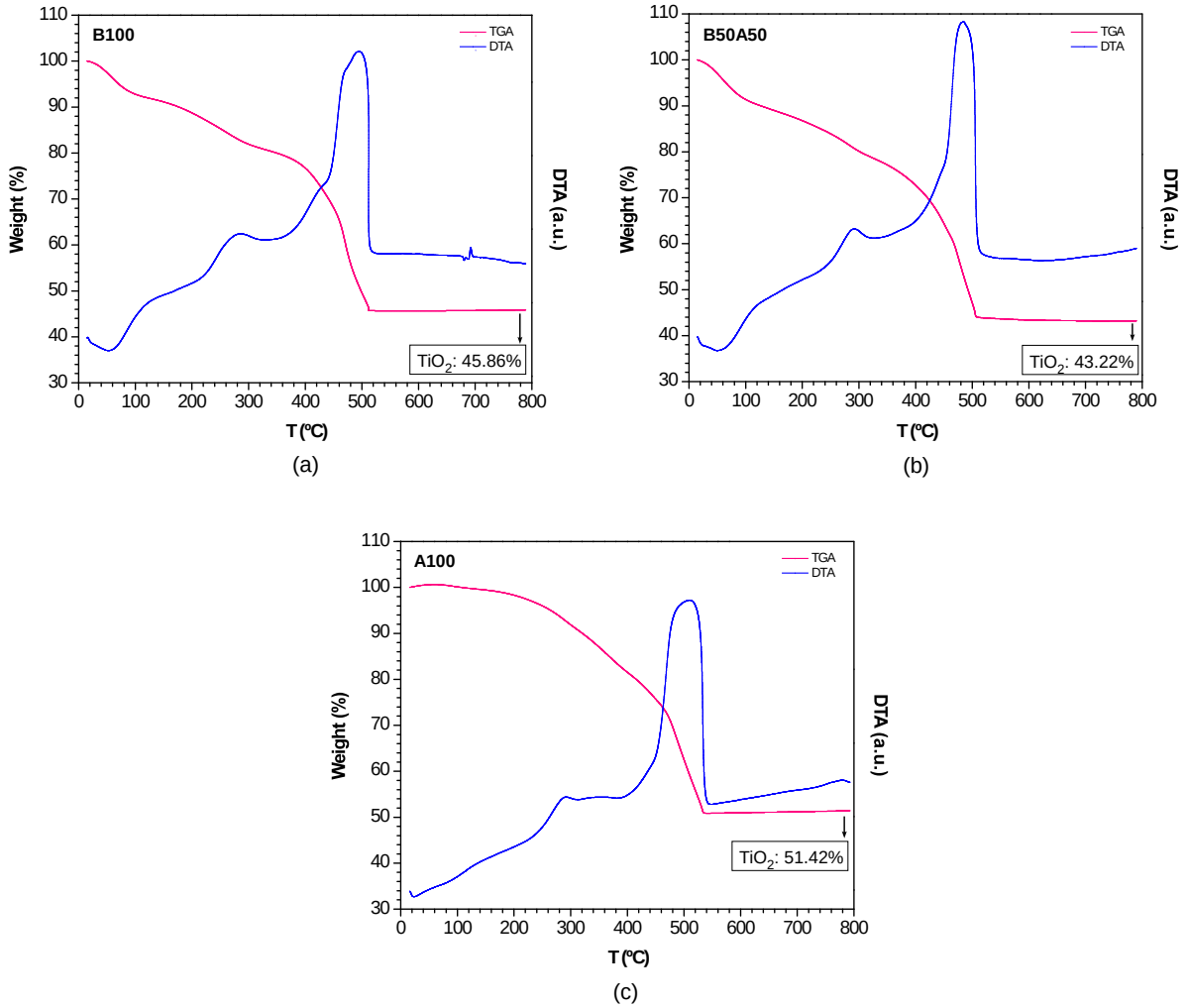

Figure 5.29. TGA-DTA curves of (a) B100, (b) B50A50 and (c) A100.

Attenuated total reflectance - Fourier-transform infrared spectroscopy (ATR-FTIR). The infrared spectra of metallogels and the assignation of the main vibration modes are gathered in Figure 5.30. The bands shaded in yellow (Figure 5.30b) correspond to stretching and deformation vibrations of $–NH_2$ group, and are, therefore, only observable in B50A50 and A100 samples. The rest of the bands are coincident in the three samples.

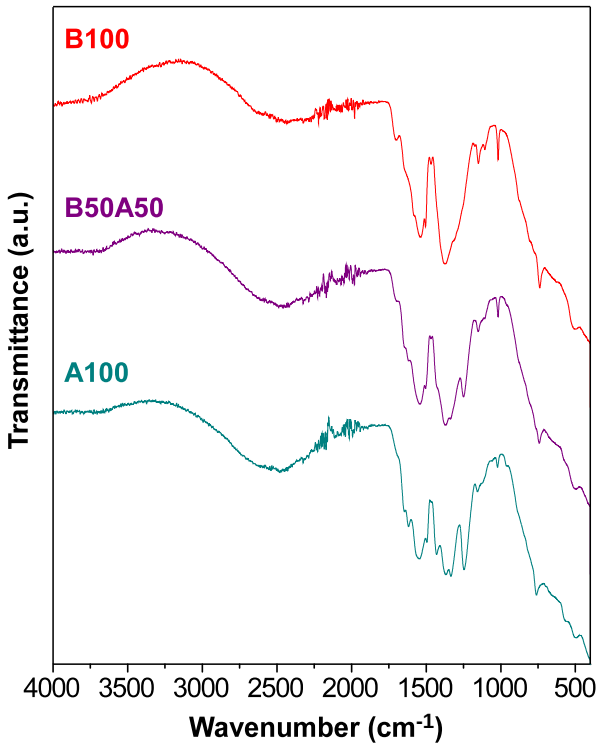

(a)

Wavenumber (cm^{-1})	Band assignation
1700, sh	ν_{asym} (COO)
1620, m	δ_{ip} (NH_2)
1560, s	ν (C_{ar}–C)
1500, sh	ν_{ring} (C_{ar}–C_{ar})
1420, sh	ν (C_{ar}-N)
1370, s	ν_{sym} (COO)
1335, sh	δ_{ip} (NH_2)
1250, s	δ_{oop} (NH_2)
1020, w	δ (C-H)
760, s	δ_{oop} (C-H) + δ_{oop} (O-C-O)
~500, w	ν (Ti–OCO)

(b)

Figure 5.30. (a) FTIR spectra and (b) band assignments for Ti(IV)/BDC/NH_2BDC-based MOAs (s: strong, m: medium, w: weak and sh: shoulder signals; *sym*: symmetric, *asym*: asymmetric, *ip*: in plane, *ring*: ring stretching, *ar*: aromatic, *oop*: out of plane of stretching (ν) or bending (δ) modes).

5.3.1.3. Photocatalytic H_2 generation experiments

For hydrogen evolution (HER) experiments a known amount of wet MOGs (neat and Pt(IV)-doped hydrogels) to get 5 mg of dried samples (see Table 5.9) were placed in glass vials along with 2 mL of a 0.1 M triethanolamine solution (TEOA, pH = 7, acting as electron donor). Non-doped samples were tested with and without the addition of a Pt-based co-catalyst. In the former cases, 12.3 µL of a 20.9 mM hexachloroplatinic acid solution (H_2PtCl_6, 1 wt, % with respect to dried samples) were also added. The vials were capped with rubber septa, sonicated for 20 min and purged for 10 min with N_2 gas. Samples were irradiated using a solar light simulator and the set-up explained in Section 2.34.3 of Chapter 2 with an intensity of 1 sun (100 $mW{\cdot}cm^{-2}$) and under AM 1.5G conditions (wavelength distribution of sunlight going through 1.5 atmospheres

(zenith angle of 48.2°) for a global (G) spectrum including diffused and scatter light). The water bath where the samples were mounted with continuous stirring was maintained at 25 °C and the constant purge flow rate of N_2 was established at 5 mL·min^{-1} throughout the 12 h experiments. H_2 evolution was monitored by gas chromatography using an auto-sampler programmed to inject 2 mL of the selected headspace steam. Each sample was measured in triplicate and results are given as the mean value together with standard deviation (σ), which was calculated according to the equation 5.2:

$$\sigma = \sqrt{\frac{\sum (x - \bar{x})^2}{n-1}} \qquad \text{equation 5.2}$$

Table 5.9. Photocatalytic H_2 generation conditions used for testing Ti/BDC/NH_2BDC-based and Pt(IV)-doped MOGs.

Sample	Hydrogel %V[a]	Wet MOG (mg)	TEOA 0.1 M (mL)	H_2PtCl_6 20.9 mM (µL)[b]
B100	87.1%	39	2	none or 12.3 µL
B50A50	89.7%	48	2	none or 12.3 µL
A100	95.3%	107	2	none or 12.3 µL
Pt@B100	90.8%	54	2	none
Pt@B50A50	92.7%	68	2	none
Pt@A100	94.9%	97	2	none

[a] Solvent volume percentage (%V) found out in hydrogels by conventional drying and weighting comparison.
[b] Experiments performed with neat MOGs were performed in absence and in presence of H_2PtCl_6 as co-catalyst. Doped MOGs were measured without adding Pt-based co-catalyst.

5.3.2. RESULTS AND DISCUSSION

5.3.2.1. Characterization of Ti/BDC/NH_2BDC MOGs

Chemical characterization

Chemical analysis combining ^{1}H-NMR and TGA measurements allowed to estimate the chemical formula of the Ti(IV)/BDC/NH_2BDC MOGs (Table 5.10). Note that, ESI-MS analysis above described (Section 5.2.2.1) indicate that under the synthesis conditions herein employed for Ti/carboxylate metal-organic gels the metal centre is mainly assembled as Ti_8O_8 type clusters. Accordingly, the formula of each MOG have been normalized to octanuclear Ti-clusters, which show the presence of 2 – 3 dicarboxylato linkers and a set of formate and OH^-/H_2O pairs that would complete the coordination sphere to compensate the linker vacancies, as discussed in previous chapter for Zr and Ti MOFs.[61]

Table 5.10. Chemical formula estimated for synthesized Ti(IV)/BDC/NH_2BDC-based MOGs.

Sample[a]	Formula
B100	$Ti_8O_8(OH)_4(BDC)_{3.33}(HCOO)_{1.14}(H_2O)_{4.2}(OH)_{4.2}$
B50A50	$Ti_8O_8(OH)_4(BDC)_{1.01}(NH_2BDC)_{1.16}(HCOO)_{1.32}(H_2O)_{6.34}(OH)_{6.34}$
A100	$Ti_8O_8(OH)_4(NH_2BDC)_{2.96}(HCOO)_{0.94}(H_2O)_{5.14}(OH)_{5.14}$

Figure 5.31 shows the comparison of experimental PXRD patterns of MOXs with respect to those simulated for referential MIL-125 and MIL-125-NH_2 titanium(IV)-MOFs. The MOXs samples exhibited a short range ordering broad peak at 2θ = 6 – 7°. As aforementioned (Section 5.2.2.1), this peak is concordant with the maximum intensity reflection present in MIL-125 family (Miller index: (1 0 1); 2θ = 6.8°), that comes from the interplanar distances set by BDC and NH_2BDC linkers between titanium clusters.

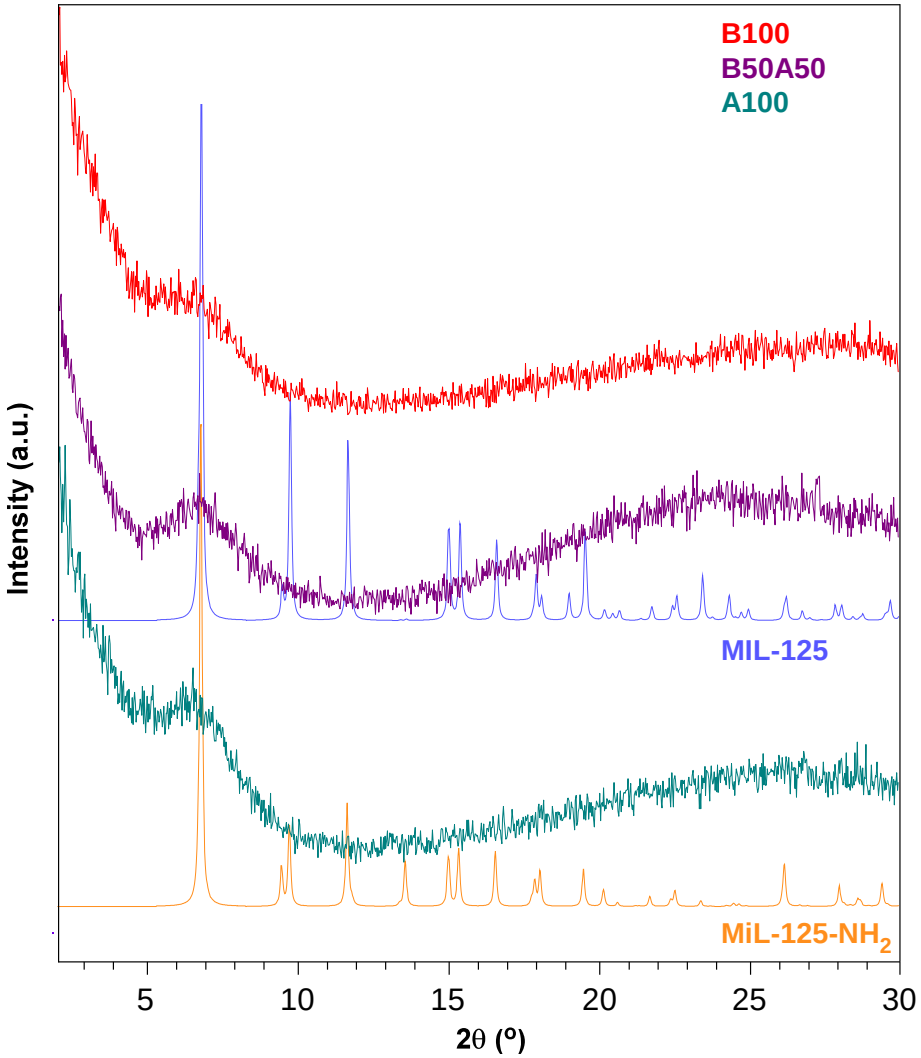

Figure 5.31. PXRD patterns of B100, B50A50 and A100 in comparison to MIL-125 and MIL-125-NH_2.

X-ray photoelectron spectroscopy (XPS) of B100 samples allowed to identify the Ti 2p signals characteristic from Ti(IV) oxo-clusters, and C 1s and O 1s bands of organic BDC linker (Figure 5.32), further explained in previous section (5.2.2.1).

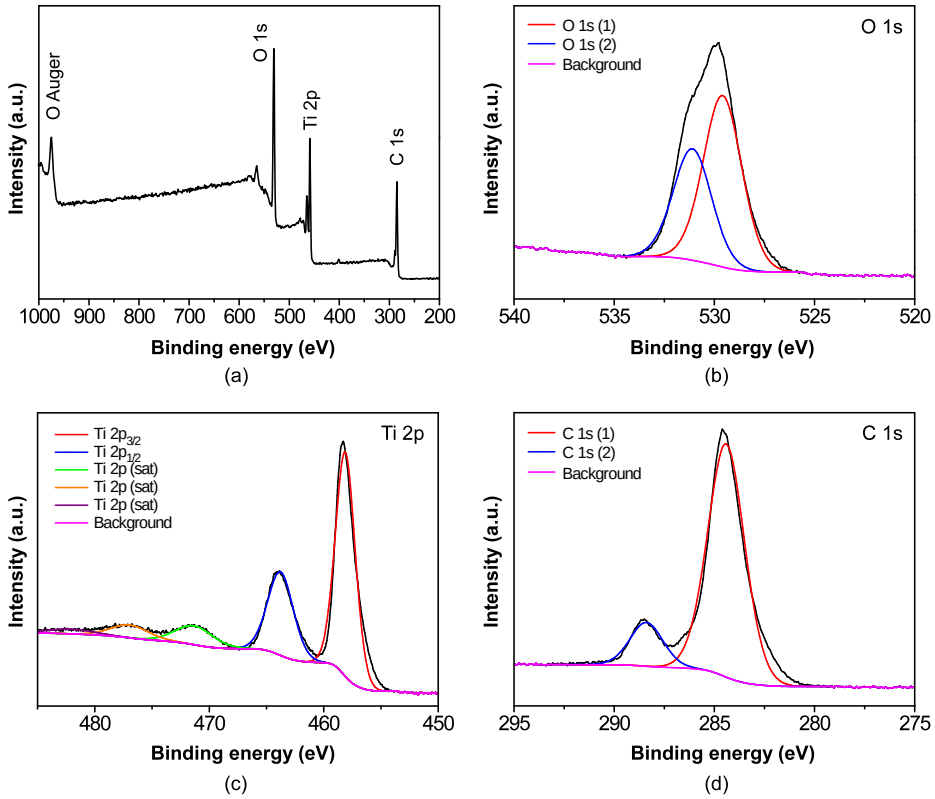

Figure 5.32. (a) XPS full spectrum and high resolution spectrum for (b) O 1s, (c) Ti 2p and (d) C 1s peaks of B100 sample. *Sat* refers for characteristic satellite peaks.

Microstructural characterization

Microstructure of the obtained materials was studied by cryogenic transmission electron microscopy (cryoTEM) carried out on hydrogels (Figure 5.33). This technique allows to freeze the system in the wet gels, prior to any drying process, which precludes possible microstructural changes taking place during sample drying. Micrographs show the microstructure of original wet MOGs comprised of metal-organic tiny nanoparticles of less than 5 nm. These nanoparticles are entangled into a meso- and macroporous microstructural network which provides a meaningful external surface area.

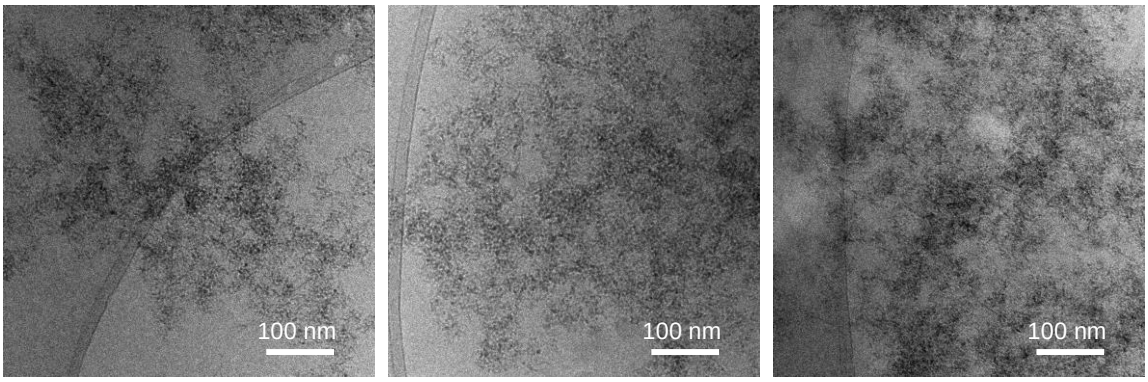

Figure 5.33. cryoTEM micrographs of (a) B100, (b) B50A50 and (c) A100 taken at 80kX magnifications.

To get further microstructural details, N_2 adsorption measurements were performed at 77 K on MOAs. Figure 5.34 shows the isotherms of each pristine MOA sample and Table 5.11 summarizes the adsorption data extracted from them. All samples exhibit a type II/IV isotherm according to the IUPAC classification,[58] with a narrow hysteresis loop at relative high pressure ($p/p° > 0.8$) characteristic of materials with a combined contribution of mesopores and macropores, which agree with the microstructural feature observed in cryoTEM images. The BET surface area calculated for aerogels ranges from 408 to 604 $m^2 \cdot g^{-1}$. Again, these surface areas can be regarded as relatively high compared to other aerogel systems (see Section 5.2.2.1), due to the small particle size and lightness of titanium. Total pore volumes range from 0.926 to 1.238 $cm^3 \cdot g^{-1}$, considerable smaller than TCPP-based ones, since these measures were done until $p/p°$ values of 0.96, which allows to analyse only pores smaller than 50 nm (*i.e.* in the range of mico-/mesopores). This means that none macropore is observed herein, but its contribution is probably going to be notorious. According to the data subtracted from t-plot analysis, the microporosity implies only a minor contribution to the total surface area and pore volume of the MOAs, which may be ascribed to the absence of crystallinity.

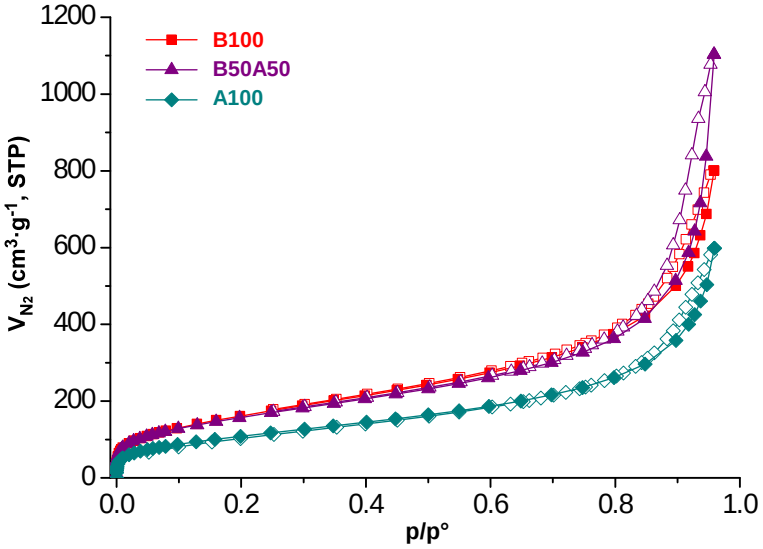

Figure 5.34. Nitrogen adsorption isotherms (77 K) for BDC/NH_2BDC-based MOAs. Close symbols for adsorption curves and open symbols for desorption.

Table 5.11. Posority data extracted from isotherms for BDC/NH_2BDC-based MOAs.[a]

Sample	S_{BET} ($m^2 \cdot g^{-1}$)	S_{micro} ($m^2 \cdot g^{-1}$)	S_{ext} ($m^2 \cdot g^{-1}$)	V_{micro} ($cm^3 \cdot g^{-1}$)	V_{meso} ($cm^3 \cdot g^{-1}$)
B100	604	42	562	0.012	1.226
B50A50	580	60	520	0.023	1.683
A100	408	8	400	0	0.926

[a] S_{BET} stands for BET specific surface area. Micropore surface area (S_{micro}) and volume (V_{micro}) are estimated from the t-plot calculation. External surface area is calculated by subtracting the microporous contribution from the total area ($S_{ext} = S_{BET} - S_{micro}$) and V_{meso} is obtained by subtracting the contribution of micropore volume to the pore volume for pores ≤ 50 nm.

Optical properties

UV-Vis diffuse reflectance spectroscopy (DRS) was performed in the samples to analyse their optical properties prior to the light conducted HER experiments. As before, the Kubelka-Munk function, $F(R) = (1-R_\infty)^2/2 \cdot R_\infty$ ($R_\infty = R_{sample} / R_{standard}$),[49] was used for the data treatment to represent the UV-Vis absorption spectra. The collected and transformed data of MOXs are gathered in Figure 5.35. As can be observed, sample containing BDC linker starts absorbing next to the UV region with a small absorption in the range of 400 – 450 nm and a steep jump at around 350 nm, while the inclusion of NH_2BDC chromophore linker in B50A50 and A100 makes the material active for absorption in the visible region, starting to absorb in the 600 – 550 nm range with a sharp increase at 500 nm. The comparison with UV-Vis DRS data found in literature for their chemically analogous but crystalline MOFs, MIL-125 and MIL-125-NH_2, respectively, show small differences in their absorption behaviour: MIL-125 and MIL-125-NH_2 show a sharper absorption edge at 350 nm and 500 nm, respectively, which can be related with their crystalline order.[19]

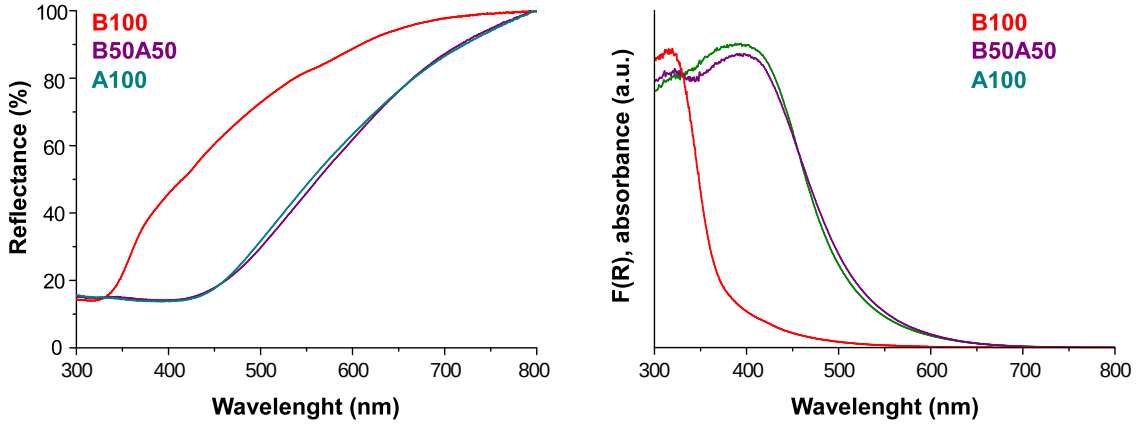

Figure 5.35. UV-Vis diffuse reflectance spectroscopy of BDC/NH_2BDC-based MOXs (a) as measured (R,%) and (b) transformed to absorbance using the Kubelka-Munk function (F(R)).

5.3.2.2. Pt(IV)-doped MOGs characterization

Doping content of Pt(IV)-doped MOGs was determined by X-ray fluorescence spectroscopy (XRF). As shown in Table 5.12, the MOG based solely in benzene-1,4-dicarboxylato (BDC) reached the smallest amount of platinum, whereas the inclusion of 2-aminobenzene-1,4-dicarboxylato (NH_2BDC) linker in the network helped to increase the doping content to 0.5 and 0.6% (w_{Pt}/w_{MOG}) in B50A50 and A100, respectively. These Pt-loadings mean half of the targeted ratio used during doping process, that was stablished to 1% (w_{Pt}/w_{MOG}).

Table 5.12. Relative titanium and platinum content (wt_M, % of total metal) and platinum content (wt_{MOG}, % of total network) of doped MOGs.

Sample	Relative Ti content (wt_M, %)	Relative Pt content (wt_M, %))	Pt content in MOG (wt_{MOG}, %)
Pt@B100	99.60	0.40	0.1
Pt@B50A50	98.48	1.52	0.5
Pt@A100	98.04	1.96	0.6

PXRD of Pt@B100 shows a similar diffraction pattern found for B100 with no additional peaks and the microstructure of the gel after platinum doping is retained (Figure 5.36). As can be seen, HAADF-TEM image and element mapping analysis of supercritical-dried Pt@B100 as representative sample shows a fine and homogeneous distribution of platinum thorough all the metal-organic porous network. Besides, N_2 adsorption isotherm shape and extracted data (S_{BET} = 617 g·cm^3, V_T = 1.73 cm^3·g^{-1} for p/p° = 0.96) is analogous to that of the parent sample explained above.

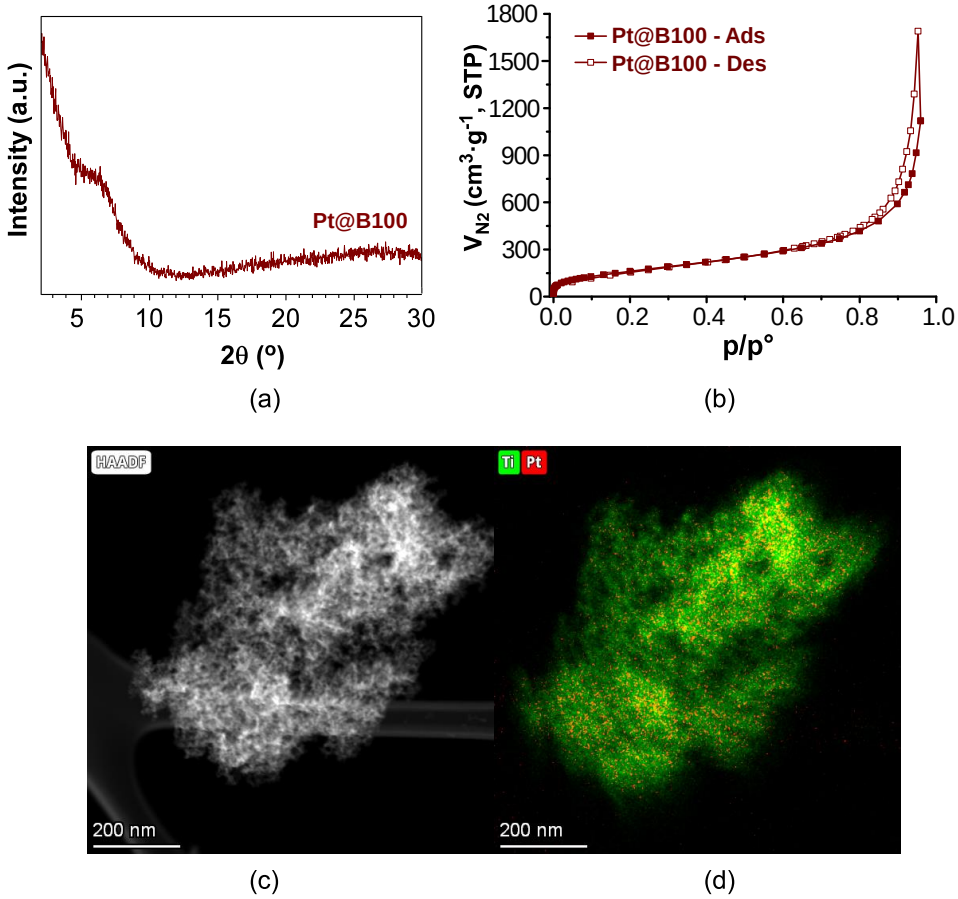

Figure 5.36. (a) PXRD, (b) N_2 adsorption isotherm, (c) HAADF-TEM micrograph and (d) Ti and Pt element mapping of Pt@B100 aerogel.

5.3.2.3. Photocatalytic hydrogen evolution reaction (HER) experiments

Photocatalytic H_2 production experiments were performed under solar-simulated irradiation light using herein prepared metal-organic hydrogels as catalysts and an aqueous solution containing 0.01 M triethanolamine (TEOA) as a sacrificial electron donor. The experiments were run for 16 h. Figure 5.37 shows the cumulative hydrogen production along the reaction time for neat gels with and without the addition of H_2PtCl_6 (1% w_{Pt}/w_{MOG}) as co-catalyst. B100 sample without co-catalyst reaches a production of 4.6 ± 0.5 μmol of H_2 after the 16 h irradiation, with a mean activity of 56 ± 5 $\mu mol_{H_2} \cdot g_{MOG}^{-1} \cdot h^{-1}$. The addition of H_2PtCl_6 helps to increase the production of H_2 up to 15 ± 1 μmol with an improved activity of 227 ± 11 $\mu mol_{H_2} g_{MOG}^{-1} \cdot h^{-1}$. Interestingly, the MOG containing NH_2BDC as linker (A100) does not produce hydrogen and the gel based on a mixture of both bridging ligands (A50B50) produces a small amount of hydrogen, almost negligible, in comparison, regardless the addition of the co-catalyst.

The inclusion of the amino-functionalized linker seems to be self-defeating for photocatalytic hydrogen production under these experimental conditions in these systems despite the light absorption properties of the materials in the visible region is

enhanced. At this point, we must consider that the photocatalytic mechanism in this kind of metal-organic assembles usually takes place by a ligand to metal charge transfer (LMCT) in which an electron from the HOMO comprised by π-type orbitals of the ligand is promoted to the metal-centred LUMO (empty d orbitals).[17] This phenomenon produces a spatial separation of the photogenerated charges (holes, h^+ and electrons, e^-), which enlarge their mean lifetime and allow the progress of the corresponding oxidation and reduction photoreactions. As a result, an eventual and partial reduction of Ti(IV) to Ti(III) takes place, as demonstrated by electron paramagnetic resonance measurements.[18] Besides, the formation of Ti(III) is evidenced by a colour change of the sample (note that d-d transitions in octahedral titanium(III) complexes, $t_{2g}^1\ e_g^0$, render usually blue-violet colour).[22] The formation of Ti(III) seems to indicate that the photoreduction of water (*i.e.* HER) is more sluggish than photooxidation of sacrificial agent semireaction.

This colour change occurs in B100 sample without the addition of co-catalyst (Figure 5.38), in which an intense blue colour is observed along and after the light irradiation experiments due to the accumulation of Ti(III) species (the blue colour disappear in the post-irradiated samples after some hours as Ti(III) goes back to Ti(IV) once the reaction has concluded). Contrarily, A100 or B50A50 samples did not show any colour change. This fact could mean that the ligand-to-metal charge transfer (LMCT) is not active for these materials or that the h^+/e^- pair lifetime in amino-functionalized samples is reduced or affected because of a limit access of the hole scavenger (electron donor in the photooxidation semireaction). However, the former explanation should lead to an average result in terms of H_2 production for the sample containing both ligands (B50A50), which is opposed to the experimental observation and thus, it makes more likely a lifetime reduction or a favoured recombination of the hole-electron pair prompted by the inclusion of amino-functionalized linkers in the material.

In the case of B100 using the co-catalyst, the colour of the catalyst after irradiation turns slightly brownish instead of blue (Figure 5.38), which can be ascribed to the formation of colloidal Pt(0)[62] due to the reduction of the co-catalyst during the photocatalytic process. This colour and the hydrogen production enhancement also suggest that platinum accelerates the transfer of the photoelectrons and therefore, Ti(III) formation is not evidenced. Note that the efficiency of the co-catalyst requires a good contact with the catalyst in order to favour the electron transfer, thus it is expected that the colloidal Pt has been deposited onto the MOG. In the case of B50A50 and A100 a darker brownish colour also appears when using the co-catalyst, that could also mean the formation of colloidal Pt(0), but this does not promote effectively the overall reaction.

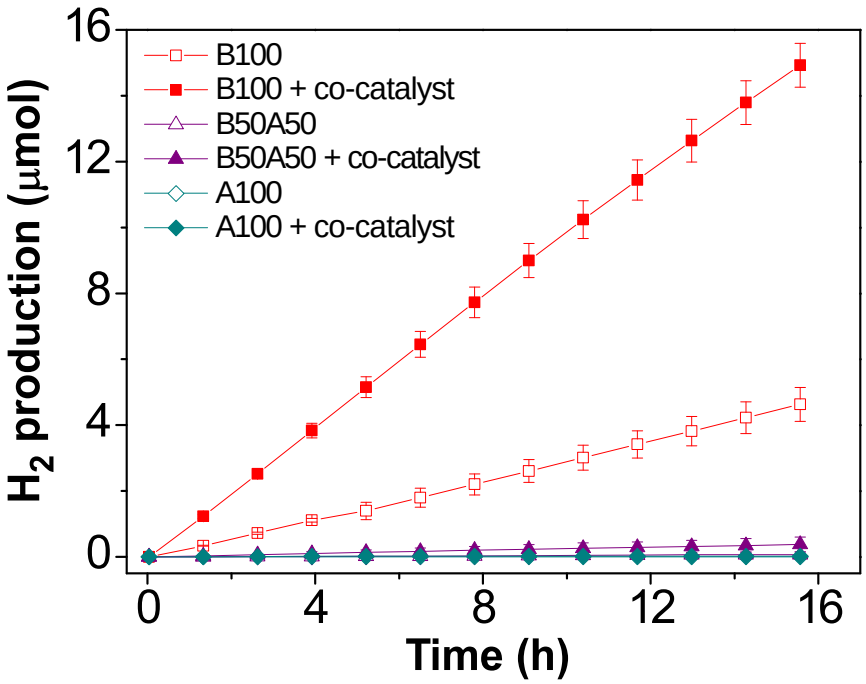

Figure 5.37. Photocatalytic H_2 generation in neat MOGs with and without 1% w_{Pt}/w_{MOG} of H_2PtCl_6 as co-catalyst.

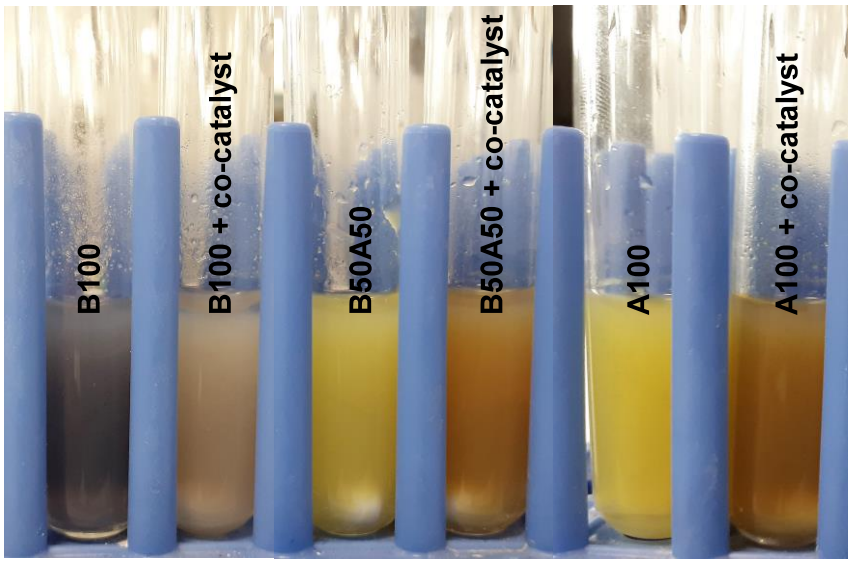

Figure 5.38. Appearance of gels after HER experiments with and without the addition of H_2PtCl_6 as co-catalyst.

When Pt(IV)-doped samples are tested the same tendency is observed. Pt@B100 samples generate a comparable but slightly smaller hydrogen production to that of B100 with co-catalyst, but Pt@B50A50 and Pt@A100 exhibited a poor hydrogen production (Figure 5.39). Precisely upon the explored reaction time, Pt@B100 produced 13 ± 7 µmol of H_2, with a mean activity value of 110 ± 98 $\mu mol_{H_2} \cdot g_{MOG}^{-1} \cdot h^{-1}$. The higher standard deviation in this case could come from an inhomogeneous distribution of the platinum along the doped-MOG, which can be crucial when working with small samples of catalyst (*ca.* 5 mg). Despite this result makes the in-situ addition of the

platinum a more controllable procedure, the reproducibility of the Pt-doped samples could be improved scaling up the experiments. It deserves to note that, as previously analysed, the average amount of Pt in this doped sample is 0.1% ($w_{Pt}/w_{dried\text{-}MOG}$), which is ten times smaller than the amount of platinum added in-situ in the experiments using H_2PtCl_6 as co-catalyst. This result suggests that the in-situ addition of the co-catalyst wastes a meaningful amount of Pt probably because not all of the added Pt gets in contact with the photocatalyst and therefore, it does not contribute to the photoelectron transfer and HER. Effectively, when the amount of incorporated platinum in B100 sample in the experiments using co-catalyst after recovering and cleaning the sample was analysed by XRF, this turned out to be 0.5% ($w_{Pt}/w_{dried\text{-}MOG}$), a bit higher than in Pt@B100. This can explain the small better performance in terms of activity (mean values of 227 ± 11 and 110 ± 98 $\mu mol_{H_2} \cdot g_{MOG}^{-1} \cdot h^{-1}$ for B100 with co-catalyst and Pt@B100, respectively) and it also means that the in-situ doping process using light irradiation is more efficient. The colour of the samples during and after the HER experiments using Pt-doped samples are comparable to that of neat gels when using co-catalyst due to the same reason explained before.

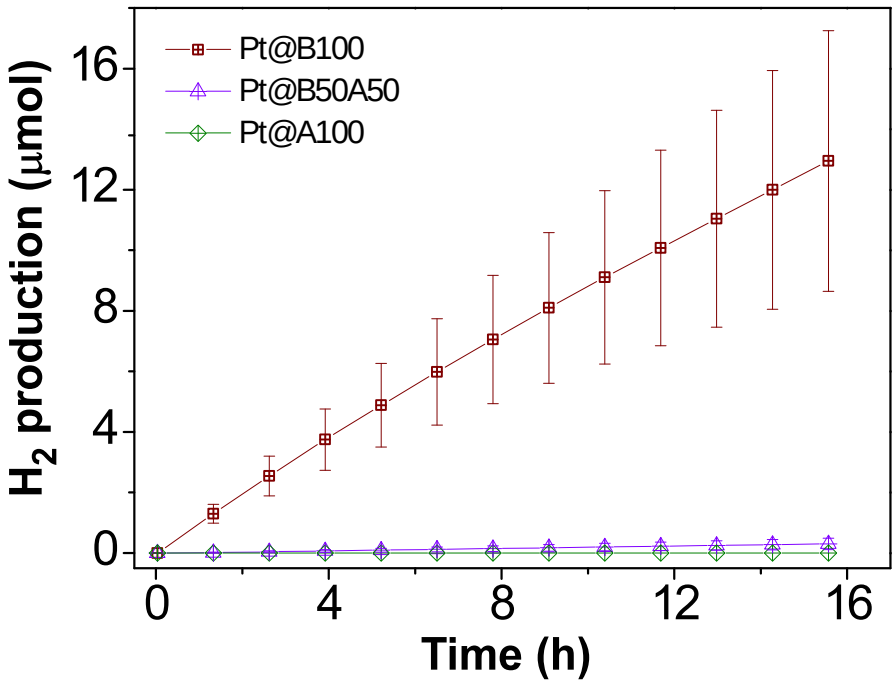

Figure 5.39. Photocatalytic H_2 generation in Pt(IV)-doped MOGs.

To end up with the photocatalytic HER experiments, a last set of tests were performed using UV filter and B100 (with and without added co-catalyst) and Pt@B100 photocatalytic materials. In these experiments an UV filter allowed to irradiate the system only with the visible light (λ > 400 nm) provided by the solar simulator. The HER yields followed the similar trend observed after 16 h of irradiation (H_2 production of 9.1 μmol, 23.2 μmol and 14.5 μmol for B100, B100 with co-catalyst and Pt@B100, respectively), but surprisingly, the activity for hydrogen production overpassed that

achieved when using the full emission spectra provided by the lamp (overall solar spectrum) in the three cases (Figure 5.40). At this point we might consider that, as previously mentioned, since ligand-ligand transitions for BDC and metal-metal transitions for the cluster take place in UV region, the absorption in the visible region observed in Figure 5.35 is ascribed to LMCT which according to previous studies leads the HER mechanism. The photoelectron promoted to higher energy levels upon UV absorption do not necessarily contribute to the photoreduction and can decay through other radiative or not radiative processes.[63] In this scenario, and considering that the power of the lamp (100 $mW \cdot cm^{-2}$) allows to assume that an excess of photons are reaching the sample, a competing situation between the absorption of visible and UV photons in the generation of photoelectrons would result in a decay of HER compared to a situation in where solely visible photons are employed. Additional experiments and theoretical calculations should be performed in order to further analyse and understand this phenomena.

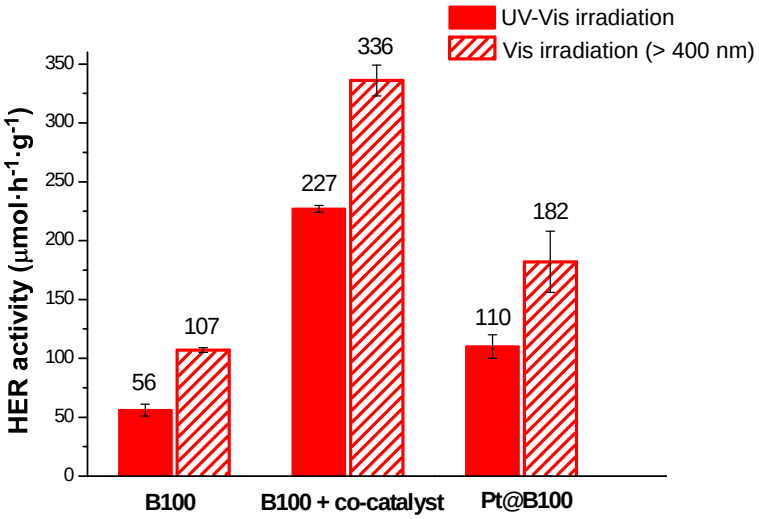

Figure 5.40. Photocatalytic H_2 generation activity comparison for neat and doped BDC-based MOGs under UV-Vis or Vis (400 nm cut-off filter) irradiation conditions.

If we compare the activities achieved with the values found in the literature for MIL-125 and MIL-125-NH_2–based catalyst (40 – 4000 $\mu mol \cdot g^{-1} \cdot h^{-1}$),[64] the values obtained here would be located in the low range of production of H_2, but it is interesting to remark that under visible-light only the aminated or post-modified derivatives are active, while non-aminated ones are only active under UV-Vis irradiation.[65] This makes interesting the fact that B100 metal-organic gel, based on Ti(IV) and BDC linker, not only is active, but it improves a bit its activity when exposure only to visible-light irradiation, what requires further studies for understanding.

In order to analyse B100 sample after HER experiments, TEM-mapping measurements were performed in B100 sample after the HER experiments using co-catalyst (Figure 5.41). It allowed to observe the platinum agglomeration on the surface of the gel as consequence of the in-situ reduction of Pt(IV) into Pt(0) while irradiation, which results crucial in promoting H_2 production, as previously explained.

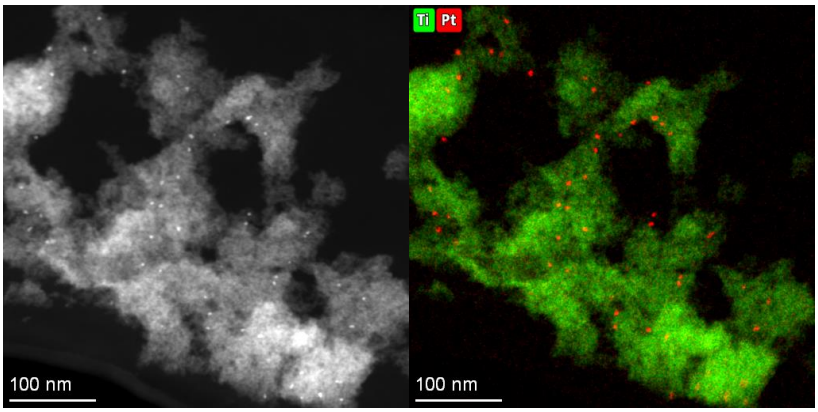

Figure 5.41. HAADF-TEM micrograph and Ti and Pt element mapping taken on B100 cleaned xerogel after HER experiment using H_2PtCl_6 as co-catalyst.

5.4. CONCLUSIONS

In this chapter two family of Ti(IV)-based metal-organic gels have been presented, which are suitable for performing CO_2 reduction and H_2 production under visible light and simulated solar irradiation, respectively.

Firstly, in the Cu(II)-doped porphyrin-based MOGs family the TCPP ligand has been successfully incorporated, as well as different amounts of copper dopant during a post synthetic modification procedure. The aerogels obtained after a supercritical drying process present a considerable high surface area (600-800 m^2g^{-1}) and suitable optical properties. This features enable the materials as efficient catalysts for the photoreduction of carbon dioxide into alcohols (methanol and ethanol) under visible-light irradiation. The post-synthetic metalation with Cu(II) boosts alcohols production rate and apparent quantum yield, reaching maximum values of 642 $\mu mol \cdot g^{-1} \cdot h^{-1}$ and 20%, respectively. Besides, the presence of copper(II) counterbalances the selectivity towards ethanol from a 10% in pristine MOA to a 76% in Cu(II)-doped ones.

On the other hand, the Ti(IV)/BDC and Ti/NH_2-BDC gels obtained present analogous microstructural features but only BDC-based system have demonstrated to be active under simulated solar irradiation for the production of H_2. When platinum is included as co-catalyst in the reaction media or alternatively anchored in the MOG structure, the HER performance is markedly increased. In this regard, despite the in-situ addition of the co-catalyst provides somewhat greater activities for H_2 production than Pt(IV)-doped MOG, it implies a greater amount of Pt in the reaction media. Interestingly, these

materials show an increase in the activity when irradiated only with visible light (λ >400 nm) probably due to a competing situation between the absorption of visible and UV photons in the generation of photoelectrons when exposed to the overall sun spectrum, being the UV-mediated one not active/accessible for reducing protons.

5.5. References

1 A. Fujishima and K. Honda, Electrochemical photolysis of water at a semiconductor electrode, *Nature*, 1972, **238**, 37–38.

2 T. Inoue, A. Fujishima, S. Konishi and K. Honda, Photoelectrocatalytic reduction of carbon dioxide in aqueous suspensions of semiconductor powders, *Nature*, 1979, **277**, 637–638.

3 J. Albo, M. Alvarez-Guerra and A. Irabien, Electro-, photo-, and photoelectro-chemical reduction of CO_2, in *Heterogeneous Catalysts: Advanced Design, Characterization and Applications*, eds. W. Y. Teoh, A. Urakawa, Y. H. Ng and P. Sit, WILEY-VCH GmbH, First Edit., 2021, pp. 649–669.

4 E. A. Elgohary, Y. M. A. Mohamed, H. A. El Nazer, O. Baaloudj, M. S. S. Alyami, A. El Jery, A. A. Assadi and A. Amrane, A Review of the use of semiconductors as catalysts in the photocatalytic inactivation of microorganisms, *Catalysts*, 2021, **11**, 1498.

5 A. M. Asiri and E. Lichtfouse, Conversion of carbon dioxide into hydrocarbons Vol.1: Catalysis, in *Enviromental chemistry for a sustainable world*, Springer, Cham, Switzerland, 2019, vol. 40.

6 J. K. Stolarczyk, S. Bhattacharyya, L. Polavarapu and J. Feldmann, Challenges and prospects in solar qater splitting and CO_2 reduction with inorganic and hybrid nanostructures, *ACS Catal.*, 2018, **8**, 3602–3635.

7 K. C. Christoforidis and M. Fernández-García, Photoactivity and charge trapping sites in copper and vanadium doped anatase TiO_2 nano-materials, *Catal. Sci. Technol.*, 2016, **6**, 1094–1105.

8 K. C. Christoforidis and P. Fornasiero, Photocatalysis for hydrogen Production and CO_2 reduction: The case of copper-catalysts, *ChemCatChem*, 2019, **11**, 368–382.

9 K. C. Christoforidis and P. Fornasiero, Photocatalysis for hydrogen production and CO_2 reduction: The case of copper-catalysts, *ChemCatChem*, 2019, **11**, 368–382.

10 F. Sordello, P. Calza, C. Minero, S. Malato and M. Minella, More than one century of history for photocatalysis, from past, present and future perspectives, *Catalysts*, 2022, **12**, 1572.

11 X. Chen and S. S. Mao, Titanium dioxide nanomaterials: Synthesis, properties, modifications, and applications, *Chem. Rev.*, 2007, **107**, 2891–2959.

12 X. Chen, L. Liu, P. Y. Yu and S. S. Mao, Increasing solar absorption for photocatalysis with black hydrogenated titanium dioxide nanocrystals, *Science*, 2011, **331**, 746–750.

13 A. V. Akimov, A. J. Neukirch and O. V. Prezhdo, Theoretical insights into photoinduced charge transfer and catalysis at oxide interfaces, *Chem. Rev.*, 2013, **113**, 4496–4565.

14 J.-L. Wang, C. Wang and W. Lin, Metal–organic frameworks for light harvesting and photocatalysis, *ACS Catal.*, 2012, **2**, 2630–2640.

15 T. Zhang and W. Lin, Metal–organic frameworks for artificial photosynthesis and photocatalysis, *Chem. Soc. Rev.*, 2014, **43**, 5982–5993.

16 S. Wang and X. Wang, Multifunctional metal-organic frameworks for photocatalysis, *Small*, 2015, **11**, 3097–3112.

17 R. Li, W. Zhang and K. Zhou, Metal–organic-framework-based catalysts for photoreduction of CO_2, *Adv. Mater.*, 2018, **30**, 1705512.

18 Y. Li, H. Xu, S. Ouyang and J. Ye, Metal–organic frameworks for photocatalysis, *Phys. Chem. Chem. Phys.*, 2016, **18**, 7563–7572.

19 Y. Horiuchi, T. Toyao, M. Saito, K. Mochizuki, M. Iwata, H. Higashimura, M. Anpo and M. Matsuoka, Visible-light-promoted photocatalytic hydrogen production by using an amino-functionalized Ti(IV) metal-organic framework, *J. Phys. Chem. C*, 2012, **116**, 20848–20853.

20 T. Hisatomi, J. Kubota and K. Domen, Recent advances in semiconductors for photocatalytic and photoelectrochemical water splitting, *Chem. Soc. Rev.*, 2014, **43**, 7520–7535.

21 J. He, J. Wang, Y. Chen, J. Zhang, D. Duan, Y. Wang and Z. Yan, A dye-sensitized Pt@UiO-66(Zr) metal–organic framework for visible-light photocatalytic hydrogen production, *Chem. Commun.*, 2014, **50**, 7063–7066.

22 Y. Fu, D. Sun, Y. Chen, R. Huang, Z. Ding, X. Fu and Z. Li, An amine-functionalized titanium metal-organic framework photocatalyst with visible-light-induced activity for CO_2 reduction, *Angew. Chemie Int. Ed.*, 2012, **51**, 3364–3367.

23 D. Sun, Y. Fu, W. Liu, L. Ye, D. Wang, L. Yang, X. Fu and Z. Li, Studies on photocatalytic CO_2 reduction over NH_2-UiO-66(Zr) and its derivatives: Towards a better understanding of photocatalysis on metal-organic frameworks, *Chem. - A Eur. J.*, 2013, **19**, 14279–14285.

24 T. Toyao, M. Saito, Y. Horiuchi, K. Mochizuki, M. Iwata, H. Higashimura and M. Matsuoka, Efficient hydrogen production and photocatalytic reduction of nitrobenzene over a visible-light-responsive metal–organic framework photocatalyst, *Catal. Sci. Technol.*, 2013, **3**, 2092.

25 L. Shen, W. Wu, R. Liang, R. Lin and L. Wu, Highly dispersed palladium nanoparticles anchored on UiO-66(NH_2) metal-organic framework as a reusable and dual functional visible-light-driven photocatalyst, *Nanoscale*, 2013, **5**, 9374.

26 H. Yang, X.-W. He, F. Wang, Y. Kang and J. Zhang, Doping copper into ZIF-67 for enhancing gas uptake capacity and visible-light-driven photocatalytic degradation of organic dye, *J. Mater. Chem.*, 2012, **22**, 21849.

27 L. Wang, P. Jin, J. Huang, H. She and Q. Wang, Integration of copper(II)-porphyrin zirconium metal–organic framework and titanium dioxide to construct Z-Scheme System for highly improved photocatalytic CO_2 reduction, *ACS Sustain. Chem. Eng.*,

2019, **7**, 15660–15670.

28 S. Jansson, The light-harvesting chlorophyll ab-binding proteins, *Biochim. Biophys. Acta - Bioenerg.*, 1994, **1184**, 1–19.

29 R. Giovannetti, The Use of spectrophotometry UV-Vis for the study of porphyrins, in *Macro To Nano Spectroscopy*, InTechOpen, London, United Kingdom, 2012.

30 C. Lin, C. Han, H. Zhang, L. Gong, Y. Gao, H. Wang, Y. Bian, R. Li and J. Jiang, Porphyrin-based metal–organic frameworks for efficient photocatalytic H_2 production under visible-light irradiation, *Inorg. Chem.*, 2021, **60**, 3988–3995.

31 K. Zhang, S. Goswami, H. Noh, Z. Lu, T. Sheridan, J. Duan, W. Dong and J. T. Hupp, An iron-porphyrin grafted metal–organic framework as a heterogeneous catalyst for the photochemical reduction of CO_2, *J. Photochem. Photobiol.*, 2022, **10**, 100111.

32 Z. Wang, Z. Liu, J. Huang, Y. Chen, R. Su, J. He, G. Lv, B. Gao, W. Zhou, Y. Wang, Z. Wang and Q. Li, Zr_6O_8-porphyrinic MOFs as promising catalysts for the boosting photocatalytic degradation of contaminants in high salinity wastewater, *Chem. Eng. J.*, 2022, **440**, 135883.

33 D. Xie, S. Wang, S. Li, W. Yang and Y.-S. Feng, A two-dimensional Bi-based porphyrin metal–organic framework photocatalyst for white light-driven selective oxidation of sulfides, *Catal. Sci. Technol.*, 2022, **12**, 3254–3260.

34 A. Aziz, A. R. Ruiz-Salvador, N. C. Hernández, S. Calero, S. Hamad and R. Grau-Crespo, Porphyrin-based metal-organic frameworks for solar fuel synthesis photocatalysis: band gap tuning via iron substitutions, *J. Mater. Chem. A*, 2017, **5**, 11894–11904.

35 P. Sehgal and A. K. Narula, Metal substituted metalloporphyrins as efficient photosensitizers for enhanced solar energy conversion, *J. Photochem. Photobiol. A Chem.*, 2019, **375**, 91–99.

36 A. Angulo-Ibáñez, M. Perfecto-Irigaray, I. Merino-Garcia, N. Luengo, A. M. Goitandia, J. Albo, E. Aranzabe, G. Beobide, O. Castillo and S. Pérez-Yáñez, Metal-organic aerogels based on titanium(IV) for visible-light conducted CO2 photoreduction to alcohols, *Mater. Today Energy*, 2022, **30**, 101178.

37 C. Zlotea, D. Phanon, M. Mazaj, D. Heurtaux, V. Guillerm, C. Serre, P. Horcajada, T. Devic, E. Magnier, F. Cuevas, G. Férey, P. L. Llewellyn and M. Latroche, Effect of NH_2 and CF_3 functionalization on the hydrogen sorption properties of MOFs, *J. Chem. Soc. Dalt. Trans.*, 2011, **40**, 4879–4881.

38 D.-W. Zhang and W.-T. Chen, Two novel tcpp porphyrinic compounds: in situ syntheses, characterization and reaction mechanism, *J. Chil. Chem. Soc.*, 2017, **62**, 3381–3385.

39 J. Albo, M. I. Qadir, M. Samperi, J. A. Fernandes, I. de Pedro and J. Dupont, Use of an optofluidic microreactor and Cu nanoparticles synthesized in ionic liquid and embedded in TiO_2 for an efficient photoreduction of CO_2 to methanol, *Chem. Eng. J.*, 2021, **404**, 126643.

40 L. Patiny and A. Borel, ChemCalc: A building block for tomorrow's chemical infrastructure, *J. Chem. Inf. Model.*, 2013, **53**, 1223–1228.

41 M. Dan-Hardi, C. Serre, T. Frot, L. Rozes, G. Maurin, C. Sanchez and G. Férey, A new photoactive crystalline highly porous titanium(IV) dicarboxylate, *J. Am. Chem. Soc.*, 2009, **131**, 10857–10859.

42 S. Wang, H. Reinsch, N. Heymans, M. Wahiduzzaman, C. Martineau-Corcos, G. De Weireld, G. Maurin and C. Serre, Toward a rational design of titanium metal-organic frameworks, *Matter*, 2020, **2**, 440–450.

43 S. Yuan, J.-S. Qin, C. T. Lollar and H.-C. Zhou, Stable metal–organic frameworks with group 4 metals: Current status and trends, *ACS Cent. Sci.*, 2018, **4**, 440–450.

44 A. P. Smalley, D. G. Reid, J. C. Tan and G. O. Lloyd, Alternative synthetic methodology for amide formation in the post-synthetic modification of Ti-MIL125-NH_2, *CrystEngComm*, 2013, **15**, 9368–9371.

45 S. Yuan, T. F. Liu, D. Feng, J. Tian, K. Wang, J. Qin, Q. Zhang, Y. P. Chen, M. Bosch, L. Zou, S. J. Teat, S. J. Dalgarno and H. C. Zhou, A single crystalline porphyrinic titanium metal-organic framework, *Chem. Sci.*, 2015, **6**, 3926–3930.

46 Q. R. Ding, G. L. Xu, L. Zhang and J. Zhang, Ligand-directed assembly engineering of trapezoidal {Ti_5} building blocks stabilized by dimethylglyoxime, *Dalt. Trans.*, 2019, **48**, 9916–9919.

47 G. Lan, K. Ni, S. S. Veroneau, X. Feng, G. T. Nash, T. Luo, Z. Xu and W. Lin, Titanium-based nanoscale metal-organic framework for type I photodynamic therapy, *J. Am. Chem. Soc.*, 2019, **141**, 4204–4208.

48 K. N. Solo'ev, V. N. Knyukshto and G. D. Egorova, New features of the phosphorescence of copper complexes of meso-trtraarylporphyrins, *J. Appl. Spectrosc.*, 1999, **66**, 743–747.

49 P. Makuła, M. Pacia and W. Macyk, How to correctly determine the band gap energy of modified semiconductor photocatalysts based on UV-Vis spectra, *J. Phys. Chem. Lett.*, 2018, **9**, 6814–6817.

50 M. Gouterman, Study of the effects of substitution on the absorption spectra of porphin, *J. Chem. Phys.*, 1959, **30**, 1139–1161.

51 M. Gouterman, Spectra of porphyrins, *J. Mol. Spectrosc.*, 1961, **6**, 138–163.

52 Y. Fu, H. Yang, R. Du, G. Tu, C. Xu, F. Zhang, M. Fan and W. Zhu, Enhanced photocatalytic CO_2 reduction over Co-doped NH_2-MIL-125(Ti) under visible light, *RSC Adv.*, 2017, **7**, 42819–42825.

53 H. Xiao, W. Zhang, Q. Yao, L. Huang, L. Chen, B. Boury and Z. Chen, Zn-free MOFs like MIL-53(Al) and MIL-125(Ti) for the preparation of defect-rich, ultrafine ZnO nanosheets with high photocatalytic performance, *Appl. Catal. B Environ.*, 2019, **244**, 719–731.

54 P. J. Linstrom and W. G. Mallard, NIST Chemistry WebBook, NIST Standard Reference Database Number 69, *Natl. Inst. Stand. Technol. Gaithersbg. MD, 20899*, (accessed: November 2022).

55 K. Zhu, M. Zhang, X. Feng, L. Qin, S. Z. Kang and X. Li, A novel copper-bridged graphitic carbon nitride/porphyrin nanocomposite with dramatically enhanced photocatalytic hydrogen generation, *Appl. Catal. B Environ.*, 2020, **268**, 118434.

56 R. R. Solís, A. Gómez-Avilés, C. Belver, J. J. Rodriguez and J. Bedia, Microwave-assisted synthesis of NH2-MIL-125(Ti) for the solar photocatalytic degradation of aqueous emerging pollutants in batch and continuous tests, *J. Environ. Chem. Eng.*, 2021, **9**, 106230.

57 H. Yamashige, S. Matsuo, T. Kurisaki, R. C. C. Perera and H. Wakita, Local structure of nitrogen atoms in a porphine ring of meso-phenyl substituted porphyrin with an electron-withdrawing group using X-ray photoelectron spectroscopy and X-ray absorption spectroscopy, *Anal. Sci.*, 2005, **21**, 635–639.

58 M. Thommes, K. Kaneko, A. V. Neimark, J. P. Olivier, F. Rodriguez-Reinoso, J. Rouquerol and K. S. W. Sing, Physisorption of gases, with special reference to the evaluation of surface area and pore size distribution (IUPAC Technical Report), *Pure Appl. Chem.*, 2015, **87**, 1051–1069.

59 L. Li, X. Wang, T. Liu and J. Ye, Titanium-based MOF materials: from crystal engineering to photocatalysis, *Small Methods*, 2020, **4**, 2000486.

60 J. Santos-Lorenzo, R. San José-Velado, J. Albo, G. Beobide, P. Castaño, O. Castillo, A. Luque and S. Pérez-Yáñez, A straightforward route to obtain zirconium based metal-organic gels, *Microporous Mesoporous Mater.*, 2019, **284**, 128–132.

61 M. Taddei, G. M. Schukraft, M. E. A. Warwick, D. Tiana, M. J. McPherson, D. R. Jones and C. Petit, Band gap modulation in zirconium-based metal–organic frameworks by defect engineering, *J. Mater. Chem. A*, 2019, **7**, 23781–23786.

62 G. Marzun, C. Streich, S. Jendrzej, S. Barcikowski and P. Wagener, Adsorption of colloidal platinum nanoparticles to supports: Charge transfer and effects of electrostatic and steric interactions, *Langmuir*, 2014, **30**, 11928–11936.

63 J. Wang, A. S. Cherevan, C. Hannecart, S. Naghdi, S. P. Nandan, T. Gupta and D. Eder, Ti-based MOFs : New insights on the impact of ligand composition and hole scavengers on stability, charge separation and photocatalytic hydrogen evolution, *Appl. Catal. B Environ.*, 2021, **283**, 119626.

64 N. S. Abdul Mubarak, K. Y. Foo, R. Schneider, R. M. Abdelhameed and S. Sabar, The chemistry of MIL-125 based materials: Structure, synthesis, modification strategies and photocatalytic applications, *J. Environ. Chem. Eng.*, 2022, **10**, 106883.

65 Y. Horiuchi, T. Toyao, M. Saito, K. Mochizuki, M. Iwata, H. Higashimura, M. Anpo and M. Matsuoka, Visible-light-promoted photocatalytic hydrogen production by using an amino-functionalized Ti(IV) metal–organic framework, *J. Phys. Chem. C*, 2012, **116**, 20848–20853.

Chapter 6

Conclusions and publications

6.1. CONCLUSIONS

According to the established objectives, this PhD thesis have allowed to further explore the inspiring area of the design and synthesis of metal-organic materials and to assess their performance in the electrochemical and photochemical conversion of CO_2 and hydrogen production. Despite the conclusions related to each of the defined specific objectives are detailed at the end of Chapters 3, 4 and 5, below a summary of the major conclusions are gathered:

1. The inclusion doping metals in copper-based MOFs (HKUST-1(Cu,M_D)) to afford heterometallic catalysts, allows to tune the reaction rates and Faradaic efficiencies of the electrochemical conversion of CO_2 into alcohols, in such a way that Pd(II) worsens the activity provided by the homometallic copper while Ru(III) provides a marked improvement.

2. Despite bismuth(III) cannot be successfully used as doping metal following the aforementioned via, the preparation and application of a bimetallic Cu/Bi electrocatalyst comprised by physical blends of HKUST-1(Cu) and CAU-17(Bi) have demonstrated to reach reaction rates and Faradiac efficiencies far greater than any previously analyzed metal-organic framework and close to the maximum values reported for electrocatalysts.

3. Unfortunately, both types of MOFs (HKUST-1 and CAU-17) have a limited stability in the reaction media and the performance decay to low-moderate values after certain time of reaction (*ca*. 60 min).

4. Considering the aforementioned conclusions, we succeeded developing a new family of robust MOFs named as EHU-30 and based on groups 4 metals (Zr(IV) and Hf(IV)) and benzene-1,4-dicarboxylato ligand with or without amino-type functional groups.

5. The structural elucidation of this family revealed that it comprises the first known polymorphic series of the paradigmatic UiO-66 which settled in 2008 the fruitful chemistry of the group 4 metals (Ti, Zr, Hf) MOFs.

6. The assessment of this family as electrocatalyst in the electrochemical CO_2 reduction, demonstrates that the achieved performance does not surpass that achieved with HKUST-1 family, but conversely, the production rates and Faradic efficiencies do not decay along the explored reaction time (400 min) which can be ascribed to the greater stability of the coordination framework.

7. The fine tuning of the reaction conditions allowed us to develop Ti(IV) metal-organic gels and aerogels consisting of nanoscopic metal-organic framework particles entangled into a meso-/macroporous structure with the capability of behaving as photocatalyts under visible light.

8. Accordingly, Cu/porphyrine functionalized Ti(IV) metal-organic gels demonstrated to photocatalyze the CO_2 photoreduction into alcohols with performances that overpassed that reported for MOFs and inorganic catalysts. Interestingly the presence of copper(II) played a crucial role counterbalancing the selectivity towards more demanding ethanol production.

9. Developed pristine Ti(IV) metal-organic gels showed relatively low yields in the hydrogen evolution reaction, but their activity was markedly boosted upon the *in situ* addition of platinum in the reaction media or by doping with platinum the gel framework. Despite of this improvement, the overall performance is still below that provided by conventional materials and thus further work is still required to improve these metal-organic materials.

6.2. PUBLICATIONS RESULTING FROM THIS PhD THESIS

The results obtained during the development of this PhD thesis have yielded a total of five research articles (numbers 1–5. of the below detailed publications) and they include directly the work described in chapters 3 and 4. However, part of the results have allowed me to be co-authoring of other two published works (numbers 6. and 7.), but they have not been included in their fullness in this thesis manuscript as these results form a cooperative work with another PhD student. See below details of the published articles and of the quality figures of the journals corresponding to the publication year:

[1] **Authors:** Perfecto-Irigaray, M.; Albo, J.; Beobide, G.; Castillo, O.; Irabien, A.; Pérez-Yáñez, S.
Title: Synthesis of heterometallic metal–organic frameworks and their performance as electrocatalyst for CO_2 reduction
Journal: *RSC Advances,* **2018**, 8, 21092-21099.
DOI: https://doi.org/10.1039/C8RA02676A
Quartil and position in the JCR category: Q2, 68/172 (*Chemistry, Multidisciplinary*)
Impact Index: 3.049

[2] **Authors:** Albo J.; Perfecto-Irigaray, M.; Beobide G.; Irabien A.

Title: Cu/Bi metal-organic framework-based systems for an enhanced electrochemical transformation of CO_2 to alcohols
Journal: *Journal of CO_2 Utilization,* **2019**, 33, 157 - 165.
DOI: https://doi.org/10.1016/j.jcou.2019.05.025
Quartil and position in the JCR category: Q1, 36/172 (*Chemistry, Multidisciplinary*)
Impact Index: 5.993

[3] **Authors:** Perfecto-Irigaray, M.; Beobide, G.; Castillo, O.; da Silva, I.; Garcia-Lojo, D.; Luque, A.; Mendia, A.; Pérez-Yáñez, S.
Title: $[Zr_6O_4(OH)_4(\text{benzene-1,4-dicarboxylato})_6]_n$: a hexagonal polymorph of UiO-66
Journal: *Chemical Communications,* **2019**, 55, 5954-5957.
DOI: https://doi.org/10.1039/C9CC00802K
Quartil and position in the JCR category: Q1, 34/177 (*Chemistry, Multidisciplinary*)
Impact Index: 5.996

[4] **Authors:** Perfecto-Irigaray, M.; Beobide, G.; Calero, S.; Castillo, O.; da Silva, I.; Gutierrez-Sevillano, J. J.; Luque, A.; Pérez-Yáñez, S.; Velasco, L. F.
Title: Metastable Zr/Hf-MOFs: the hexagonal family of EHU-30 and their water-sorption induced structural transformation

Journal: *Inorganic Chemistry Frontiers,* **2021**, 8, 4767–4779.
DOI: https://doi.org/10.1039/D1QI00997D
Quartil and position in the JCR category: Q1, 3/45 (*Chemistry, Inorganic & Nuclear*)
Impact Index: 6.569

[5] **Authors:** Landaluce, N.; Perfecto-Irigaray, M.; Albo, J.; Beobide, G.; Castillo, O.; Irabien, A.; Luque, A.; Mendez A. S. J.; Platero-Prats, A. E.; Pérez-Yáñez, S.
Title: Copper(II) invigorated EHU-30 for continuous electroreduction of CO_2 into value-added chemicals
Journal: *Scientific Reports,* **2022**, 12, 8505.
DOI: https://doi.org/10.1038/s41598-022-11846-w
Quartil and position in the JCR category: Q1, 19/135 (*Multidisciplinary Sciences*)
Impact Index: 4.997

[6] **Authors:** Angulo-Ibanez, A.; Perfecto-Irigaray, M; Merino-Garcia, I; Luengo, N.; Goitandia, A. M.; Albo, J.; Aranzabe, E.; Beobide, G.; Castillo, O.; Pérez-Yáñez, S.
Title: Metal-organic aerogels based on titanium(IV) for visible-light conducted CO_2 photoreduction to alcohols
Revista: *Materials Today Energy,* **2022**, 30, 101178.
DOI: https://doi.org/10.1016/j.mtener.2022.101178
Quartil and position in the JCR category: Q1, 59/345 (*Materials Science, Multidisciplinary*);
Impact Index: 9.257

[7] **Authors:** Angulo-Ibanez, A.; Luengo, N.; Aranzabe, E.; Beobide, G.; Castillo, O.; Goitandia, A. M.; Pérez-Yáñez, S.; Perfecto-Irigaray, M.; Villamayor, A.
Title: Low temperature curable titanium-based sols for visible light photocatalytic coatings for glass and polymeric substrates
Journal: *New Journal of Chemistry,* **2022**, 46, 16192-16202.
DOI: https://doi.org/10.1039/D2NJ02173K
Quartil and position in the JCR category: Q2, 80/179 (*Chemistry, Multidisciplinary*);
Impact Index: 3.925

Porosity in the solid state has always been a striking point in materials science, but in the last decades the study of this type of compounds has experienced an outstanding development due to the appearance of new porous materials such as MOFs that are extending from the nanoscale to the macroscale with endless underlying applications.

Herein presented PhD thesis is based on the development of porous metal-organic materials, such as metal-organic frameworks (MOFs), metal-organic gels (MOGs) and metal-organic aerogels (MOAs), which are further employed for CO_2 valorization, water adsorption and photocatalytic hydrogen production. Each type of material has been specifically designed with the aim of obtaining the best performance in a specific application: (i) Cu(II)-based heterometallic MOFs for electrochemical conversion of CO_2 into alcohols, (ii) robust Zr(IV)- and Hf(IV)-based MOFs for improving the stability in electrochemical conversion of CO_2, and (iii) Ti(IV) based MOGs and MOAs for photochemical CO_2 reduction and hydrogen evolution reaction.